

(4)

GRADUATE AERONAUTICAL LABORATORIES

CALIFORNIA INSTITUTE OF TECHNOLOGY

NOMINALLY 2-DIMENSIONAL FLOW ABOUT
A NORMAL FLAT PLATE

Derek Lisoski

1993

AD-A274 472



DTIC
ELECTED
DEC 22 1993

93-30847

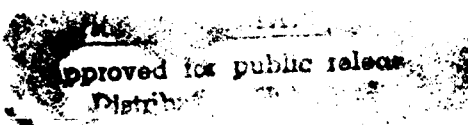


104083

Firestone Flight Sciences Laboratory

Guggenheim Aeronautical Laboratory

Karman Laboratory of Fluid Mechanics and Jet Propulsion



83 12 21 187

Pasadena

Unclassified

SECURITY CLASSIFICATION OF THIS PAGE

Form Approved
OMB No. 0704-0188

REPORT DOCUMENTATION PAGE

1a. REPORT SECURITY CLASSIFICATION <u>Unclassified</u>		1b. RESTRICTIVE MARKINGS													
2a. SECURITY CLASSIFICATION AUTHORITY		3. DISTRIBUTION/AVAILABILITY OF REPORT Approved for public release; distribution is unlimited.													
2b. DECLASSIFICATION/DOWNGRADING SCHEDULE		5. MONITORING ORGANIZATION REPORT NUMBER(S)													
4. PERFORMING ORGANIZATION REPORT NUMBER(S) N00014-90-J-1589		7a. NAME OF MONITORING ORGANIZATION Office of Naval Research													
6a. NAME OF PERFORMING ORGANIZATION Graduate Aeronautical Labs California Inst. of Technology	6b. OFFICE SYMBOL (If applicable)	7b. ADDRESS (City, State, and ZIP Code) 800 N. Quincy Street Arlington, Virginia 22217-5000													
8a. NAME OF FUNDING/SPONSORING ORGANIZATION Office of Naval Research	8b. OFFICE SYMBOL (If applicable)	9. PROCUREMENT INSTRUMENT IDENTIFICATION NUMBER N00014-90-J-1589													
8c. ADDRESS (City, State, and ZIP Code) 800 N. Quincy Street Arlington, VA 22217-5000	10. SOURCE OF FUNDING NUMBERS PROGRAM ELEMENT NO. PROJECT NO. TASK NO. WORK UNIT ACCESSION NO.														
11. TITLE (Include Security Classification) Nominally 2-Dimensional Flow About A Normal Flat Plate (Unclassified)															
12. PERSONAL AUTHOR(S) Derek Lisoski															
13a. TYPE OF REPORT Annual	13b. TIME COVERED FROM <u>10/1/92</u> TO <u>9/30/93</u>	14. DATE OF REPORT (Year, Month, Day) 1993 August 1	15. PAGE COUNT												
16. SUPPLEMENTARY NOTATION Ph. D. thesis															
17. COSATI CODES <table border="1"><tr><th>FIELD</th><th>GROUP</th><th>SUB-GROUP</th></tr><tr><td></td><td></td><td></td></tr><tr><td></td><td></td><td></td></tr><tr><td></td><td></td><td></td></tr></table>		FIELD	GROUP	SUB-GROUP										18. SUBJECT TERMS (Continue on reverse if necessary and identify by block number) bluff body; vortex shedding; near wake; accelerating body drag.	
FIELD	GROUP	SUB-GROUP													
19. ABSTRACT (Continue on reverse if necessary and identify by block number) Towing tank and water channel experiments and a two-dimensional vortex element numerical model were used to study the forces experienced by a bluff flat plate set normal to a nominally two-dimensional flow. Intrinsic (small scale) and extrinsic (large scale) three-dimensional motions in the experimental flow were isolated and their separate and combined effects on forces and overall wake development were studied. Transient flow development starting from rest, as well as steady flow conditions, were investigated.															
20. DISTRIBUTION/AVAILABILITY OF ABSTRACT <input checked="" type="checkbox"/> UNCLASSIFIED/UNLIMITED <input type="checkbox"/> SAME AS RPT. <input type="checkbox"/> DTIC USERS		21. ABSTRACT SECURITY CLASSIFICATION Unclassified													
22a. NAME OF RESPONSIBLE INDIVIDUAL Dr. Thomas F. Swean, Jr.		22b. TELEPHONE (Include Area Code) 703/696-4025	22c. OFFICE SYMBOL												

19. ABSTRACT (continued)

Towing tank experiments indicated that normal plates required sixty to one hundred chord lengths of travel to establish steady vortex shedding. An initial drag peak during acceleration was followed by a drag minimum of $C_d \approx 1.3$ reached while the wake was confined to a symmetric vortex bubble. Subsequent to the breakdown of this bubble, a region of symmetric flow with $C_d \approx 1.6$ and no vortex shedding was apparent for twenty to thirty chord lengths, followed by the final onset of vortex shedding which occurred exponentially. During this onset forces overshot their final steady-state values ($\bar{C}_d \approx 2.0$). Flows with less large scale extrinsic three dimensionality (higher aspect ratio, "more two-dimensional" end conditions, and stratified flow) had longer development times and higher subsequent overshoot levels.

Small geometric asymmetries (angle of attack variations) increased the minimum drag level seen after the acceleration and resulted in an earlier breakdown of the closed wake, followed by an immediate transition to steady shedding. The breakdown of the initial bubble in this case was more coherent spanwise and did not result in a long-lasting symmetric non-shedding flow.

During "steady-state" shedding, modulation in the vortex shedding amplitude at a time scale of five to ten Strouhal periods resulted in a twenty percent fluctuation in mean drag level, with a corresponding increase in rms lift. This modulation accompanied a slow oscillation in the formation distance of the shed vorticity, the period of which was Reynolds number independent but decreased with increasing aspect ratio, reaching a minimum value of six Strouhal periods for aspect ratios greater than ten.

Agreement between three-dimensional experimental and two-dimensional numerical-model results was good at early times, indicating the experiments were two-dimensional until the breakdown of the closed wake bubble following the initial acceleration. Prior to this breakdown the numerical model of a normal plate gave a drag coefficient $C_d \approx 0.9$, similar to that given by the Kirchhoff-Rayleigh free-streamline prediction but lower than experiments. Small asymmetries of the 2d model resulted in an increase in the minimum drag level to $C_d \approx 1.2$. Subsequent to the closed wake breakdown, drag levels of $\bar{C}_d \approx 3.3$ are 65% higher than steady-state experimental values.

Although no region corresponding to the post-acceleration non-vortex-shedding seen experimentally was found in the basic numerical results, the addition of circulation decay to the numerical-model resulted in a region which appeared qualitatively similar. This circulation decay also decreased mean drag levels ($\bar{C}_d \approx 2.6$) and gave an exponential shedding onset with subsequent long period shedding modulation.

Stabilizing spanwise stratification of the experimental flow had little effect for Richardson numbers $Ri \lesssim 10$ (based on chord). For $Re = 1000$ and $Ri = 13.3$ a longer lasting post-acceleration closed wake was followed by strong initial shedding and a large drag overshoot, with a subsequent decrease in shedding amplitude and increase in formation distance to the levels seen in the unstratified $Re = 1000$ case, which exhibited considerable Reynolds number dependence. For plates at 90° angle of attack the symmetric non-vortex shedding region was reduced in duration and subsequent "steady-state" drag levels were increased ten to fifteen percent ($\bar{C}_d \approx 2.11$) from the unstratified case.

**NOMINALLY 2-DIMENSIONAL FLOW ABOUT
A NORMAL FLAT PLATE**

**Thesis by
Derek Lee Ashton Lisoski**

**In Partial Fulfillment
of the Requirements for the degree of**

Doctor of Philosophy

**California Institute of Technology
Pasadena, California**

1993

(Submitted March 9th, 1993)

Revised August 1st, 1993

Accesion For	
NTIS	CRA&I
DTIC	TAB
Unannounced	
Justification _____	
By _____	
Distribution / _____	
Availability Codes	
Dist	Avail and / or Special

A-1

DTIC QUALITY INSPECTED 3

©1993

Derek Lisoski

All Rights Reserved

ACKNOWLEDGMENTS

Firstly, I would like to thank my Mom and Dad, without whose continuing support this project, and many others, could never have been completed. I am also deeply indebted to my advisor Anatol Roshko, whose gentle advice and counsel was invaluable and much appreciated.

Thanks are additionally extended to the rest of my committee, Don Coles, Tony Leonard, Morteza Gharib and John List; as well as to Phil Tokumaru, Dan Keelan, John Budzinski, Greg Cardell, Greg Smedley and Jay Hammer for a great deal of help, advice and friendship.

I would also like to thank Charles Williamson, who designed and constructed the X-Y Towing Tank and lent a great deal of advice early in the project; the aeronautics shop personnel: George Lundgren, George Wilson, and Phil Wood, for their help in the design and construction of my apparatus (and for teaching me as much as they could about machining) and Herb Gaebler, Harry Hamaguchi and Pavel Svitek in the Hydro Lab, who helped me setup and run my water channel experiments.

Finally, computer time used for the numerical results has apparently been donated by Caltech's Jet Propulsion Laboratory, to whom I am grateful.

This research was supported by the Ocean Technology Program of the Office of Naval Research, ONR Grant No. N00014-90-J-1589. It had been initiated with funds from the Air Force Office of Scientific Research URI on Unsteady and Separating Flows, AFOSR Grant No. F49620-86-C-0134.

Dedicated to my parents

ABSTRACT

Towing tank and water channel experiments and a two-dimensional vortex element numerical model were used to study the forces experienced by a bluff flat plate set normal to a nominally two-dimensional flow. Intrinsic (small scale) and extrinsic (large scale) three-dimensional motions in the experimental flow were isolated and their separate and combined effects on forces and overall wake development were studied. Transient flow development starting from rest, as well as steady flow conditions, were investigated.

A force balance was used to measure the unsteady lift and drag of vertically oriented models projecting through a free surface with various lower end conditions; simultaneous LIF flow visualizations imaged the structure of the vortices in the wake. Plate aspect ratio, lower end condition and angle of attack were varied to effect changes in large scale three-dimensional motions, while changes in Reynolds number and Richardson number (flow stratification) modified the small scale three dimensionality intrinsic to the flow.

Towing tank experiments indicated that normal plates required sixty to one hundred chord lengths of travel to establish steady vortex shedding. An initial drag peak during acceleration was followed by a drag minimum of $C_d \approx 1.3$ reached while the wake was confined to a symmetric vortex bubble. Subsequent to the breakdown of this bubble, a region of symmetric flow with $C_d \approx 1.6$ and no vortex shedding was apparent for twenty to thirty chord lengths, followed by the final onset of vortex shedding which occurred exponentially. During this onset forces overshot their final steady-state values ($\bar{C}_d \approx 2.0$). Flows with less large scale extrinsic three dimensionality (higher aspect ratio, "more two-dimensional" end conditions, and stratified flow) had longer development times and higher subsequent overshoot levels.

Small geometric asymmetries (angle of attack variations) increased the minimum drag level seen after the acceleration and resulted in an earlier breakdown of the closed wake, followed by an immediate transition to steady shedding. The breakdown of the initial bubble in this case was more coherent spanwise and did not result in a long-lasting symmetric non-shedding flow.

During "steady-state" shedding, modulation in the vortex shedding amplitude at a time scale of five to ten Strouhal periods resulted in a twenty percent fluctuation in mean drag level, with a corresponding increase in rms lift. This modulation accompanied a slow oscillation in the formation distance of the shed vorticity, the period of which was Reynolds number independent but decreased with increasing aspect ratio, reaching a minimum value of six Strouhal periods for aspect ratios greater than ten.

Agreement between three-dimensional experimental and two-dimensional numerical-model results was good at early times, indicating the experiments were two-dimensional until the breakdown of the closed wake bubble following the initial acceleration. Prior to this breakdown the numerical model of a normal plate gave a drag coefficient $C_d \approx 0.9$, similar to that given by the Kirchhoff-Rayleigh free-streamline prediction but lower than experiments. Small asymmetries of the 2d model resulted in an increase in the minimum drag

level to $C_d \simeq 1.2$. Subsequent to the closed wake breakdown, drag levels of $\overline{C_d} \simeq 3.3$ are 65% higher than steady-state experimental values.

Although no region corresponding to the post-acceleration non-vortex-shedding seen experimentally was found in the basic numerical results, the addition of circulation decay to the numerical-model resulted in a region which appeared qualitatively similar. This circulation decay also decreased mean drag levels ($\overline{C_d} \simeq 2.6$) and gave an exponential shedding onset with subsequent long period shedding modulation.

Stabilizing spanwise stratification of the experimental flow had little effect for Richardson numbers $Ri \lesssim 10$ (based on chord). For $Re = 1000$ and $Ri = 13.3$ a longer lasting post-acceleration closed wake was followed by strong initial shedding and a large drag overshoot, with a subsequent decrease in shedding amplitude and increase in formation distance to the levels seen in the unstratified $Re = 1000$ case, which exhibited considerable Reynolds number dependence. For plates at 90° angle of attack the symmetric non-vortex shedding region was reduced in duration and subsequent "steady-state" drag levels were increased ten to fifteen percent ($\overline{C_d} \simeq 2.11$) from the unstratified case.

TABLE OF CONTENTS

Copyright	ii
Acknowledgments	iii
Abstract	v
Table of contents	vii
List of figures	xi
Nomenclature	xvii
Ch. 1 Introduction	1.1
1.1 Historical Perspective	1.1
1.2 Present Study History and Objectives	1.5
1.3 Thesis Outline	1.6
Ch. 2 Apparatus and Procedures	2.1
2.1 Preface	2.1
2.2 Force Balance and Amplifier	2.2
2.3 Data Acquisition	2.4
2.4 Data Analysis	2.4
2.5 Flat Plate Models	2.5
2.5.1 Flow Visualization	2.6
2.5.2 Plate Mount	2.7
2.5.3 End Plates and End Conditions	2.8
Ch. 3 X-Y Towing Tank Experiments	3.1
3.1 Preface	3.1
3.2 X-Y Towing Tank Description	3.2
3.3 X-Y Towing Tank Procedures	3.6
3.4 Typical X-Y Towing Tank Result	3.7
3.5 Filtering	3.11
3.6 Repeatability	3.12
3.7 Angles of Attack	3.13
3.8 Reynolds Numbers	3.15
3.9 Plate Thickness	3.18
3.10 Blockage Effects	3.18
3.11 End Conditions	3.20
3.12 Starting Profiles	3.23

3.13	Shedding Modulation	3.24
3.14	Exponential Shedding Onset	3.25
3.15	Flow Visualizations	3.26
3.16	Summary	3.33
Ch. 4	Free Surface Water Tunnel Experiments	4.1
4.1	Preface	4.1
4.2	Free Surface Water Tunnel Description	4.1
4.3	Free Surface Water Tunnel Procedures	4.3
4.4	Typical Free Surface Water Tunnel Result	4.4
4.5	Blockage Effects	4.9
4.6	Reynolds Numbers	4.11
4.7	Plate Stiffness	4.14
4.8	Angles of Attack	4.15
4.9	Aspect Ratio Effects	4.17
4.10	End Condition Effects - End Plate Angles	4.17
4.11	Summary	4.26
Ch. 5	Two-Dimensional Numerical Model Experiments	5.1
5.1	Preface	5.1
5.2	CFD Calculations	5.1
5.3	Typical CFD Result	5.3
5.4	Model Parameters	5.4
5.5	Unfiltered Result	5.6
5.6	Angles of Attack	5.7
5.7	Plate Thickness	5.12
5.8	Acceleration Profiles	5.14
5.9	Circulation Decay	5.17
5.10	Merging Parameter	5.22
5.11	Long Time Histories	5.23
5.12	Vortex Flow Visualizations	5.28
5.13	Summary	5.38
Ch. 6	Stratified X-Y Towing Tank Experiments	6.1
6.1	Preface	6.1
6.2	X-Y Towing Tank Stratification	6.1
6.3	Richardson Number	6.2

6.4	Stratification Profiles	6.4
6.5	Typical Stratified Flow Result	6.5
6.6	End Conditions	6.5
6.7	Ensemble Averaged Results	6.7
6.8	Stratified Flow Visualizations	6.10
6.9	Summary	6.16
Ch. 7	Comparison Of Results	7.1
7.1	Preface	7.1
7.2	Comparison to Previous Results	7.3
7.3	X-Y Towing Tank And Free Surface Water Tunnel Results	7.5
7.3.1	Unsteady Starting Regime	7.5
7.3.2	Extrinsic Effects - Large Scale Three Dimensionality	7.10
7.3.3	Reynolds Number Effects	7.11
7.3.4	Shedding Modulation	7.12
7.4	Comparison Of Numerical and Experimental Results	7.14
7.4.1	Circulation Decay	7.21
7.5	Stratification Effects - Small Scale Three Dimensionality	7.24
7.6	Remaining Questions	7.27
Ch. 8	Conclusions	8.1
References	R.1
App. A	Further Details of Apparatus and Procedures	A.1
A.1	Preface	A.1
A.2	Flat Plate Details	A.1
A.3	Flow Visualization Camera	A.1
A.4	Force Balance Calibration	A.2
A.5	Force Balance Data Analysis	A.2
A.6	X-Y Towing Tank	A.6
A.7	Free Surface Water Tunnel	A.9
A.8	X-Y Towing Tank Stratification Profiles	A.12
App. B	Experimental Conditions	B.1
App. C	Drag Coefficient Scaling	C.1

- X -

LIST OF FIGURES

Fig. 1.1	Some published experimental results for drag coefficient and Strouhal number of nominally two-dimensional normal flat plates	1.3
Fig. 1.2	Some published numerical results for drag coefficient and Strouhal number of nominally two-dimensional normal flat plates	1.4
Fig. 2.1	Coordinates and sign convention	2.1
Fig. 2.2	Schematic drawing of force balance	2.3
Fig. 2.3	Computerscope channel signals	2.4
Fig. 2.4	Digital filtering function in non-dimensional frequency	2.5
Fig. 2.5	Flat plate model nomenclature	2.6
Fig. 2.6	Flat plate model used for flow visualization	2.6
Fig. 2.7	Definitions of planes used for flow visualization	2.7
Fig. 2.8	Pivoting flat plate model mount	2.8
Fig. 2.9	Five flat plate model end conditions	2.9
Fig. 3.1	Perspective view of the GALCIT X-Y towing tank facility	3.1
Fig. 3.2	Schematic drawing of the GALCIT X-Y towing tank facility	3.3
Fig. 3.3	Illustration of force errors due to waviness in X-Y towing tank rails	3.5
Fig. 3.4	Schematic of "theoretical" force history from the X-Y towing tank	3.8
Fig. 3.5	Typical force histories from the X-Y towing tank	3.10
Fig. 3.6	Effects of digital filtering on result of Fig. 3.5	3.11
Fig. 3.7	Ensemble average and individual $\alpha = 90^\circ$ towing tank runs to illustrate repeatability	3.12
Fig. 3.8	Effects of small angle of attack variations in X-Y towing tank	3.13
Fig. 3.9	Ensemble average and individual $\alpha = 87.5^\circ$ towing tank runs illustrating repeatability	3.14
Fig. 3.10	Comparison of various Reynolds numbers in X-Y towing tank at $\alpha = 90^\circ$	3.15
Fig. 3.11	Ensemble average and rms levels for $Re = 1000$ and 5000 in X-Y towing tank	3.16
Fig. 3.12	Ensemble average power spectra for $Re = 1000$ and 5000 in X-Y towing tank	3.17
Fig. 3.13	Effects of plate thickness in X-Y towing tank	3.19
Fig. 3.14	Effects of blockage in X-Y towing tank	3.20
Fig. 3.15	End condition effects in X-Y towing tank	3.21

Fig. 3.16	Effects of various end plate angles	3.22
Fig. 3.17	Aspect ratio effects in X-Y towing tank	3.23
Fig. 3.18	Effect of varying t_a^*	3.24
Fig. 3.19	Force history showing long period ($6 \times T_s$) shedding amplitude modulation	3.25
Fig. 3.20	Exponential nature of shedding onset	3.25
Fig. 3.21	Force histories from X-Y towing tank flow visualization runs	3.26
Fig. 3.22	X-Y towing tank flow visualizations; $\alpha = 90^\circ$, $Re = 5000$	3.27
Fig. 3.23	X-Y towing tank flow visualizations; $\alpha = 90^\circ$, $Re = 5000$	3.28
Fig. 3.24	X-Y towing tank flow visualizations; $\alpha = 90^\circ$, $Re = 5000$	3.29
Fig. 3.25	X-Y towing tank flow visualizations; $\alpha = 87.5^\circ$, $Re = 5000$	3.30
Fig. 3.26	X-Y towing tank flow visualizations; $\alpha = 87.5^\circ$, $Re = 5000$	3.31
Fig. 3.27	X-Y towing tank flow visualizations; $\alpha = 87.5^\circ$, $Re = 5000$	3.32
Fig. 4.1	Schematic drawing of GALCIT free surface water tunnel facility	4.2
Fig. 4.2	Typical free surface water tunnel result	4.5
Fig. 4.3	Same run as in Fig. 4.2 with various horizontal (x/C) scales to show detail	4.6
Fig. 4.4	Non-dimensional frequency f^* spectra for typical run (from Fig. 4.2)	4.7
Fig. 4.5	Exponential growth and decay of shedding modulation (from Fig. 4.3)	4.8
Fig. 4.6	Calculation of average C_d mean crossing interval	4.9
Fig. 4.7	Effect of tunnel blockage	4.10
Fig. 4.8	Effect of Reynolds number (freestream velocity)	4.12
Fig. 4.9	Low Reynolds number result, $Re = 1500$	4.13
Fig. 4.10	Effects of plate stiffness	4.14
Fig. 4.11	Mean ($\overline{C_d}$, $\overline{C_l}$) and rms (instantaneous) coefficient values for different angles of attack	4.15
Fig. 4.12	Angle of attack (α) effects	4.16
Fig. 4.13	Aspect ratio effects	4.18
Fig. 4.14	Shedding intermittency at low $AR = 6$ aspect ratio	4.19
Fig. 4.15	Effects of <i>FBIW</i> angle at $AR = 15$	4.20

Fig. 4.16	<i>FBW</i> angle and Aspect Ratio effects - part 1	4.21
Fig. 4.17	<i>FBW</i> angle and Aspect Ratio effects - part 2	4.22
Fig. 4.18	Summary of results for various aspect ratios	4.23
Fig. 4.19	Effect of end condition on power spectra at $AR = 15$	4.24
Fig. 4.20	Effect of aspect ratio on power spectra with <i>FBW</i> at 0°	4.25
Fig. 4.21	Flow visualization results from free surface water tunnel	4.27
Fig. 5.1	Plate model using 80 node description	5.2
Fig. 5.2	Typical results for 80 node model at $\alpha = 90^\circ$	5.4
Fig. 5.3	C_d convergence with various model parameters	5.5
Fig. 5.4	Comparison of filtered ($f_{co}^* = .4$, $f_w^* = 0.1$) and unfiltered data	5.6
Fig. 5.5	Effects of small angle of attack variations	5.7
Fig. 5.6	Effect of angle of attack on shedding onset - flow visualization	5.9
Fig. 5.7	Effect of angle of attack on shedding onset - continued from Fig. 5.6	5.10
Fig. 5.8	Effects of plate thickness	5.13
Fig. 5.9	Non-dimensional acceleration times	5.15
Fig. 5.10	Low drag $\alpha = 87.5^\circ$ shedding onset	5.16
Fig. 5.11	Data from Kiya and Arie, 1980	5.17
Fig. 5.12	Effects of circulation decay parameter λ	5.19
Fig. 5.13	Effect of circulation decay λ at $t^* = 18.69$ with $\alpha = 90^\circ$	5.20
Fig. 5.14	Shedding at different times (at \approx same phase) for $\lambda = 0.86$	5.21
Fig. 5.15	Effects of merging parameter D0 on non-impulsive start	5.23
Fig. 5.16	Long time histories with no circulation decay ($\lambda = 1.0$)	5.24
Fig. 5.17	Long time histories with circulation decay $\lambda = 0.86$	5.25
Fig. 5.18	Power spectra for various λ	5.26
Fig. 5.19	Time averaged mean pressure coefficient distributions for $\alpha = 90^\circ$ and 87.5°	5.27
Fig. 5.20	Force histories for numerical flow visualization runs with $\lambda = 1.0$	5.28
Fig. 5.21	Force histories for numerical flow visualization runs with $\lambda = 0.86$	5.29

Fig. 5.22	Numerical flow visualizations, $\lambda = 1.0, \alpha = 90^\circ$	5.30
Fig. 5.23	Numerical flow visualizations continued, $\lambda = 1.0, \alpha = 90^\circ$	5.31
Fig. 5.24	Numerical flow visualizations, $\lambda = 1.0, \alpha = 87.5^\circ$	5.32
Fig. 5.25	Numerical flow visualizations continued, $\lambda = 1.0, \alpha = 87.5^\circ$	5.33
Fig. 5.26	Numerical flow visualizations, $\lambda = 0.86, \alpha = 90^\circ$	5.34
Fig. 5.27	Numerical flow visualizations continued, $\lambda = 0.86, \alpha = 90^\circ$	5.35
Fig. 5.28	Numerical flow visualizations, $\lambda = 0.86, \alpha = 87.5^\circ$	5.36
Fig. 5.29	Numerical flow visualizations continued, $\lambda = 0.86, \alpha = 87.5^\circ$	5.37
Fig. 6.1	Method used to stratify the X-Y towing tank	6.2
Fig. 6.2	Results of three different stratifications of the X-Y towing tank	6.3
Fig. 6.3	Specific gravity profiles for stratification #3	6.4
Fig. 6.4	Richardson number effects	6.6
Fig. 6.5	Effects of stratification on large scale (end condition) effects	6.7
Fig. 6.6	Ensemble average and rms levels with stratification #3 for $Re = 1000$ ($Ri = 13.3$) and $Re = 5000$ ($Ri = 0.53$) with $\alpha = 87.5^\circ$	6.9
Fig. 6.7	Ensemble averaged power spectra with stratification #3 for $Re = 1000$ ($Ri = 13.3$) and $Re = 5000$ ($Ri = 0.53$) with $\alpha = 87.5^\circ$	6.10
Fig. 6.8	Force histories from stratified X-Y towing tank flow visualization runs	6.11
Fig. 6.9	Stratified X-Y towing tank flow visualizations; $\alpha = 90^\circ$, $Re = 1000$, $Ri = 5.48$	6.12
Fig. 6.10	Stratified X-Y towing tank flow visualizations; $\alpha = 90^\circ$, $Re = 1000$, $Ri = 5.48$	6.13
Fig. 6.11	Stratified X-Y towing tank flow visualizations; $\alpha = 87.5^\circ$, $Re = 1000$, $Ri = 5.48$	6.14
Fig. 6.12	Stratified X-Y towing tank flow visualizations; $\alpha = 87.5^\circ$, $Re = 1000$, $Ri = 5.48$	6.15
Fig. 7.1	Experimental C_d comparison to previous results	7.4
Fig. 7.2	Numerical model C_d comparison to different vortex element models	7.5
Fig. 7.3	Effects of angle of attack for ensemble averaged results at $Re = 5000$	7.6
Fig. 7.4	Comparison of drag levels during intermittent shedding in free surface water tunnel and early startup up in X-Y towing tank with $\alpha = 90^\circ$, $Re \approx 5000$	7.8
Fig. 7.5	Examples of exponential shedding onset in X-Y towing tank and free surface water tunnel with $\alpha = 90^\circ$, $Re \approx 5000$	7.9
Fig. 7.6	Comparison of ensemble averaged experimental runs at $Re = 5000$ and $Re = 1000$ with $\alpha = 87.5^\circ$	7.12
Fig. 7.7	Examples of long period shedding modulation in X-Y towing tank and free surface water tunnel with $\alpha = 90^\circ$, $Re \approx 5000$	7.13

Fig. 7.8	Comparison of experimental and 2d numerical model results for various angles of attack	7.15
Fig. 7.9	Comparison of experimental and 2d numerical model results for various acceleration times t_a^* with $\alpha = 87.5^\circ$	7.17
Fig. 7.10	C_d and C_l PDF (normalized histogram) comparison of experiments and 2d numerical model	7.18
Fig. 7.11	Numerical model time averaged pressure coefficient at $\alpha = 90^\circ$	7.19
Fig. 7.12	Power spectra of experimental and 2d numerical model force coefficients with $\alpha = 87.5^\circ$, $Re = 5000$	7.20
Fig. 7.13	Comparison of results from experiments and 2d numerical models with and without circulation decay for $\alpha = 87.5^\circ$, $Re \approx 5000$	7.22
Fig. 7.14	C_d and C_l PDF (normalized histogram) comparison of experiments and 2d numerical models with $\lambda = 1.0$ and 0.86 at $\alpha = 90^\circ$	7.23
Fig. 7.15	Comparison of stratified and unstratified ensemble averaged X-Y towing tank results with $\alpha = 87.5^\circ$	7.25
Fig. 7.16	Comparison of unstratified and stratified experimental and 2d numerical model results	7.26
Fig. A.1	Flat plate model details	A.1
Fig. A.2	Camera control circuit	A.2
Fig. A.3	Schematic of apparatus used to calibrate the force balance	A.3
Fig. A.4	Typical force balance calibration record	A.4
Fig. A.5	Force balance amplifier and data analysis block diagram	A.5
Fig. A.6	Layout of X-Y towing tank drive system electronics	A.7
Fig. A.7	Integrated x accelerometer output giving velocity vs. position	A.8
Fig. A.8	Height profile of X-Y towing tank bottom with varying water depths	A.8
Fig. A.9	Layout of single channel free surface water tunnel LDV System	A.9
Fig. A.10	Comparison of two LDV measuring systems	A.10
Fig. A.11	Streamwise and Cross-stream (z direction) velocity profiles in free surface water tunnel	A.11
Fig. A.12	Conductivity probe calibration	A.12
Fig. A.13	Schematic of conductivity probe used to measure density (salinity) gradients	A.13
Fig. A.14	Specific gravity profiles for stratifications #1 and #2	A.14
Fig. B.1	Page one of run parameters for unstratified X-Y towing tank experiments	B.2
Fig. B.2	Page two of run parameters for unstratified X-Y towing tank experiments	B.4
Fig. B.3	Run parameters for free surface water tunnel experiments	B.6
Fig. B.4	Run parameters for CFD experiments	B.8
Fig. B.5	Run parameters for stratified X-Y towing tank experiments	B.10
Fig. C.1	Drag coefficient scaling	C.1

NOMENCLATURE

$\left(\cdot\right)^*$	- Non-dimensional Variable
$\left(\cdot\right)_b$	- Balance Coordinates [cm]
$\left(\cdot\right)_{cg}$	- Center of Gravity Coordinates [cm]
$\left(\cdot\right)_I$	- Inertial
$\left(\cdot\right)_d$	- Lift Direction
$\left(\cdot\right)_d$	- Drag Direction
$\left(\cdot\right)_m$	- Moment Direction
$\left(\cdot\right)_{s1}$	- Stratification # 1
A	- Plate Area [cm ²] (= d × C)
a	- Plate Acceleration [cm/sec ²] ($= \frac{U_{\infty}}{t_s}$)
Age_i	- CFD Code - Age of the i^{th} Vortex [sec]
AR	- Plate Aspect Ratio (= d/C)
B	- Plate Blockage (= C/W)
C	- Plate Chord [cm]
C_d	- Drag Coefficient ($= \frac{F_d}{\frac{1}{2}\rho U_{\infty}^2 A}$)
C_{d_i}	- Initial Drag Coefficient ($= \frac{\pi}{4t_s^2}$)
$\overline{C_d}$	- Time Averaged Mean (Steady-state) Drag Coefficient
C_l	- Lift Coefficient ($= \frac{F_l}{\frac{1}{2}\rho U_{\infty}^2 A}$)
C_m	- Moment Coefficient ($= \frac{F_m}{\frac{1}{2}\rho U_{\infty}^2 A}$)
C_p	- Pressure Coefficient ($= \frac{P - P_{\infty}}{\frac{1}{2}\rho U_{\infty}^2}$)
D	- Load Cell D Output [volts]
$D0$	- CFD Code - Vortex Merging Parameter
d	- Plate Depth [cm]
EPA	- End Plate Angle [deg]
F_d	- Drag Force [N]
F_l	- Lift Force [N]
F_m	- Moment [N × m]
f	- Frequency [hz]
f^*	- Non-dimensional Frequency ($= \frac{fC}{U_{\infty}}$)
f_{co}	- Low-pass Filter Cut-off Frequency [hz]
f_{co}^*	- Non-dimensional Low-pass Filter Cut-off Frequency ($= \frac{f_{co} C}{U_{\infty}}$)
f_s	- Vortex Shedding Frequency [hz]

f_w	- Low-pass Filter Width [hz]
f_w^*	- Non-dimensional Low-pass Filter Width ($= \frac{L_w C}{U_\infty}$)
g	- Gravity [cm/sec ²]
h	- Plate Thickness [cm]
h/C	- Plate Thickness to Chord Ratio ($= \frac{h}{C}$)
M	- Model Mass [grams]
N	- Number of Runs In An Ensemble
N_1	- Load Cell N1 Output [volts]
N_2	- Load Cell N2 Output [volts]
N_a	- CFD Code - Number Of Acceleration Timesteps
N_s	- CFD Code - Number of Vortices In One Strouhal Cycle ($= \frac{T_s}{\Delta t}$)
N_v	- CFD Code - Approximate Number of Vortices To Maintain
N_w	- CFD Code - Number Of Nodes Used To Describe Plate Geometry
n	- Number of Time Steps Run
P_∞	- Freestream static pressure [N/m ²]
R	- Run Time [sec]
Re	- Reynolds Number ($= Re_u = \frac{C U_\infty}{\nu} = Re_a \sqrt{2 t_a^*}$)
Re_a	- Acceleration Reynolds Number ($= \frac{C \sqrt{a} C}{\nu}$)
Ri	- Richardson Number (based on Chord) ($\cong g \frac{\partial S_a}{\partial z} \frac{C^2}{U_\infty^2}$)
R_o	- CFD Code - Distance From Wall To Creation Points [cm]
S	- Plate Span [cm]
S_g	- Specific Gravity ($= \frac{\rho}{\rho_0}$)
S_t	- Strouhal Number (Non-dimensional Sheding Frequency) ($= \frac{L_w C}{U_\infty}$)
T_s	- Strouhal period ($= \frac{1}{S_t}$)
T	- Temperature [deg C]
t	- Time [sec]
t^*	- Non-dimensional Time ($= t U_\infty / C$)
t_a	- Carriage Acceleration Time [sec]
t_a^*	- Non-Dimensional Carriage Acceleration Time ($= \frac{U_\infty t_a}{2C}$)
U_∞	- Freestream Velocity or Steady-state Carriage Velocity [cm/sec]
U_s	- Separating Shear Layer Velocity [cm/sec]
U_{ref}	- Reference Velocity [cm/sec]
W	- Test Section Width [cm]
x	- Carriage Streamwise Position [cm]
x_a	- Carriage Position At Time t_a [cm]

x^*	- Non-dimensional Position ($= x/C$)
y	- Cross-stream Coordinate [cm]
z	- Spanwise Coordinate [cm]
$\frac{\partial S_x}{\partial z}$	- Specific Gravity Gradient [γ_{cm}]
α	- Plate Angle of Attack [deg]
β	- Plate Bevel Angle [deg]
Γ	- CFD Code - Vortex Circulation [cm ² /sec]
Γ_o	- CFD Code - Initial ($t = 0$) Vortex Circulation [cm ² /sec]
Γ_i	- CFD Code - Circulation of the i^{th} Vortex [cm ² /sec]
Δt	- CFD Code - Time Step Size [sec]
Δs	- CFD Code - Average Spacing Of Wall Nodes [cm]
θ	- Plate Rotary Offset [deg] ($= \alpha - 90$)
λ	- CFD Code - Circulation Decay Parameter
ν	- Fluid Kinematic Viscosity [cm ² /sec]
ρ	- Fluid Density [g/cm^3]
ρ_o	- Reference Fluid Density [g/cm^3]
σ	- CFD Code - Vortex Core Radius [cm]
τ	- CFD Code - Time Constant For Circulation Decay [sec]
τ_o	- Mean C_d crossing interval [$U_\infty t/C$ units]
NEP	- No End Plate
WEP	- With End Plate
NBW	- Near Bottom Wall (Grazing)
FBW	- False Bottom Wall

CHAPTER 1

Introduction

In 1927 A. Fage and F. Johansen wrote a paper entitled, "On the flow of air behind an inclined flat plate of infinite span," which has since become one of the canonical works in the field of bluff body flow research. The first sentence of this paper read, "The general form of the flow behind an infinitely long thin flat plate inclined at a large angle to a fluid stream of infinite extent has been known for many years past." In the intervening sixty-five years a great deal has been discovered about the specific details of this class of flow, and it has become increasingly apparent that knowing the "general form" is insufficient. Much remains to be learned. In particular, the effects of three-dimensional motions present in the flow are still not well understood; in the experimental and practical absence of infinite flat plates and flow fields of infinite extent, the importance of understanding such effects is obvious. This research attempts to shed light on some of the effects that three dimensionality can have on the forces experienced by a normal flat plate in a uniform oncoming stream, and how it can subsequently affect the global development of the wake.

1.1 Historical Perspective

Bluff body flows are by nature very complex. Inevitably they involve boundary layer, free shear layer and wake flows, all accompanied by associated instabilities and non-linear interactions with each other and with the bluff body itself. A normal flat plate is in many ways the simplest possible bluff body, since it has geometrically fixed separation points, and since the interaction between the body and the near wake formation region is minimized. One might therefore expect that a major portion of bluff body research would have centered around normal flat plates. However, in comparison to the bulk of contemporary literature dealing with circular cylinder flows (as an example), very few results have been published for normal flat plates. This probably reflects the more practical engineering uses of circular cylinders, and the fact that much of bluff body research is driven by a desire to understand fluids interacting with engineering structures.

Of the normal flat plate results which *are* available, few present unsteady time histories. Typically Strouhal shedding frequency, force and/or pressure coefficients are presented only as time averaged mean and fluctuating quantities, with little further attempt to characterize the flow. Unfortunately, many of the phenomena associated with three-dimensional motions are obscured when considering only time averaged results. It is only when one considers the unsteady nature of the flow itself that many features become apparent.

Early attempts to characterize the mean flow about normal flat plates were made by Kirchhoff (1869) and were later extended by Rayleigh (1876) to include the case of plates at angle of attack α to the freestream. They assumed that the shear layers leave the body at sharp edges with a separation velocity equal to the freestream velocity U_∞ , and that the base pressure is uniform and equal to the freestream pressure, giving $C_p = 0$ on the rearward face of the plate. The drag force is then entirely due to the dynamic pressure on the upstream face of the plate, and can be calculated (see for example Lamb (1932), pp. 100) as:

$$C_d = \frac{2\pi \sin \alpha}{4 + \pi \sin \alpha}.$$

This gives $C_d = 0.88$ for the case of a normal flat plate with $\alpha = 90^\circ$. However, experiments of Stanton (1903), Fage and Johansen (1927) and others subsequently obtained a time averaged mean drag coefficient of $\overline{C_d} \approx 2.0$, more than twice the value postulated by Kirchhoff. Although early experimental results were performed without the current level of knowledge about the effects of Reynolds number, blockage, end conditions, or other apparatus induced extrinsic effects, and have a commensurately large scatter, more contemporary results have confirmed a time averaged mean $\overline{C_d} \approx 2.0$ for a "two-dimensional" flow about a normal flat plate in unbounded flow (Fig. 1.1). The difference between this and the theoretical result of Kirchhoff was attributed by Fage and Johansen (1927) to a mean free shear layer velocity much greater than the value U_∞ assumed by Kirchhoff; this is at least in part a result of the unsteady nature of the wake. Roshko (1954, 1955), and later Abernathy (1962), modified the classical free streamline theory with a base pressure parameter k , representing the ratio U_s/U_∞ . They also showed that the mean drag coefficient thus obtained agreed well with experimental results when the experimental value of $k = 1.54$ found by Fage and Johansen was used.

The success of modified theoretical treatments is limited to mean quantities. They do not predict levels of unsteady fluctuation in base pressure and force level resulting from the unstable nature of the free shear layers, their roll up, and the consequent vortex shedding of the bluff body. Many more recent experimenters, some of whom are listed in the table of Fig. 1.1, have tried to better understand the dynamics of the wake and wake-body interaction in rectangular cylinder flows by changing plate porosity, imposing forcing, inserting wake splitter plates, increasing cylinder thickness, or by adding various forms of end plate or varying end condition. But in each case, typically only time averaged mean quantities were considered. Furthermore, implicit in most studies was the assumption that the mean flow was two-dimensional and could be considered free of large global effects due to three-dimensional motions.

Currently, the only technique by which a truly two-dimensional flow can be achieved is through numerical flow modeling. Although computer capabilities are not yet at the point where they can produce fully three-dimensional simulations, in the last few years an increasing number of two-dimensional computer models have been developed for bluff body flows. Here again most have dealt with circular cylinders, which reflects not only their predominance in the experimental literature but also the ease of dealing numerically with

Source (Year)	AR B.C.	h/C	Re	\bar{C}_d	St	Comments
Experimental Results:						
Present (1993)	6 to 23 Various	4% to 20%	1,000 to 12,500	2.07	0.149	Free surface water tunnel results. No blockage corrections applied
Stanton (1903)	1 to 60 NEP	?	2,500 to 30,000	1.1 to 1.76	—	Highest aspect ratio at lowest Re End conditions unclear - likely no end plate
Wieselsberger (1922)	1 to "∞" NEP	?	O(100,000) ?	1.18 to 2.0	—	Effects of aspect ratio (Re independent)
Fage & Johansen (1927)	14.1 TSW	3%	150,000	1.84	0.146	Thin sharp edged normal flat plate; small gap from tunnel walls. C_d corrected for blockage
Flaschbart (1932)	50 to 200 SW	1.5% to 5%	1,000 to 6,000	1.96	—	Reynolds number effects on normal flat plates; open jet tunnel Re independent for $Re > 6000$; $C_{d,\min} = 1.6 @ Re = 2500$
Schubauer & Dryden (1935)	6 NEP	?	30,000 to 60,000	1.26 to 1.32	—	Effects of freestream turbulence on low AR normal flat plates (high turbulence → high C_d)
Lindsey (1938)	44 TSW	29%	840 to 310,000	2.0	—	Effects of compressibility. Result quoted is for $Re = 10,000$, $M = 0.4$, using triangular section with 30° bevel
Delany & Sorensen (1953)	7 to 21 TSW	50%	11,000 to 2,300,000	2.20	0.19	Quoted result is for $Re = 100,000$, rectangular cylinder. Strouhal number is for cylinder with rounded corners
Roshko (1954)	13.5 TSW?	16%	4,000 to 10,000	1.74	0.135	C_d estimated from C_{pb}
Arie & Rouse (1956)	12 TSW	8.3%	75,000 ?	2.1	—	Sharp edged flat plates with wake splitter plates. Results quoted had no splitter plate
Fair, Lawford & Eyre (1957)	1 to 20 NEP	?	80,000	1.1 to 1.5	0.086 to 0.115	Effects of aspect ratio on thin flat plates high C_d at AR = 20
Abernathy (1962)	1.5 to 6 TSW	6% to 19%	36,000 to 140,000	2.15	0.150	Inclined sharp edged plates quoted normal flat plate results with C_d estimated from C_{pb}
Nakaguchi et. al. (1967)	20 WEP	10% to 400%	20,000 to 60,000	2.0	0.135	Rectangular cylinders of various thicknesses
Castro (1971)	15 TSW	4%	25,000 to 90,000	1.87	0.14	This perforated plates; results quoted are no perforation, corrected for blockage
Bearman & Trueman (1972)	17+ TSW?	20%	20,000 to 70,000	2.05	0.14	Rectangular cylinders, various thicknesses, wake splitter plates. Thin plate with no splitter results quoted
Ranga-Raju & Singh (1975)	4 to 13 TSW	"0%"	>1000	1.80	—	Study of wake splitter plates and blockage effects Low blockage, no splitter plate results quoted
Modi & El-Sherbiny (1977) El-Sherbiny & Modi (1983)	2.3 to 18 TSW	?	10,000 to 120,000	2.0	0.149	Blockage effects on sharp edged plates; low blockage thin plate results quoted
Courchesne & Laneville (1979)	7 to 14 WEP	30%	20,000 100,000	2.3	—	Rectangular cylinder, studied effects of blockage and thickness
Sarpkaya & Kline (1982)	8 TSW	11%	21,000	2.2	—	Unsteady startup short run length (13 x/C max run length) Sharp edged normal flat plate
Sarpkaya & Ihrig (1986)	28 TSW	62%	20,000	1.5 to 3.0	—	Unsteady startup (75 x/C max run length) Thick rectangular cylinders
Igarashi (1986)	5 TSW?	33%	11,000 to 44,000	2.0	0.15	Rectangular Cylinders
Kiya & Matsumura (1988)	15 TSW	21.5%	23,000	—	0.146	Measured wake frequency content - 3d structures in near wake
Knisely (1990)	3.2 to 80 TSW	4% to 100%	720 to 81,000	2.0	0.15	Rectangular cylinders

FIG. 1.1 Some published experimental results for drag coefficient and Strouhal number of nominally two-dimensional normal flat plates. AR = Aspect Ratio; B.C. = Boundary Condition (NEP = No End Plates; WEP = With End Plates; NBW = Near Wall; TSW = Tunnel Side Walls); h/C = Thickness/Chord ratio

a circular geometry, particularly for finite difference codes where the inclusion of a sharp edged singularity is undesirable. Some of the results of numerical models dealing with normal flat plates are shown in Fig. 1.2.

The main thing to note about the tabulated results presented in Fig. 1.1 and Fig. 1.2 is the large difference in the mean drag coefficient between the experimental results and the two-dimensional numerical models, which in some cases have a drag of almost twice the experimental values, although typically $\overline{C_d} \approx 3.2$. There has been a tendency to think of these computer models as being wrong, and to modify them by various means so that their results conform with "two-dimensional" experiments. This is the wrong approach. The question should not be, "Why does this two-dimensional model not accurately match (three-dimensional) experimental results" but "how closely does this model represent a two-dimensional flow"? This latter question is difficult to answer. Lacking a truly two-dimensional experimental flow, the best that can be said is that there seems to be remarkably good agreement ($\overline{C_d} = 3.2 \pm 15\%$) between widely disparate two-dimensional models, including both vortex, finite element, and Navier-Stokes models by many different researchers. Where different $\overline{C_d}$ levels are found, the models have often been modified, intentionally or otherwise, to more closely represent experimental flows. Most purely two-dimensional normal flat plate results which could be found in the literature agree reasonably well with the majority of the numerical results presented in Fig. 1.2.

Since, however, numerical modeling is secondary in this thesis, for our purposes we will assume the results of our "typical" two-dimensional vortex element numerical model to be representative ($\pm 15\%$) of a purely two-dimensional flow. The validity of this assumption should be (and is being) debated elsewhere.

Source (Year)	R B.C.	h_C	Re	$\overline{C_d}$	St	Comments
Numerical Results:						
Present (1993)	2d	4% to 20%	—	3.26	0.121	Used vortex element code by Spalart, 1983
Kuwahara (1973)	2d	0	—	2.0 to 4.0	—	Early vortex element code
Sarpkaya (1975)	2d	0	—	2.4	0.154	Flat plate at $\alpha = 80^\circ$
Kiya & Arie (1980)	2d	0	—	2.0 to 3.5	0.14 to 0.16	Lower C_d values are from model using artificial circulation decay (matched to experiments)
Spalart et. al. (1983)	2d	20%?	10^7	3.5	—	Similar code to present study but with boundary layer solution
Dutta (1988)	2d	0	—	3.39	0.154	Vortex Element
Chein & Chung (1988)	2d	0	—	2.8	0.14	Circulation decay based on experimental parameter match
Raghavan et. al. (1990)	2d	2%	200	2.8	0.14	Navier stokes code (ARC2D) w/ turbulence modeling
Chua (1990)	2d	0	10,000	3.6	0.11	Reynolds number based on estimated boundary layer thickness
Pearce et. al. (1992)	2d	?	2,000 to 30,000	2.9 to 3.4	0.15 to 0.125	Finite-difference code (SIMPLE) - various grid mesh sizes finest mesh = highest C_d , best S_t match to experiments

FIG. 1.2 Some published numerical results for drag coefficient and Strouhal number of nominally two-dimensional normal flat plates. Symbols used are as given in Fig. 1.1

1.2 Present Study History and Objectives

We wish then to establish some of the differences between purely two-dimensional flows and experimental results which have in the past been considered "nominally two-dimensional." Further, we wish to understand to what extent these differences are attributable to three-dimensional motions in the experiments, and what effects the degree and type of three dimensionality have.

Experimental results are always influenced by a number of extrinsic factors, typically associated with the nature of the experimental apparatus. Some of these have in the past been "corrected for" in various ways, modifications for the effects of blockage or end condition being typical. Although not all extrinsic factors introduce three dimensionality (*e.g.*, blockage is usually considered two-dimensional) things such as end effects or large scale perturbations of the oncoming flow due to walls, convection currents or other bodies upstream can introduce three-dimensional motions. These motions are typically thought of as being "large scale" - several chord lengths or greater in extent, although they are certainly not restricted to any minimum length scale.

On the other hand intrinsic three-dimensional effects and the corresponding "small scale" three-dimensional motions are those that would be present even in a flow free of apparatus specific extrinsic effects and in the limit of infinite aspect ratio, *i.e.*, motions due to intrinsic flow instabilities. The size of the largest three-dimensional structure present in the near wake in this case is unknown. However, based on experimental evidence it is unlikely to be larger than several chord lengths. At Reynolds numbers 10^3 to 10^4 it is impossible to have a purely two-dimensional flow in an experimental situation. When one speaks of a "nominally two-dimensional experiment," ideally one means a flow from which large scale extrinsic motions have as much as possible been eliminated, and where the aspect ratio of the plate is much greater than the largest three-dimensional motions which remain.

The use of the term "near wake" in the above paragraph requires some elaboration. In the past the terms "wake instability" and "vortex shedding" have been used almost interchangeably, since in bluff body flows the two are often closely related. On the other hand it is possible to shed vorticity into the "far wake," and have an associated wake instability, without it forming vortices close to the body. It is equally possible, at least in unsteady starting flows, to have shed vorticity confined to the near wake, as is the case with an initially symmetric closed recirculating bubble. For our purposes we take the term "vortex shedding" to mean an instability of the separating free shear layers (often closely coupled to the body), causing them to roll up in the "near wake" within about five chord lengths of the body; the distance these vortices are from the body when they are shed we define as the "formation length" (Gerrard, 1966). "Kelvin-Helmholtz" or "shear layer" instability is taken to mean a small scale instability present in the shear layers close to the body (less than one chord length), while "wake instability" affects vorticity in the far wake, more than five chord lengths downstream. These definitions then indicate whether a body is "shedding vortices" (near wake shear layer

instability, short formation length) or "shedding vorticity" (far wake instability). Note that the far wakes in both cases can appear very similar, since the far wake instability is in some sense governed by the velocity profile and wake vorticity rather than the source or past history of that vorticity (Cimbala, 1988).

In this thesis we attempt to describe and explain some of the differences to be found in flows with differing amounts of large scale and small scale three dimensionality. Starting with towing tank and water tunnel experiments, we look at some of the effects of large scale "extrinsic" three-dimensional motions by varying end condition and aspect ratio. Later, intrinsic or small scale motions are modified through Reynolds number or buoyancy effects, the later by introducing a stable spanwise density gradient. A three component force balance coupled with simultaneous flow visualization was used to compare the above flows both to each other and to the results of a purely two-dimensional numerical model.

1.3 Thesis Outline

Since the experiments performed tended to proceed from one facility to another, chapters three through six are arranged in roughly chronological order, each detailing a given facility, the procedures used for that facility, and the experimental results obtained therein. Little or no attempt is made in these sections to analyze results in detail, nor to compare results with those obtained previously.

Chapter two gives details of experimental apparatus which were common to all of the experiments and describes procedures which were not specific to any one facility or set of experiments. A much greater degree of detail about apparatus, procedures, data analysis and possible sources of error is given in Appendix A; Appendix B then tabulates relevant parameters for all the experimental results presented (each of which have an associated reference number), and Appendix C gives an alternate scaling for the drag coefficient suggested by Corteletti (1992).

Beginning the four "data" chapters, chapter three details the X-Y towing tank facility and some preliminary results obtained over a wide range of experimental parameters. From this base some further experiments were performed in the GALCIT free surface water channel, and chapter four provides details of this facility and the results obtained. Numerical simulation runs were made using a very simple vortex element code, to complement those that had been done in the past using more advanced codes; chapter five presents these results. Finally, the X-Y towing tank was again used for some experiments using stably stratified salt water; results are outlined in chapter six.

The five chapters and two appendices outlined above are somewhat long and detailed, essentially providing a database from which selected results are drawn for discussion and comparison in chapter seven and final analysis and conclusions in chapter eight. Readers in a hurry may want to read only up to the end of the "Typical Result" section of chapters three through six, then proceed to chapter seven, referring back to the relevant data chapter only when additional information is required or specific details are unclear.

CHAPTER 2

Apparatus and Procedures

2.1 Preface

The intent of this chapter is to provide a brief overview of some of the experimental apparatus and procedures used for this investigation; for additional information the reader is referred to Appendix A, which in many cases provides a much more detailed description. The apparatus and procedures presented here are those that are common to all experiments, details unique to a particular experimental apparatus are presented along with the results from that facility in the following four chapters.

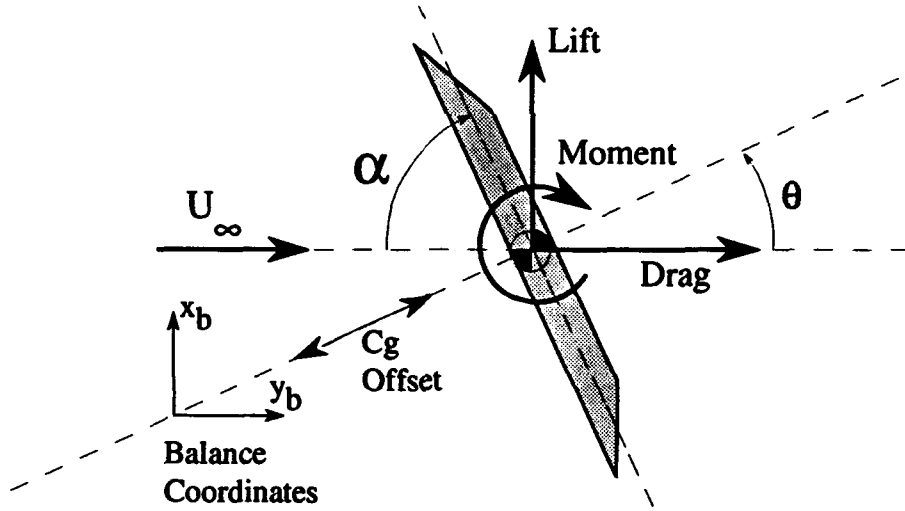


FIG. 2.1 Coordinates and sign convention (directions shown are positive)

As explained previously, the primary experimental diagnostic was a three component force balance measuring lift, drag and pitching moments on normal, $\alpha = 90^\circ$, or nearly normal flat plate models in a towing tank or water channel. The models were mounted vertically, with the upper end projecting up through the free surface and attaching to the force balance. The sign conventions and coordinate systems used are shown in Fig. 2.1.

2.2 Force Balance and Amplifier

The force balance used for all the experiments was designed for use in the X-Y towing tank facility, it was made as robust as possible to withstand the loads applied while quickly accelerating large models, while at the same time being sensitive enough to measure forces on small models at (necessarily) very low velocities.

The force balance, Fig. 2.2, was comprised of three Interface five *lb.* strain gauge load cells mounted on a rigid exterior frame. A horizontal metric platform, to which the test model is mounted, was enclosed on five sides by this framework; this platform was supported on three vertical flexures, which restrained it to horizontal motions only, and three horizontal flexures, which attached to the load cells and restrained its motion entirely. These flexure were designed with flexible ends to transmit linear longitudinal loads only, no moments or side loads were transferred. Thus the load cells measured all of the forces applied to the metric platform in a horizontal plane, the three cells resolving two normal loads (N_1 and N_2), and one side load (D), this being sufficient to give the two normal forces ($N_1 + N_2$ and D) and one moment ($\propto (N_1 - N_2)$).

The balance was calibrated by applying a series of known forces on each load cell in turn and recording the response of each cell to each load (see Appendix A, Fig. A.4). The matrix of force coefficients thus obtained was inverted to give force as a function of measured voltage. An average of many such calibrations indicated a balance accuracy of about 0.03% of full scale, or $\pm 0.0005\text{N}$ uncertainty.

This equates to an uncertainty in measured force *coefficients* as:

$$\Delta C_d = \frac{\Delta F_d}{\frac{1}{2}\rho U_\infty^2 A} \equiv \frac{\Delta F_d}{\frac{1}{2}\rho\nu^2 Re^2 AR} ;$$

where the same analysis applies for C_l and C_m . Thus $\Delta C_d \propto Re^{-2} AR^{-1}$; implying better resolution for larger aspect ratios and Reynolds numbers. Note that there are additional (facility dependent) uncertainties in calculating Re (i.e., U_∞), ρ , ν and AR , so the expected uncertainty in calculating force coefficients is somewhat larger than would be found by considering ΔF_d alone. Additional notes on the uncertainties present in different facilities will be found in succeeding chapters.

A four channel force balance amplifier and power supply was designed specifically for use with this force balance. It had a very stable power supply for energizing the strain gauge bridges in the load cells, an instrumentation amplifier with adjustable gain up to 3200, and a subsequent single ended amplifier with adjustable 4th order analog low-pass Butterworth filters and a gain of 1, 10 or 100. In addition, DC offset voltages could be introduced both before and after the final amplifier stage. For all the experiments presented herein, the load cell excitation voltage was 12.5 volts, the first stage gain was 3200 and the filters were set to a -3db f_{co} of 25 Hertz.

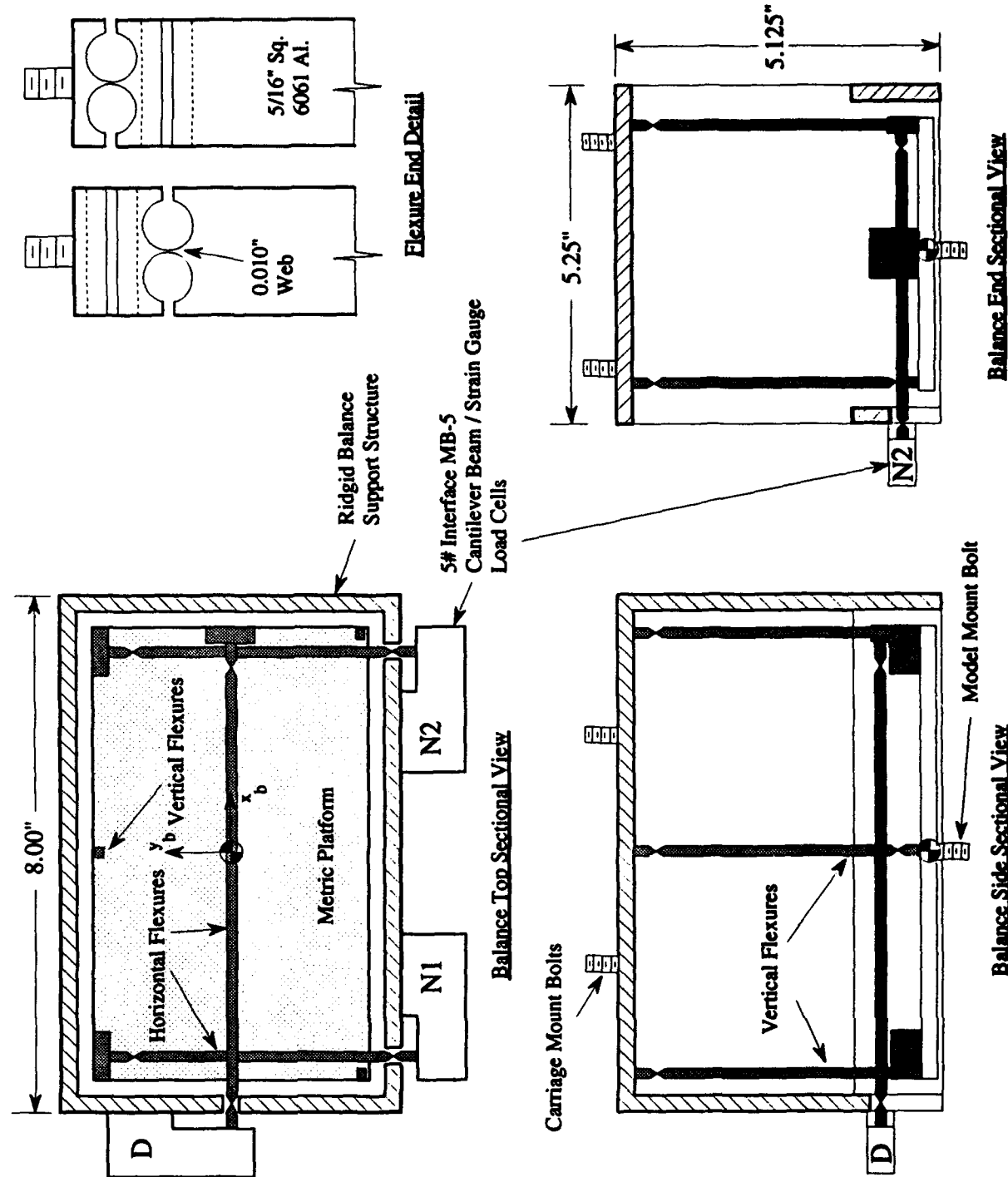


FIG. 2.2 Schematic drawing of force balance

2.3 Data Acquisition

An RC Electronics 12 bit A/D data acquisition system in a Zenith AT computer was used to record voltage levels during experiments. The A/D system was triggered by the start of the motion, and saved data directly to disk, with a user definable amount of data being saved prior to the trigger to establish initial tare offsets for the balance. The 12 bit A/D converter gave a basic accuracy of 0.005 volts; sampling rates varied from 64 to 256 μ sec, with 16 12 bit samples being averaged in real time to obtain one 16 bit number before storage to disk. Generally 7 channels of data were recorded, the channels recording the parameters as shown in Fig. 2.3.

Calibrations with a known voltage source confirmed an A/D conversion accuracy of ± 1 bit or 0.005V. Assuming no gain in accuracy from the 16 sample averaging, this leads to an uncertainty in measured forces of $\pm 0.0009N$, for a total (including the balance accuracy) of $\pm 0.001N$ uncertainty in the force measurements.

Channel #	1	2	3	4	5	6	7
Channel ID	N1	N2	D	Xvel	Xaccel	Yvel	Cam
Signal Description	Force Balance Load Cell N1	Force Balance Load Cell N2	Force Balance Load Cell D	X Carriage Command Voltage	X Direction Accelerometer Output	Y Carriage Command Voltage	Camera Shutter Closed

FIG. 2.3 Computerscope channel signals

2.4 Data Analysis

Once data was recorded to disk it was sent to a NeXT computer for subsequent processing. Complete details of this calculation procedure, which is somewhat involved, can be found in Appendix A. Simply, the initial tare voltage levels were subtracted from the subsequent (experimental) levels, the forces calculated, unwanted inertial forces removed (*i.e.*, those forces associated purely with the mass of the test model and support structure), and additional force corrections read in from an external file and applied. The resultant lift, drag and moment histories were then digitally filtered in non-dimensional frequency space. A moving average filter could then be applied, and finally, the force coefficients, power spectra and auto-correlations were calculated.

Digital filtering was a low-pass filter applied in the non-dimensional $f^* = \frac{fC}{U_\infty}$ frequency space (see Fig. 2.4). The width f_w^* and cutoff frequency f_{co}^* of this filter could be changed to reflect different levels of noise depending on run parameters, particularly U_∞ . This non-dimensional filtering is a compromise, since not all of the noise content is associated with frequencies which are fixed in non-dimensional frequency f^* . In fact, the majority of the noise (largely from mechanical vibrations) is likely to be roughly constant

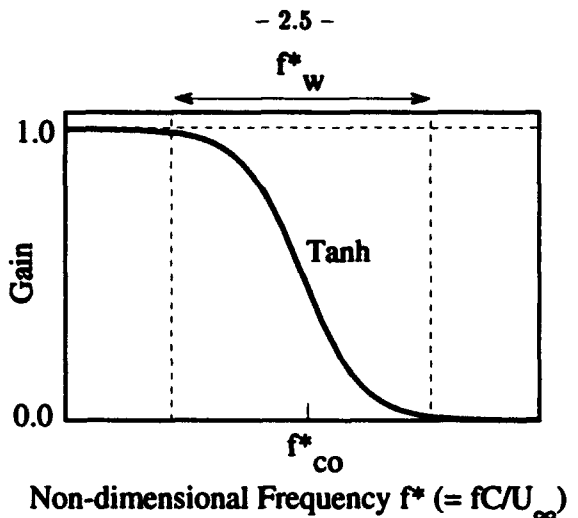


FIG. 2.4 Digital filtering function in non-dimensional frequency. Tanh filter centered at f^*_{co} with a 1% to 99% width of f^*_w

in *physical frequency*, f . However, a large part of this noise is filtered by the initial analog filter in the balance amplifier, and the remainder *will* be filtered by the non-dimensional filter, it will just be filtered to varying degrees depending on $\frac{C}{U_\infty}$. If we assume the noise frequencies to be much higher ($10\times$) than the flow frequencies of interest, this variability is insignificant. This is the case for most of the runs presented, only for $\frac{C}{U_\infty} < 0.1$ do the noise frequencies present begin to impinge on the higher non-dimensional flow frequencies.

A large part of the signal itself is dependent on non-dimensional time t^* (such as the vortex shedding frequency and starting time t_a^*) and filtering in anything other than non-dimensional frequency would distort results due to the unequal application of the filter to runs with differing $\frac{C}{U_\infty}$. Unless otherwise noted, the cutoff frequency and width of the filtering performed on data presented was kept constant at $f^*_{co} = .4$ and $f^*_w = .1$. For further details on the intricacies of digitally filtering the data, the reader is referred to Appendix A.

2.5 Flat Plate Models

With the exception of the flow visualization model, all the flat plate models were constructed of unidirectional carbon fiber plate for stiffness and light weight. They varied in chord from 2cm to 8cm and were all roughly 50 cm long. Thickness was about 3 mm for most models, the thickest was 10 mm and used a wood/carbon fiber sandwich construction. Thickness to chord ratios, h/C , varied from 4% to 20%. As shown in Fig. 2.5, the bevel angle on the downstream face for all models was 30° . Fig. A.1 in Appendix A provides a complete table of flat plate model parameters.

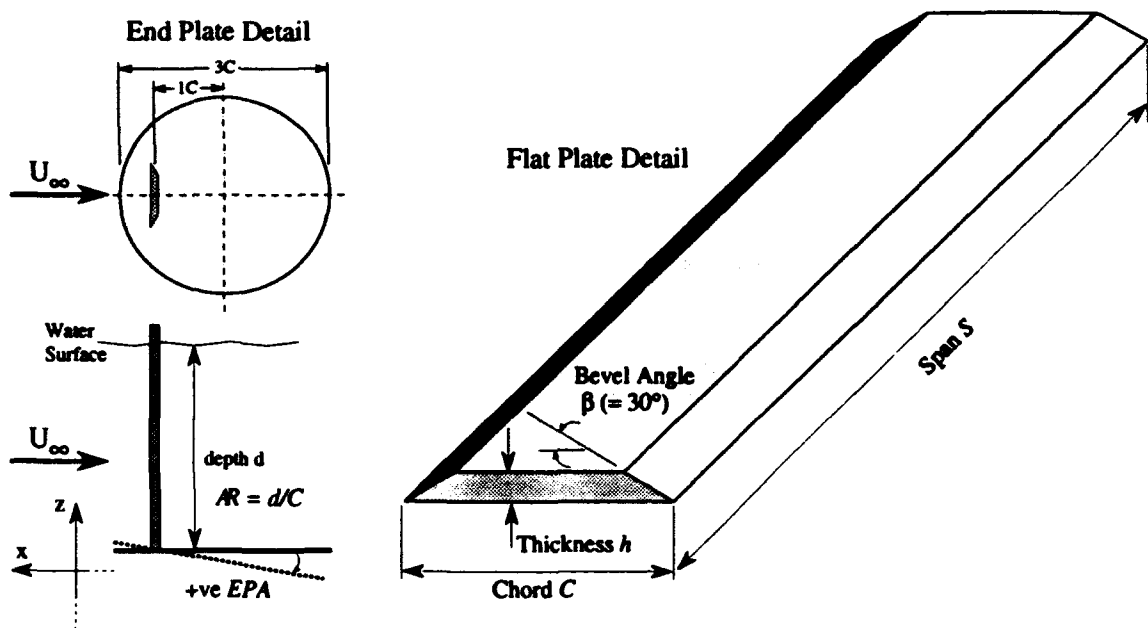


FIG. 2.5 Flat plate model nomenclature

2.5.1 Flow Visualization

The flow visualization model (Fig. 2.6) was constructed of aluminum with channels cut on the front and rear faces for the introduction of dye through a porous insert in the upstream face. This model was 6.5 mm thick, 55 cm span, 4 cm chord with a 30° bevel. Channels in the downstream face were covered with thin waterproof tape and connected to the upstream channels at the mid-span position; this allowed the dye to seep out evenly along the whole submerged span of the plate, or at a location selected by covering parts of the upstream face with tape.

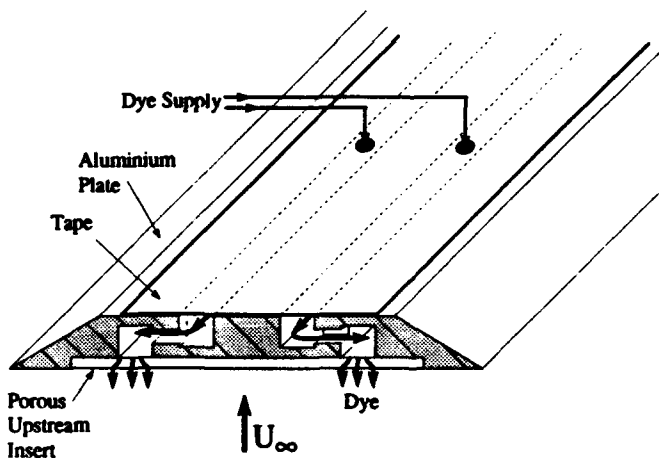


FIG. 2.6 Flat plate model used for flow visualization

Dye was introduced into the downstream channels with thin flexible tubing from a dye source elevated above the plate and force balance. Both food coloring and fluorescent fluorescene dyes were used, the former being backlit and the latter being lit with an 8W argon ion laser sheet in various orientations, Fig. 2.7.

Typically, a camera was mounted to image the flow from above, looking down spanwise onto a plane perpendicular to the plate at about mid-span, the "Perpendicular Spanwise Plane" of Fig. 2.7. Alternatively, the flow was imaged in a cross-stream direction along the whole span of the plate - the "Cross-stream Chordwise Plane." The camera shutter was controlled by a computer function generator which would trigger the shutter at user defined intervals after the motion start trigger. The output of the flash sync on the camera was recorded by the 7th channel of data acquisition to give the exact timing of pictures relative to the recorded force outputs.

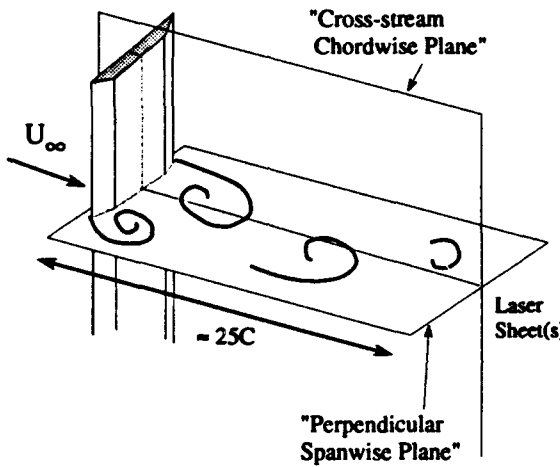


FIG. 2.7 Definitions of planes used for flow visualization

2.5.2 Plate Mount

Models were mounted vertically, at right angles to the (horizontal) metric platform of the force balance to which they were attached. A pivoted right angle brace was used as shown in Fig. 2.8. Aspect ratio changes were affected by sliding the model vertically in the mount and clamping it at the desired height. To facilitate flow visualization (typically done looking down through the free surface) models were offset from the center line of the balance, thus the "Cg Offset" shown in Fig. 2.1. Angle of attack could be adjusted to within $\pm 0.25^\circ$ by pivoting the entire mount around a pin located at the geometric center of the balance, results being read on a protractor attached to the mount. Knowing the exact location of the model relative to the center of the force balance allowed measured force results to be corrected to indicate forces and moments at the geometric center of the plate model. Moment calculations were not particularly accurate, due in part to the extremely small moment arm, as well as the accuracy required in locating the model correctly relative to the force balance. Although the linear forces of drag and lift were not so affected, moment values should generally be considered qualitative only.

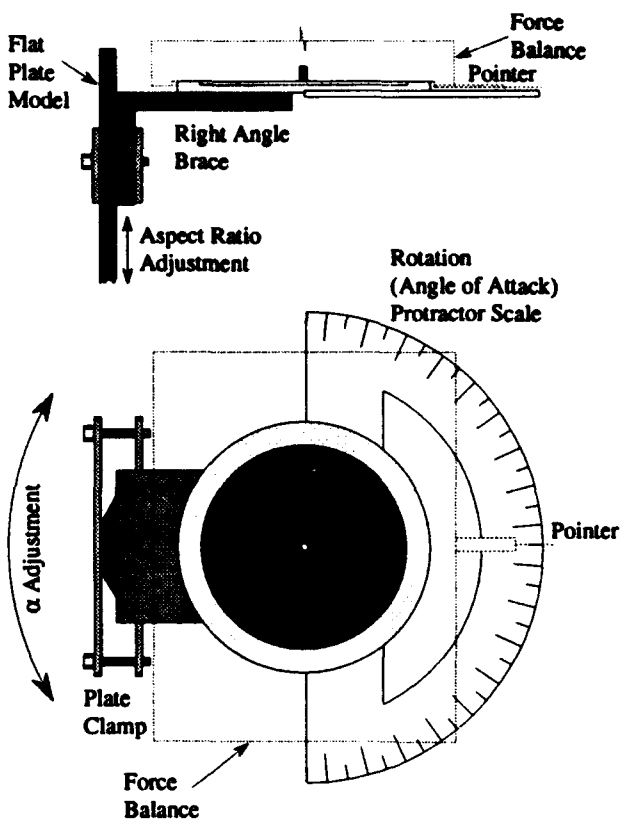


FIG. 2.8 Pivoting flat plate model mount

2.5.3 End Plates and End Conditions

One of the most important experimental parameters affecting the amount of large scale, or extrinsic, flow three dimensionality was the end conditions of the model. As shown in Fig. 2.9, one upper end condition and four different forms of lower end condition were investigated. The free surface upper end condition is known to provide a good (in the sense of minimizing extrinsic motions) end condition as long as the free surface is clean (see, for example, Slaouti and Gerrard, 1981). This is due both to the ability of the free surface to distort to match flow induced pressures, and to the lack of a no-slip condition at the free surface - *i.e.*, the ability of vortices to impinge the surface at right angles. Many authors typically double the quoted aspect ratios when one end projects through the free surface; however here we quote *AR* as the actual depth to chord ratio of the plate.

The first lower end condition, abbreviated *NEP*, was that of a simple free end, a minimum of 3 plate chord lengths from the bottom of either the X-Y towing tank or the free surface water tunnel. Due to flow around the end of the plate, this end condition was expected to have the most large scale three dimensionality and generally the highest mean base pressure.

Another lower end condition, **WEP**, used an end plate attached at right angles to the plate, parallel to the freestream. These end plates were constructed of thin (1 mm) plexiglass; they were circular, with a diameter of three to twelve times the chord of the plate upon which they were glued. The plates were offset 1 chord length from the leading edge of the end plate, as shown in Fig. 2.5. The results presented here all used plates of $3C'$ diameter, which is somewhat shorter than that recommended for consistent results independent of end plate size (Stansby, 1974 and Kubo *et al.*, 1989); however, the intent here was to vary the amount of large scale flow three dimensionality present by varying end condition, results independent of the end plate were actually undesirable.

In addition to end plates at right angles, previous experiments by Williamson (1989) on circular cylinders (albeit at much lower Reynolds numbers) have indicated an ability to affect changes in large scale flow three dimensionality by angling the end plates; here results are presented using end plates attached at angles ranging from $+20^\circ$ to -20° to the oncoming stream direction in order to modify the flow.

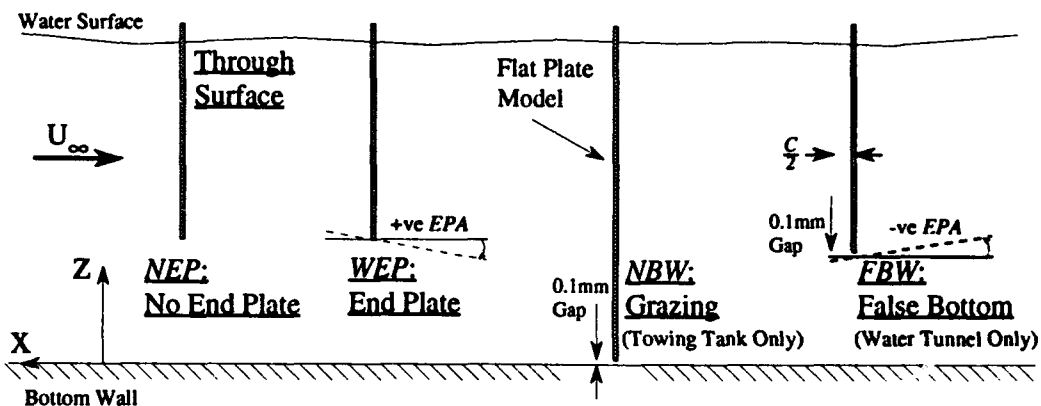


FIG. 2.9 Five flat plate model end conditions

The above two lower end conditions were applicable to both the X-Y towing tank and the free surface water tunnel ; however, the last two end conditions were with the lower end 0.1 mm from either the bottom of the towing tank or a false bottom in the water channel. In the case of the X-Y towing tank this provides an end condition, **NBW** , which is not obtainable in any other form of facility - that of a wall bounded "oncoming" flow without a boundary layer. In the free surface water tunnel the closest analogy to this is a false bottom wall (**FBW**) five chord lengths in streamwise length, with the model mounted only one half of its chord length downstream from the false bottom wall's leading edge - giving a very thin oncoming boundary layer.

The combination of the free surface upper end condition and a **NBIV** end condition in the towing tank has been shown by Slaouti and Gerrard (1981) to provide, for a circular cylinder, a flow with relatively little large scale three dimensionality. By analogy the **FBIV** condition in the free surface water tunnel could also be expected to provide reasonably "two-dimensional" flow. These two conditions were considered to have the least extrinsic flow three dimensionality; conversely, the **NEP** case was considered as having the most, with the **WEP** condition at various angles giving intermediate amounts.

CHAPTER 3

X-Y Towing Tank Experiments

3.1 Preface

The GALCIT X-Y towing tank facility, Fig. 3.1, was designed to study unsteady fluid dynamics (Williamson, 1988). Unlike a wind tunnel or water channel it is well suited to such studies, particularly in the unsteady startup regime, due to the ability of the carriage-model combination to accurately follow a pre-programmed unsteady trajectory. Since most carriage systems in use today tend to have upper velocity limits of a few tens of cm/second, maximum Reynolds numbers obtainable are somewhat limited, although the use of water permits higher Reynolds numbers than unsteady wind tunnels at the same velocity.

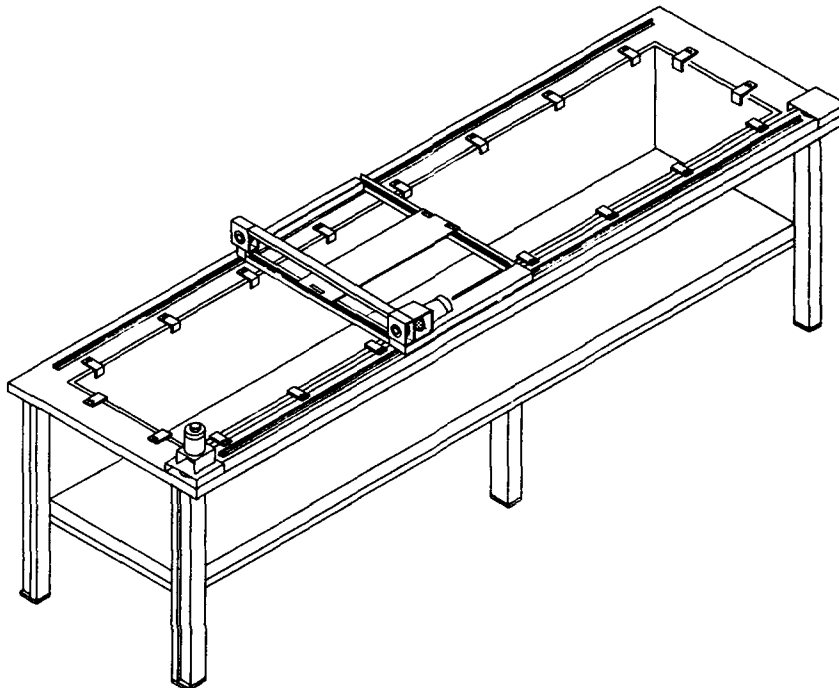


FIG. 3.1 Perspective view of the GALCIT X-Y towing tank facility

One of the main drawbacks of towing tanks is the inevitably limited length of run which can be achieved. To investigate steady-state behavior beyond the initial start-up regime, where the flow is still affected by the form of unsteady starting profile used, requires either a very long tank or very small experimental bodies. Small experimental bodies again limit the maximum Reynolds numbers which can be achieved and place higher demands on the carriage drive system to achieve a given starting profile, due to the increased

physical acceleration required for a given non-dimensional starting time t_a^ .* Obviously towing tanks are also of limited width and depth, tending to limit the size of the test body from blockage considerations and reduce the maximum aspect ratios obtainable. For test bodies mounted vertically, as were the flat plate models used here, the aspect ratio and thickness to chord ratio are further limited by the maximum length of model which can safely be cantilevered out from the carriage.

The primary diagnostic originally envisioned was flow visualization, which is facilitated by the low velocities and the large number of visualization techniques available in water. However, most of the experimental results presented here are force histories, although low Reynolds numbers and aspect ratios limit the maximum forces produced by the test body and increase the difficulty of accurately determining forces. There is a further problem encountered when measuring forces that is associated with carriage vibration: although the ambient noise level may be very low compared to the typical velocity rms levels found in a wind tunnel, the "noise" is produced through the carriage by body motion itself. Thus not only is it accompanied by accelerations of the whole body, it is also well correlated along the span of the plate, and contributes significantly to the noise level in the force signals.

A compromise must therefore be struck between maximum run length desired, minimum aspect ratio, maximum Reynolds numbers, minimum measurable forces, maximum blockage, minimum plate thickness and (Ch. 6) minimum Richardson numbers. This can sometimes be a difficult balance to achieve; this chapter presents some results of experiments designed to establish not only the qualitative and quantitative unsteady flow behavior, but to establish the optimum values of a wide range of different parameters for studying such behavior.

3.2 X-Y Towing Tank Description

The X-Y towing tank, Fig. 3.2, is a glass sided tank with interior dimensions of 450 cm long, 96 cm wide and 78 cm deep. It is supported on six legs which can be adjusted to level the tank bottom. Except for a single cross piece across the bottom at the midpoint, it is surrounded entirely by glass to facilitate flow visualization from any perspective.

On top of the tank two parallel cylindrical rails are mounted; an "X" carriage resting on teflon slider bearings is driven along these rails by a pulley and cable drive from a DC servo motor and gear box mounted at one end. Test bodies are mounted to a "Y-carriage," which slides on two parallel rails mounted on the X-carriage, this motion being driven by a DC servo motor mounted to the X-carriage. This whole arrangement was rather like a large computer X-Y plotter, the "paper" being replaced by the water in the tank, and the "pen" by the test body.

Each DC servo drive motor was attached to a PMI optical encoder with a resolution of 1024 counts per revolution. With the gearing that was used, this gave about 1500 counts/cm in the X direction and 512 counts/cm in Y. These encoders were attached to a Galieo DMC400b position controller in a Zenith AT

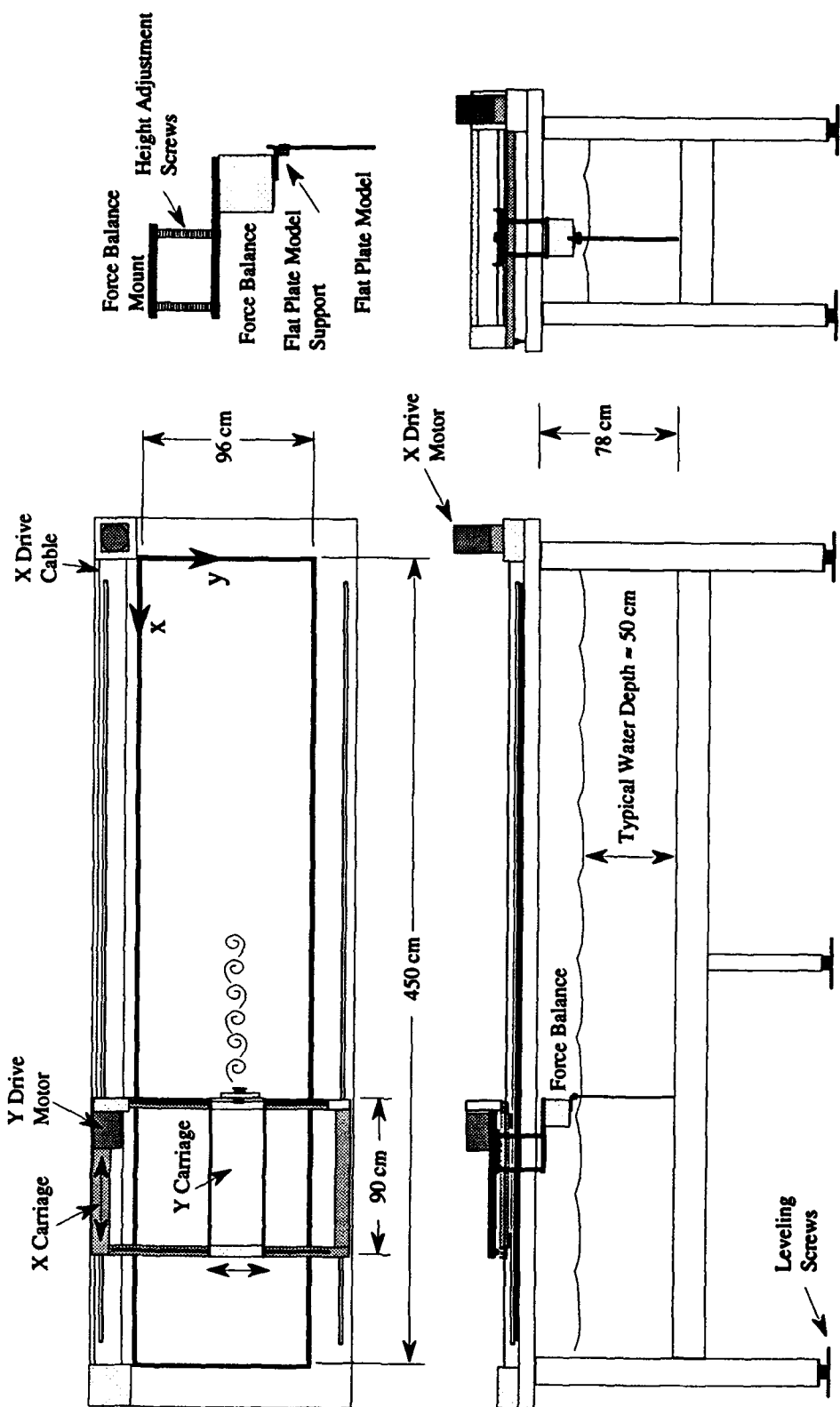


FIG. 3.2 Schematic drawing of the GALCIT X-Y towing tank facility

computer. A maximum speed (limited by the ability of the motor controller to keep up) of about 25 cm/s in X and 15 cm/s in Y was realized using this arrangement. A computer program was written which allowed the user to input position profiles for both X and Y axes in the form of a linear plus a sinusoidal motion:

$$X \text{ Position} = C t + D \sin(E t + F)$$

$$Y \text{ Position} = G t + H \sin(I t + J)$$

where C, D, E, F, G, H, I and J are user defined constants and t is time. The resulting velocity profile was then multiplied by a user selected starting profile for a specified acceleration time t_a :

None	: Velocity $\times 1.0$
Linear	: Velocity $\times \frac{t}{t_a}$
Exponential	: Velocity $\times (1 - \exp(-\frac{A t}{t_a}))$
Inverse Exponential	: Velocity $\times (\exp(\frac{0.693 t}{t_a}) - 1)$
$\frac{1}{4} \sin$: Velocity $\times \sin(\frac{\pi t}{2 t_a})$
$\frac{1}{2} \sin$: Velocity $\times \frac{1}{2}(1 - \cos \frac{\pi t}{t_a})$

where A and t_a are user specified. Specifying the motion in this fashion allows very complex motions to be built up; the carriage can execute everything from a linear plunging motion in one axis to a pure elliptical orbit. So, for example, to get a linear increase in velocity to a final velocity of 10 cm/s in an acceleration time of 2s, one would specify $C = 10$ and a Linear starting profile with $t_a = 2s$.

Motions were accurate to within about ± 1 mm and ± 10 msec for carriage velocities of 10 cm/s, over the length of the tank and runs of thirty seconds duration. Additional accuracy checks were made using an accelerometer and integrating the resultant signal, results are given in Appendix A. These results indicated about a 0.1% uncertainty in mean carriage velocity at 10 cm/sec, or about ± 0.1 mm/sec; with a similar rms level within a run.

Test models were mounted on the force balance which was in turn mounted beneath the Y-carriage on an adjustable height mount, see the detail in Fig. 3.2. This balance mount allowed the balance to be leveled easily, as well as providing the ability to move the entire balance/model apparatus up or down into the tank, thus affecting model depth and providing an additional method of adjusting aspect ratio (sliding the model in the plate mount being the first method, as described in Sec. 2.5.2) while keeping the relative orientation of the balance and the model the same.

The bottom of the tank was made as level and as flat as possible by adjusting the tank legs; the addition of water to the tank would then deflect the bottom up to 1 mm from its dry position. This deflection is important from the standpoint of the NBIV end condition (Sec. 2.5.3); Appendix A gives some profiles of the tank bottom with varying amounts of water in the tank.

The carriage rails were leveled to ensure that the water was as uniform a distance as possible from the rails along the length of the tank, commensurate with the rails also being as uniform a distance as possible

from the tank bottom. Inevitably there was a slight waviness (less than ± 1 mm/meter) in the X-carriage rails, due at least in part to the flexing of the tank as water was added or drained. Fig. 3.3 gives a grossly exaggerated view of this waviness and its effect on force measurements.

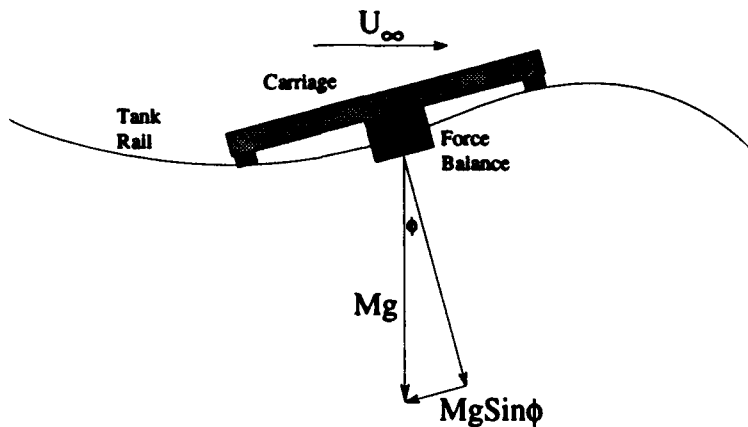


FIG. 3.3 Illustration of force errors due to waviness in X-Y towing tank rails

Consider a model mount and test plate with a combined mass M of 500g or $Mg \approx 5N$. For a wave in the rails of amplitude 1 mm/meter (a maximum slope of 0.06°); $\sin(\phi) \approx 1 \times 10^{-3}$. So the apparent force $Mg \sin(\phi)$ due to carriage tilting is $\approx 5 \times 10^{-3}N$, or about five times the uncertainty of the force measurement. Particularly at the lower Reynolds numbers, where force signal levels were very low, this can have an appreciable affect relative to the fluid dynamic forces inferred. Consider an experiment in water ($\rho = 1000 \text{ kg/m}^3$, $\nu = 1 \times 10^{-6} \text{ m}^2/\text{sec}$) at $Re = 1000$, $AR = 10$. Then:

$$\text{Apparent } C_d = \frac{5 \times 10^{-3} N}{\frac{1}{2} \rho \nu^2 Re^2 AR} \approx 1.0 .$$

This is obviously an appreciable error when compared to the typical $C_d \approx 2.0$ for a flat plate. A correction, described below and in Appendix A, was applied to account for this error.

Lift force histories are subject to the same kind of error, due to side to side tilting of the carriage; similarly, unless the center of gravity of the model is exactly aligned with the center of the balance, moment errors can also be introduced. However, except at low Reynolds numbers ($Re < 2500$) a larger "error" in C_l comes from inaccuracies in setting α , typically about $\pm 0.25^\circ$. Based on projected area, this would lead to a variation in C_l of $\pm .01$, but due to the bevels the actual C_l variation will be somewhat larger.

Moment results were based on a small moment arm (chord) which was offset a considerable distance from the geometric center of the balance to facilitate flow visualization. Thus not only were C_m calculations subject to the same errors as lift and drag, these errors were multiplied by the ratio of these distances (typically about 5) and divided by a small moment arm (typically .05), rendering moment results quite unreliable for anything but qualitative analysis.

Fluid density ρ was accurate to within $\pm 1 \text{ kg/m}^3$, plate depth could be measured to within 0.5 mm and chord to within .01 mm; given a 0.1 mm/sec uncertainty in U_∞ and $\Delta F_d = .001 \text{ N}$ this leads to an uncertainty in force coefficients of $\Delta C_d = \pm 0.02$ (1%) at $Re = 5000$, or $\Delta C_d = \pm 0.23$ (11.4%) at $Re = 1000$. Statistical variation from run to run is commensurately higher for low Reynolds number; for this reason the low Reynolds number results presented will typically be an ensemble average of many runs.

3.3 X-Y Towing Tank Procedures

For all the experiments detailed in this report, only the X-carriage motion capability was used, the Y-Carriage was locked rigidly in place. Additionally, only linear starting profiles were used, although t_a was varied, see Fig. 3.4 and Sec. 3.12.

The background fluid motion in the tank at the start of a run was a strong function of the length of time the tank was left undisturbed between runs. If too little time elapsed the tank retained residual motions from the previous run. Too much time allowed convection cells to be set up from a thermal imbalance between the surface and the tank bottom. It was found, using a dye tracer (potassium permanganate crystals), that stirring the tank immediately after a run to obtain a uniform initial turbulence level and then leaving the tank one or two hours gave the lowest level of background motion for the start of the next run. The initial stirring was performed with a 1/4" grid screen dragged through the tank several times.

Runs were all started with the carriage in exactly the same location on the rails; at the end of each run backlash was removed from the drive system by reversing the carriage back beyond this point and then going forward again to the correct location.

Teflon slider bearings were used on the X carriage because once they were in motion, they exhibited the lowest level of vibration and carriage noise. Unfortunately, this form of bearing was prone to stick slightly at the start of carriage motion, particularly if some time had elapsed since the carriage had moved. Before each run the X carriage was raised on three jackscrews and the bearings and rails thoroughly lubricated with silicone grease. The carriage was then lowered until it almost touched the rails. A few seconds before the start of a new run the weight of the carriage was lowered onto the rails; this gave very smooth and repeatable carriage starts and subsequent motion.

In addition to the data analysis and procedures outlined in Sec. 2.4, the use of the towing tank required that some additional corrections to be applied. Due to the unsteady starting motion there is a non-fluid-dynamic inertial force associated with the mass of the model and model mount. The effect of this mass on the drag was experimentally determined for each model by ensemble averaging many carriage runs with no water in the tank. Accelerometer output was scaled as a function of plate mass to best fit the resulting drag force, the scale factor being proportional to an effective model/mount mass in the drag direction. Experimental force results with water in the tank were corrected by subtracting the instantaneous carriage accelerometer output multiplied by the calculated scale factor of the plate+mount mass. Since the accelerometer also recorded the

effects (in the drag direction) of the waviness in the rails, this technique also corrected for that error, although to correct for buoyancy when the carriage was not accelerating the effective model mass was reduced by the mass of the fluid displaced by the plate.

Since the accelerometer recorded only x-accelerations, this technique could be used only for drag corrections. Lift and moment force results from the runs with no water yielded a force vs. position history as a linear function of model mass, with the forces due entirely to the tilting of the carriage. This history was saved in a correction file; subsequent experiments were corrected by interpolating model mass (corrected for buoyancy) and carriage position in this file and subtracting the forces and moments thus determined. Although this theoretically corrected for carriage tipping, it did not account for changes in rail geometry when the tank was filled, thus C_l resolution remained poor at lower Reynolds numbers and aspect ratios. For extremely sensitive runs at $Re \leq 1000$, a more elaborate correction scheme was required; this scheme is described fully in Appendix A, along with additional details of the towing tank facility, the procedures used and data analysis techniques.

3.4 Typical X-Y Towing Tank Result

Fig. 3.4 gives a schematic drawing of what, intuitively, one might expect a force history from the X-Y towing tank to look like, given a linear increase in carriage velocity (constant carriage acceleration) to a final velocity U_∞ in time t_a , or non-dimensional time t_a^* , where:

$$t_a^* = \frac{U_\infty t_a}{2C} = \frac{x_a}{C} .$$

The horizontal axis in these plots is non-dimensional position $x^* = x/C$; for any time $t > t_a$ (ie. during steady motion) this is equivalent to nondimensional time $t^* = U_\infty t/C$ less the starting distance x_a/C . Note that the starting velocity profile is shown as a function of position: $U(x^*) = U_\infty \sqrt{x^*/t_a^*}$.

The global flow at early time $t^* = 0^+$ could be expected to be inviscid and irrotational, since the vorticity in the boundary layer has not yet had time to diffuse far from the body. The potential flow will be streamwise symmetric and viscous forces on the body will be zero, but there will be an unsteady force due to a finite acceleration and apparent mass. The apparent mass is equivalent to the mass of fluid contained in a circumscribed cylinder (see, for example, Batchelor, 1967, Ch. 6) and the initial drag coefficient can be calculated as:

$$C_{d_i} = \frac{\text{Apparent Mass} \times \text{Acceleration}}{\frac{1}{2}\rho U_\infty^2 \mathcal{A} C^2} = \frac{\rho \pi C^3 \mathcal{A} U_\infty}{2\rho U_\infty^2 \mathcal{A} C^2 t_a} = \frac{\pi}{4t_a^*} .$$

So, for example, with $t_a^* = 1.31$, $C_{d_i} = 0.6$. If the apparent mass is taken to be a constant throughout the motion, then we expect an equivalent drop in C_d at the end of the acceleration, as illustrated.

Except for the unsteady force C_{d_i} , the drag initially will be zero, since the flow is streamwise symmetric; but we expect the drag coefficient to immediately begin increasing for $t^* > 0^+$. Since drag

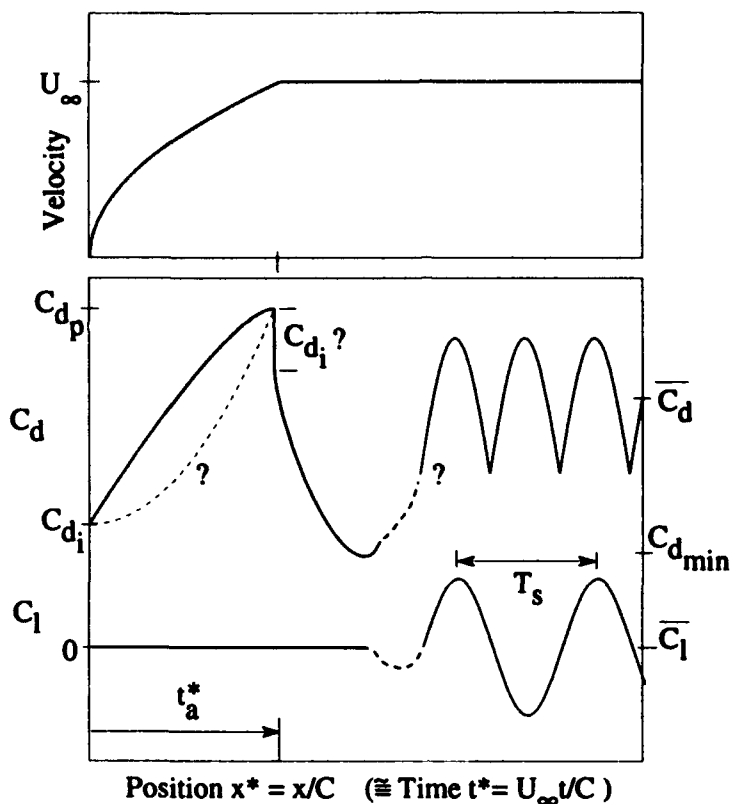


FIG. 3.4 Schematic of "theoretical" force history from the X-Y towing tank , assuming a linear increase (with time) in carriage velocity to U_∞ in non-dimensional time $t_a^* = \frac{U_\infty t_a}{C}$

coefficients are based on the final steady freestream velocity U_∞ , even if the instantaneous drag coefficient of the flow configuration at early times was constant, we would expect them to initially increase due simply to the increasing velocity. The nature of this increase depends on the flow configuration and unsteady starting profile used; Cortelezzi (1992) indicates that any power law profile can be collapsed by a proper scaling of C_d and t^* . For a linear velocity increase, were the instantaneous drag coefficient to be constant, we would expect a parabolic increase in C_d . If, as one would expect, the instantaneous drag coefficient is decreasing as the size of the initial re-circulating wake bubble grows, C_d would be concave downwards, as illustrated; with the peak C_d occurring at the end of the unsteady acceleration, provided that this acceleration was shorter than the time required for the initial symmetric bubble to become unstable and break.

At the end of the acceleration we expect an immediate drop of magnitude $C_{d,i}$ and a slow decrease to a drag minimum associated with an initially symmetric recirculating wake and a high base pressure coefficient. This increase in base pressure is likely connected to the increasing strength of the recirculating vortex pair (Leonard, 1993) inducing an upstream velocity against the rear face of the plate , with the shear layers separating at a correspondingly higher angle to the freestream.

Eventually the recirculating bubble will become unstable, the symmetry will break down and the shear layers will begin to roll up alternately behind the body, leading to the well known Karman vortex street with a

Strouhal shedding period of T_s in the lift and $2T_s$ in the drag. Accompanying this shedding would presumably be an increase in the mean drag level to $\bar{C}_d \approx 2.0$ as found by Fage and Johansen, 1927 and many others.

The relative magnitudes of the Strouhal fluctuations in lift and drag depend on several factors. Although lift forces can be generated by chordwise viscous stresses on the front and rear faces of the plate, at the Reynolds numbers considered here the lift is generated primarily by pressure forces acting on the beveled portion of the rear face of the plate. Increasing plate thickness would increase the lift (even if the global flow was unchanged) by virtue of the increased area on which pressure forces act. Increasing or decreasing the bevel angle for a given thickness will also change the lift, since it changes the location and distribution of the area on the rearward face on which lift can be generated. A greater bevel angle (more nearly rectangular plate) moves the lift generating area toward the outer edges of the rear face, while a sharper bevel tends to distribute the lift generation area more uniformly across the base. Note that for a normal plate, if the (instantaneous) base pressure changes uniformly across the rearward face, there will be NO lift generated, although there may still be considerable fluctuation in the drag: it is only the non-uniformity of instantaneous base pressure which can generate lift. Even for nearly normal plates the direct contribution to lift of a 2.5° angle of attack change from $\alpha = 90^\circ$ equates to lift fluctuations only 5% as large as corresponding drag fluctuations, assuming uniform instantaneous base pressures. The relative magnitudes of C_l and C_d fluctuations depend not only on plate thickness and bevel angle, but also on the uniformity of the instantaneous pressure distribution on the downstream face of the plate.

When these experiments were initially undertaken, it was felt that the entire starting process described above might occur in something less than thirty chord lengths of motion. Fig. 3.5, which is a typical experimental result from the X-Y towing tank, indicates that the process takes somewhat longer, and is considerably less predictable, than what was originally envisioned.

The result shown in Fig. 3.5 was for a plate of $AR = 17$ with the lower end near the bottom of the tank, $\alpha = 90^\circ$, $h/C = 10.3\%$, $Re = 5000$ and $t_a^* = 1.31$. Some of the qualitative features are quite similar to those conceived theoretically, although $C_{d,i}$ (which is shown in the inset and is about 20% higher than theoretical) is strongly affected by both the degree and type of filtering used, and is not distinguishable at all at the end of the acceleration due to the smoothing. There is an initial peak, $C_{dpeak} = 3.4$, corresponding to the acceleration region, followed by a drag minimum $C_d \approx 1.3$ during the initial symmetric recirculating bubble.

This region then gives way to twenty or thirty chord lengths of motion with $\bar{C}_d \approx 1.6$ and very little oscillation in either lift or drag to indicate organized vortex shedding. This region will later be shown to correspond to an open wake with a wake instability far downstream, but no roll-up of the shear layers close to the body as is the case for classical vortex shedding. A slow, almost exponential increase in oscillation level and mean drag begins at about $t^* = 40$, reaching a peak at $t^* = 65$ and then falling off to a lower level

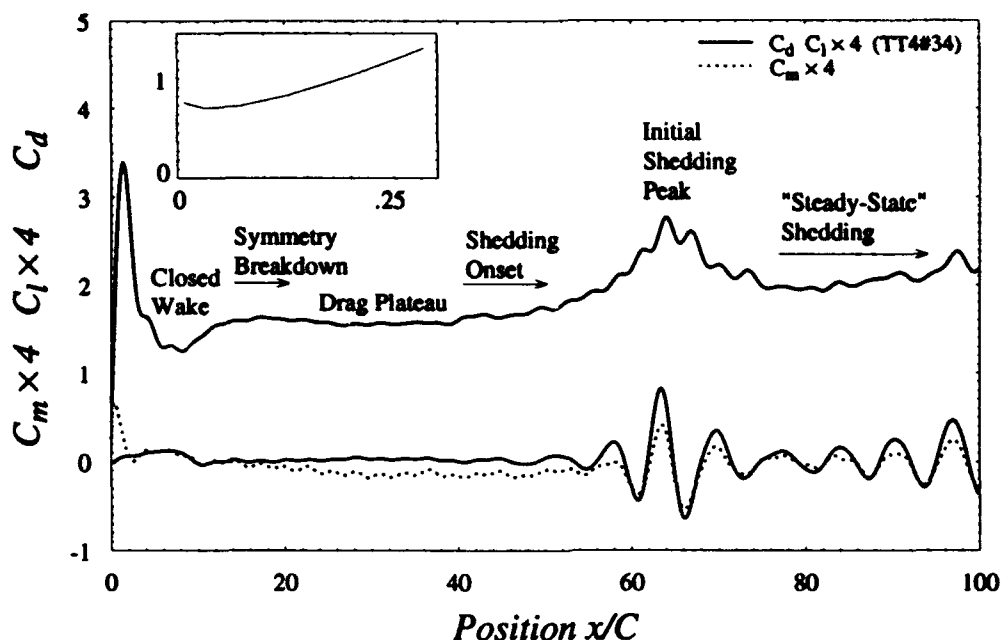


FIG. 3.5 Typical force histories from the X-Y towing tank. $C = 3\text{cm}$, $\mathcal{AR} = 17$ (NBIV end condition), $l/C = 10.3\%$, $\alpha = 90^\circ$, $U_\infty = 15.75 \text{ cm/s}$ ($Re = 5000$), $t_a^* = 1.31$

oscillation with period $T_s \approx 7$ before once again beginning to increase toward the end of the run. Note that this run was 100 chord lengths in duration, and shows no real indication of having reached an "equilibrium" shedding state, at least in the classical sense.

The relative unreliability of moment measurements is illustrated in this figure, with a non-zero C_m , even for $\alpha = 90^\circ$. The fluctuating component of moment should be reasonably accurate however, and the fact that it is comparable to the fluctuating lift is an indication that both quantities are produced primarily by pressure forces, rather than viscous stresses which would not produce appreciable moment. Because the moment results apparently contain no additional qualitative information not already illustrated by the lift, and because their inaccuracy renders them unsuitable for anything but qualitative comparison, moment results will not be shown further.

Two qualitative impressions stand out: Firstly, the length of time which this run takes to reach "steady-state" is much longer than had originally been anticipated. Secondly, the existence of a low drag ($C_d = 1.6$) non-shedding region was not anticipated, nor was the apparent modulation in the vortex shedding once it began. Many of the inconsistencies between this run and the classical model of figure Fig. 3.4 will be explored in the remainder of this chapter.

3.5 Filtering

The ambient noise level in the force measurement results is illustrated in the top plot Fig. 3.6, which presents the same results as Fig. 3.5 without any digital filtering having been applied. The results in such a form are too noisy to allow accurate determination of C_d , at either the beginning or end of the acceleration region, although there does seem to be a sharp decrease in drag corresponding to the end of this region.

The bottom plot of Fig. 3.6 gives the same result filtered with several different combinations of filtering parameters. Note the much decreased oscillation level for the result with $f_{co}^* = 0.15$ ($\approx S_t$) and from the inset plot the effect on the initial peak height of increased filtering. The inset plot also illustrates the effects

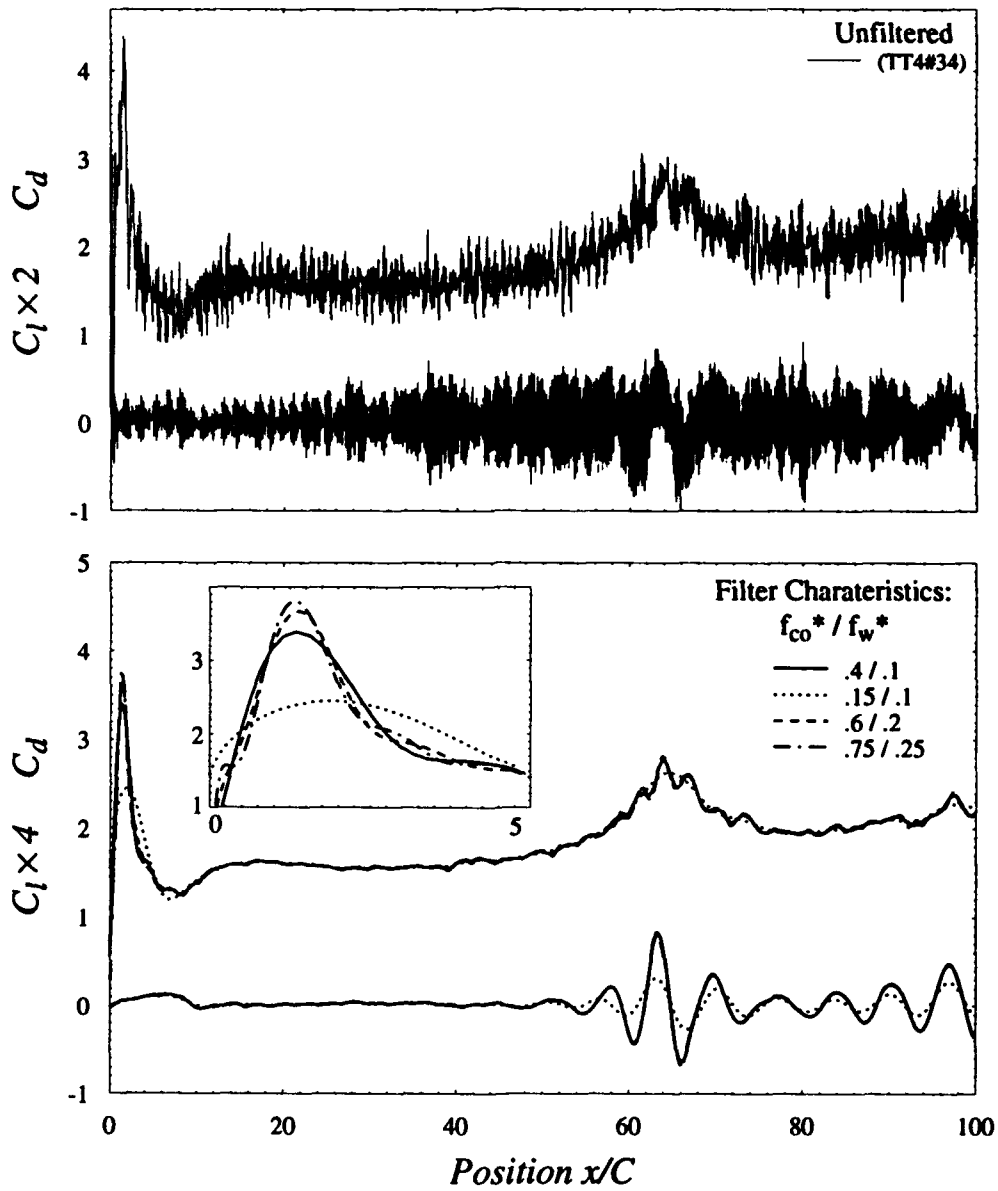


FIG. 3.6 Effects of digital filtering on result of Fig. 3.5

of filtering at very early times, where the initial drag impulse leads to some ringing from the sharp cutoff in the frequency domain. A $f_{co}^* = .4$ and $f_w^* = .1$ provided the best result from the standpoint of maintaining the S_t and $2S_t$ oscillations while at the same time minimizing ringing from a sharp cutoff in the frequency domain. All of the results presented here will be filtered using these parameters unless otherwise noted.

When comparing results from run to run, consistent results can only be achieved by filtering with the same non-dimensional frequency filter parameters. When filtering in this manner it is important that the highest fluid dynamic frequencies, such as those corresponding to t_a^* , S_t , and $2S_t$, always be well below the physical noise frequencies which are being filtered out. As Reynolds number is increased or chord is decreased the non-dimensional fluid dynamic frequencies correspond to higher *physical* frequencies, and with the same non-dimensional filtering parameters the noise level in the signals will be increased due to reduced filtering at the physical noise frequencies. An additional effect is the nonlinear response as the driving frequencies approach the natural frequency of the balance. For these reasons the smallest chord that was used was 3 cm, and the fastest acceleration $t_a^* = 0.5$; with the acceleration profiles and high Reynolds number results being performed with $C = 5\text{cm}$ to maximize the non-dimensional and physical frequency separation.

3.6 Repeatability

The "typical" run shown in Fig. 3.5 was repeated many times to establish the statistical repeatability of various portions of the force history; ensemble averaged and some individual results for $Re = 5000$ are shown in Fig. 3.7, along with the corresponding rms levels ($\times 4$). The runs are initially very repeatable, with uniform rms levels of ≈ 0.05 ; the initial peak height, the drag minimum in the symmetric bubble region, and the subsequent drag plateau at $C_d \approx 1.6$ are all consistent from run to run.

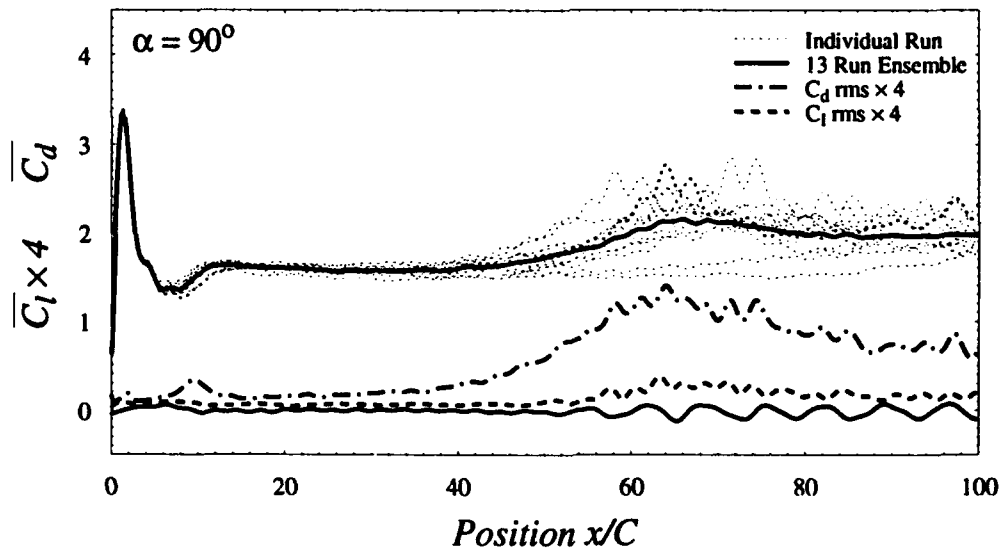


FIG. 3.7 Ensemble average and individual runs to illustrate repeatability. $\alpha = 90^\circ$, $Re = 5000$, $t_a^* = 1.31$. For $80 < t_a^* < 100$ $\bar{C}_d = 1.97$ and $\bar{C}_l = -.003$

The point at which shedding begins however, varies widely, with an associated increase in the C_d rms levels to ≈ 0.3 at about $t^* = 40$ when the earliest onset is noticed. The level of the initial shedding peak also varies, with low overshoots seeming to correspond to later shedding onset. In the final "steady-state" shedding portion, C_d rms has decreased to ≈ 0.2 and C_l rms to 0.05.

3.7 Angles of Attack

The existence of a long lasting region with no shedding, and the large variation in the shedding onset time, made it very difficult to obtain average results in the steady-state shedding portions of each run, the situation being exacerbated when larger chord plates, with corresponding shorter runs lengths, were used.

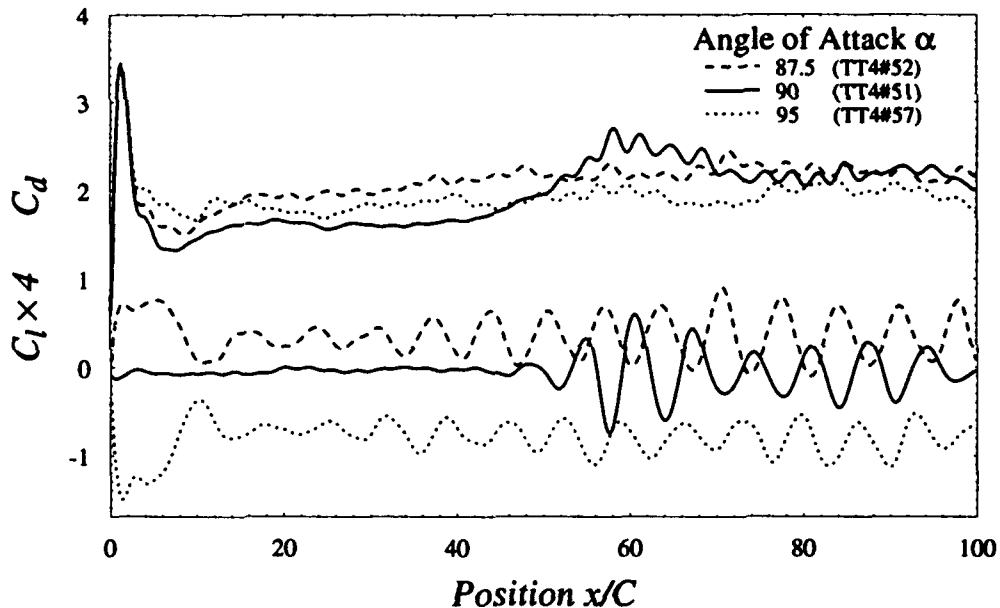


FIG. 3.8 Effects of small angle of attack variations. $t_a^* = 1.31$; $h/C = 10.3\%$; Mean values for $80 < t^* < 100$; Solid Line: $\alpha = 90^\circ$, $\bar{C}_d = 2.17$, $\bar{C}_l = -0.13$; Dashed Line: $\alpha = 87.5^\circ$, $\bar{C}_d = 2.19$, $\bar{C}_l = .086$; Dotted Line: $\alpha = 95^\circ$, $\bar{C}_d = 1.98$, $\bar{C}_l = -.194$

The introduction of a small asymmetry, in the form of a change in angle of attack to $\alpha = 87.5^\circ$ or $\alpha = 95^\circ$, resulted in a much more uniform shedding onset, as can be seen from Fig. 3.8. This asymmetry increased the minimum level to which the drag fell in the symmetric bubble region, and eliminated the non-shedding region which was seen with $\alpha = 90^\circ$. Instead, shedding began almost immediately after the acceleration. Evidently, the slight asymmetry serves to quickly break the initial re-circulating bubble.

It is interesting to note from this figure that the initial transient lift level of $C_l \approx 0.25$ remains even after the drag reaches a minimum. Presumably the lift is being produced primarily by pressure forces on the downstream plate bevels, of which the bevel most nearly aligned with the flow (*i.e.*, the upper one) will predominate. An asymmetric pressure distribution on the trailing face could then be expected to produce

correspondingly more lift than drag if the pressure were lower near the bevels. Based purely on a geometrical projection, the lift shedding oscillation should be only 5% as large (at $\alpha = 87.5^\circ$) as the fluctuation in drag; that they are of comparable magnitude gives an additional indication of the asymmetry of the instantaneous pressure distributions on the rearward face.

A nine run ensemble average at $\alpha = 87.5^\circ$ is shown in Fig. 3.9; it indicates a much reduced variation in shedding onset and a correspondingly more uniform rms level over the whole run. For $80 < t^* < 100$ $\overline{C_d} = 2.06$ and $\overline{C_l} = 0.085$, which can be compared to $2.06 \times \sin(2.5^\circ) = .088$, indicating that the mean $\overline{C_l}$ is within 7% of the value that would be expected by taking a pure geometrical projection of the base pressure. These runs used either an end plate or near-wall lower end condition, at varying aspect ratios from $\mathcal{A}R = 6$ to $\mathcal{A}R = 17$, so the rms levels are somewhat higher than those obtained for runs with identical run conditions.

Although shedding begins almost immediately after the symmetric bubble breaks, it does appear to increase in amplitude (evidenced by increased mean and fluctuating force levels) at about $t^* = 40$, building to a peak at $t^* = 60$. This may be an indication of the importance of wake vorticity (which is non-existent at early times) in determining the steady-state flow; in this way the $\alpha = 87.5^\circ$ case is somewhat analogous to the exponential onset seen in the $\alpha = 90^\circ$ case. The increased consistency and earlier shedding onset at $\alpha = 87.5^\circ$ is important for later results using larger chord plates, in which it was desired to achieve steady-state shedding as early as possible in each run.

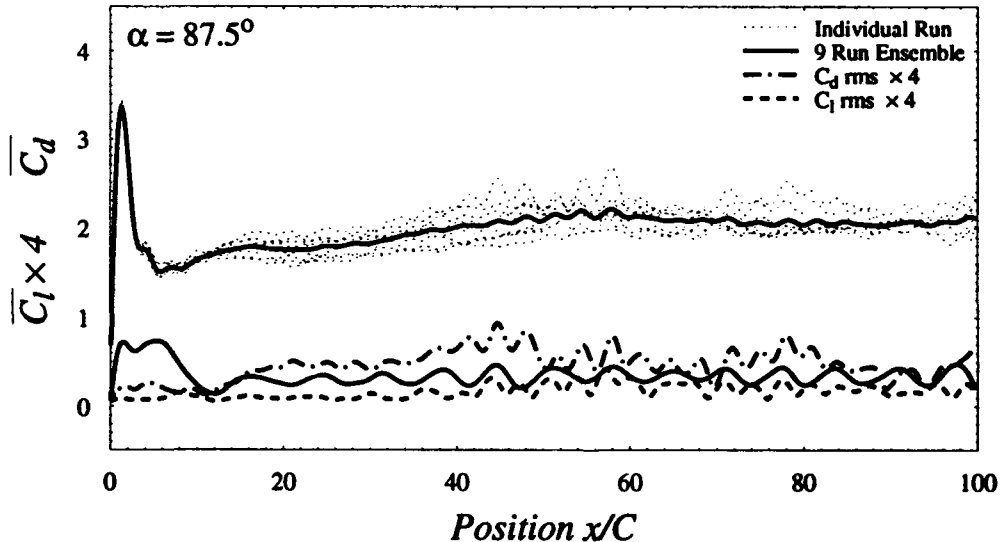


FIG. 3.9 Ensemble average and individual runs to illustrate repeatability. $\alpha = 87.5^\circ$, $Re = 5000$, $t_a^* = 1.31$. For $80 < t_a^* < 100$ $\overline{C_d} = 2.06$, $\overline{C_l} = .085$

3.8 Reynolds Numbers

Although for a fully separated flow such as that studied here one would expect very little variation with Reynolds number for $Re \gtrsim 3000$ (see, for example, Tritton, 1988 and Flachbart, 1935) several different Reynolds numbers were explored to establish this. Fig. 3.10 indicates very little qualitative changes with an increase in Re from 2500 to 7500, the shedding onset time being known to be unrepeatable even at the same Reynolds number. The initial peak height is somewhat larger at the higher Reynolds number, which is likely due primarily to the non-dimensional frequency of the initial peak being closer to the physical natural frequency of the balance, as well as being closer to the physical frequencies of carriage vibration, with a correspondingly decreased digital filtering effectiveness. Results at Reynolds numbers up to $Re = 12,500$ using a larger chord plate ($C = 5\text{cm}$ instead of 3cm) with lower physical frequencies and correspondingly higher reliability, do not indicate a larger initial peak. Similarly the apparent trend to higher post-acceleration drag minima does not occur with the larger plate, and may again be an effect of filtering.

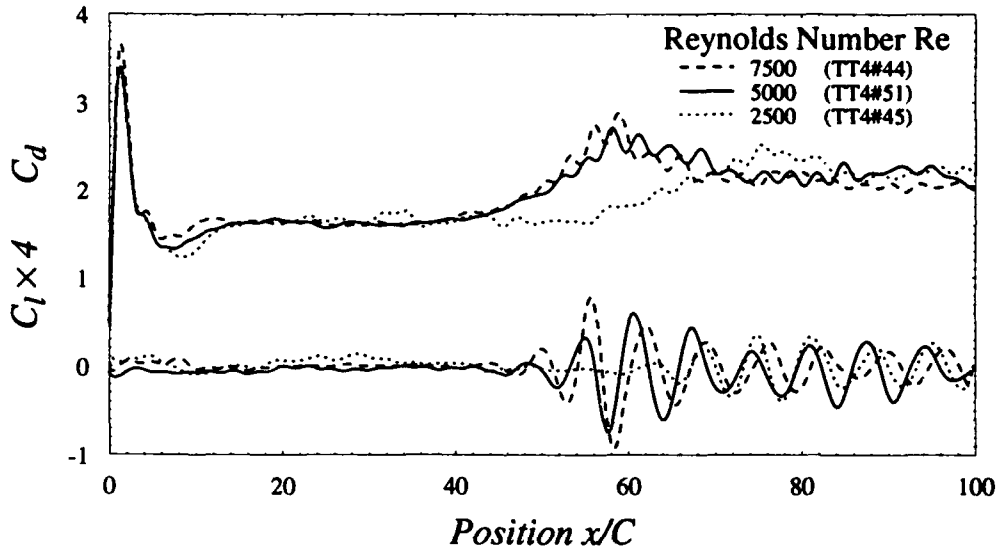


FIG. 3.10 Comparison of various Reynolds numbers. $\alpha = 90^\circ$, $AR = 10$, $t_a^* = 1.31$; Dotted Line: $Re = 2500$; Solid Line: $Re = 5000$; Dashed Line: $Re = 7500$

Ensemble averaged results and rms levels for both $Re = 5000$ and $Re = 1000$ are shown in Fig. 3.11. Note that the horizontal scale is expanded from those that have previously been presented; these runs used a larger chord plate ($C = 5\text{cm}$) at $\alpha = 87.5^\circ$ and a larger number of runs (27 at $Re = 5000$ and 54 at $Re = 1000$) to obtain more consistent and reliable results.

For $Re = 5000$ and $20 < t^* < 60$ the values $\overline{C_d} = 2.14$ and $\overline{C_l} = .094$ are about 8% and 14% higher, respectively, than those obtained in the same interval with the smaller chord plate in Fig. 3.9. This may be due to the increased blockage of the larger plate, an effect which will be discussed further below. The rms levels of these runs in the same interval $\overline{C_{d,rms}} = .134$ and $\overline{C_{l,rms}} = .026$ are lower than those obtained with the smaller plate ($\overline{C_{d,rms}} = .142$ and $\overline{C_{l,rms}} = .043$ for the same interval), which reflects the increased

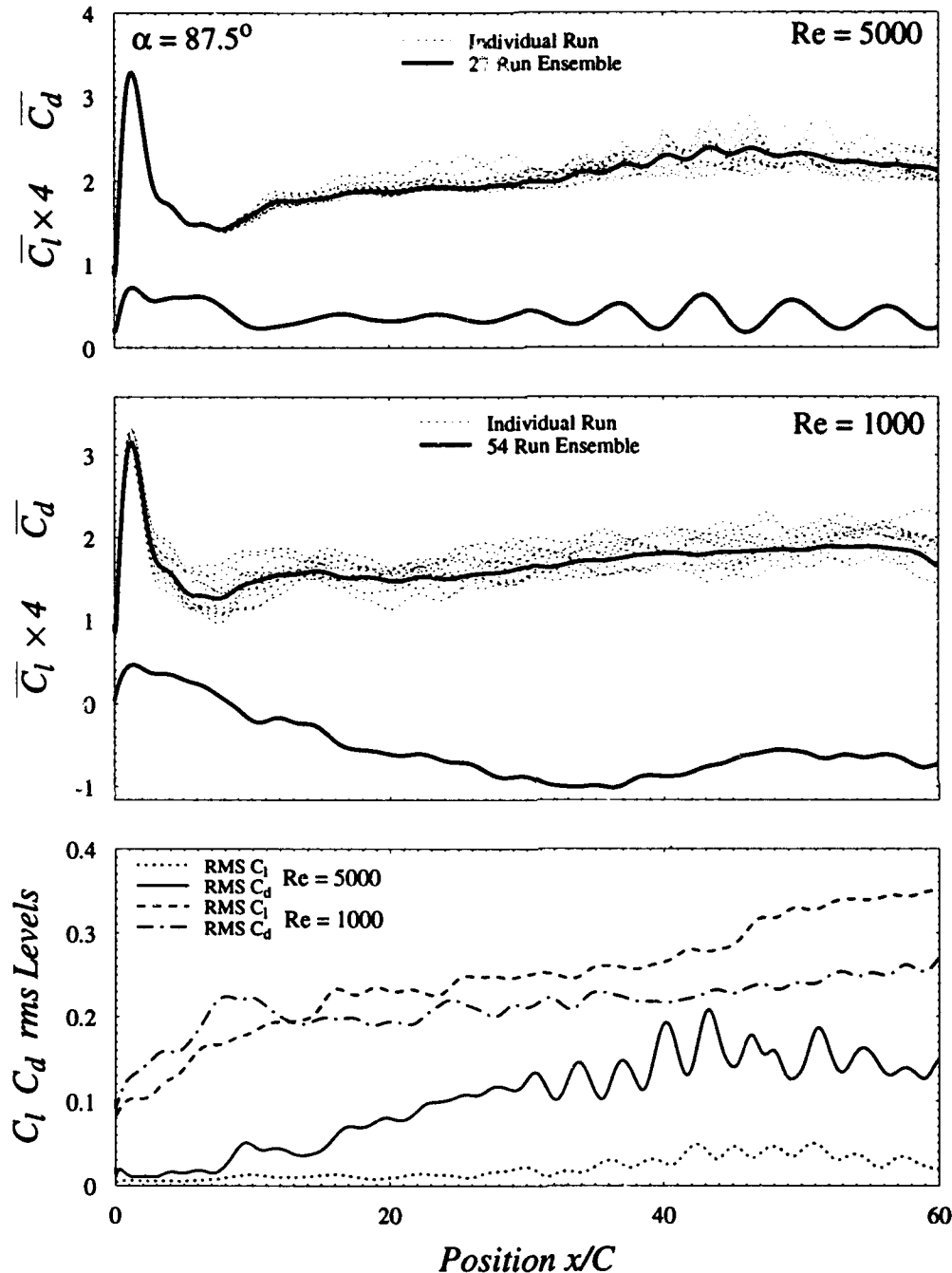


FIG. 3.11 Ensemble average and rms levels for $Re = 1000$ and 5000 . $\alpha = 87.5^\circ$, $hC = 6.8\%$, $AR = 10$, $t_a^* = 1.31$. For $20 < t^* < 100$ at $Re = 5000$: $\bar{C}_d = 2.14$, $\bar{C}_l = .094$, $\bar{C}_{d_{rms}} = .134$, $\bar{C}_{l_{rms}} = .026$; at $Re = 1000$: $\bar{C}_d = 1.73$, $\bar{C}_l = -.295$, $\bar{C}_{d_{rms}} = .227$, $\bar{C}_{l_{rms}} = .282$

consistency of these runs, which all used an identical AR and NBW end condition. Note the phase (but not amplitude) correlation in the shedding, which is apparent in both the rms levels and the ensemble averaged force results. The first several shedding oscillations are again of lower amplitude, with the shedding "taking hold" at about $t^* = 40$; again an indication of the importance of wake vorticity in affecting the steady-state shedding behavior.

At $Re = 1000$ the rms levels at early times are much higher than the $Re = 5000$ case, the initial level being the most indicative of the statistical run to run variation. Later in the run the rms levels (particularly of the drag) at the two Reynolds numbers are much closer together due to the addition of similar levels of uncertainty from the flow state itself. For $20 < t^* < 60$ $\bar{C}_d = 1.73$, considerably lower than the value at $Re = 5000$. The uncertainty in the ensemble result is $1/\sqrt{N}$ times the rms level, where N is the number of ensemble results used in the average. As was noted at the end of Sec. 3.2, the force balance balance uncertainty at $Re = 1000$ is $\approx \pm 0.25$ in C_d , and the rms level of the ensemble $.227/\sqrt{54} = .031$ equates to a total uncertainty in the ensemble averaged \bar{C}_d of about ± 0.28 . This would still indicate a somewhat smaller drag at $Re = 1000$ than at $Re = 5000$; which would be in agreement with the results of Flaschbart (1935), for example.

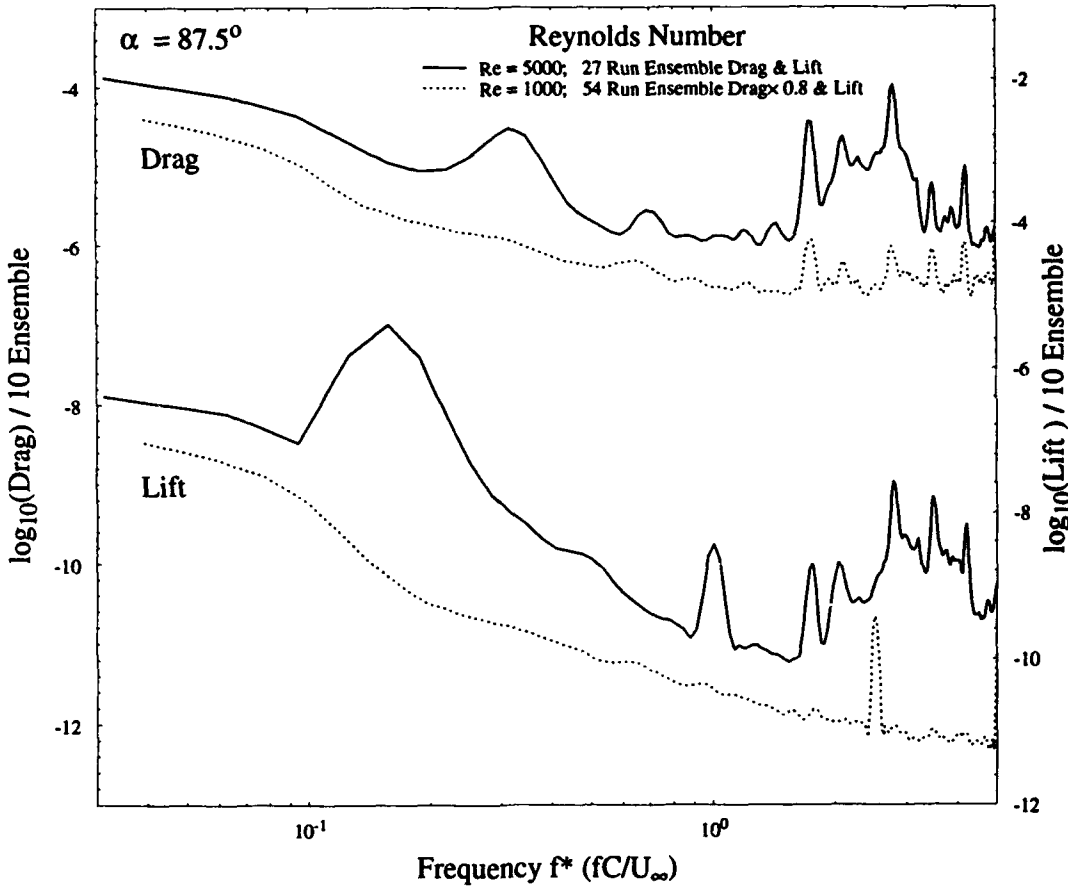


FIG. 3.12 Ensemble average power spectra for $Re = 1000$ and 5000 . $\alpha = 87.5^\circ$, $h/C = 6.8\%$, $AR = 10$, $t_a^* = 1.31$. Spectra are for $20 \leq t^* < 60$

Most surprisingly, at $Re = 1000$ there is an apparent lack of shedding oscillation in the lift signal, which although it is inaccurate should still show some indication of shedding if it was present. There appears to be an uncorrelated period $2T_s$ oscillation still present in the drag results, although ensemble averaged power spectra (Fig. 3.12) indicate the drag has almost no peak at $2S_t$. Flow visualization (Ch. 6, in stratified flow)

indicates that the vortex shedding is occurring with a much larger formation distance at $Re = 1000$. The plate is followed by at least two chord lengths of dead water, with vortices tending to shed into the wake at the downstream end of this dead water region; there is no shear layer roll-up in the immediate proximity of the plate as there is in both the classical picture of vortex shedding and at $Re = 5000$. This has two effects; firstly, the base pressure fluctuations are reduced by the remoteness of the vortex shedding, decreasing fluctuations in both lift and drag. Secondly, the fluctuations which do occur are probably more uniform across the base of the plate, which decreases the fluctuation level in the lift without affecting fluctuations in the drag. The power spectra in Fig. 3.12 appear to retain some small peak in the drag at $f^* = S_t$, while the formerly much larger lift peak at $Re = 5000$ is completely absent at $Re = 1000$.

3.9 Plate Thickness

Fig. 3.13 gives results for three different plate thickness from $l/C = 6.8\%$ to 20% with $C = 4$ or 5 cm; more extreme examples can be found in, for example, Nakaguchi (1968), or Bearman (1972). The primary effect is an increased level of initial lift and subsequent fluctuation level with increased thickness. This provides further evidence that the lift is due almost exclusively to pressure forces acting on the plate bevels, with the ratio of initial peak lift being directly related to thickness. The thicker plates seem to develop an initial asymmetry and vortex shedding somewhat earlier, with a corresponding increase in the drag minima following the acceleration. This is most noticeable in the $\alpha = 87.5^\circ$ case, and is likely due to the closer proximity of the downstream face of the plate to the vortex formation region serving as a destabilizing influence on the initial vortices. The minimum drag is also increased with increased thickness at $\alpha = 90^\circ$, although for this case the initial shedding onset does not occur consistently earlier. The initial peak heights are higher for the increased thickness for both $\alpha = 90^\circ$ and $\alpha = 87.5^\circ$, again likely due to the downstream face of the plate being closer to the low pressure vortex cores in the formation region.

3.10 Blockage Effects

The nominal intent of Fig. 3.14 is to present several results with varying chord to tank-width ratios to establish the effects of blockage on the mean flow. This figure also serves to illustrate many of the problems encountered when performing experiments in the confines of the X-Y towing tank using plates with either very small or very large chord lengths.

The lowest blockage ratio case, $B = 2.1\%$, used a 2 cm chord model accelerated to 24 cm/s ($Re = 5000$) in 0.22 sec to give $t_a^* = 1.31$. This acceleration is somewhat greater than the carriage is accurately capable of, as evidenced by the very high initial acceleration overshoot and carriage bouncing seen in both the drag and lift histories. However, despite this the subsequent history appears to be fairly typical of previous results.

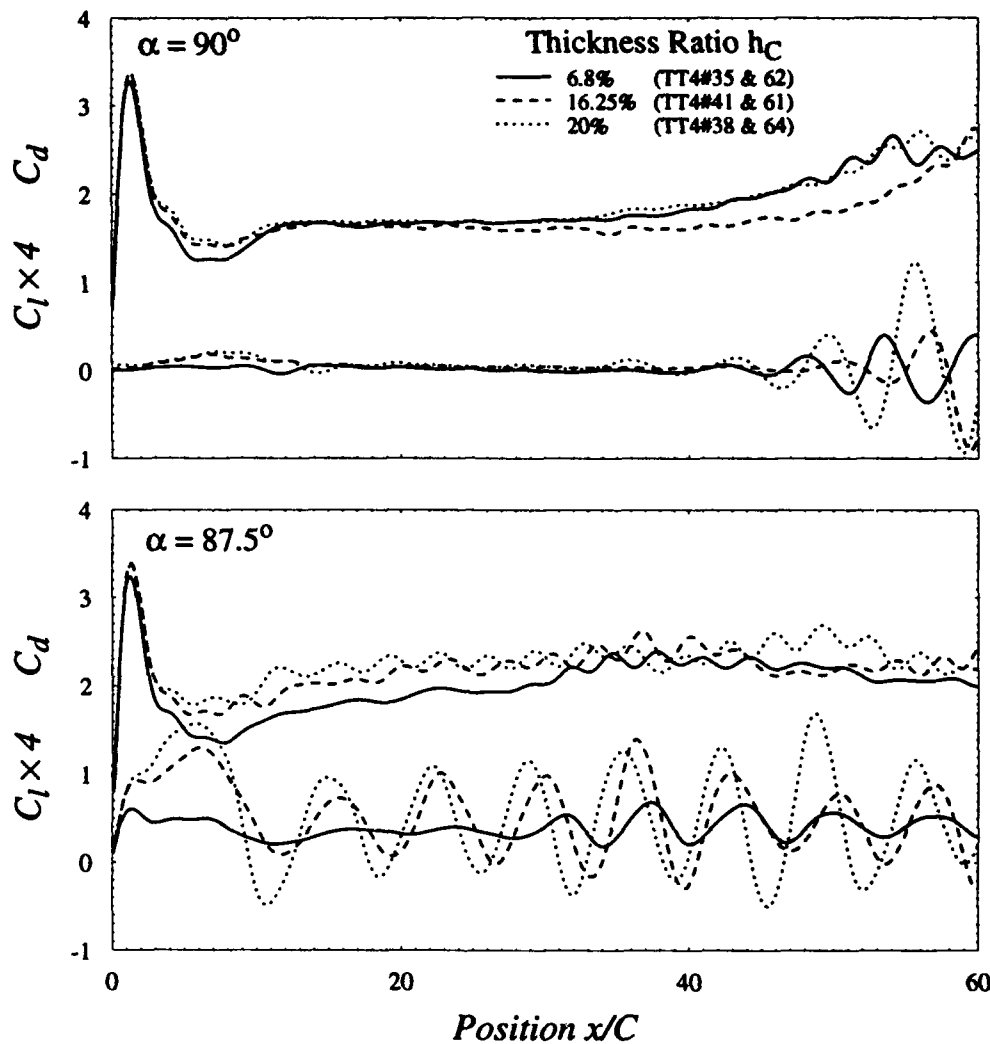


FIG. 3.13 Effects of plate thickness. $C = 5\text{cm}$, $Re = 5000$, $AR = 10$, $t^* = 1.31$, α as noted. Solid line: $h/C = 6.8\%$; Dashed Line: $h/C = 16.25\%$ ($C = 4\text{cm}$); Dotted Line: $h/C = 20\%$

A plate with the same thickness ($h/C = 16.25\%$) as the previous case but $C = 4\text{ cm}$ and $B = 4.2\%$ gives considerably better agreement to previous runs in the initial acceleration region, although the later time flow is essentially unaffected by the increased blockage. This plate was nominally at $\alpha = 90^\circ$, although the lift increase during the acceleration and the high drag minima would indicate a slight asymmetry in α .

Both of the previous runs had an $AR = 10$ plate with a NBW end condition, but for the highest blockage $B = 8.4\%$ case a plate with $C = 8\text{ cm}$ was used, restricting maximum aspect ratio to $AR = 6$ and the maximum length of run to 40 chord lengths. In addition, this case used a thin plate with $h/C = 4\%$. The effect of decreased thickness (cf. Fig. 3.13) would tend to offset any drag rise due to the increased blockage, so the slightly *lower* initial peak and drag minima may result primarily from decreased thickness. The lower velocity and thus the low physical frequencies associated with this run also reduce the initial peak height due to better filtering of the high frequency noise, as evidenced by the decreased width of the initial peak.

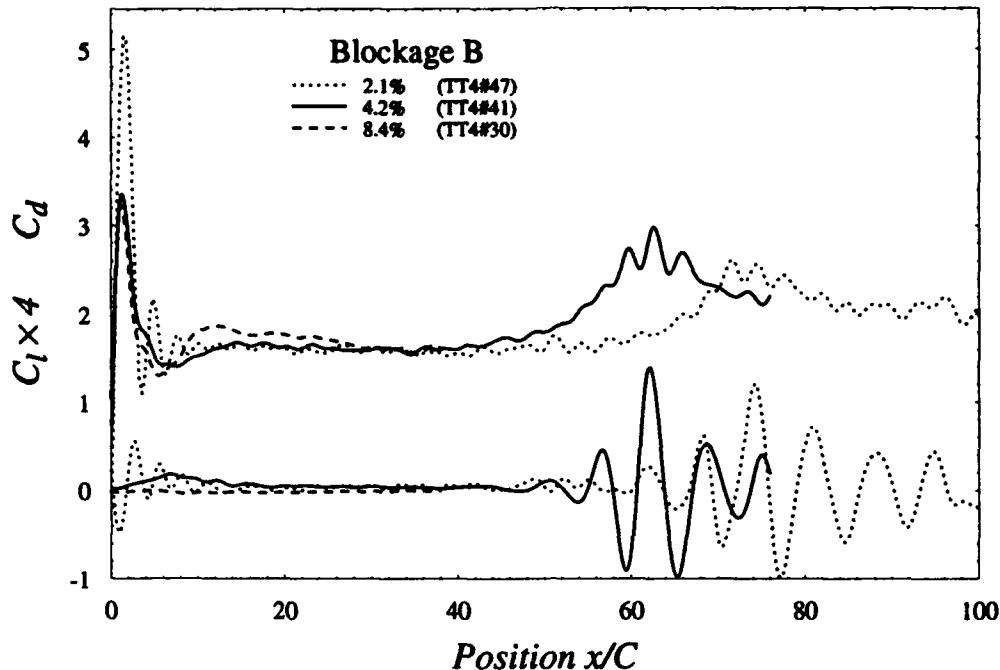


FIG. 3.14 Effects of blockage. $Re = 5000$, $AR = 10$, $t_a^* = 1.31$, $\alpha 90$. Solid line: $B = 4.2\%$, $h/C = 16.25\%$; Dashed line: $B = 8.4\%$ $h/C = 4\%$

There appears to be very little difference between runs after the acceleration, although all of these results are at fairly low blockage ratio, and time averaged mean coefficients are difficult to estimate due to the restricted run lengths. As was noted above, ensemble averaged results (Fig. 3.9 and Fig. 3.11) would indicate an 8% increase in \bar{C}_d from 1.98 to 2.14 for an increase in blockage from $B = 3.2\%$ to $B = 5.3\%$; although since the plates had different h/C ratios (10.3% vs. 6.8%) and AR , some of this increase may be due to thickness.

3.11 End Conditions

We attempt in this section to establish some of the effects of extrinsic ("large scale") three dimensional motions by changing end conditions and aspect ratio. In theory the conditions at either end of the plate are primary factors which influence the extrinsic three dimensionality - an infinite aspect ratio plate would, by definition, have only intrinsic three-dimensional motions. We present results using the same model as was used for the "typical" case of Fig. 3.5, again at $\alpha = 90^\circ$, for several different aspect ratios with the same end condition, and several different end conditions with the same aspect ratio. This effectively establishes both the optimum end condition (in the sense of least extrinsic 3d) and illustrates some effects that large scale 3d motions have on the flow.

Fig. 3.15 gives results for three different end conditions at two different aspect ratios. The free end (NEP) condition effectively suppresses organized vortex shedding at both $AR = 10$ and at $AR = 17$, as evidenced by the very low oscillation amplitude in both the lift and drag. This NEP condition also results in a

lower initial peak height and a higher post-acceleration drag minima (or the total elimination of this minima) than the other cases, with these differences being more pronounced for the lower $\text{AR} = 10$ case.

The run at $\text{AR} = 10$ with an end plate (WEP) behaves in an intermediate manner: the shedding oscillation is more pronounced, the peak height is higher and the drag minima is lower than in the NEP case, but these levels have not yet reached those seen for the NBW condition. At an $\text{AR} = 17$ the WEP and NBW conditions are essentially indistinguishable except for the initial peak height, which is still somewhat lower for both the NEP and WEP end conditions.

It would appear from these results that the near bottom wall (NBW) end condition provides the most consistently 2-dimensional flow, since an AR change from 10 to 17 has little noticeable effect when this end condition is used.

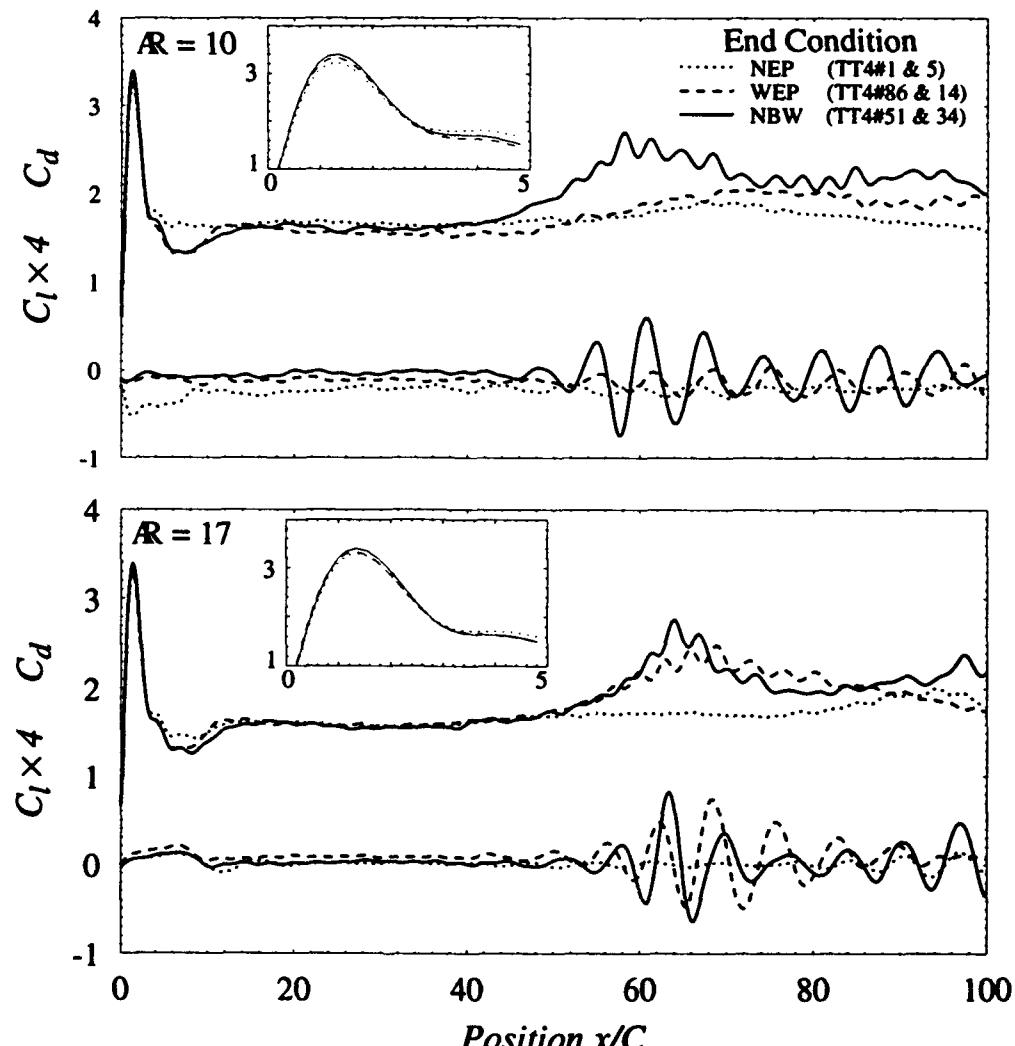


FIG. 3.15 End conditions. $\alpha = 90^\circ$, $h/C = 10.3\%$, $Re = 5000$, $t_a^* = 1.31$, AR as noted. Solid Line: NBW (Near Bottom Wall); Dashed Line: WEP (With End Plate); Dotted Line: NEP (No End Plate)

To further study end condition effects an end plate was mounted at various angles from $+20^\circ$ to -20° (Williamson, 1989), with positive end plate angle (*EPA*) corresponding to outwardly oriented end plates, as shown in Fig. 3.16. The largest angles of $\pm 20^\circ$ give initial results similar to those seen with a free end - namely an increase in the minimum drag level following the acceleration. These angles also result in a higher peak drag and a higher mean drag prior to shedding, although both these effects are likely due to the additional separated flow over, and high drag of, the end plate. The *EPA* = 0° and $+5^\circ$ cases show very little difference for early times, although with $+5^\circ$ *EPA* the initial shedding onset appears to occur somewhat earlier.

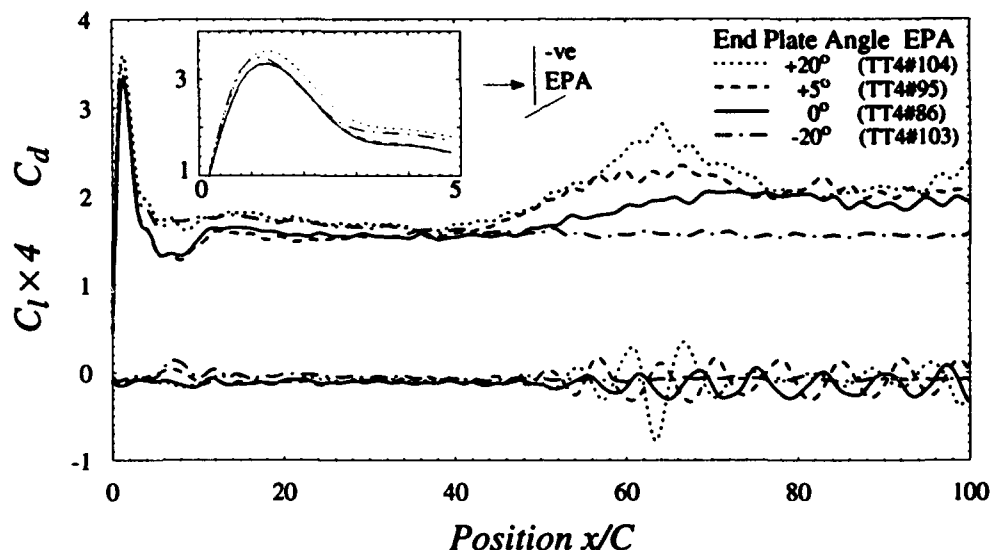


FIG. 3.16 Various end plate angles. $AR = 10$ (WEP end condition), $h/C = 10.3\%$, $\alpha = 90^\circ$, $Re = 5000$, $t_a^* = 1.31$. Dotted Line: *EPA* = $+20^\circ$; Dashed Line: $+5^\circ$; Solid Line: 0° ; Chain Line: -20°

The primary effect of *EPA* is seen in a comparison of the steady-state shedding behavior for $+20^\circ$ and -20° . For *EPA* = $+20^\circ$ shedding begins at about $t^* = 40$, with a large initial drag increase and subsequent oscillation levels comparable to those seen in the *EPA* = 0° case. Conversely, for an *EPA* of -20° organized shedding is suppressed for the entire 100 chord lengths of the run, with little variation in the mean drag level after the initial acceleration peak. This is indicative of the large influence that end plate angle can exert on the vortex shedding behavior.

For the results presented in Fig. 3.17 the aspect ratio was changed by moving the plate vertically in its mount, the balance vertically in the tank and changing the water level to maintain the same NBW end condition for all cases. There is very little difference between these runs that can not be ascribed to typical run to run variation, although the smaller aspect ratio cases did have slightly higher post-acceleration drag minima, indicating an increased instability or asymmetry of the symmetric recirculating bubble. The lack of any large scale effects again indicates that the NBW end condition provides a two-dimensional flow reasonably independent of end conditions, with even the lowest $AR = 6$ providing results consistent with those of $AR = 17$ cases.

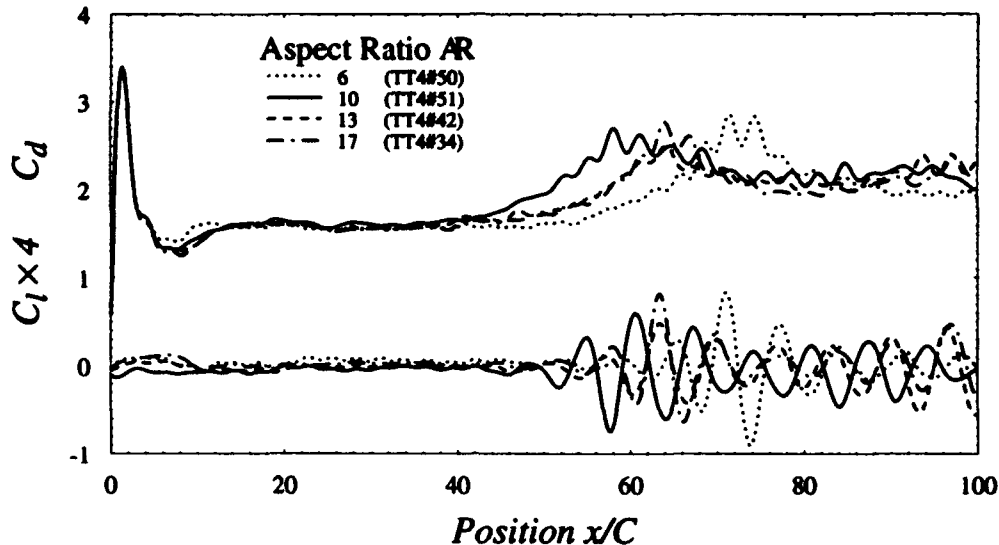


FIG. 3.17 Aspect ratio effects. $Re = 5000$, NBW end condition, $h/C = 10.3\%$, $\alpha = 90^\circ$, $t_a^* = 1.31$. Dotted Line: $AR = 6$; Solid Line: $AR = 10$; Dashed Line: $AR = 13$; Chain Line: $AR = 17$

3.12 Starting Profiles

Results for four different acceleration times at both $\alpha = 90^\circ$ and $\alpha = 87.5^\circ$ are shown in Fig. 3.18. The inset to this plot shows initial $C_{d,i}$ levels, although as was previously noted these levels are strongly affected by both the type and degree of digital filtering used. Experimental $C_{d,i}$ levels of 0.05, .17, .75 and 2.1 are all higher than the theoretical values of .04, .16, .6 and 1.6 found for $t_a^* = 20, 5, 1.31$ and .5, respectively.

For runs in which the acceleration region does not exceed the typical duration of the initial symmetric starting bubble the post acceleration force histories fall to similar levels. For an intermediate $t_a^* = 5.0$, the post acceleration minima is shifted to later times, denoting a delayed state of development of the recirculating bubble even at the same non-dimensional position. Subsequent flow development does not show any consistent changes with varying acceleration time.

Note again for the case $\alpha = 87.5^\circ$ that the lift during the acceleration region remains high even while the drag is falling to its minimum level. The initial peak lift is achieved at the same time as the initial drag peak (*i.e.*, at the end of the acceleration region) but the degree to which the lift then remains high depends on t_a^* . For $t_a^* = 0.5$ and 1.31 the post-acceleration lift remains fairly constant and fairly high throughout the drag minima associated with the symmetric recirculating bubble. The lift in the $t_a^* = 5.0$ case, on the other hand, decays rapidly after its initial peak even though the corresponding drag level drops to the same minima as did the two shorter t_a^* cases. This may indicate that for a longer acceleration the vortex asymmetry present in the recirculating bubble is such as to move one vortex more directly behind the plate, effectively reducing its influence on the lift (which is produced primarily at the beveled edges) without affecting the drag level significantly.

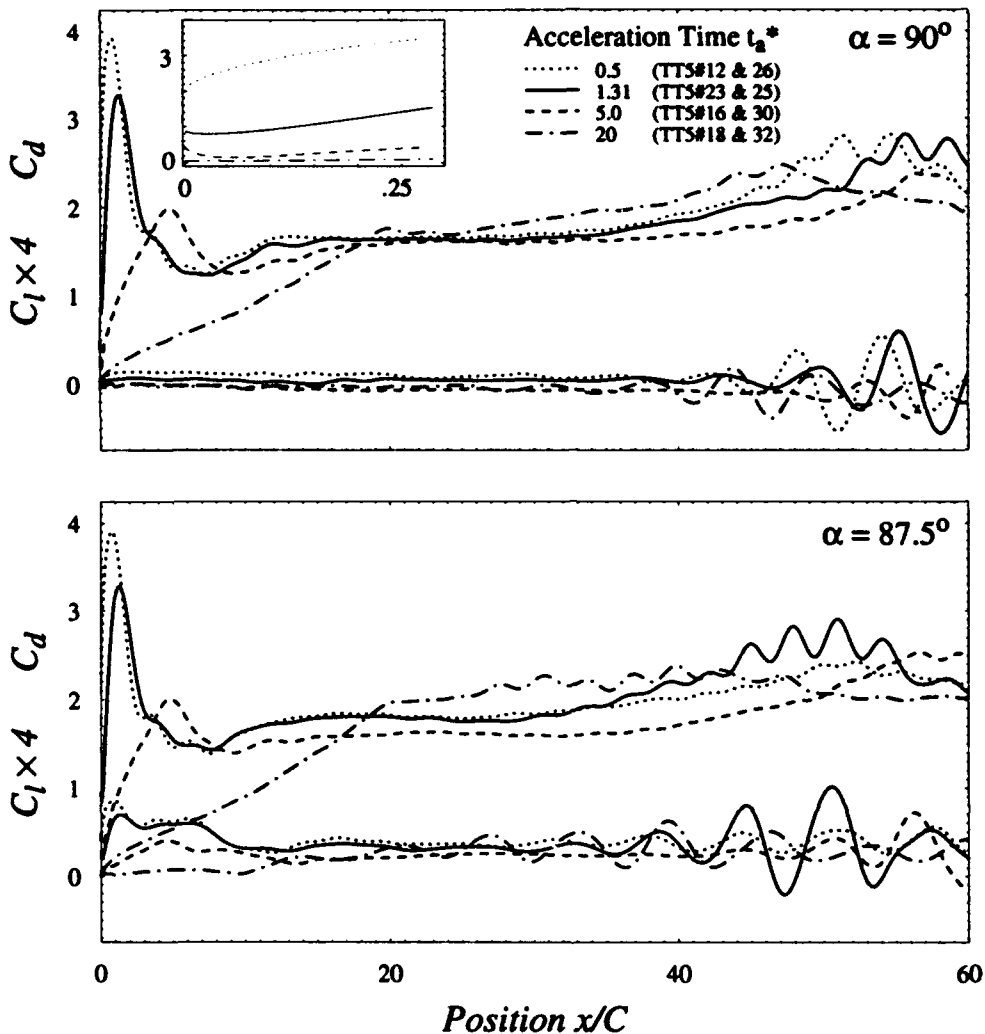


FIG. 3.18 Effect of varying t_a^* . $Re = 5000$, $AR = 17$ (NBW end condition), $h/C = 6.8\%$ ($C = 5\text{cm}$), α as noted. Dotted Line: $t_a^* = 0.5$; Solid Line: $t_a^* = 1.31$; Dashed Line: $t_a^* = 5.0$; Chain Line: $t_a^* = 20$

3.13 Sheding Modulation

Many of the problems encountered in accurately quantifying steady-state shedding results related to the long period modulation which was apparent in the vortex shedding itself. This modulation is particularly noticeable for the result presented in Fig. 3.19, in which the initial symmetry breaks down early enough that one complete modulation cycle is apparent in the "steady-state" region. The period of this modulation is roughly $6T_s$, making the towing tank and its inherently limited run lengths unsuitable for a detailed study of this phenomena. For this reason the experiments were moved to a continuous flow free surface water tunnel to allow a true steady-state to be achieved; the results from this facility will be presented in the next chapter.

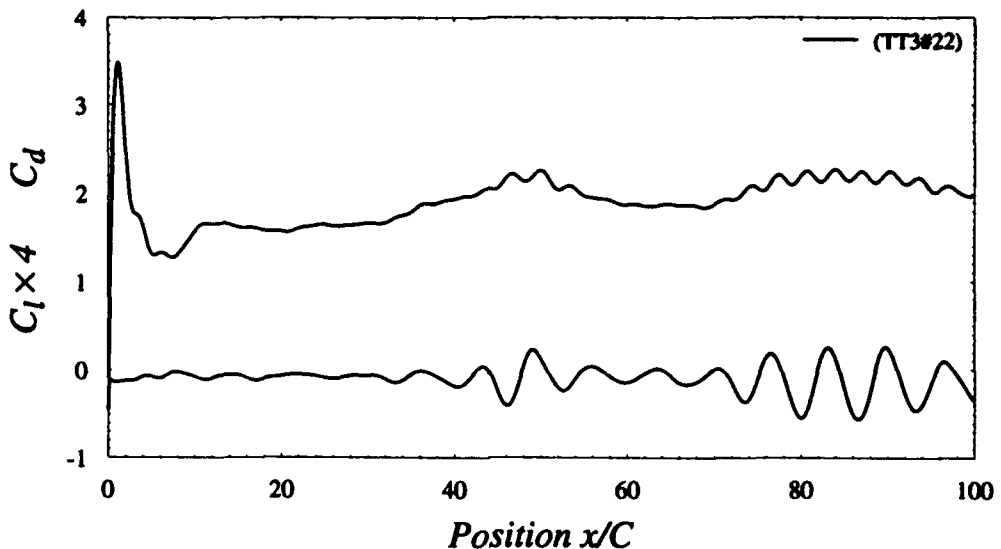


FIG. 3.19 Force history showing long period ($6 \times T_s$) shedding amplitude modulation. $C = 3\text{cm}$, $\text{AR} = 15$ (NBW end condition), $h/C = 10.3\%$, $\alpha = 90^\circ$, $U_\infty = 12 \text{ cm/s}$ ($Re = 3600$), $t_a^* = 1.0$

3.14 Exponential Shedding Onset

As has been alluded to earlier, in many cases the initial shedding onset appears to be exponential. Fig. 3.20 presents the lift history of the typical run shown in Fig. 3.5 on a linear scale, and a rectified lift value on a logarithmic scale. The almost linear increase in shedding amplitude on the log scale would indicate that, at least for this case, the shedding onset occurs exponentially.

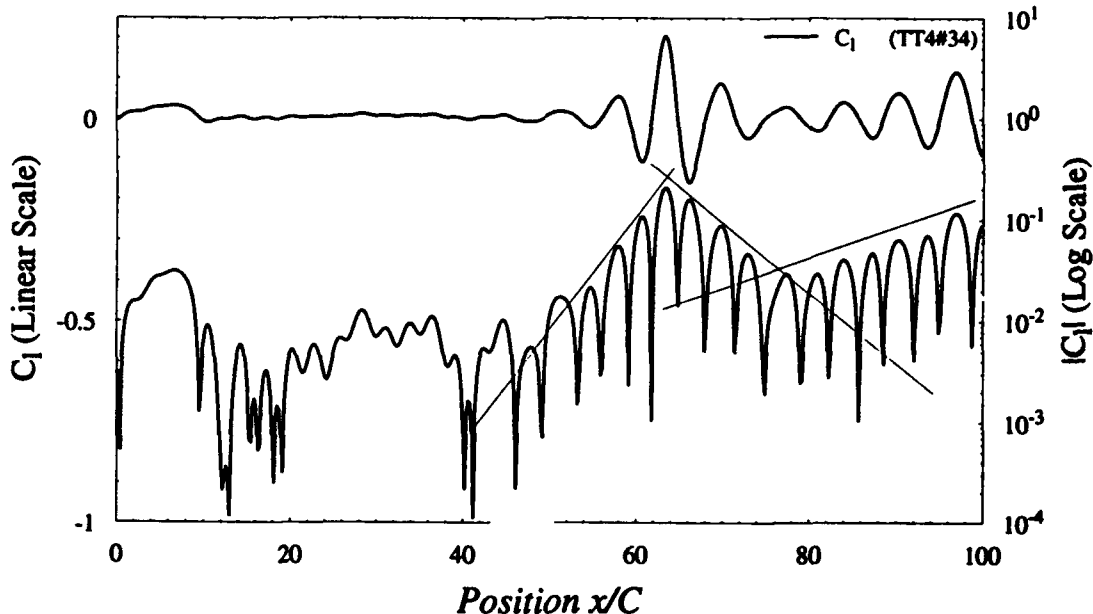


FIG. 3.20 Exponential shedding onset. $Re = 5000$, $\text{AR} = 17$ (NBW end condition), $h/C = 10.3\%$, $\alpha = 90^\circ$, $t_a^* = 1.31$. C_l history from Fig. 3.5 plotted on linear and log axes - straight lines added for emphasis

3.15 Flow Visualizations

Further verification of the nature of the shedding onset and the subsequent steady-state flow was obtained through flow visualization using a horizontal laser sheet to illuminate fluorescent dye released from a narrow chordwise slit on the upstream face of the model (see Sec. 2.5.1) and provide a cross sectional view of the wake in the perpendicular spanwise plane (Fig. 2.7). Force histories for flow visualization runs are given in Fig. 3.21; with symbols corresponding to the flow visualization frames presented in the subsequent six figures.

Two frames at $t^* = 6.74$ and $t^* = 16.74$ are given in Fig. 3.22 and Fig. 3.25 for $\alpha = 90^\circ$ and $\alpha = 87.5^\circ$ respectively. Note the similarity of the external bubble shape for these two cases at $t^* = 6.74$, with a somewhat increased instability (larger scale structure) in the upper shear layer and increased bubble

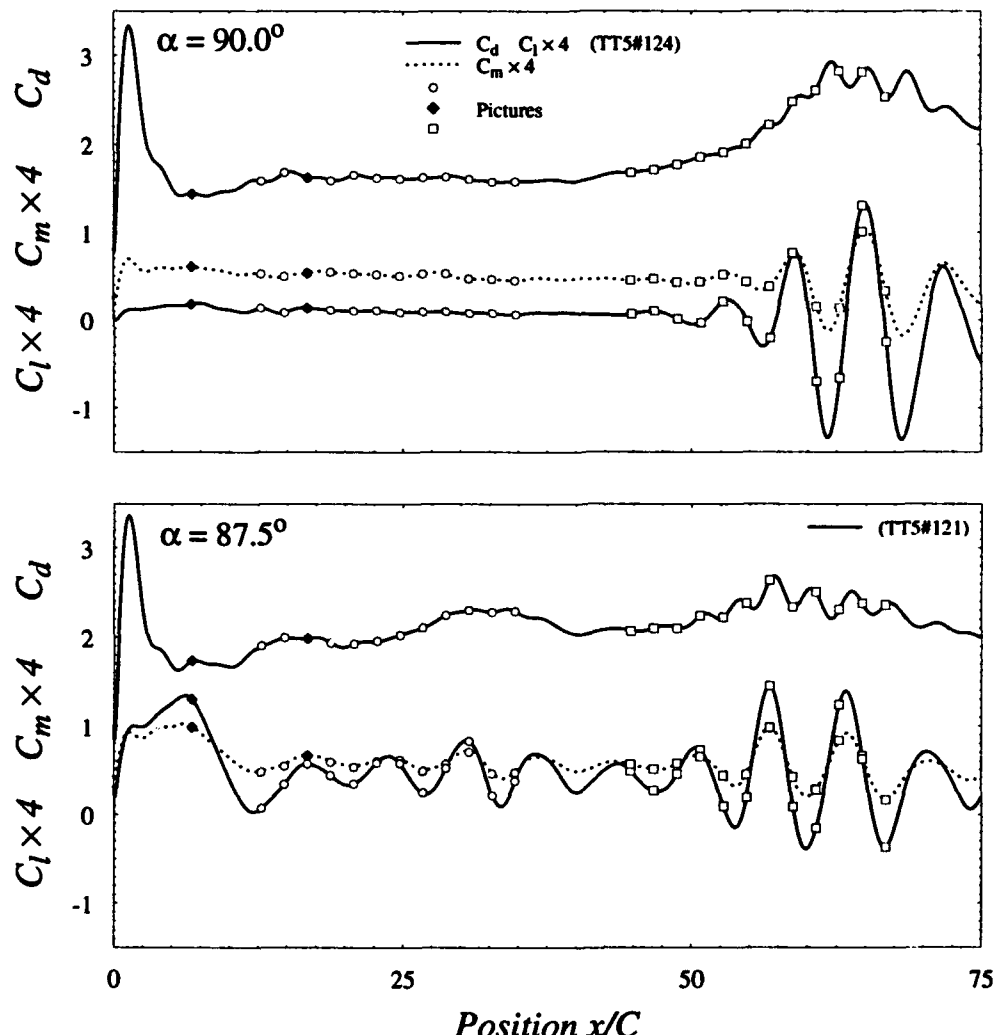


FIG. 3.21 Force histories from flow visualization runs. $C = 5$ cm, $Re = 5000$, $\mathcal{R} = 10$ (NBW end condition), $h/C = 16.25\%$, $t_d^* = 1.31$, α as noted. Solid symbols denote positions of pictures in Fig. 3.22 and Fig. 3.25; open symbols are frames in Fig. 3.23, Fig. 3.24, Fig. 3.26 and Fig. 3.27

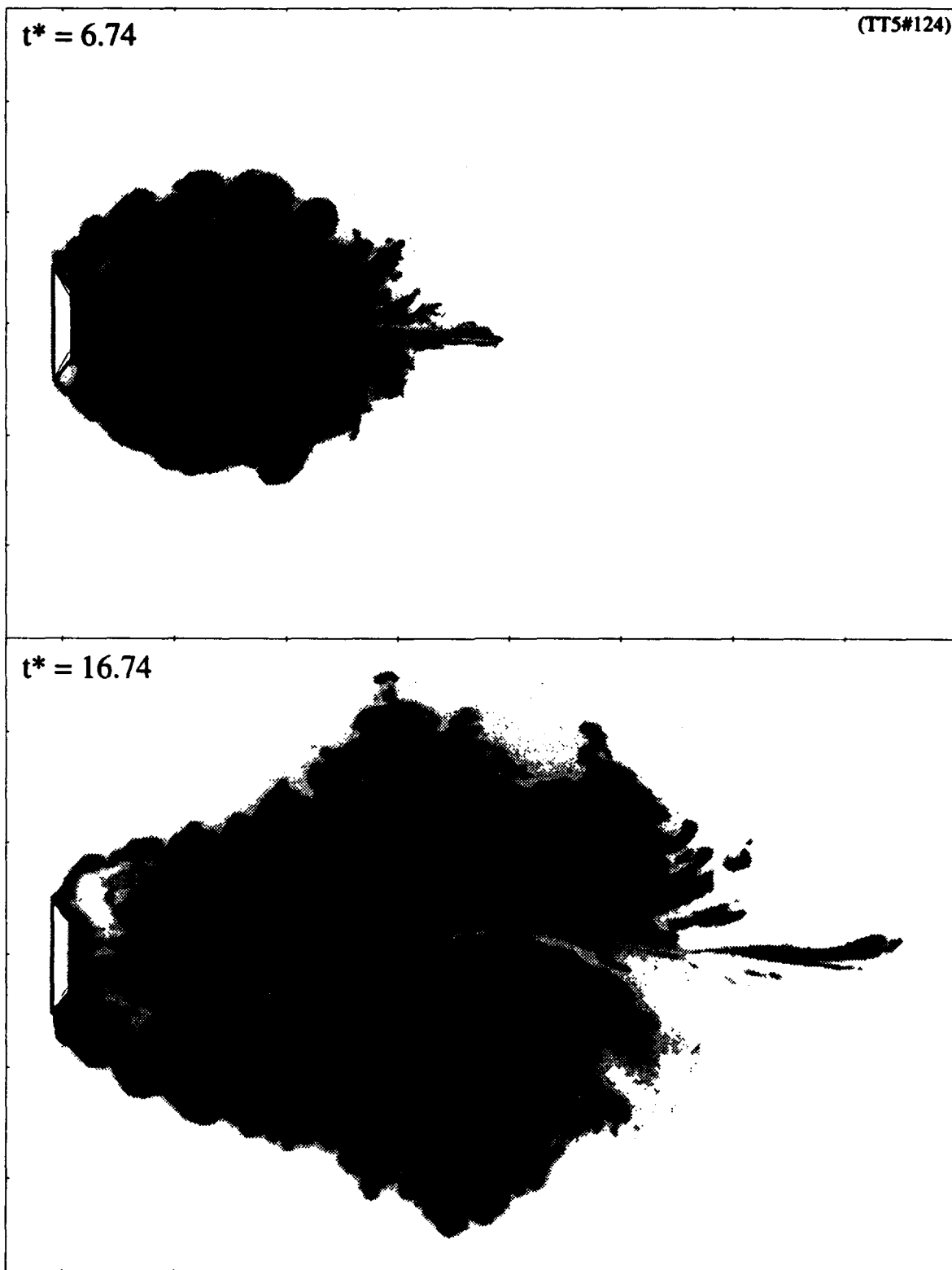


FIG. 3.22 X-Y towing tank flow visualizations; times as noted. $\alpha = 90^\circ$, $Re = 5000$, $AR = 10$ (NBW end condition), $h/C = 16.25\%$, $t_a^* = 1.31$

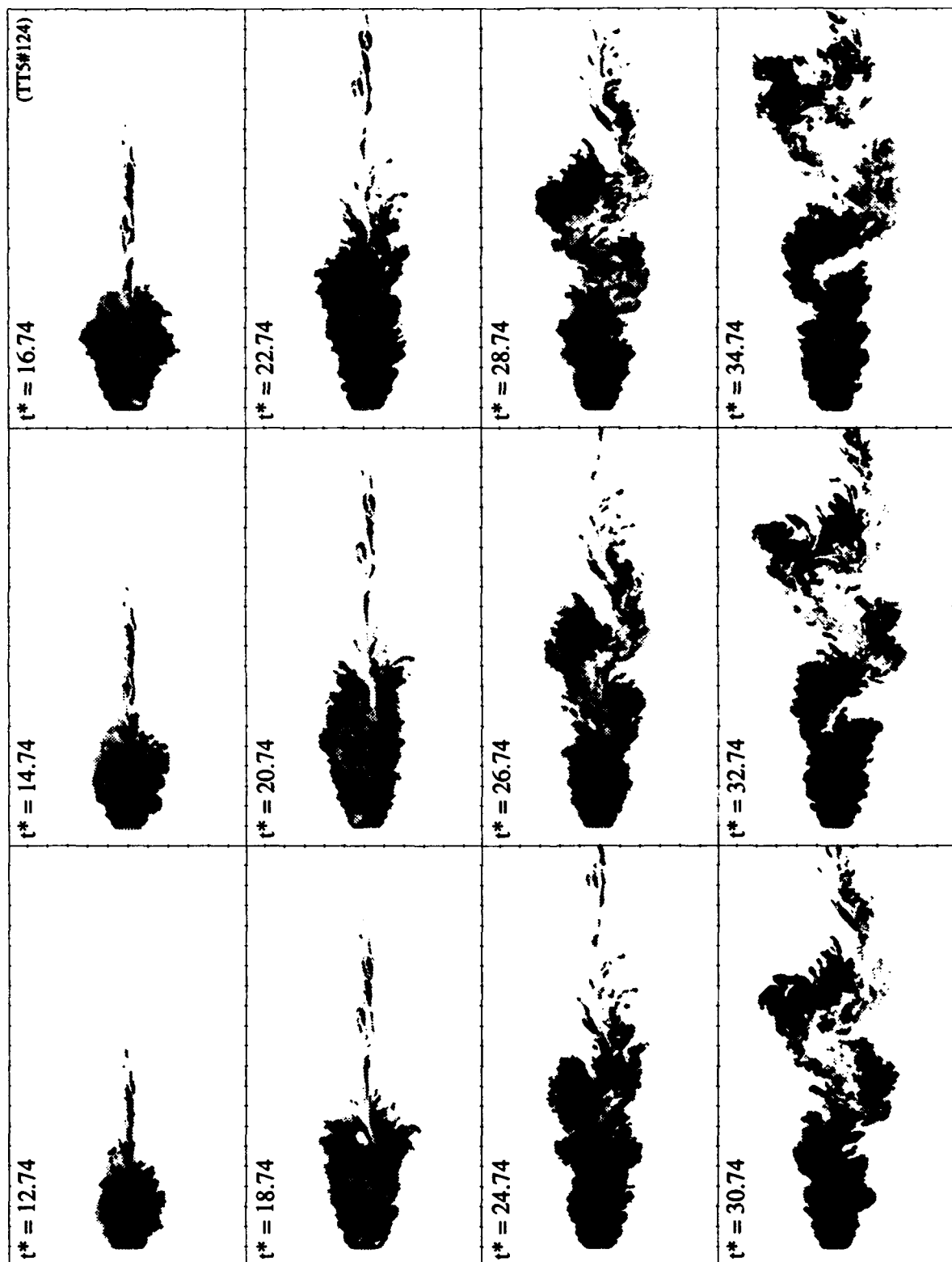


FIG. 3.23 X-Y towing tank flow visualizations; times as noted. $\alpha = 90^\circ$, $Re = 5000$, $AR = 10$ (NBW end condition), $h/C = 16.25\%$, $t_a^* = 1.31$

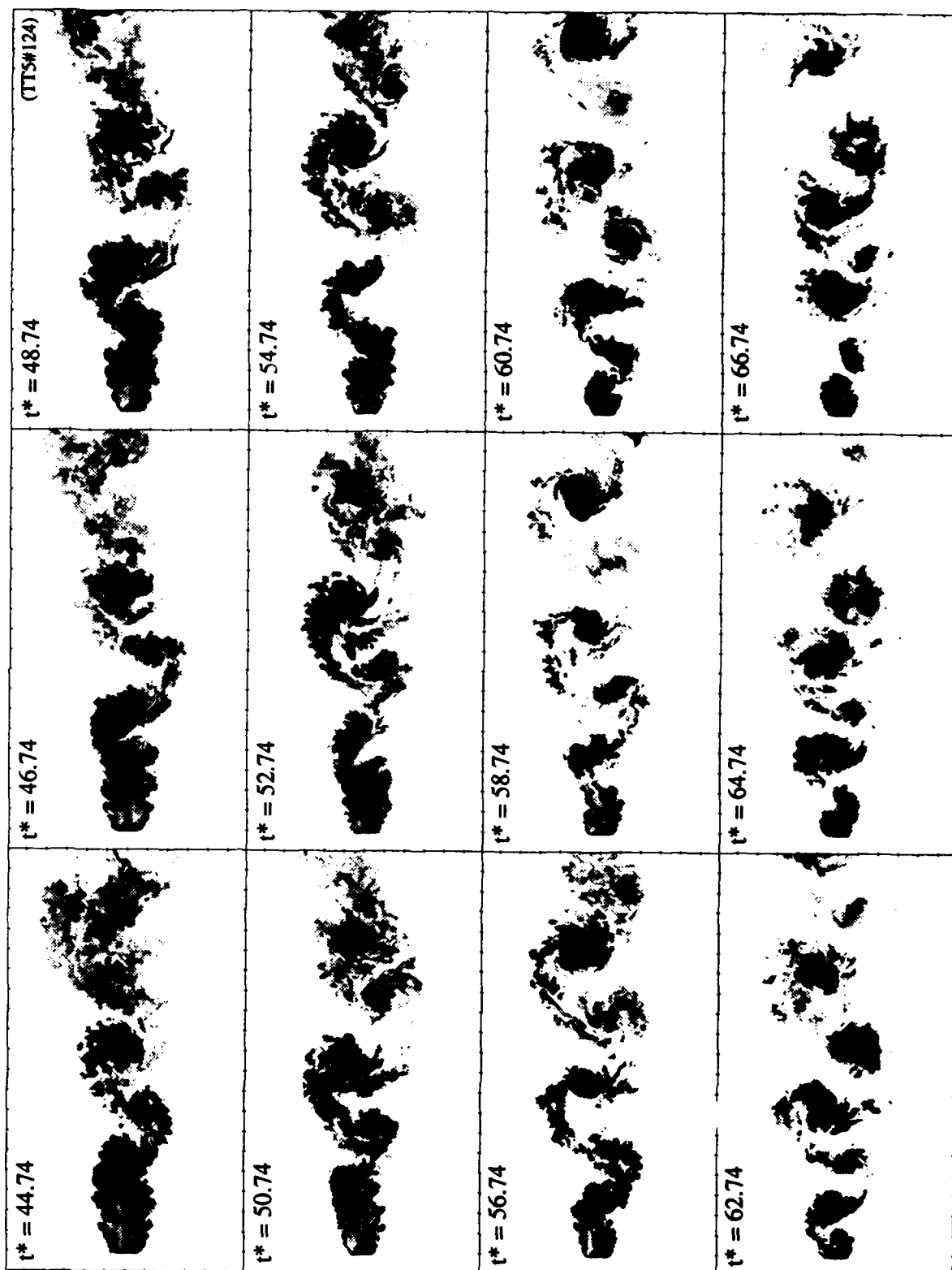


FIG. 3.24 X-Y towing tank flow visualizations; times as noted. $\alpha = 90^\circ$, $Re = 5000$, $AR = 10$ (NBW end condition), $h/C = 16.25\%$, $t_a^* = 1.31$. Vertical columns are at a roughly constant phase of shedding

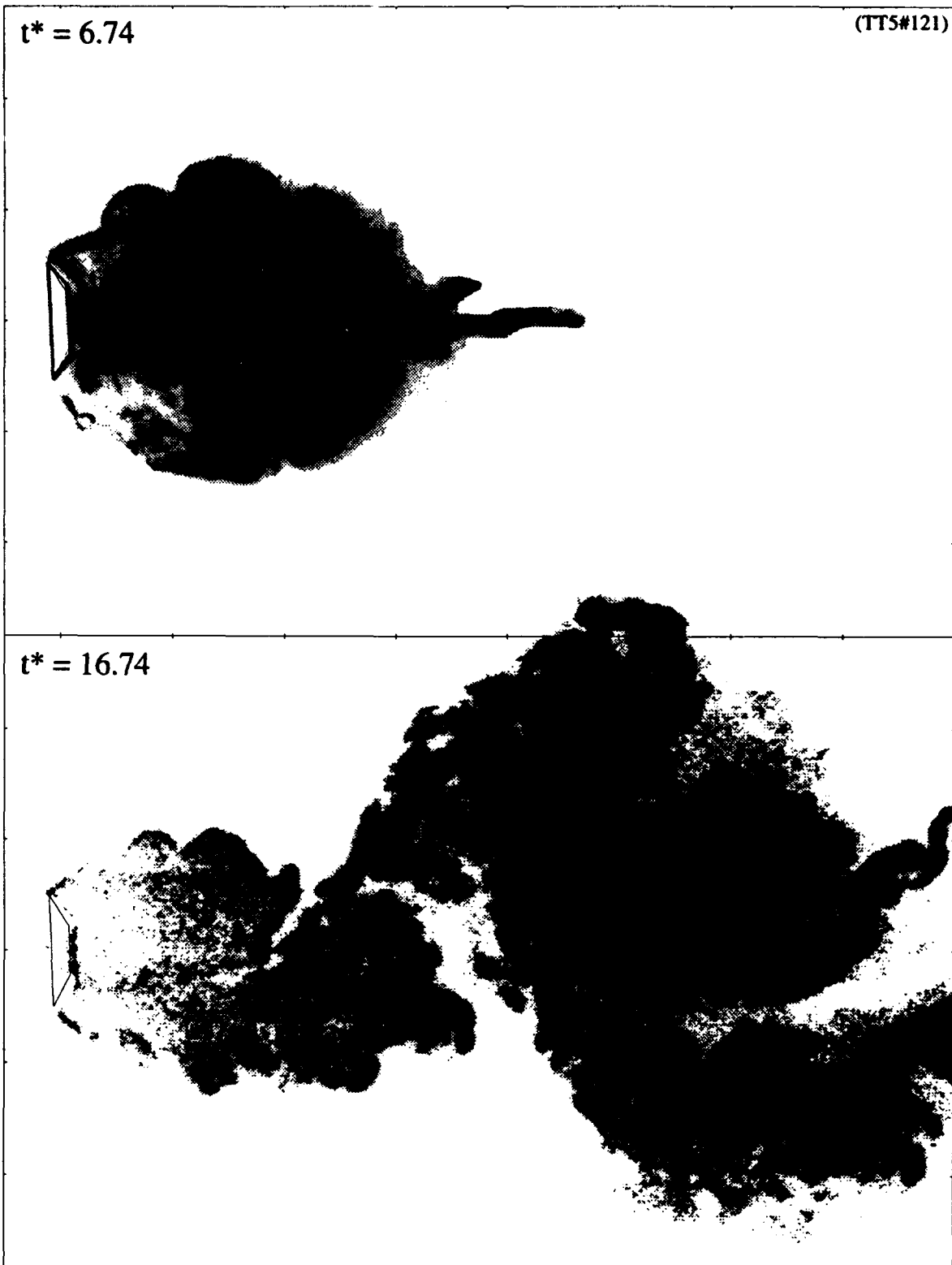


FIG. 3.25 X-Y towing tank flow visualizations; times as noted. $\alpha = 87.5^\circ$, $Re = 5000$, $AR = 10$ (NBW end condition), $h/C = 16.25\%$, $t_a^* = 1.31$

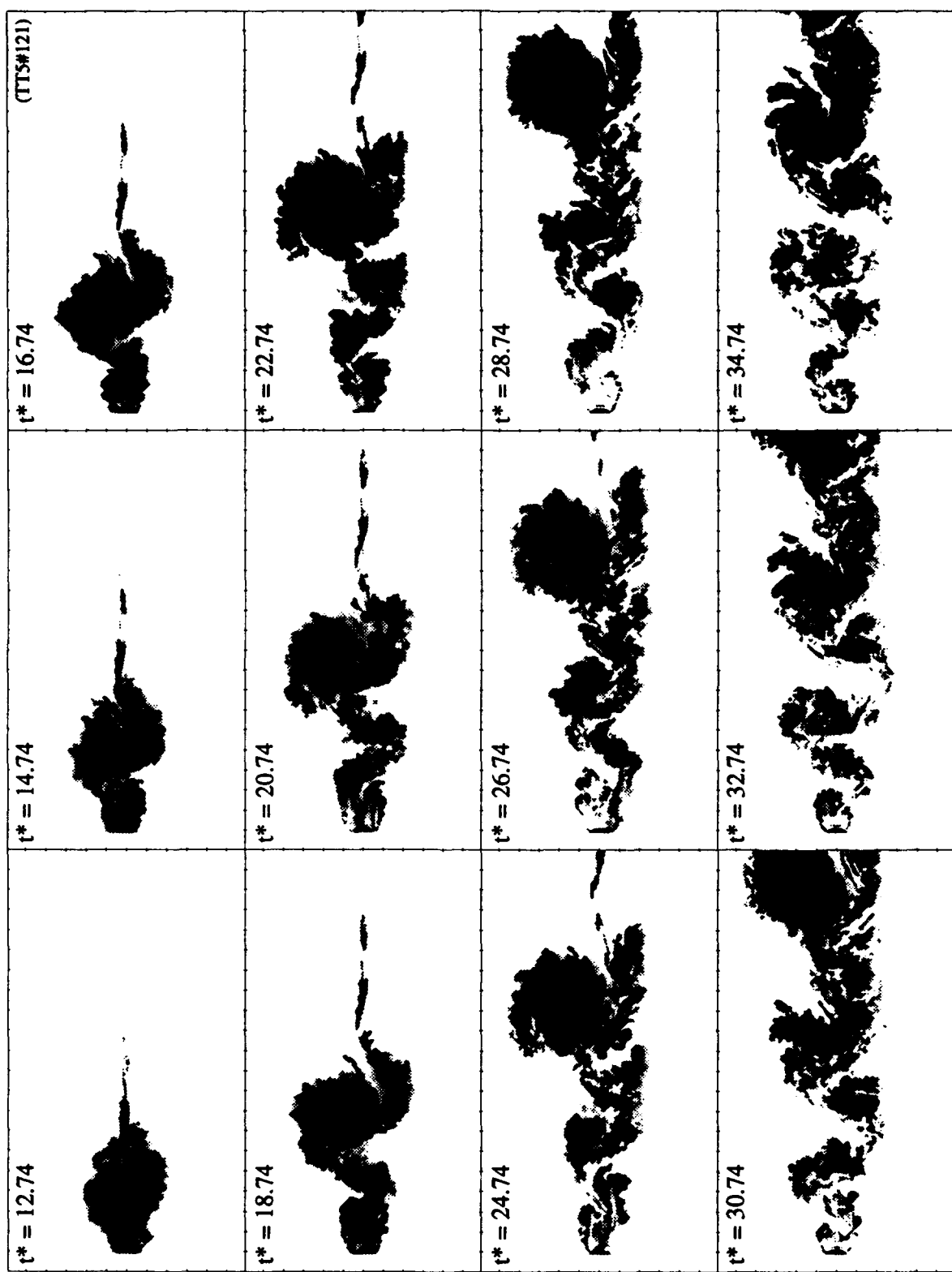


FIG. 3.26 X-Y towing tank flow visualizations; times as noted. $\alpha = 87.5^\circ$, $Re = 5000$, $AR = 10$ (NBW end condition), $h/C = 16.25\%$, $t_a^* = 1.31$. Vertical columns are at a roughly constant phase of shedding

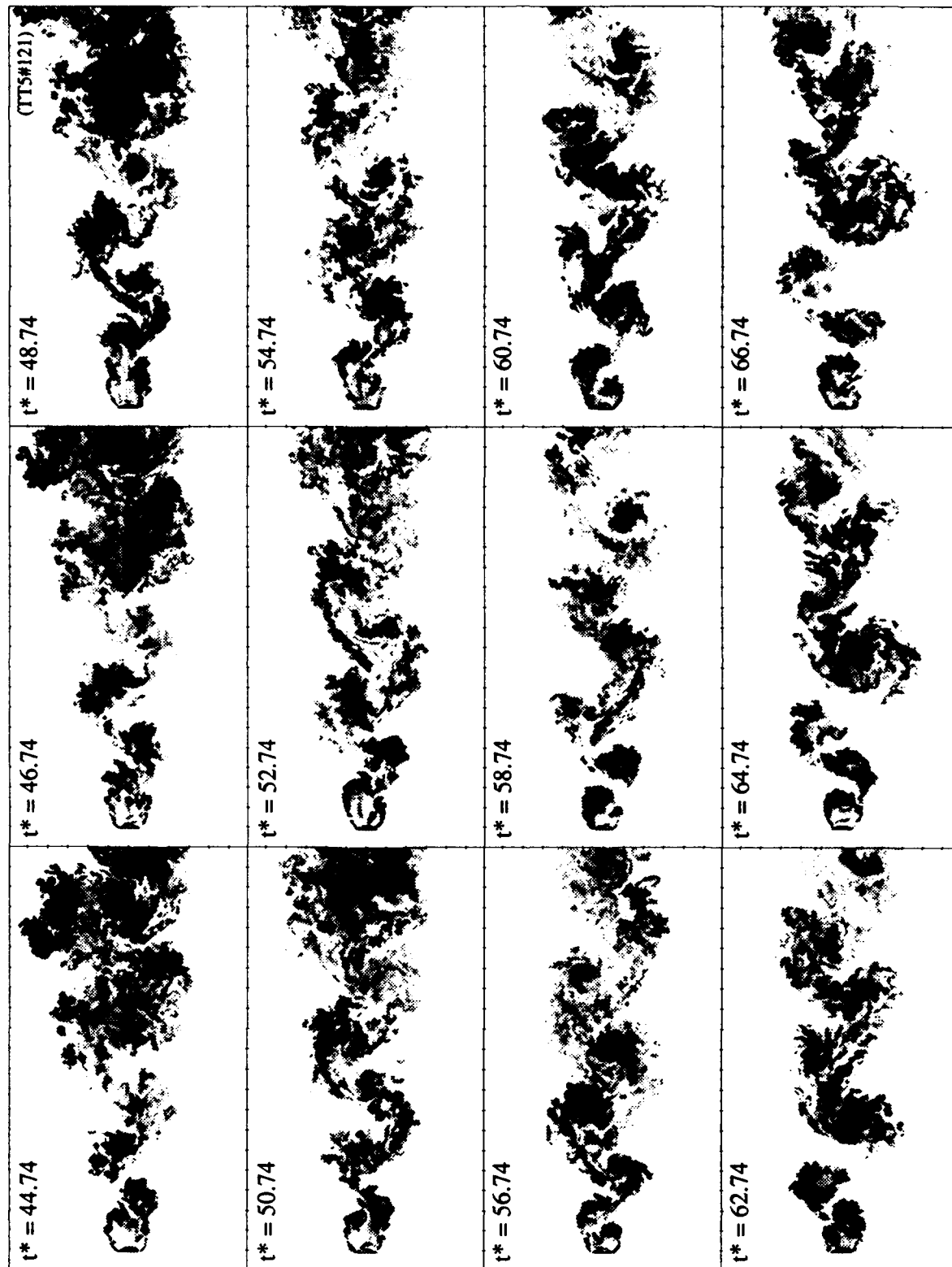


FIG. 3.27 X-Y towing tank flow visualizations; times as noted. $\alpha = 87.5^\circ$, $Re = 5000$, $AR = 10$ (NBW end condition), $h/C = 16.25\%$, $t_a^* = 1.31$. Vertical columns are at a roughly constant phase of shedding

length for $\alpha = 87.5^\circ$. By $t^* = 16.74$ there is considerably more development for the $\alpha = 87.5^\circ$ case, with the initial symmetric bubble having broken and a near wake instability beginning to roll up behind the plate, albeit with a large formation distance. In contrast, the $\alpha = 90^\circ$ result at the same time shows a large stagnant region of fluid being pulled along with the plate and no evidence of large scale shear layer roll up or wake instability.

This lack of near wake shear layer roll up (*i.e.*, vortex shedding) for $\alpha = 90^\circ$ continues throughout the next sequence of photos shown in Fig. 3.23, although by about $t^* = 25$ a far wake instability begins to be apparent. This instability moves closer to the plate throughout the sequence shown in Fig. 3.24, until by $t^* \approx 65$ the picture is very much that of classical vortex shedding, although with a very short formation region giving rise to the large lift fluctuation and drag levels apparent in the force traces.

The results shown in Fig. 3.26 for $\alpha = 87.5^\circ$ show a qualitatively similar picture, but the flow develops much faster, with "steady-state" shedding by $t^* \approx 30$. Fig. 3.27 shows a long period change in the formation distance associated with the shedding amplitude modulation apparent in the force histories.

3.16 Summary

Several of the most interesting results to come from the experiments detailed in this chapter had not been envisioned "theoretically." Firstly, the time in which the flow develops is considerably longer than originally had been expected - some runs traveled 100 chord lengths without vortex shedding beginning, with a typical onset time (for $\alpha = 90^\circ$) being about 40 to 60 x/C. The initially symmetric recirculating bubble breaks after 10 to 20 chord lengths but, for $\alpha = 90^\circ$, it is followed by a long lasting (20 to 30 chord lengths) low drag ($C_d = 1.6$) non-vortex-shedding region. During this period, the vorticity shed into the wake is unstable and results in an oscillation of the far wake, but the shear layers do not roll-up immediately behind the plate as they do in the classical vortex shedding case. The subsequent onset of vortex shedding occurs quite slowly, and in many cases appears almost exponential in nature, with the initial drag peak and lift fluctuation being considerably larger than subsequent vortex shedding oscillations.

The time for which the initial symmetric bubble and ensuing lack of shedding lasts is sensitive to small disturbances - indeed its existence is likely due at least in part to the highly quiescent and uniform external flow present in the towing tank. Small asymmetries, such as a change in angle of attack to $\alpha = 87.5^\circ$, effectively eliminate the non-shedding regime and greatly increase the minimum drag level seen immediately after the acceleration.

Finally, the "steady-state" vortex shedding which does eventually develop has a long period ($6T_s$) modulation in the force amplitudes; a phenomena which is difficult to study in the confines of the towing tank, and which is the subject of the following chapter.

CHAPTER 4

Free Surface Water Tunnel Experiments

4.1 Preface

In the course of X-Y towing tank experiments it became apparent that the low-frequency force modulation would require further investigation. Since the X-Y towing tank cannot provide for very long run times, this effect could not be studied in that facility, so the force balance and associated equipment were moved to the GALCIT free surface water tunnel (FSWT). This is a continuous flow facility that allowed truly steady-state flow to be established, and made feasible the acquisition of force data over very long run times - typically many thousands of chord lengths. This made it feasible to study the effects of various parameters on the period and nature of the shedding amplitude modulation, and to see if or how it was related to the three-dimensional nature of the experimental flow.

4.2 Free Surface Water Tunnel Description

The FSWT facility (Fig. 4.1) and its associated equipment has been used by many researchers, and has been described in detail elsewhere (Tokumaru, 1991; Lang, 1985; Ward, 1976). The working section of the tunnel is plexiglas, 51 cm wide by 244 cm long with a maximum water depth of 52 cm. A two component LDV system installed on a three degree of freedom traverse was used for measuring tunnel velocities; for these experiments only the streamwise component of velocity was recorded. Upstream screens served to improve the flow quality, with a resulting freestream rms of about 0.5%. The maximum tunnel velocity is on the order of 3 m/sec, but for these experiments velocities similar to those obtainable in the X-Y towing tank were used, with the limitation that the minimum reliable tunnel velocity was about 5 cm/sec, below which surging at the impeller blade frequency became increasingly apparent.

The LDV/traverse system was situated upstream of the balance station; LDV output was amplified and filtered before a phase lock loop was used to lock a square wave onto the LDV frequency. This square wave was input to a frequency to voltage converter to give a voltage output proportional to tunnel velocity (frequency), which was then recorded on one channel of the force balance data acquisition system; allowing simultaneous acquisition of force and velocity data. This system agreed to within about 0.5% with results obtained with a different LDV system used in the past.

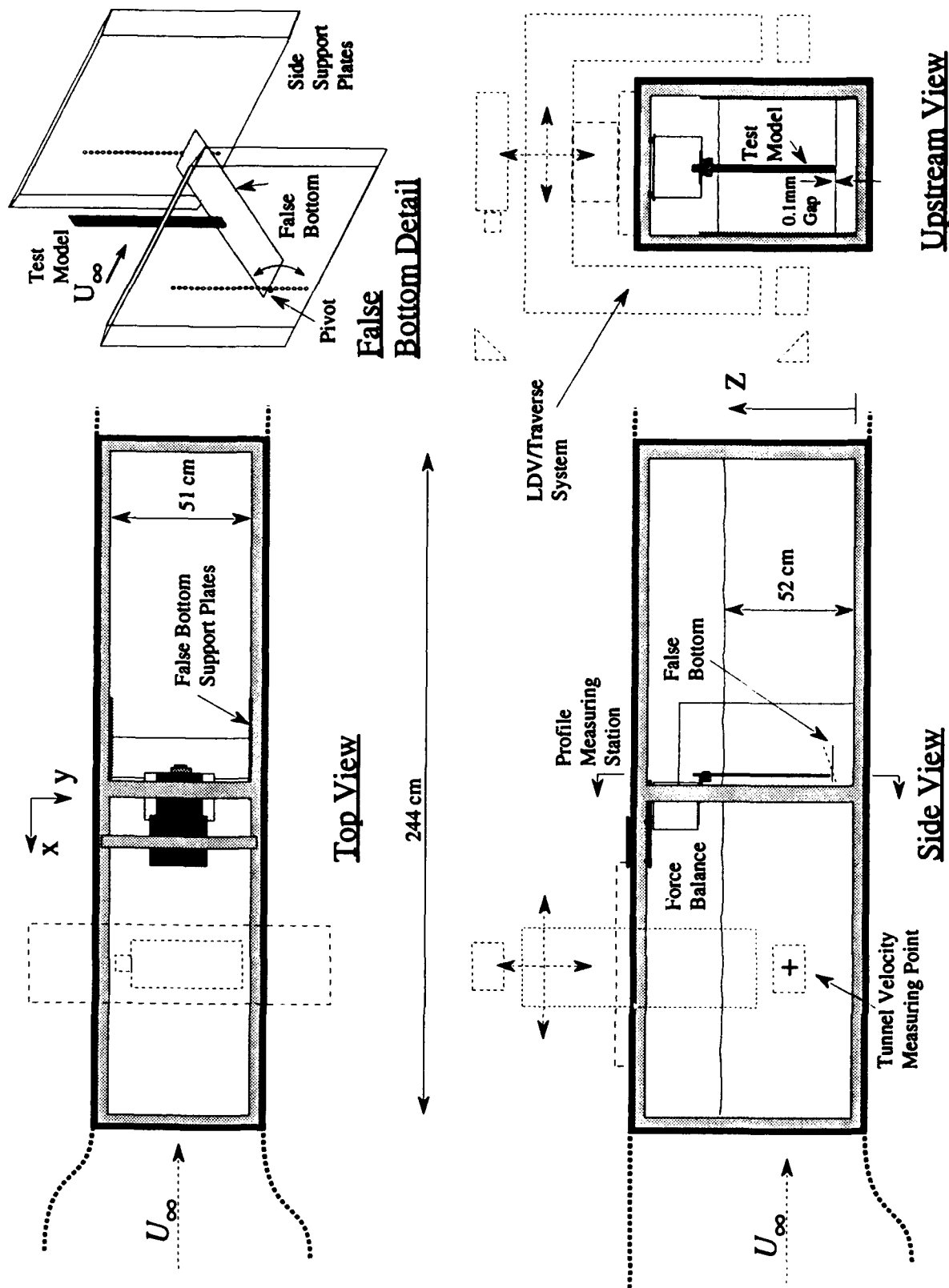


FIG. 4.1 Schematic drawing of GALCIT free surface water tunnel facility

The force balance was rigidly mounted at about the mid-point of the test section; with flat plate models projecting vertically through the free surface, in much the same way as they were mounted in the X-Y towing tank . Force directions and balance/model orientation relative to U_∞ were the same as in the X-Y towing tank experiments, as were the flat plate models and end plates themselves.

For runs with the "false bottom wall" lower end condition (*FBW*) a thin aluminum streamwise end plate was installed spanning the test section, sufficiently above the floor of the tunnel to avoid the boundary layer on the bottom wall. These end plates were attached to two thin plexiglas plates which were slid down inside the tunnel side walls (Fig. 4.1); end plates could be pivoted at different depths for aspect ratio adjustment and to provide different end plate angles. The lower ends of the test models were placed about 0.01 mm above the false bottom plate, in a somewhat analogous manner to that used for *NBV* end conditions in the X-Y towing tank .

Appendix A gives further details of LDV calibration, comparisons to previous methods of velocity measurement, tunnel velocity profiles, velocity spectra and other assorted details.

4.3 Free Surface Water Tunnel Procedures

Due to a filter pump which continuously circulated water, there was a constant small velocity (1 mm/sec) in the tunnel, which made it difficult to establish an initial zero flow tare level for force measurements. A barrier was installed around the model between runs, effectively eliminating this drift velocity. Tare levels were taken with this barrier in place; it was then removed prior to the tunnel being run, then replaced at the end of a run or set of runs and another tare level taken.

Run times varied, but were typically on the order of 15 minutes, sufficient to provide several thousand chord lengths of motion even at the lowest tunnel velocities. Since these run times were much longer than those used in the X-Y towing tank , the slow drifting of balance zero levels became a problem, as evidenced by initial and final tare levels being different by up to 30 mV. This error was reduced by linearly correcting the tare levels from the beginning to the end of each run or set of runs, effectively making this uncertainty about 10 mV, or .002N (equivalent to $\Delta C_d \approx .01$ @ $Re = 6000$ and $AR = 10$). Since the balance was rigidly clamped to the tunnel, problems such as rail waviness were eliminated and vibration levels reduced, so the force results overall could be expected to be of about the same accuracy as similar runs in the X-Y towing tank .

Calculation of accurate force *coefficients*, on the other hand, depends on accurate tunnel velocity information being available. The LDV system provided the most accurate indication of freestream velocity, roughly the same level of accuracy as the rms level of the tunnel, or about 0.5%. Force coefficients were calculated using the mean tunnel velocity recorded over the whole length of a run; except for a first-order correction (see Appendix A) applied for blockage due to the side support walls in the *FBW* end condition

cases, no blockage corrections were performed. Overall then, mean values of force coefficients are accurate to within 1 to 2% at $Re = 6000$.

Due to the longer run times, data was acquired using a 256 μsec sampling interval, with 16 samples again being averaged before storage to disk. To further conserve on disk storage, only four channels of data were acquired, the first three being the force balance signals as before, and the fourth being the tunnel velocity signal rather than the X-carriage command voltage. Subsequent data analysis and filtering was performed using methods identical to those used for the X-Y towing tank results.

Various Reynolds numbers, aspect ratios, angles of attack, blockages, thickness ratios and end conditions were investigated. Three end conditions were explored, free end (*NEP*) and end plate (*WEP*) runs were done with the lower end of the plate sufficiently high above the bottom wall of the tunnel so as to be outside the lower boundary layer. Aspect ratios were changed in these cases by raising the plate in the balance mount and clamping it at the desired depth. False bottom wall runs (*FBW*) were performed as described above, aspect ratio changes being effected by raising both the plate and the false bottom to a different depth. Various end plate angles were used for both the *WEP* and *FBW* runs.

Appendix A provides additional details about velocity measurement uncertainties and data analysis.

4.4 Typical Free Surface Water Tunnel Result

Many parameters, primarily aspect ratio AR and end condition, were changed to affect the amount of large scale (extrinsic) three-dimensionality present in the flow and to note the effect (or lack of effect) on the period and nature of the shedding amplitude modulation. Additionally, some parameters *not* expected to have an immediate effect on extrinsic three-dimensionality, such as blockage, Reynolds number, plate stiffness and angle of attack, were changed to see if the amplitude modulation was at all related to these factors.

A typical result using an end plate at 0° is shown in Fig. 4.2. For this experiment $Re = 6000$, $AR = 10$, $\alpha = 90^\circ$, $C = 3\text{cm}$, $h/C = 10.3\%$, and blockage, based on chord/tunnel width, was $B = 5.9\%$. Except as otherwise noted, the rest of the runs presented in this chapter were performed with similar attributes. A mean C_d of 2.07 with a Strouhal shedding period of $S_t = .149$ is in good agreement with previous results (e.g. Fage and Johansen, 1927; Roshko, 1954 & 1955) when the effects of blockage are considered (see Sec. 4.5). As was previously discussed, the moment is sensitive to small errors, the slow drift in mean C_m level apparently being due to the zero level of the balance changing; for this reason further moment results will not be presented.

The effect of tunnel velocity will be investigated further in Sec. 4.6, but note here that velocity is constant to within about 0.5% rms and appears uncorrelated with the drag fluctuation, which has a 6% rms level. The long period modulation appears to occur on a time scale of roughly $4C/x/C$, or about 6 Strouhal periods T_s ; this calculation will be discussed in greater detail below.

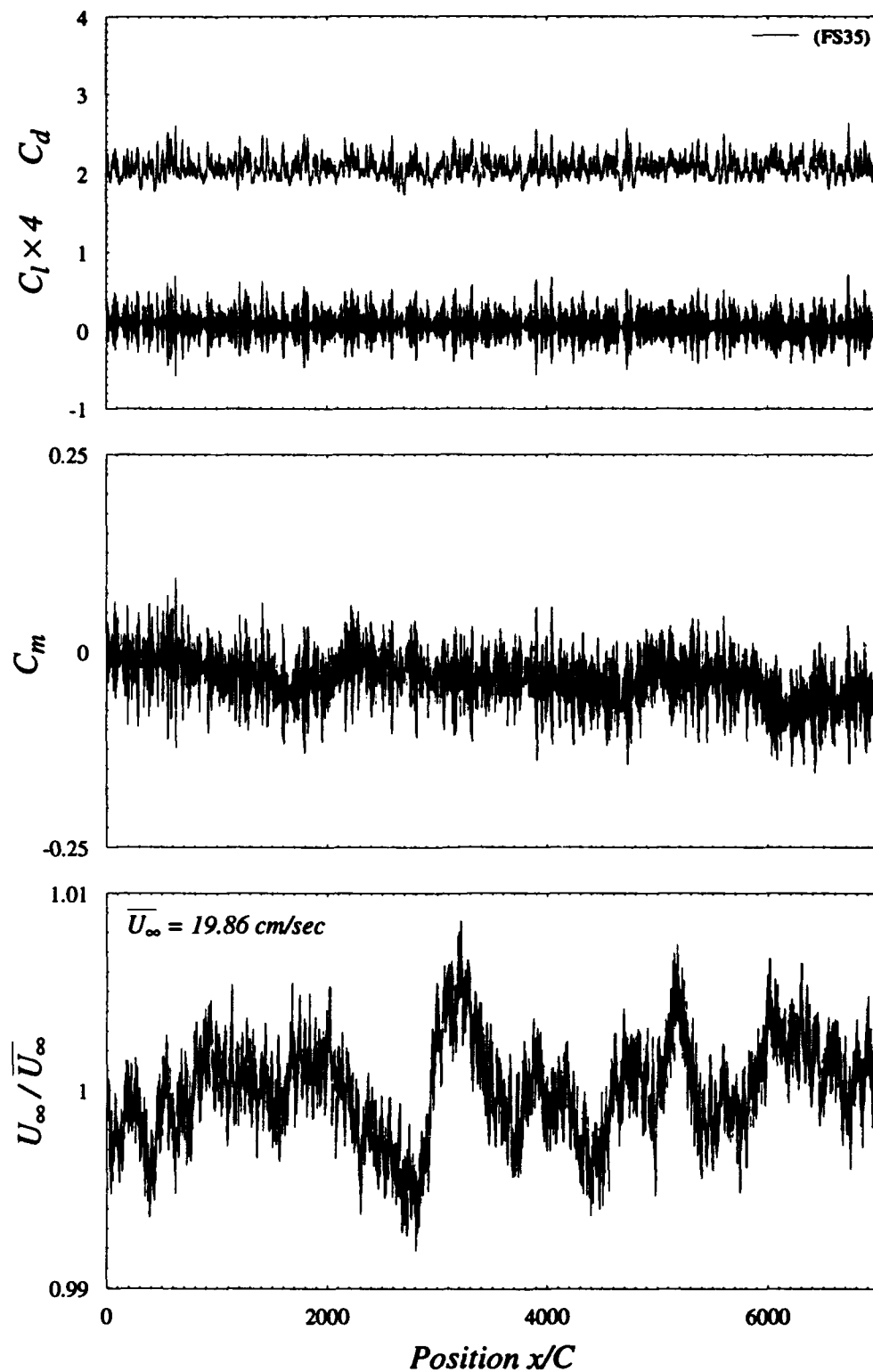


FIG. 4.2 Typical free surface water tunnel result. $Re = 6000$, $AR = 10$, $\alpha = 90^\circ$, $C = 3\text{cm}$, $l/C = 10.3\%$, $WEP @ 0^\circ$, $B = 5.9\%$. Note arbitrary origin and width of horizontal scale. $\overline{C_d} = 2.07$; $S_t = .149$; $\tau_o = 19.3$

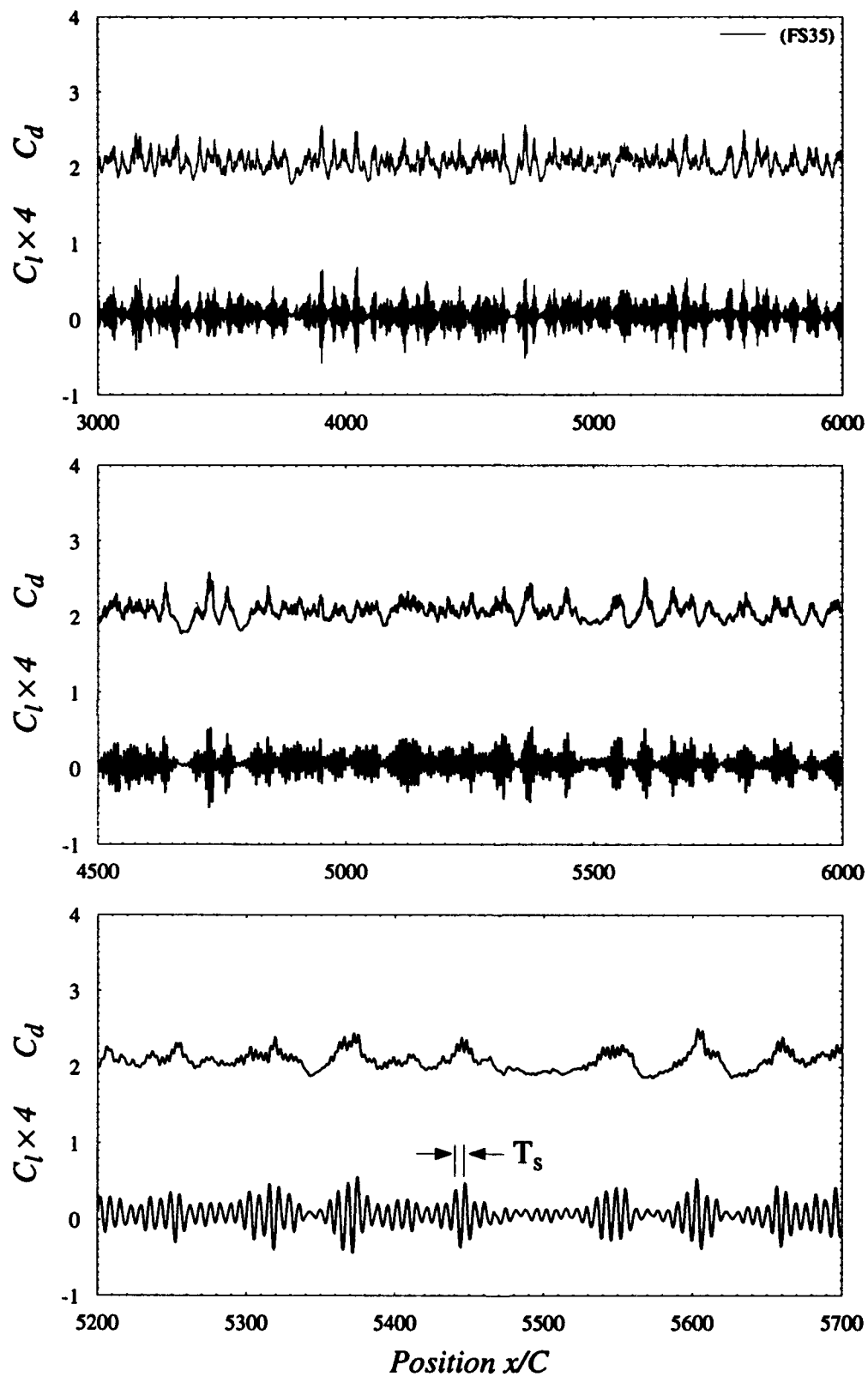


FIG. 4.3 Same run as in Fig. 4.2 with various horizontal (x/C) scales to show detail. Highest frequencies are due to vortex shedding

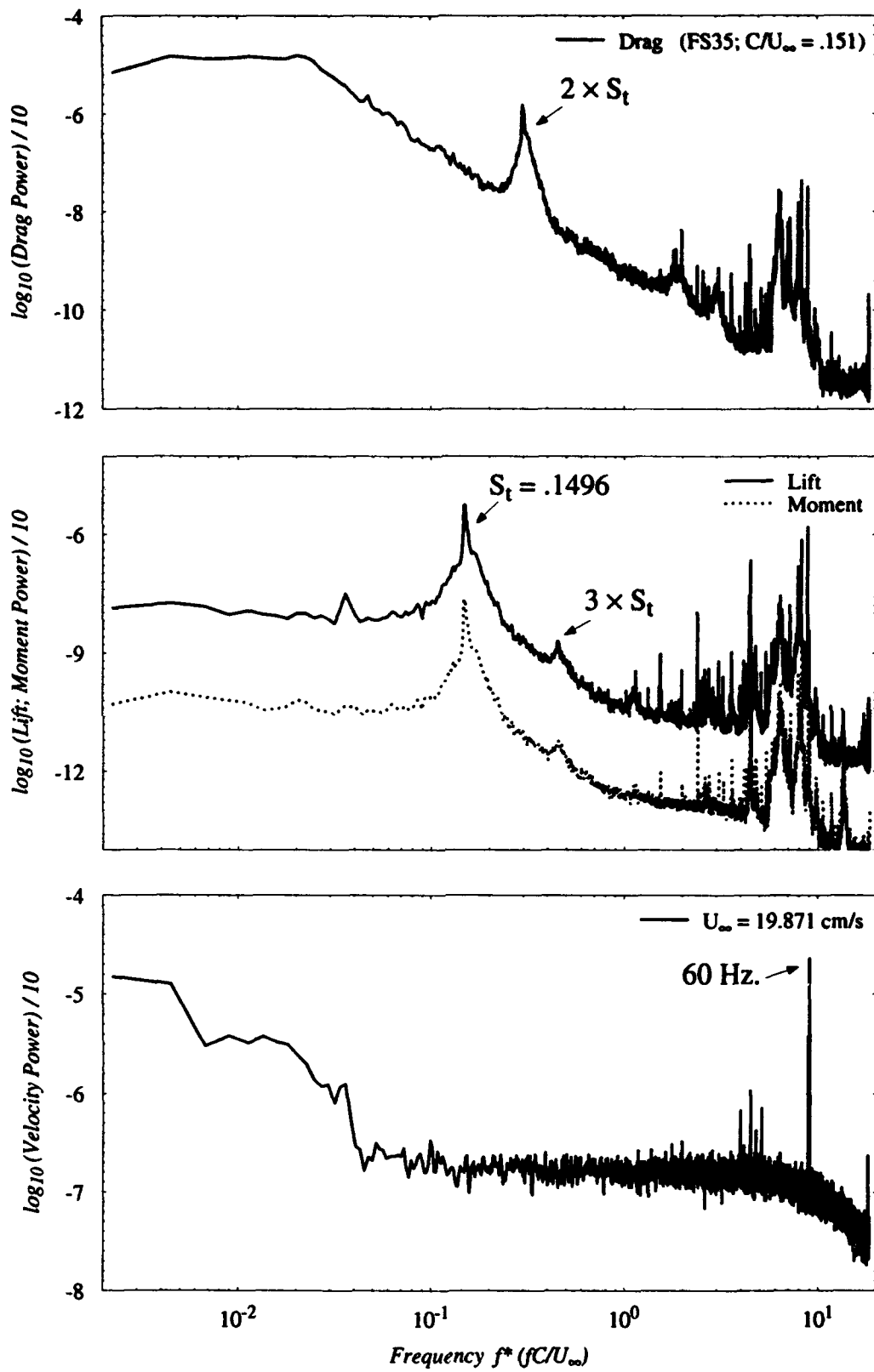


FIG. 4.4 Non-dimensional frequency f^* spectra for typical run (from Fig. 4.2)

Note too that the horizontal scale is roughly 70 times the extent of those presented previously. The "high" frequencies in the force signals are in fact the long period amplitude modulation which was apparent towards the end of the towing tank runs, a conclusion which is made clearer by expanding to horizontal scale until the vortex shedding frequencies can be distinguished, as is illustrated in Fig. 4.3.

Fig. 4.4 gives the power spectra in non-dimensional frequency f^* for the above run. Apparently there is not a well defined peak at the low frequency ($f^* = 1/6$) at which the shedding modulation is occurring in this run. There is a lot of power in the drag signal at low frequency (much more so than in the lift) but this power is broadband, characteristic of the chaotic or at least non-periodic nature of the modulation. In fact, the shedding occasionally appears to grow and decay almost exponentially - as can be seen from the log scale representation of rectified C_l shown in Fig. 4.5. Further discussion of this will be left until Ch. 7.

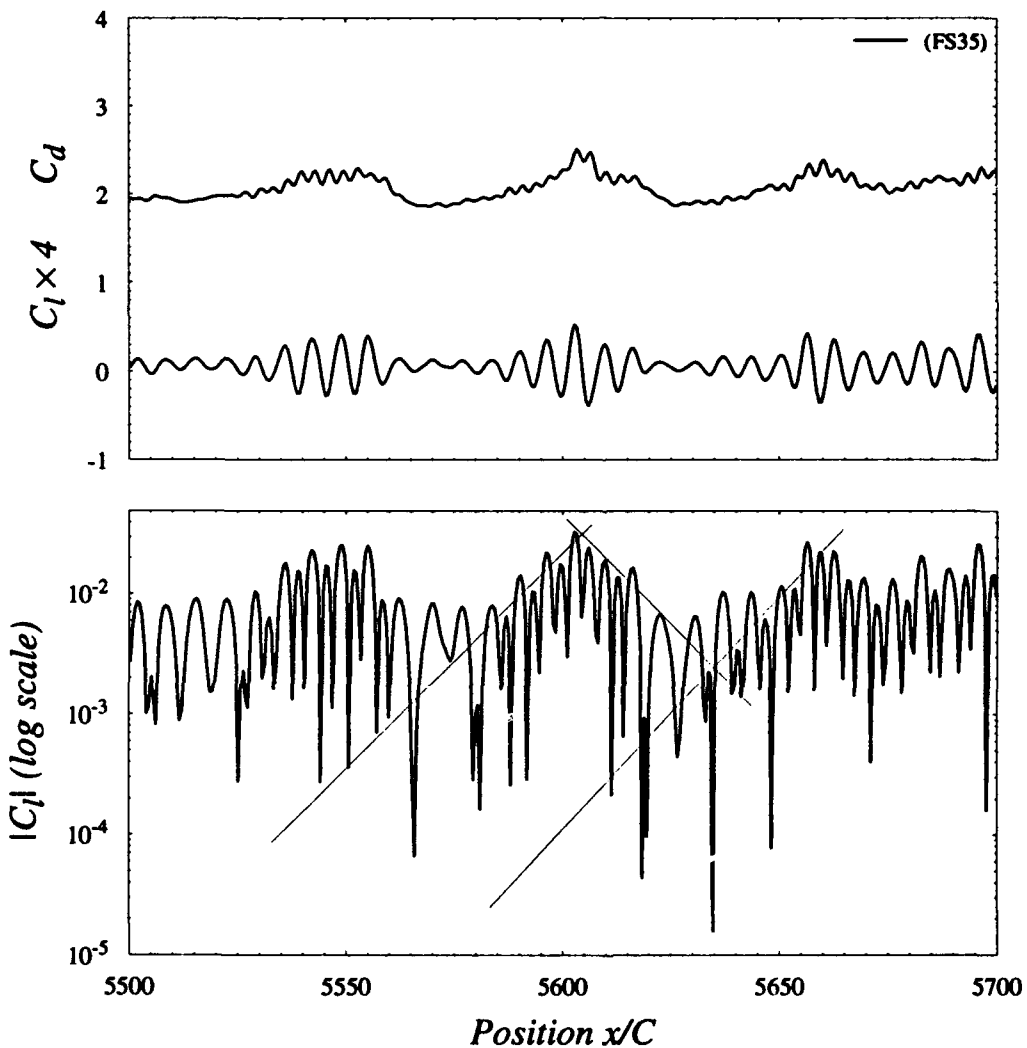


FIG. 4.5 Exponential growth and decay of shedding modulation (from Fig. 4.3); $\overline{C_d} = 2.07$, $S_t = .149$, $\tau_o = 19.3$. (Straight lines added for emphasis, note non-zero $\overline{C_l}$)

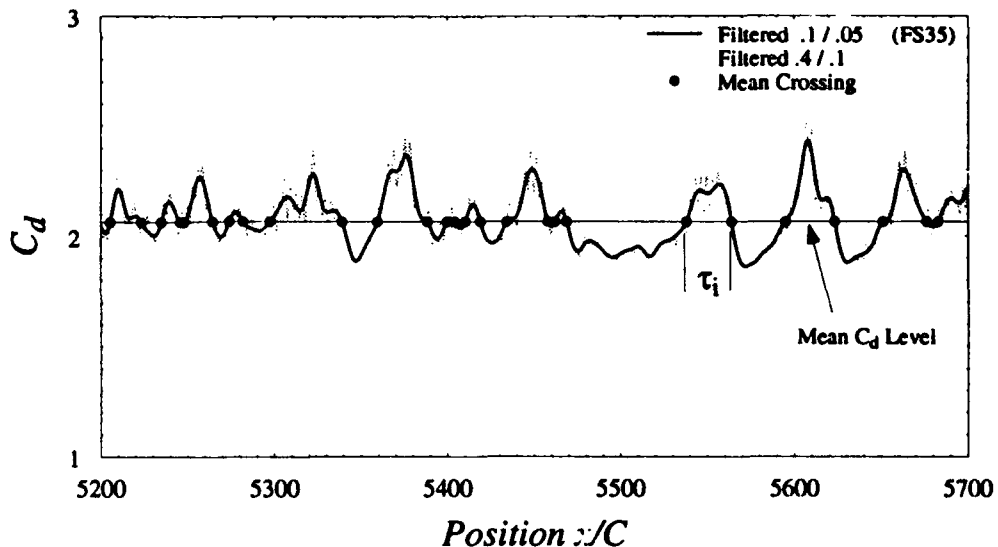


FIG. 4.6 Calculation of average C_d mean crossing interval: $\tau_o = \frac{1}{N} \sum_{i=1}^N \tau_i$

The nature of the long period shedding modulation makes it somewhat difficult to accurately characterize; in fact, many of the following results are somewhat qualitative in nature, with the resulting necessity of presenting full force *histories*, rather than being able to quote a single number in some way representative of the modulation. Nonetheless, one possible way to characterize the long period is shown in Fig. 4.6. The data is first digitally filtered to remove frequencies above the Strouhal frequency ($f_{co}^* = .1$, $f_w^* = .05$) and then the interval between points at which C_d crosses the \bar{C}_d level is noted. The average of these intervals over the course of a run is then representative of the mean half-period of the long-period modulation:

$$\tau_o = \frac{1}{N} \sum_{i=1}^N \tau_i$$

Since the rms of τ_i is high (usually $\approx 100\%$), and the total number of intervals N fairly low, there is a large uncertainty in τ_o . For this case $N = 367$, $\tau_o = 19.3$ (whence the time scale of roughly $40 x/C$ quoted above) and the rms level of $\tau_i = 74\%$; leading to an rms uncertainty in τ_o of $\approx 4\%$. This is better than many other runs, which typically had uncertainties of 5% to 10% in τ_o .

4.5 Blockage Effects

The effects of blockage on the flow about sharp edged bluff bodies has been studied by many authors (e.g. Maskell, 1963; Ranga-Raju and Singh, 1975; Awbi, 1983; Ramamurthy, 1989), most of whom come up with techniques of correcting time-averaged mean \bar{C}_d or \bar{S}_t , typically by modifying the presumed freestream velocity to account for increases due to area restriction in the tunnel. Many of these corrections are empirical in nature, and seek to obtain the "true" result which could be expected in unconfined two-dimensional flow; blockage in such a flow could be expected to be influenced purely by the ratio of plate chord to tunnel width. In

a three-dimensional flow geometry such as that used in the present experiments, blockage also increases with increasing *aspect ratio*, at the same time the effects of large-scale three-dimensionality could be expected to decrease. Isolating these two effects and applying a correction to account only for the changes due to blockage is very difficult; corrections have been obtained (Maskell, 1963) for general finite *AR* (three-dimensional) cases, but since the degree to which the flow is three-dimensional is one of the parameters we are attempting to change, applying such a generalized correction is somewhat counterproductive. Also, since we are primarily concerned with the *character* of the vortex shedding or force levels, a purely *two-dimensional* correction affecting only time-averaged mean levels would not yield additional useful information, so no attempt was made to correct the results presented.*

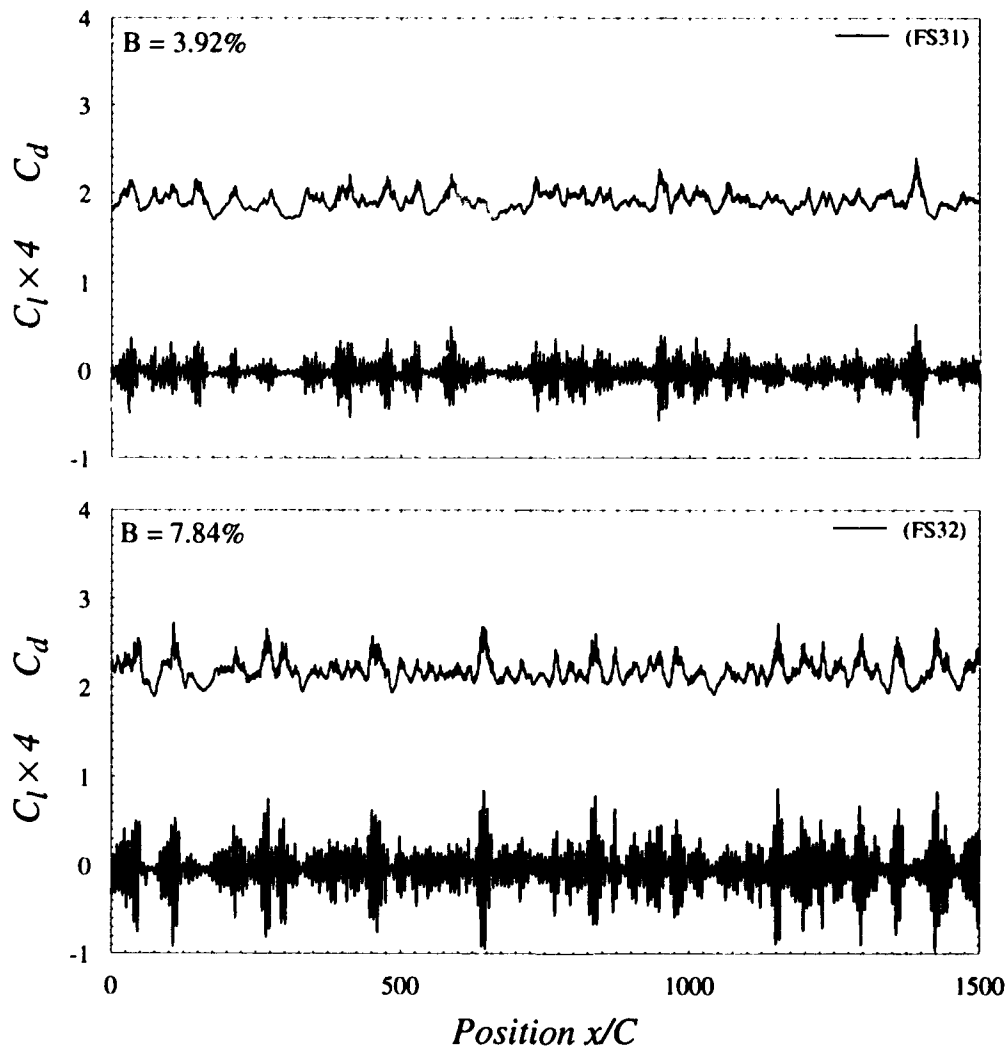


FIG. 4.7 Effect of tunnel blockage. $B = 3.92\%$: $C = 2\text{cm}$, $h/C = 16.25\%$, $\overline{C_d} = 1.92$, $C_d \text{rms} = 5.6\%$, $C_l \text{rms} = .039$, $S_t = .146$, $\tau_o = 21.3$. $B = 7.84\%$: $C = 4\text{cm}$, $\overline{C_d} = 2.19$, $C_d \text{rms} = 5.9\%$, $C_l \text{rms} = .062$, $S_t = .15$, $\tau_o = 18.3$

* Other than that the calculated freestream velocity was increased 2.5% to account for the decreased test section width due to the installation of side support plates for the false bottom (LDV velocity measurements were taken upstream of these plates).

However, it is important to understand the affects of blockage, and how it may affect the flow at various AR . Fig. 4.7 gives an indication of the effects of increasing blockage (based on C/W). Higher blockage results in higher mean drag levels and higher S_t frequencies, which is consistent with previously reported results (e.g. Abernathy, 1962). Rms force levels increase with increasing blockage, although this effect is most pronounced in C_l ; higher blockage also gives a slightly lower τ_o , although the decrease is well within the expected uncertainty.

In the interests of comparing to previous results one could apply, for example, the blockage correction suggested by Maskell, 1963:

$$C_{dc} = \frac{C_d}{1 + \epsilon C_d B}.$$

Where $\epsilon = 0.96$ for two-dimensional flow, leading to $\overline{C_d}_c = 1.79$ for $B = 3.9\%$ and $\overline{C_d}_c = 1.88$ for $B = 7.8\%$; which compare within 4% and 1%, respectively, to Fage and Johansen's results corrected in a similar manner; corrections applied to S_t (Awbi) yield similar agreement.

To minimize the effects of blockage in all of the following results, C, and thus B, has been kept constant: $C = 3\text{cm}$, $B = 5.9\%$. Although this is a fairly low blockage ratio, one should keep in mind that some of the changes found with changing aspect ratio are no doubt attributable to blockage effects.

4.6 Reynolds Numbers

Although Fig. 4.2 and Fig. 4.4 would indicate that tunnel freestream velocity was not a direct influence on the long period amplitude modulation, a number of cases were run at Reynolds numbers from 1000 to 15000 to see if any effect could be seen. Fig. 4.8 gives results from three of these runs spanning $Re = 3000$ to 9000; for this range $\overline{C_d}$ is fairly constant at ≈ 2.0 , and $S_t = .148$. Qualitatively there is not a great deal of difference between signals at the three different Reynolds numbers; τ_o is slightly higher ($\tau_o = 23.7$) at the lowest Reynolds number, but this is still almost within the expected uncertainty. Also, since physical run times were kept constant, more (non-dimensional) data was collected at the higher run velocities; the number of intervals recorded for the three Reynolds numbers were: 143, 375 and 561, respectively; since interval rms levels were roughly constant, higher Reynolds numbers results are considerably more reliable. It is possible to see considerably more low-frequency noise in the lift signal at $Re = 3000$; a reflection of the fact that the sensitivity to balance zero drift and other errors is increased by almost an order of magnitude over the $Re = 9000$ case; due to the low force levels at the lower velocities; this too may account for some of the increase in τ_o .

Balance uncertainties are even more apparent in Fig. 4.9, which presents results for $Re = 1000$. The large non-zero $\overline{C_l} = -0.163$ at $\alpha = 90^\circ$ and the higher than expected $\overline{C_d}$ are both attributable to uncertainty in determining force coefficients at these low forcing levels; typically about ± 0.12 at this Reynolds number. Although it was difficult to measure accurately, the three-bladed tunnel impeller was turning at roughly 2.5 rpm at this velocity. This gave a blade passage period of eight seconds, or $t^* = 13.9$ per cycle. The

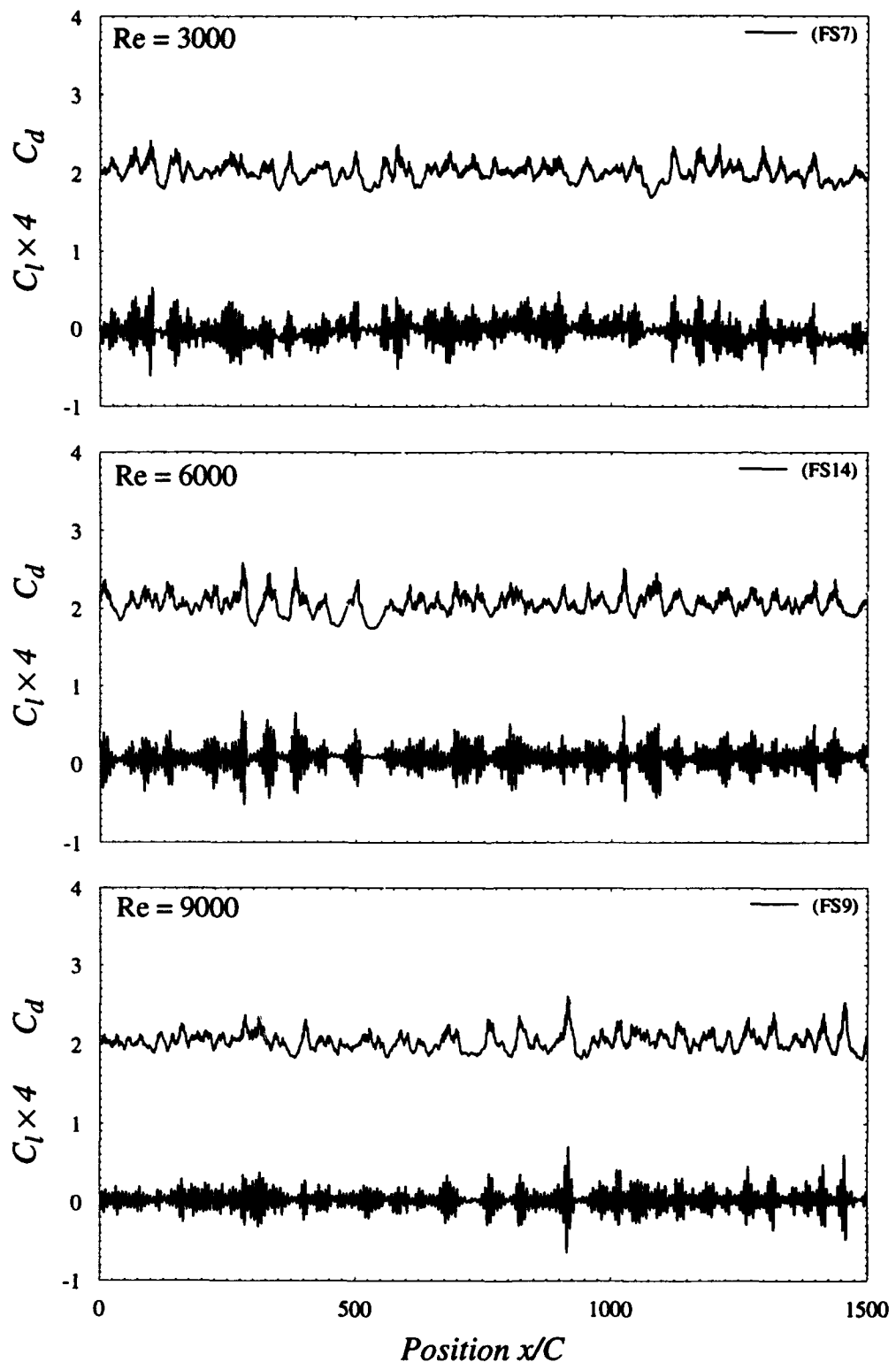


FIG. 4.8 Effect of Reynolds number (freestream velocity). $Re = 3000$: $U_\infty = 9.49$ cm/s, $\overline{C_d} = 1.98$, $S_t = .148$, $\tau_o = 23.7$. $Re = 6000$ (cf. Fig. 4.2): $U_\infty = 19.87$ cm/s, $\overline{C_d} = 2.06$, $S_t = .148$, $\tau_o = 18.9$. $Re = 9000$: $U_\infty = 30.71$ cm/s, $\overline{C_d} = 2.03$, $S_t = .148$, $\tau_o = 19.6$

oscillations apparent in both the freestream velocity and the drag are due to this impeller induced fluctuation in the freestream. Although it is difficult to establish τ_o or S_t from the limited data available, it would appear that coherent shedding occurs in only one location (at $t^* \approx 225$) in this run, implying an unusually long modulation period. However, at $Re = 1000$ considerable low Reynolds number effects are expected (Flaschbart (1935) and Ch. 3) and the intermediate "non-shedding" may be simply regions with large formation distances and low shedding amplitudes typical of results at $Re = 1000$.

The above results effectively eliminate fixed frequency sloshing or vibrational modes as a source of the long period modulation for flows independent of Reynolds numbers ($Re > 3000$) and provide additional support for the conclusion that the long period modulation is not related directly to changes in tunnel velocity.

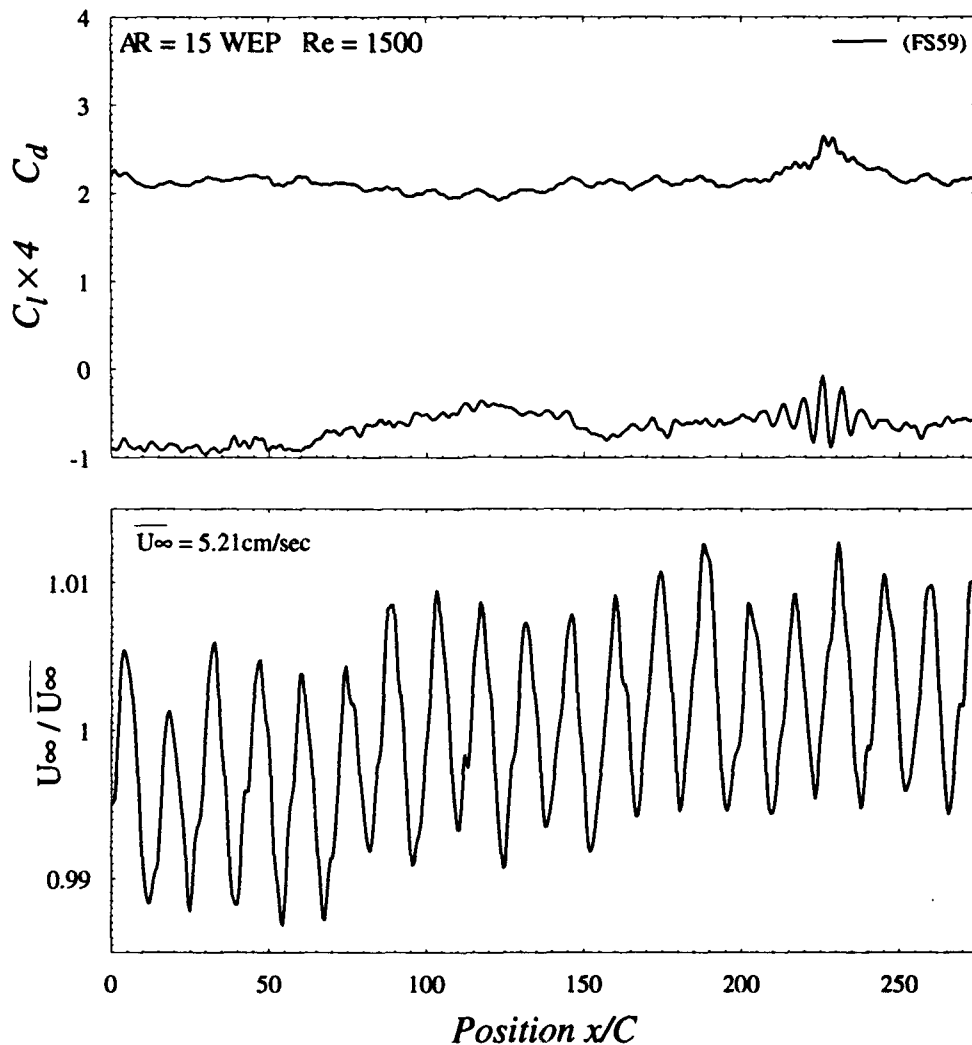


FIG. 4.9 Low Reynolds number result. $Re = 1500$, $AR = 15$, $\alpha = 90^\circ$, $C = 3\text{cm}$, $h/C = 10.3\%$, $WEP @ 0^\circ$, $B = 5.9\%$. Note width of horizontal scale. $U_\infty = 5.21 \text{ cm/s}$, $\bar{C}_d = 2.13$, $\bar{C}_l = -0.163$; S_t and τ_o were not measurable

4.7 Plate Stiffness

It was thought that another potential source for the modulation was a coupled interaction of the flow with vibrational modes of the (cantilevered) plate model. Although these vibrational modes are presumably at a roughly fixed frequency at least an order of magnitude above the S_t frequency, and the modulation was relatively constant over a wide range of tunnel velocities (as shown above), it was deemed expedient to change the vibrational characteristics of the model and to note any effect. This had already been done indirectly by virtue of using numerous different plate models of widely varying material and geometric properties, but an additional test using a single plate was also performed. For this test .004" tungsten guy wires were strung from the plate mount to the lower end of the plate, increasing its stiffness considerably; these wires were thin enough that they did not interfere with the flow ($Re_w \approx 20$), although the drag was corrected for the additional drag of the wires (about a 2% correction).

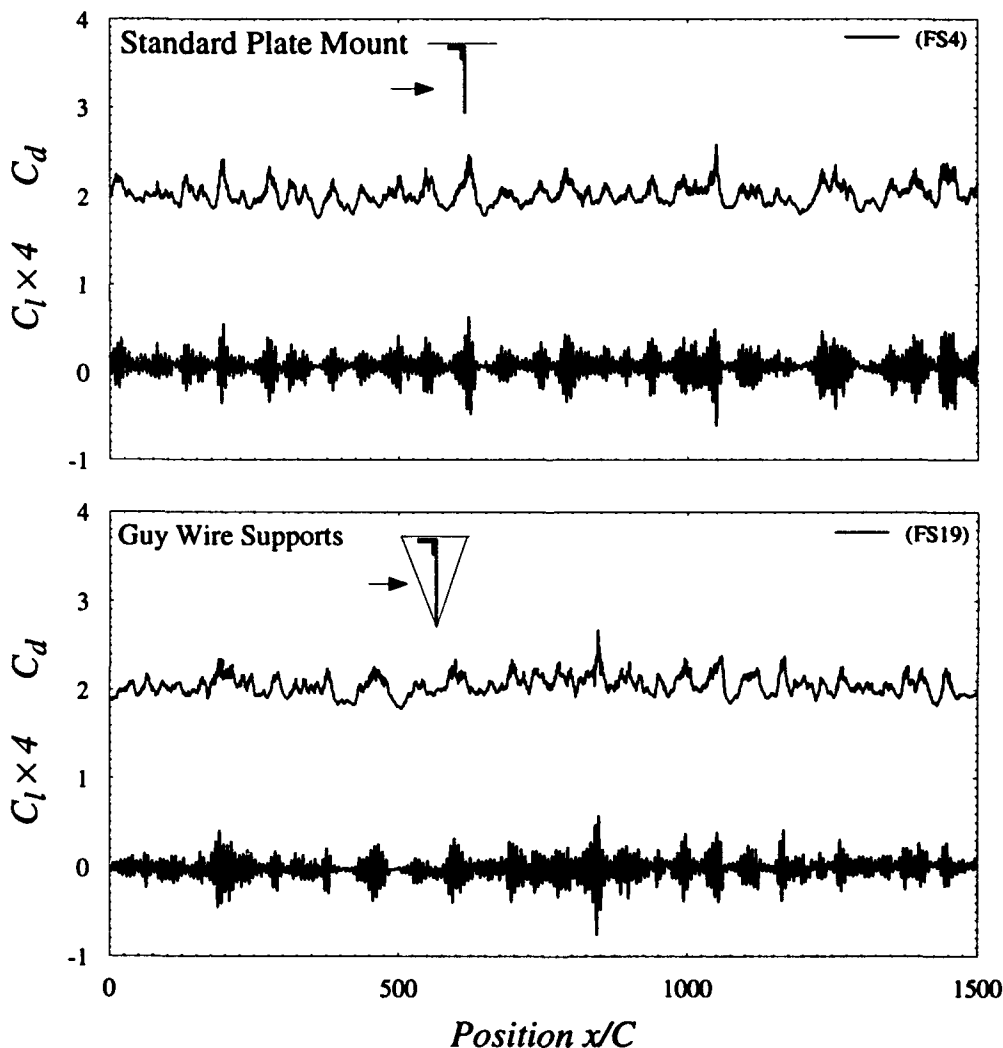


FIG. 4.10 Effects of plate stiffness. Upper plot is standard (cantilever) plate mount; $\overline{C_d} = 2.02$, $S_t = .148$, $\tau_o = 21.8$. Lower plot is same plate/mount with .004" tungsten guy wire supports added; $\overline{C_d} = 2.05$, $S_t = .146$, $\tau_o = 20.4$

Fig. 4.10 gives the results of these runs. Results are very close to those found for the typical run, with a slight decrease in the S_t number for the stiffened case, although the change is only about 3%. Qualitatively the runs look very similar, the change in τ_o being well within the expected uncertainty. Although there is doubtless some interaction between the vibration of the model and the flow, it appears that plate vibration does not significantly affect the long period modulation or time averaged mean results.

4.8 Angles of Attack

By way of introducing a spanwise uniform flow perturbation, small changes in angle of attack from 90° were introduced. As can be seen from Fig. 4.11 and Fig. 4.12, the main effect of a 10° change from $\alpha = 85$ to $\alpha = 95$ was to change the value of \overline{C}_l from $+0.18$ to -0.18 , with the rest of the results remaining essentially unchanged from the typical case. Force coefficient results are summarized in Fig. 4.11; at $\alpha = 90$ results of five repeated "typical" runs are shown, 4 of which have already been presented. The scatter at $\alpha = 90$ is typical of the repeatability of the results, although most of the \overline{C}_l scatter is due to inaccuracies in setting the angle of attack exactly (typically $\pm 0.5^\circ$) rather than any inherent un-repeatability.

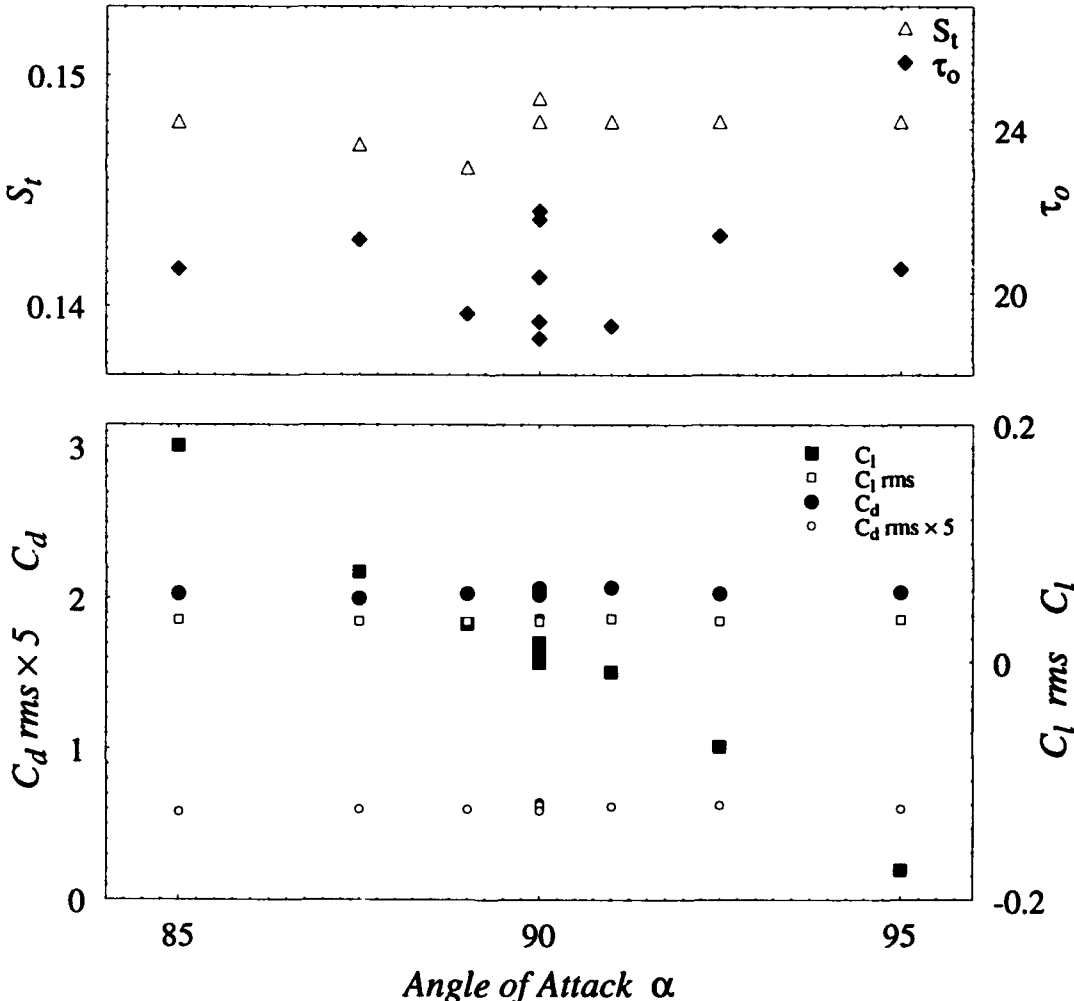


FIG. 4.11 Mean (\overline{C}_d , \overline{C}_l) and rms (instantaneous) coefficient values for different angles of attack

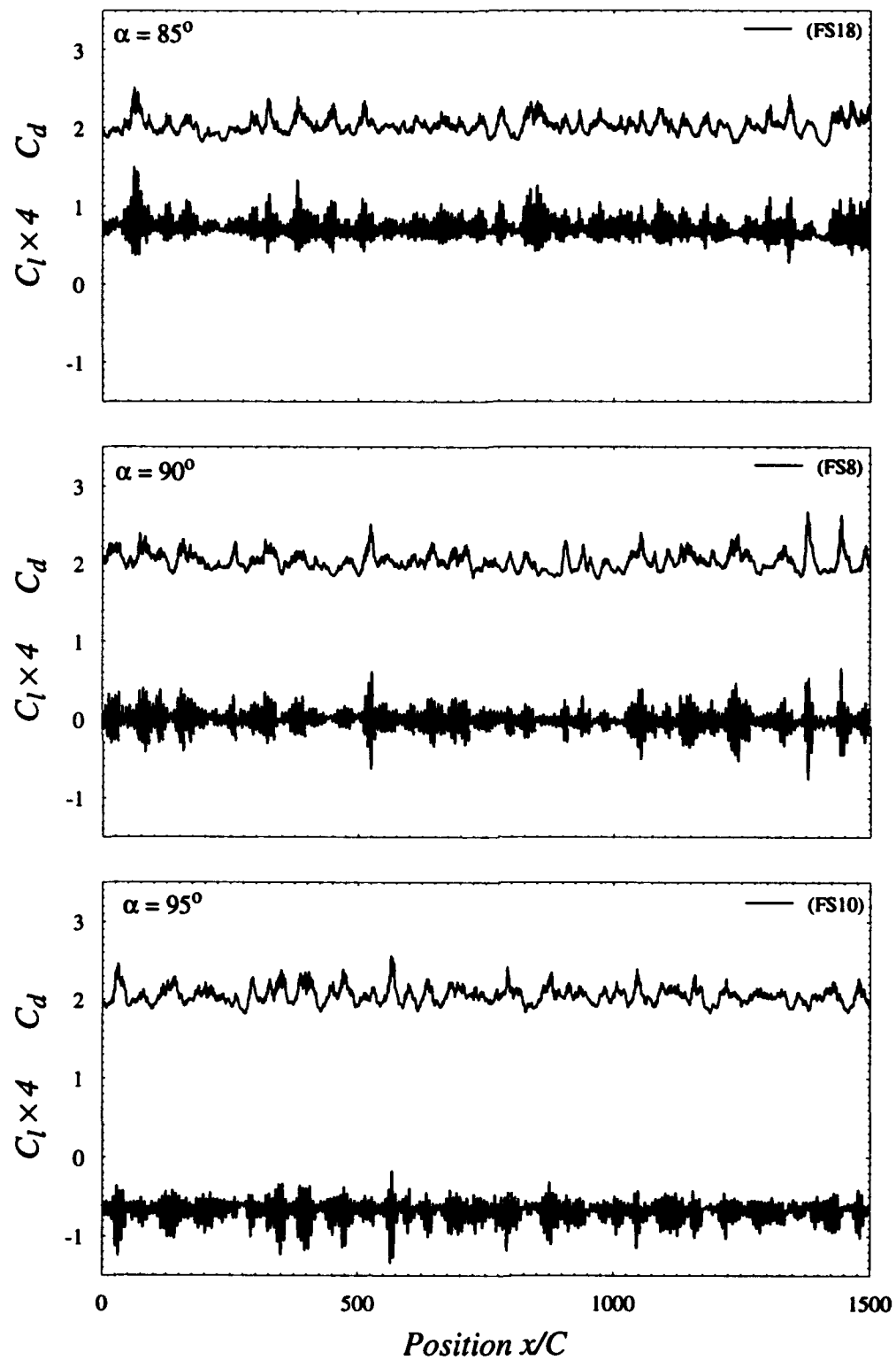


FIG. 4.12 Angle of attack (α) effects. $\alpha = 85$: $\overline{C_d} = 2.03$, $\overline{C_l} = +0.18$, $S_t = .148$, $\tau_o = 20.6$. $\alpha = 90$ (cf. Fig. 4.2): $\overline{C_d} = 2.03$, $\overline{C_l} = +0.0008$, $S_t = .148$, $\tau_o = 20.4$. $\alpha = 95$: $\overline{C_d} = 2.04$, $\overline{C_l} = -0.18$, $S_t = .148$, $\tau_o = 20.6$.

4.9 Aspect Ratio Effects

Changes in aspect ratio produced the results shown in Fig. 4.13. Obviously there is considerable change with an increase in aspect ratio from $AR = 6$ to $AR = 10$; the most notable difference being that at the lower aspect ratio there are regions in which little or no evidence of vortex shedding is present. Considering for the moment only those regions in which shedding is occurring, we note that $\overline{C_d}$ increases from 1.86 at $AR = 6$ to $\overline{C_d} = 2.13$ at $AR = 15$; as explained in Fig. 4.7, at least part of this increase can be attributed to the increased blockage at higher aspect ratios. τ_o increases from .143 to .151, this too may be due to increased blockage: a run (which is not shown) using a 2cm chord model at $AR = 23$ had an identical $S_t = .151$, as well as almost an identical area blockage ($23 \times 2 \approx 15 \times 3$), albeit only 2/3 the blockage B. In going from $AR = 6$ to $AR = 10$ τ_o decreases considerably from 31.7 to 21.3, but then seems to level out and remain at about $\tau_o = 20$ for further increases in AR .

Further experimentation using different plate models and tunnel velocities revealed that the vortex shedding intermittency at $AR = 6$ was repeatable, with a typical result being shown in Fig. 4.14 (note the expanded horizontal scale from most previous results). The drag coefficient during the shedding portions of the run was $\overline{C_d} = 1.86$ with a corresponding $S_t = .143$ and $\tau_o = 31.7$; these are considerably lower and higher, respectively, than the values which might be expected by extrapolating higher aspect ratio results. During intervals with little or no vortex shedding, the drag coefficient was $\overline{C_d} = 1.39$, with no evidence of shedding in the lift or drag histories. The tunnel velocity was again steady to within about $\pm 1\%$, and did not appear correlated with the shedding/no-shedding intervals. These results will be discussed further in Ch. 7.

4.10 End Condition Effects - End Plate Angles

All of the results presented so far have used an end plate as a lower end condition; results in this section are for an $AR = 15$ case with a false bottom wall at various angles for a lower end condition. It was thought that perhaps angling of an end plate could be used to promote parallel vortex shedding, as had been done previously at much lower Reynolds numbers (Williamson, 1989). Results from a $AR = 15$ case with *FBW* angles of 0° and $\pm 2.5^\circ$ are shown in Fig. 4.15. In all cases $S_t \approx .153$ is consistent with previous results (at $AR = 15$) using an end plate; $C_d \approx 2.13$ for the *FBW* 0° and $+2.5^\circ$ cases is also consistent, with a decrease in C_d to 2.03 at *FBW* -2.5° . This drag decrease is likely reflective of the increased base pressure due to the inwardly angled end plate - that the drag does not *increase* in the *FBIW* $+2.5^\circ$ case is probably due to flow separation on the lower wall preventing an equivalent decrease in base pressure. Qualitatively, results with either positive or negative angles on the end plates look considerably more intermittent, a fact confirmed by the increase in τ_o from 19.2 to 26.2 and 29.3 for positive and negative 2.5° , respectively. This may indicate that such end plates, while perhaps providing more two-dimensional shedding, also tend to *inhibit* non-two-dimensional shedding to a greater degree than the *FBIW* 0° case, particularly in the negative *FBW* case.

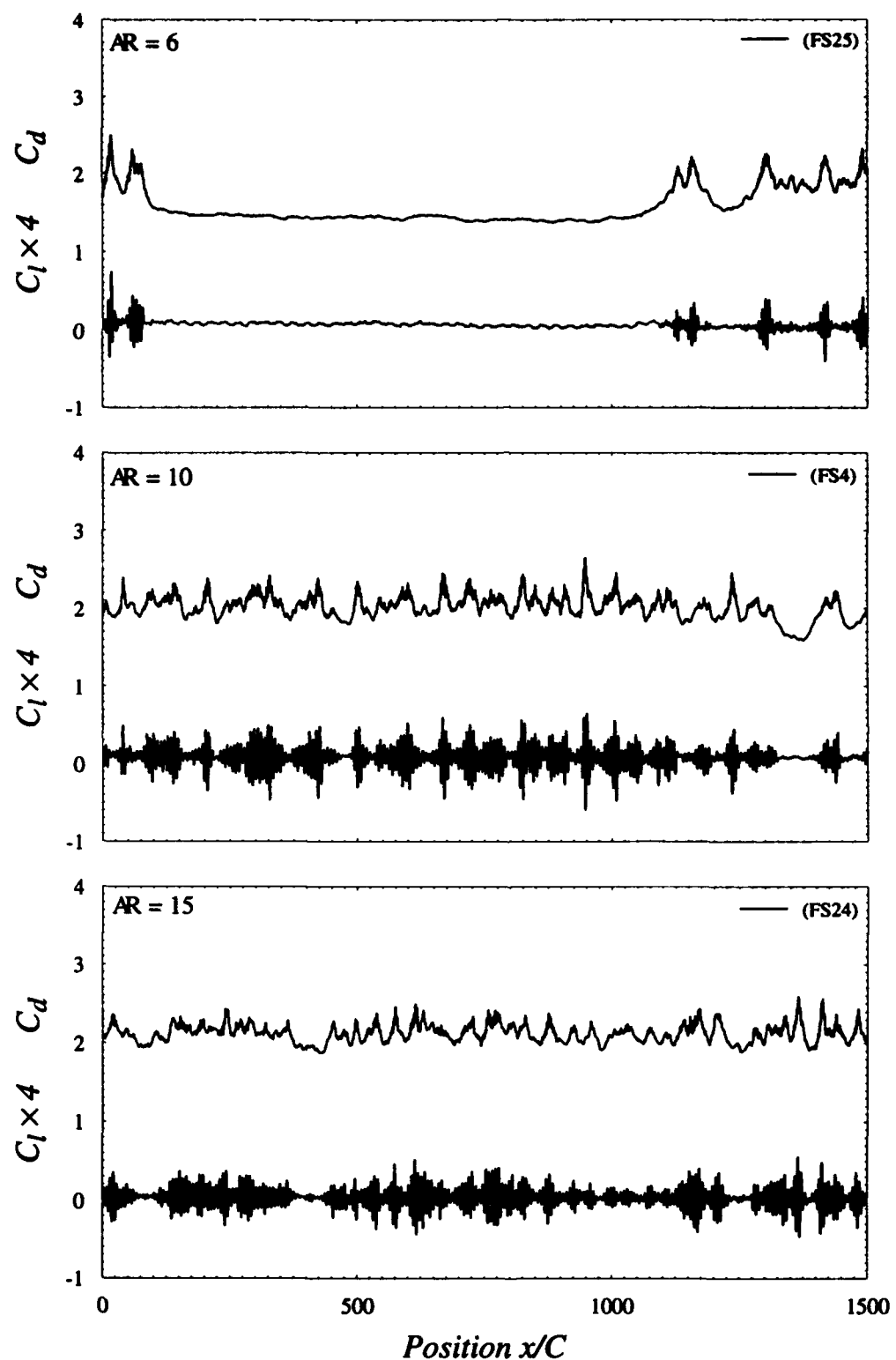


FIG. 4.13 Aspect ratio effects. $AR = 6$, Non-shedding: $\overline{C_d} = 1.39$; Shedding: $\overline{C_d} = 1.86$, $S_t = .143$, $\tau_o = 31.7$. $AR = 10$ (cf. Fig. 4.2): $\overline{C_d} = 2.02$, $S_t = .148$, $\tau_o = 21.8$. $AR = 15$: $\overline{C_d} = 2.13$, $S_t = .151$, $\tau_o = 20.7$

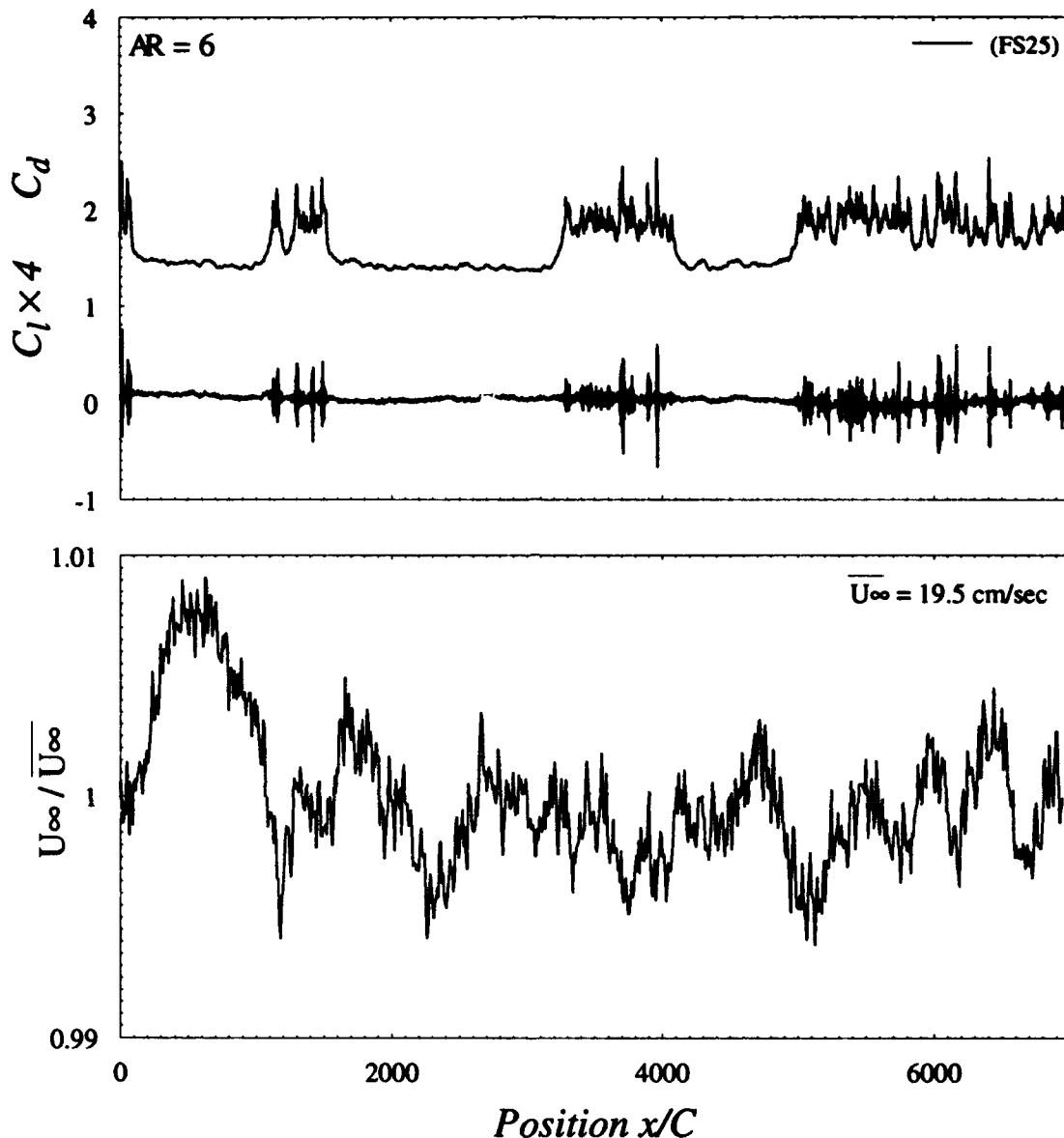


FIG. 4.14 Shedding intermittency at low $AR = 6$ aspect ratio. Non-shedding regions: $\overline{C_d} = 1.39$. Shedding regions: $\overline{C_d} = 1.86$, $S_t = .143$, $r_o = 31.7$

Of all the parameters studied, only aspect ratio and end plate angle seemed to have any significant affect on the long period amplitude modulation for Reynolds number independent cases. For this reason end plate angle was varied from $+15^\circ$ to -5° for aspect ratios of 4 to 23; a selection of results are presented in Fig. 4.16 and Fig. 4.17; Fig. 4.18 gives a more compact presentation of some time averaged mean values as a function of aspect ratio.

For $AR = 4$ the drag was very low, with no evidence of vortex shedding in any of the force results; unlike the $AR = 15$ $FBW = \pm 2.5^\circ$ degree case though, the drag is considerably higher ($C_d = 1.37$) for positive FBW angle than for 0° or negative angles. Although the end plate is no doubt changing the base

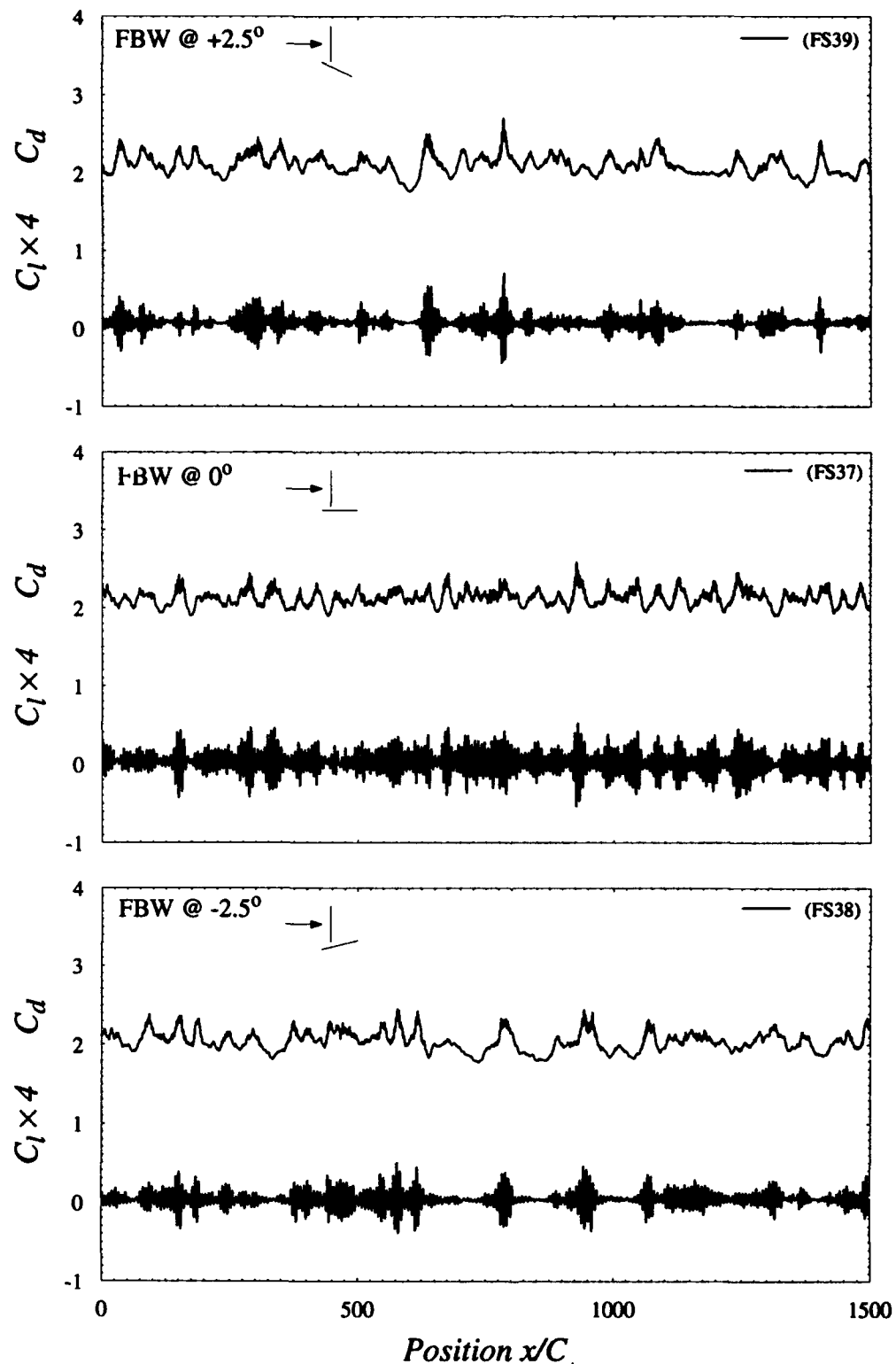


FIG. 4.15 Effects of *FBW* angle at $AR = 15$. *FBW* @ $+2.5^\circ$: $\overline{C_d} = 2.11$, $S_t = .153$, $\tau_o = 26.2$. *FBW* @ 0° (cf. Fig. 4.13): $\overline{C_d} = 2.15$, $S_t = .154$, $\tau_o = 19.2$. *FBW* @ -2.5° : $\overline{C_d} = 2.03$, $S_t = .153$, $\tau_o = 29.3$

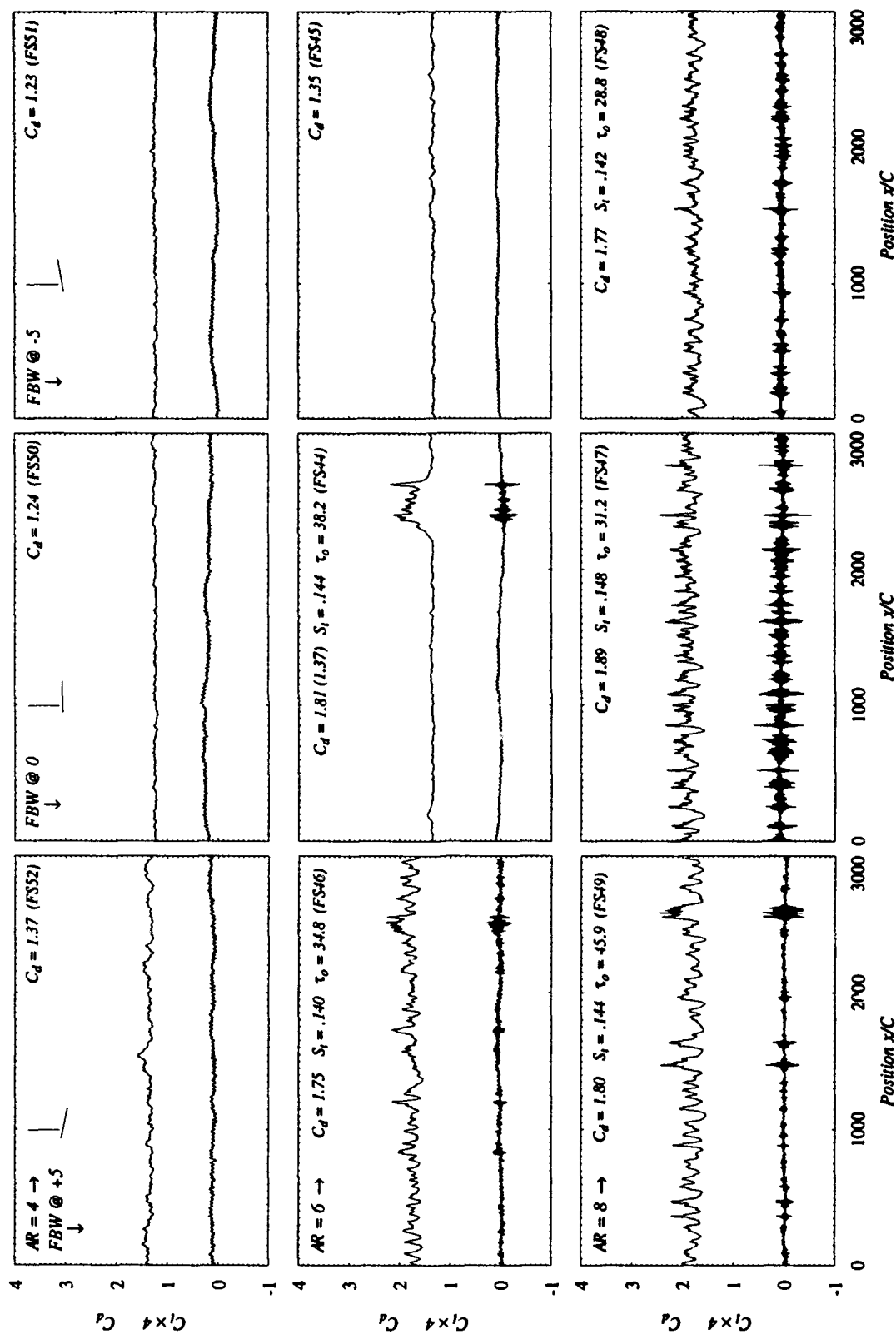


FIG. 4.16 FBW angle and Aspect Ratio effects - part 1

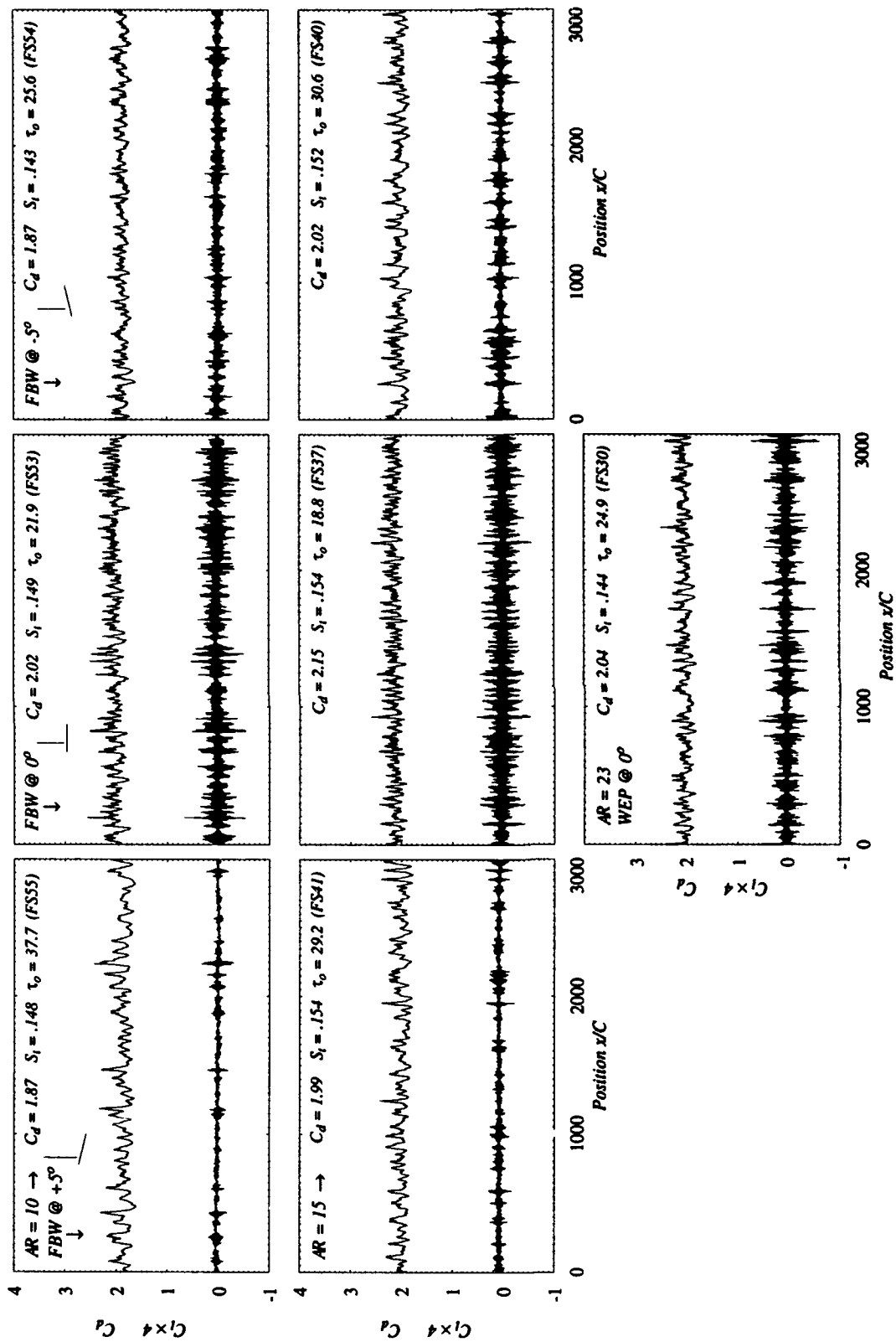


FIG. 4.17 *FBW* angle and *AR* effects - part 2. Note that *AR* = 23 case has *C* = 2cm, *h/C* = 16.25%, *B* = 3.9%

pressure, it would seem that the primary affect at these low aspect ratios is to promote or inhibit the vortex shedding "mode," which is associated with a considerably higher drag. This is apparent both from the increased unsteadiness apparent in the result with FBW at $+5^\circ$, and from the $AR = 6$ results, which show consistent vortex shedding for positive FBW , intermittent shedding at $FBW = 0^\circ$, and no shedding at all for $FBW = -5^\circ$.

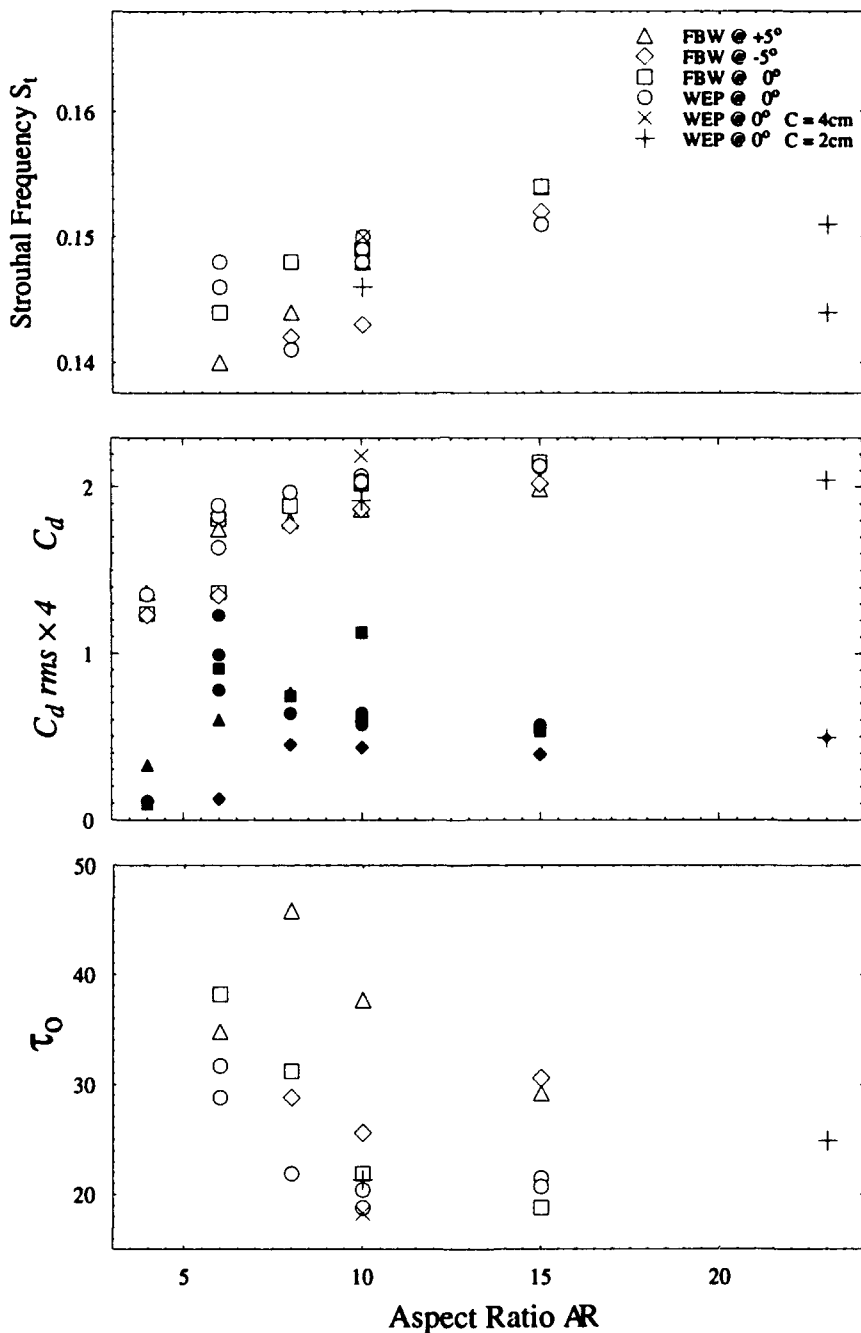


FIG. 4.18 Summary of results for various aspect ratios

Neglecting momentarily the $\mathcal{AR} = 23$ case; at higher aspect ratios the drag relative to the *FBIW* 0° case is generally lower for both positive and negative end plate angles, perhaps reflective of the increased separation from the end plate at $\pm 5^\circ$ compared to the results of Fig. 4.15 at $\pm 2.5^\circ$. There is no consistent behavior of S_t at different end plate angles; although both $\overline{C_d}$ and S_t consistently increase with increasing aspect ratio, again at least in part due to increasing blockage.

The rms level of C_d decreases considerably with increasing aspect ratio, seeming to asymptote to about 6%. τ_o increases for positive and negative *FBIW* cases relative to the 0° case, with a fairly consistent decrease in all cases with increasing \mathcal{AR} ; τ_o asymptotes to ≈ 20 at high aspect ratios.

For either positive or negative end plate angles there seems to be considerably more long period unsteadiness or modulation in the vortex shedding; this is most evident in the C_l results, which have consistently lower rms levels relative to the *FBIW* at 0° case. This could be an indication of a lack of spanwise correlation leading to a much lower rms level while maintaining roughly (within 7%) the same mean drag levels. This is somewhat inconsistent with expectations: the *FBIW* $+5^\circ$ case was expected to yield *more* spanwise correlation; while at $\mathcal{AR} = 6$ it seems to at least promote the onset of organized vortex shedding.

The $\mathcal{AR} = 23$ case used an end plate at 0° on a plate with $C = 2\text{cm}$, $h/C = 16.25\%$ and $B = 3.9\%$. Due to the different blockage and thickness it is perhaps unfair to compare results directly, nonetheless results appear to agree with other plate models at $\mathcal{AR} = 10$, and the $\mathcal{AR} = 23$ results are consistent with the values to which τ_o , $\overline{C_d}$ and S_t appear to asymptote.

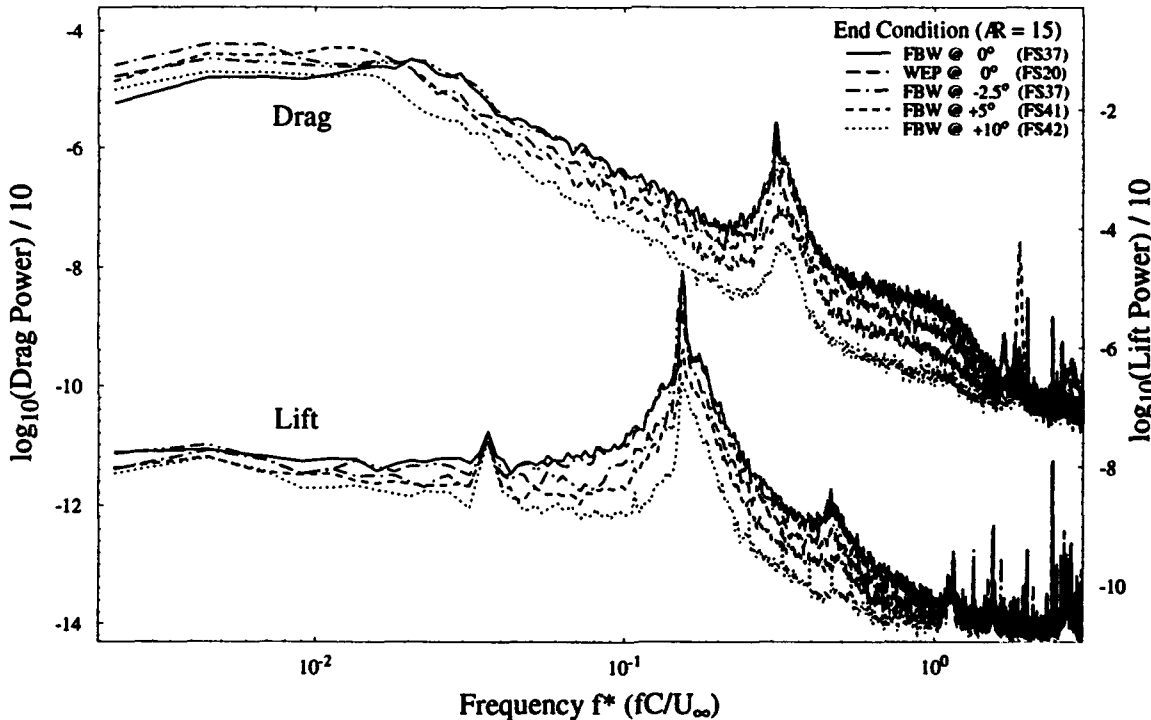


FIG. 4.19 Effect of end condition on power spectra at $\mathcal{AR} = 15$

In general then, with increasing aspect ratio there appears to be a decrease in not only the period of the modulation, but also its amplitude. The angle of the false bottom has considerably less effect for $AR \gtrsim 10$; with the primary effects being seen below $AR = 6$, where the angle of the end plate affects the shedding mode of the entire plate.

Power spectra of the lift and drag for various end conditions and aspect ratios are shown in Fig. 4.19 and Fig. 4.20, respectively. We see a noticeable decrease in the sharpness of the shedding peaks for non-zero *FBW* angle; there is little difference between positive and negative angles, so only one is shown; there is also little difference between the *WEP* and *FBW* at 0° cases. There is a 7% decrease in drag between the $\pm 5^\circ$ and 0° results, but this is insufficient to account for the shift in the curves, at least some of the power lost at the S_t frequency and above reappears at lower frequencies, as would be expected from the increased long period modulation apparent from the time histories.

There is a broadband "hump" in drag power from $f^* \approx .5$ to 1 (an alternate interpretation could be a frequency roll-off beginning at $f^* \approx 1$) which is readily apparent in the $AR = 15$ case; this bump is not repeated in the lift spectra; it is, however, repeatable in drag at $AR = 15$ with an end plate (Fig. 4.19).

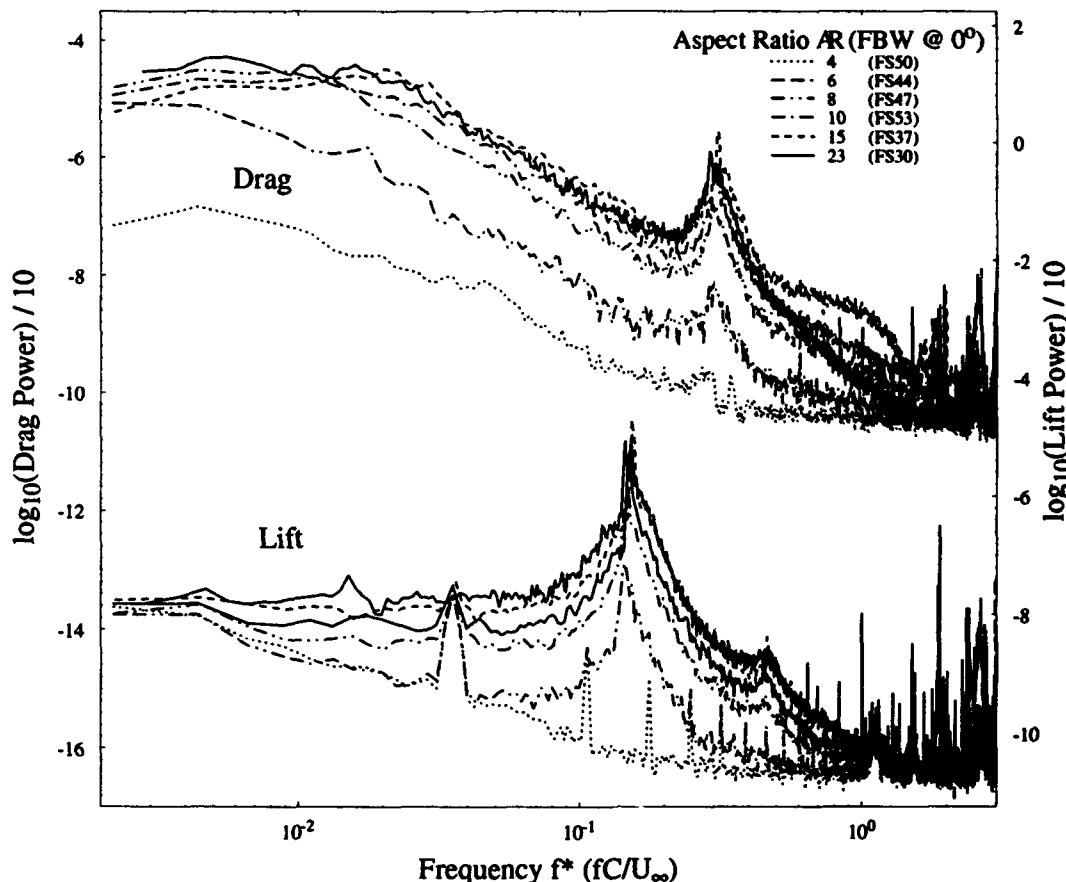


FIG. 4.20 Effect of aspect ratio on power spectra with *FBW* at 0° . Note that $AR = 23$ case has $C = 2\text{cm}$, $h/C = 16.25\%$, $B = 3.9\%$

The bump becomes progressively less pronounced as end plate angle increases, and from Fig. 4.20, either increasing or decreasing aspect ratio also greatly reduces the power in this frequency band. Blockage is a potential source of this frequency band; however, runs with $AR = 10$ and both higher and lower blockage (width and area) exhibited spectra similar to other $AR = 10$ cases, none of which exhibited such a band. The fact that the hump is progressively reduced by varying end plate angle also argues against blockage. Another possibility is plate vibration and its interaction with the shedding; the $AR = 23$ case used a plate with considerably different chord (blockage) and stiffness, perhaps accounting for the lack of power in this band for that case. However, the fact that this hump is repeatable with an end plate but an otherwise identical plate would argue against plate vibration as a source, since the end plate considerably changes the vibration characteristics. Further investigation will be required to explain this frequency band.

Since the power spectra are not normalized and represent drag power, rather than C_d power, one would expect a decrease in power with decreasing AR purely due to the decrease of drag with smaller plate areas. This can be seen in Fig. 4.20; where the signals with the lowest AR have the lowest power. The basic shape of the spectrum is the same for each case (except for the aforementioned frequency band) down to $AR = 6$, where the intervals without vortex shedding begin to decrease the peak sharpness until at $AR = 4$ there is no well defined peak at the expected S_t . Note that in the $AR = 4$ case the lift power is low enough that spikes from either aliasing or sub-harmonics of the balance natural frequencies become readily apparent.

4.11 Summary

The effect on time averaged mean $\overline{C_d}$, C_l and S_t of changes in the parameters presented in this chapter are all consistent with results presented previously in the literature, where such results exist. Few researchers have presented time series data, so very little information about long period modulations in vortex shedding exists (Schewe, 1983 and Szepessy and Bearman., 1992 are notable exceptions). The results herein are somewhat inconclusive, due in part to the limited range of aspect ratios which could be achieved.

Low Reynolds number results ($Re = 1000$) again indicated force levels consistent with a large formation distance and low base pressure fluctuations and asymmetry. Although at $Re = 1000$ a very long modulation time $\tau_o = 250+$ was apparent in the vortex shedding, it is unlikely that this modulation is primarily a Reynolds number effect, since it is constant above and can be changed independently of Reynolds number for $Re \gtrsim 3000$.

It remains unclear what behavior could be expected in the absence of extrinsic three-dimensionality (*i.e.*, in the absence of large scale three-dimensional motions associated primarily with finite aspect ratio). Or somewhat related question: in the limit of infinite aspect ratio with no external influences, what is the largest spanwise coherent three-dimensional structure which would exist? The fact that the long period modulation appears to asymptote to a value of about $\tau_o = 20$, or about $6 T_s$, may indicate that for sufficiently large aspect ratios there is an instability or sub harmonic at this frequency. It is interesting that below about $AR = 6$

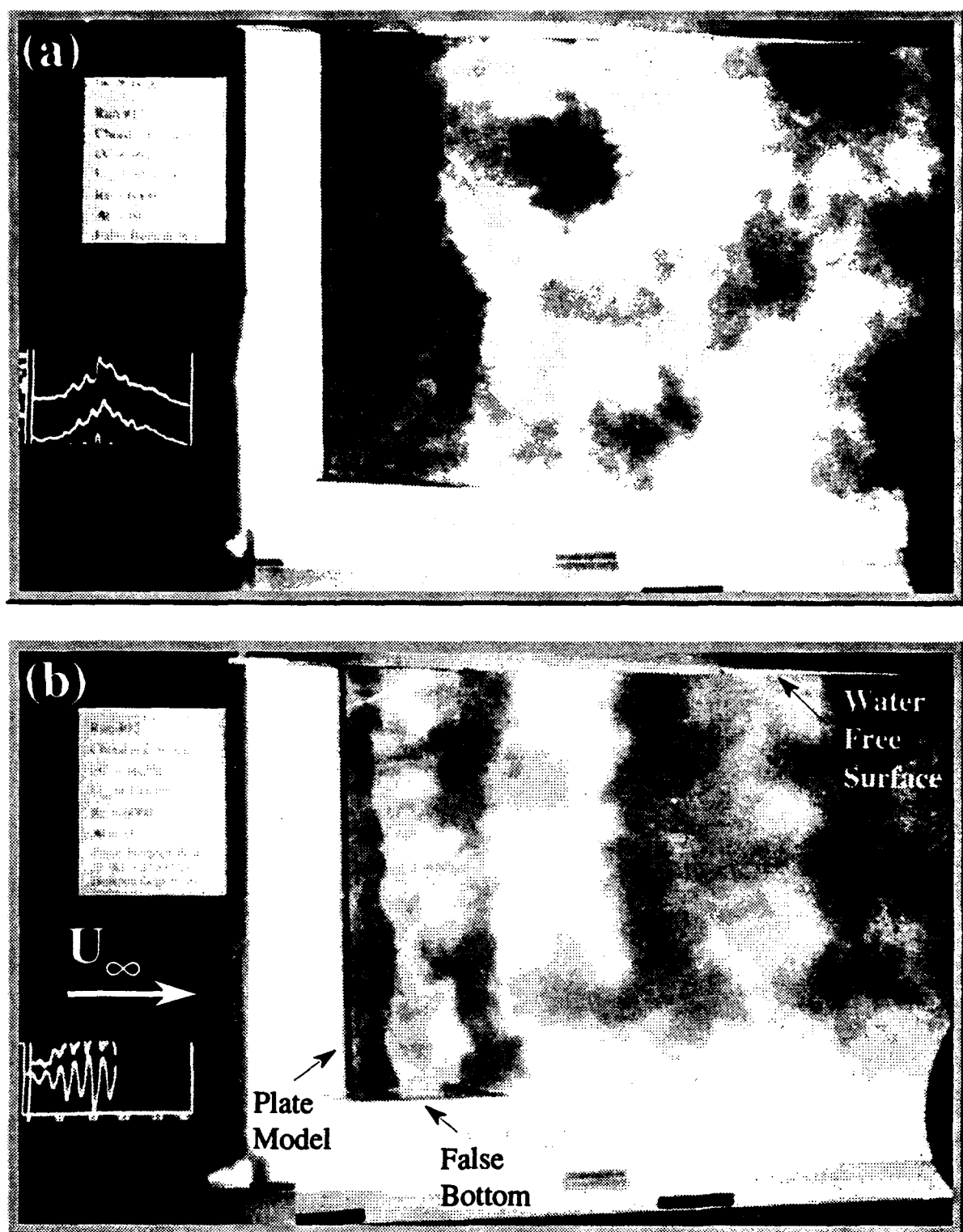


FIG. 4.21 Flow visualization results from free surface water tunnel . Flow is from left to right, $Re=6000$, two frames at different times during a single run. Frame (a) shows large formation region extent, with correspondingly low force and fluctuation levels (white traces). Note Kelvin-Helmholz shear layer vortices showing up as striations aligned with plate. Frame (b) has tighter vortex roll-up and correspondingly higher force levels

any vortex shedding which occurs lacks spanwise correlation to the point of decreasing the drag almost 40% and eliminating force fluctuations at the S_t frequency. One could postulate the existence of a 6C spanwise length scale, which would both give rise to a $6T_s$ periodicity in the force signals and also considerably affect results for aspect ratios less than several times this length (Schewe, 1983). Since eliminating extrinsic three-dimensionality is an experimental (and currently numerical) impossibility, the best that can be achieved experimentally is to increase the maximum aspect ratio that can be achieved and take pains to minimize other external influences and see if the limiting asymptote found here continues.

As a final indication of the variety to be found even within the same experimental run, Fig. 4.21 presents dye flow visualization images taken at two different times during the same run. Flow is from left to right, with the camera imaging the cross-stream (chordwise) plane. The white traces in the lower left corner are oscilloscope readings of the force balance load cells; most recent levels are on the right. The top two traces when added together are proportional to drag, their difference is moment, and the bottom trace gives lift (all three are not visible in either picture). The upper figure is at a low force/rms level, corresponding to a large formation distance and disorganized wake; striations aligned with the plate in the top picture are from the vortex sheet rolling up to form Kelvin-Helmholz vortices. The lower picture is at roughly that same point in the shedding cycle, but with a much tighter formation distance, a more organized wake structure, and considerably higher force/rms levels.

An important related question exists regarding the nature of a perfectly two-dimensional flow, with neither extrinsic nor intrinsic three-dimensionality. Such a flow is obtainable only in numerical simulation, which is the subject of the following chapter.

CHAPTER 5

Two-Dimensional Numerical Model Experiments

5.1 Preface

One of the earliest motivations for this investigation was the apparent disparity between experimental results and those obtained using a purely two-dimensional numerical model. This difference amounted to almost 60% in steady-state mean drag levels; the numerical simulation indicated levels of about $\overline{C_d} \approx 3.3$, vs. $\overline{C_d} \approx 2.0$ for experiments. Numerical simulations were initially carried out by Kiat Chua (Chua, 1990) using a vortex element code which included a novel method for treating the boundary layer flow and the surface boundary condition. This code was complex and required considerable computer resources, so run times and parameter investigations were restricted. Since only infinitesimally thin flat plate models were used, lift forces could not be obtained; and since only filtered results were available, a direct comparison to experimental results using a different filtering technique was difficult.

For these reasons a much simpler vortex element code developed by Phillippe Spalart (1983; 1988) was used to extend the previous numerical investigations to longer runs times, a wider range of parameters and varying plate thickness ratios. In addition, raw data filtering could now be accomplished in an exactly analogous way to the filtering used for the experiments, thus providing the best possible comparison. These results are not intended to be taken as state of the art in numerical simulation; they are instead an attempt to inexpensively obtain a "typical" two-dimensional vortex element simulation for as wide a range of parameters as possible. Although the comparison to other vortex element numerical calculations (and other two-dimensional models in general) is very good, results should be viewed as providing a good qualitative indication of trends and a somewhat less reliable indication of the quantitative values of force in a purely two-dimensional flow.

5.2 CFD Calculations

The numerical code used for the results presented here is a slightly modified version of "KPD1," a code that was developed by Phillippe Spalart for use in simulating a wide range of separating flows. The original code is described in detail in NASA TM 84328 (Spalart, 1983). The code was run on a CRAY X-MP/18 and a Y-MP2E/116 at Caltech's Jet Propulsion Laboratory.

Briefly, it is a vortex element code using vortex blobs which are being absorbed and re-emitted at control points around a body with each time step. The control points are determined from a user input description of the body geometry such as that shown in Fig. 5.1. Control points are established a distance R_o (roughly one vortex core diameter) from the surface, one for each node in the body description. Vortices which are inside these control points after a time step are eliminated, with new vorticity then being introduced at the control points to cancel the stream function at the wall. Time stepping was done using an Adams-Bashforth second-order scheme for the old vortices, and an explicit Euler first-order scheme for newly introduced vortices. Pairs of vortices were merged whenever a penalty function was below some tolerance, the tolerance being adjusted to roughly maintain the maximum desired number of vortices. In some versions of the original code (KPD2 and KPD3), provisions were made for the treatment of boundary layer separation, but such schemes were neither needed nor used for these experiments due to the well defined natural separation points (sharp edges).

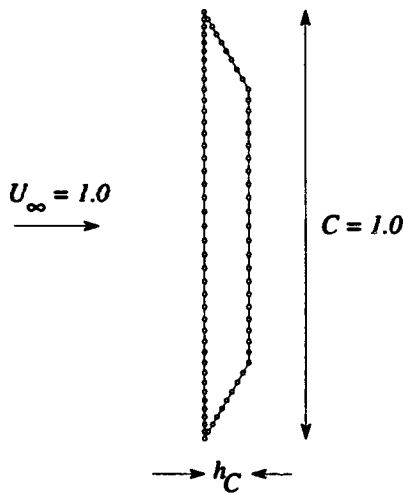


FIG. 5.1 Plate model using 80 node description; $\alpha = 90^\circ$; $h_C = 10.3\%$

Although some investigations were done to establish the influence of model parameters (Sec. 5.4), these were generally set to the values recommended by Spalart: Vortex core radius $\sigma = \Delta s / 4$; where Δs is the average node spacing ($\simeq 2/N_w$, N_w = the number of nodes used to describe the body). Distance $R_o = \Delta s / 2$; $N_v \simeq 1000$; $\Delta t = .02$ ($\Rightarrow |U_\infty| \Delta t / \Delta s \simeq 0.8$); and finally, the merging parameter $D0$ was set to 1.0.

The code was modified slightly to allow a non-impulsive linear increase to the final steady freestream velocity, with the user entering the time t_a in which to accomplish this increase. Additional body motion descriptors were added to the code, allowing mean and sinusoidal components in both X and Y directions, thus simulating the X-Y towing tank motion capabilities; these motions were added to those calculated to simulate a linear starting profile.

Finally, the ability to exponentially decrease vortex circulation Γ in time (Kiya, 1980) was added, the user inputting the time constant τ in the formula:

$$\Gamma_i(t) = \Gamma_{oi} \left(1 - \exp\left(\frac{-\tau}{Age_i}\right) \right),$$

where Age_i is the age of the i^{th} vortex ($= \Delta t \times n$), and Γ_{oi} is its initial circulation. When two vortices are merged, their age is set to their average age, and their circulation is set to the sum of their initial circulations reduced by the above exponential at that age. Further details and motivation for this calculation are left for Sec. 7.4.1.

The user was responsible for inputting a time step increment Δt , a freestream velocity U_∞ (including any angle of attack α), the acceleration time, a circulation decay time constant, any body motion parameters, the maximum desired number of vortices, and the body geometry (number of nodes and their x-y locations, Fig. 5.1).

Body shapes were chosen to exactly match those used in the X-Y towing tank ; nodes used to describe the geometry were spaced closer together near the beveled edges, the exact spacing being determined both by the number of nodes specified by the user and by the requirement that the minimum node spacing be no less than one half the maximum node spacing, as recommended by Spalart. The node spacing decreased linearly from maximum to minimum, with one node placed on the intersection of the bevel and the downstream face of the plate, and one on the tip of the plate. These requirements occasionally made it impossible for two plate models of different thickness to be represented with exactly the same number of nodes. Angle of attack simulations were done by inputting a different (rotated) model geometry for each value of α ; this was easier than rotating the freestream and then decomposing the resulting forces into the correct directions.

Filtering of the resulting data output was accomplished in non-dimensional frequency space in a way exactly analogous to the filtering used for experimental results (see Appendix A).

5.3 Typical CFD Result

Although the general form of the flow for an impulsively started infinitesimal plate has been known for some time (see for example, Kuwahara (1973)) few researchers have computed flows with finite thickness bodies. Results for a typical run of the present model at $\alpha = 90$ are shown in Fig. 5.2. Except where noted the model parameters used for these results are typical of those used for all the other results presented. Eighty nodes were used to model the plate, with $C = 1$, $U_\infty = 1.0$, $\alpha = 90$, $\Delta t = 0.02$, $N_v \simeq 1000$, $t_a^* = 1.31$ (so $t_a = 2.62$ and $N_a = 131$) and $h/C = 10.3$.

We see that after an initial peak during the acceleration, the drag falls to a low value of $C_d \simeq 0.9$ during the subsequent closed recirculating wake region. It remains at this level (with a few fluctuations) until the onset of shedding at $t^* \simeq 40$. This drag level is comparable to the theoretical free streamline value of

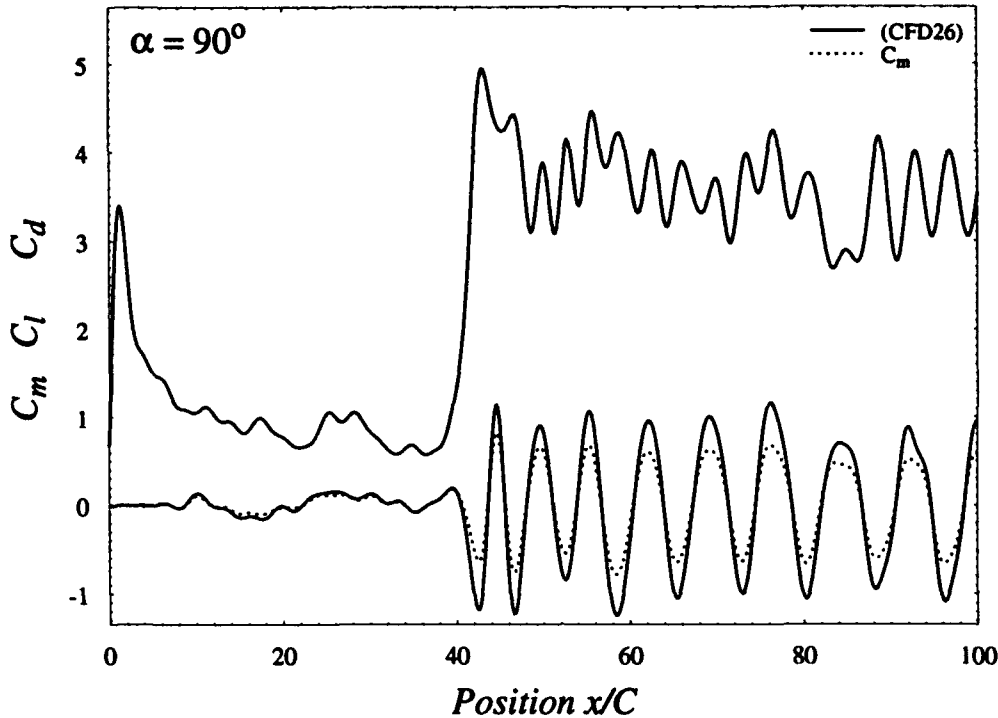


FIG. 5.2 Typical results for 80 node model $\alpha = 90^\circ$ with $C = 1$, $U_\infty = 1$, $N_v = 1000$, $\Delta t = 0.02$, $t_a^* = 1.31$, $h/C = 10.3\%$

$C_d = 0.88$ found by Kirchhoff for a normal flat plate with a separation velocity = U_∞ and $C_p = 0$ on the downstream face (see for example Lamb, 1932 pp. 100). Why this should be the case is not entirely clear. The mechanism proposed in Sec. 3.4, namely that the increasing circulation of the attached bubble induces an increased upstream flow against the rearward face of the plate resulting in higher base pressures, was in no way envisioned by the theoretical treatment, thus the similarity of the two levels may be coincidental.

The break down of this region and the transition to vortex shedding is accompanied by a steep increase in drag and an overshoot to peak values of $C_d \approx 5$ before a decrease to "steady-state" $\bar{C}_d \approx 3.3$. The first few shedding cycles have a considerably higher frequency than the final ones; later results will indicate that there is considerable variation; initial cycles can be either longer or shorter than steady-state values.

5.4 Model Parameters

A range of model parameters was investigated to establish their effects; some results are presented in Fig. 5.3. Although this type of code is not particularly conducive to time step convergence, a wide range of time steps were tried. Although initial peak height was affected slightly, there was no consistent trend, and $\Delta t = 0.02$ was chosen as being the most economical consistent with the recommendations of Spalart.

The primary effect of the other parameters investigated was to change the point at which the initial bubble breaks and vortices begin to shed, a transition which is known to be sensitive to small perturbations (Kuwahara, 1973). Until the sudden increase at the onset of shedding the drag histories follow almost identical

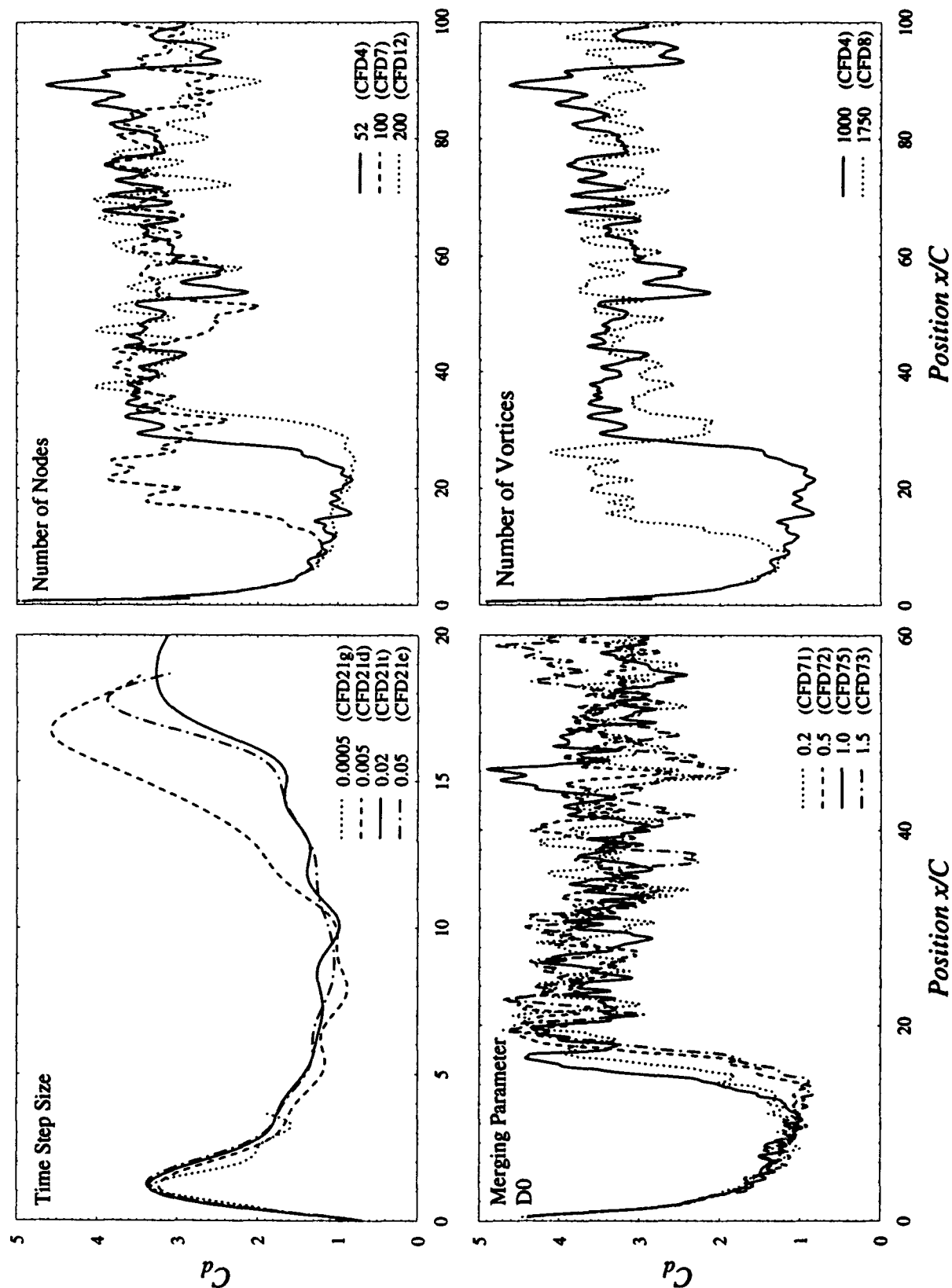


FIG. 5.3 C_d convergence with various model parameters. $\alpha = 90^\circ$; $t_a^* = 1.31$; $h/C = 6.8\%$

curves, indicating reasonable repeatability and convergence of the model in this range. After shedding begins little qualitative or quantitative change in *mean* force coefficients was noted over the range of parameters investigated.

For consistency between runs the number of nodes N_w was kept as close as possible to 80 (within ± 4), the number of vortices was set to 1000, and the merging parameter $D0$ was set to 1.0. This $D0$ value is somewhat larger than the value (5% of the body size) suggested by Spalart, but since the model in this case had its narrow dimension perpendicular to the flow, the wake region was of correspondingly larger extent, and a larger $D0$ tended to emphasize the wake vorticity at the expense of resolution close to the body (see Sec. 5.10).

5.5 Unfiltered Result

Since experimentally determined force histories proved too noisy to allow easy interpretation of unfiltered results, the less noisy unfiltered numerical result from Fig. 5.2 is shown in Fig. 5.4. Here we see the loss of detail which accompanies the filtering, in particular the smoothing of the peak and the sharp drop in drag at the end of the acceleration region. For $t_a^* = 1.31$ we expect (Sec. 3.4) an initial $C_{d_i} = \pi/4t_a^* = .6$; this would also be the decrease in C_d expected at the end of the acceleration, if the apparent mass was constant. The unfiltered result agrees reasonably well, giving a C_{d_i} result 13% higher than expected both initially and at the end of the acceleration.

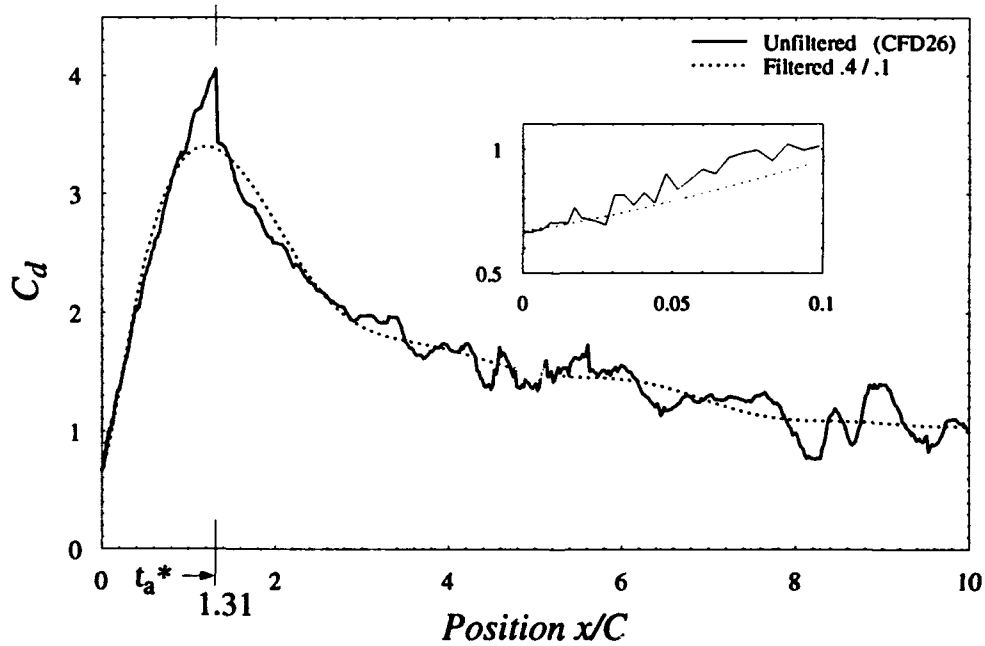


FIG. 5.4 Comparison of filtered ($f_{co}^* = .4$, $f_w^* = 0.1$) and unfiltered data. $\alpha = 90^\circ$; $t_a^* = 1.31$; $l/C = 10.3\%$

5.6 Angles of Attack

During the early startup regions the numerical flow model is very sensitive to small asymmetries, as can be seen from Fig. 5.5. A change of 0.1° to $\alpha = 89.9^\circ$ shifts the onset point of vortex shedding from $t^* = 40$ to $t^* = 15$, with less dramatic but similar shifts for increasing asymmetry.

The initial force peak and final steady-state shedding are not noticeably affected by such small changes in α ; but, accompanying a decreased onset time, the minimum level to which C_d falls following the acceleration consistently increases with increasing asymmetry. Note the difference between these cases, for geometrically imposed initial asymmetries, and the cases presented previously for various model parameter changes, in which the drag *prior* to shedding followed almost identical (Kirchhoff level) curves even though the onset time varied.

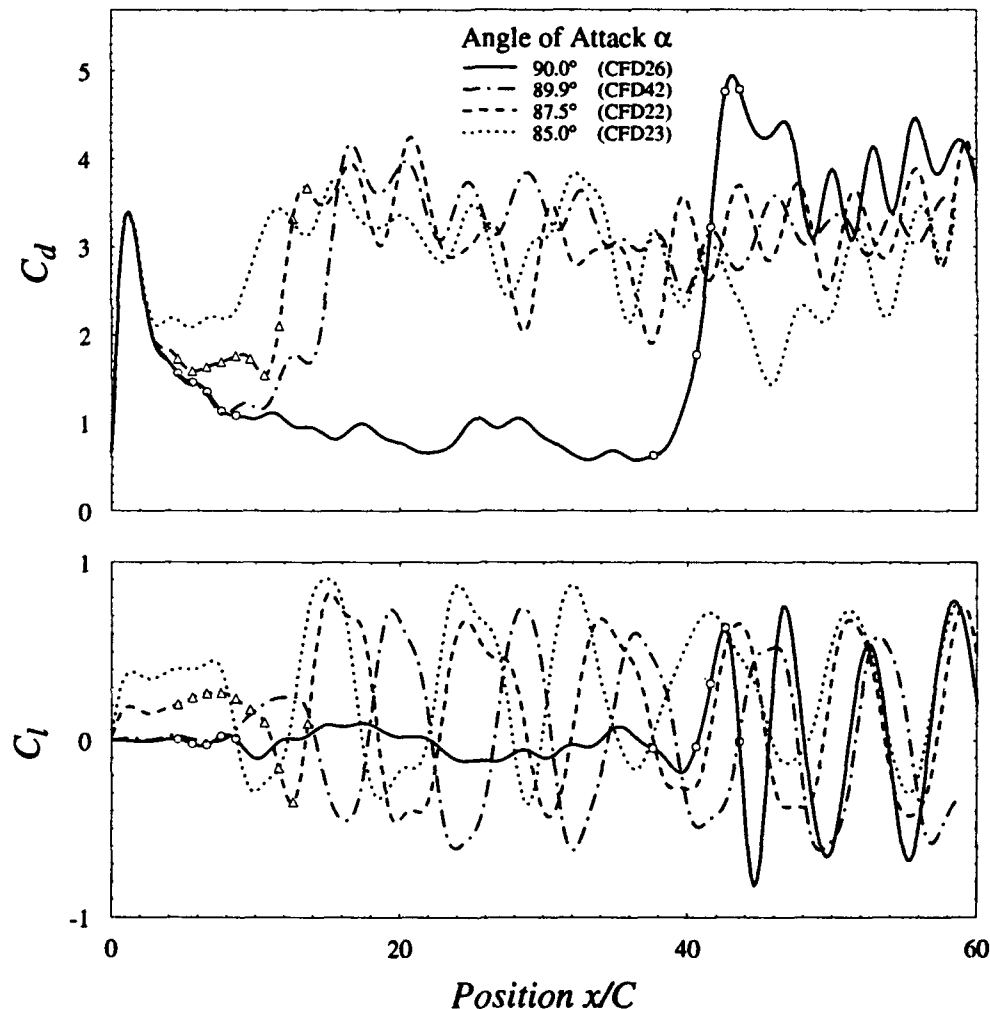


FIG. 5.5 Effects of small angle of attack variations. $t_a^* = 1.31$; $h/C = 10.3\%$; Solid Line: $\alpha = 90^\circ$; Chain Dashed Line: $\alpha = 89.9^\circ$; Dashed Line: $\alpha = 87.5^\circ$; Dotted Line: $\alpha = 85^\circ$. Open symbols denote flow visualizations shown in Fig. 5.6 and Fig. 5.7

C_l levels for various α are roughly twice what one would expect by taking a simple geometrical projection of the base pressure profile (drag), indicative of the effects of bevels. In all but the $\alpha = 90^\circ$ case the first shedding cycle is preceded by a slight increase in C_l , followed by a sharp negative C_l peak accompanying the sudden drag increase, indicating that the lower vortex is the first to be shed, as would be expected for $\alpha < 90^\circ$.

It is not clear if the increase in the minimum post-acceleration C_d level from $\overline{C_d} = 0.9$ is associated purely with increased global asymmetry of the starting bubble, if the earlier onset of shedding and its corresponding drag increase simply "runs into" the tail end of the acceleration region, or if there is a fundamentally different mechanism imposed on the global flow. Put another way, if the onset of shedding in the $\alpha = 87.5^\circ$ case (for example) were not to occur until $t^* \approx 40$, would the drag follow the same ($\overline{C_d} = 0.9$) curve that it follows in the $\alpha = 90^\circ$ case, or would it follow some curve with a higher mean drag level? If it does follow a higher curve, what is it that increases the drag from $\overline{C_d} = 0.9$?

Answering these questions is complicated considerably by the fact that the onset of shedding occurs progressively earlier in the motion with increasing asymmetry, leaving correspondingly less low drag region to analyze. Fig. 5.5 gives the impression that prior to shedding the drag does indeed follow some higher minimum curve, but it is very difficult to tell if this higher level is perhaps due only to the increasing proximity of shedding onset. Were the actual shedding transition to occur over a greater distance with increasing asymmetry, the minimum level would be increased at an earlier time; the fact that the degree of drag overshoot at shedding onset consistently decreases with increased asymmetry would tend to support this argument of a "gentler" and longer lasting transition. This then would indicate that were the shedding delayed, the minimum drag level would fall to the $\overline{C_d} = 0.9$ value.

On the other hand, the differences in the minimum C_d levels are not much greater than the fluctuations which are seen in the Kirchhoff level for $\alpha = 90^\circ$. These fluctuations will be shown to be a result of small oscillations in the position of the starting vortex pair, these oscillations being driven by a wake instability. It apparently does not take very much asymmetry in the vortex configuration to result in a large change in drag level, so the increased minimum level may be a result of the initial geometrically imposed asymmetry. In this case, were shedding delayed (without a change in the asymmetric vortex configuration), the drag would tend to follow some higher curve whose level would be determined by the degree of asymmetry.

Fig. 5.5 does not rule out a third possibility: that the initial asymmetry and/or shedding onset differences are insufficient to account for the higher minimum drag, and that it is the result of some other process imposed on the mean ($\overline{C_d} = 0.9$) flow. In this case, as in the previous one, were shedding delayed the drag would tend to follow some higher curve.

Some additional information is available; Fig. 5.6 shows vortex position flow visualizations at simultaneous times (open symbols in Fig. 5.5) for both the $\alpha = 90^\circ$ and $\alpha = 87.5^\circ$ cases. In these plots the area

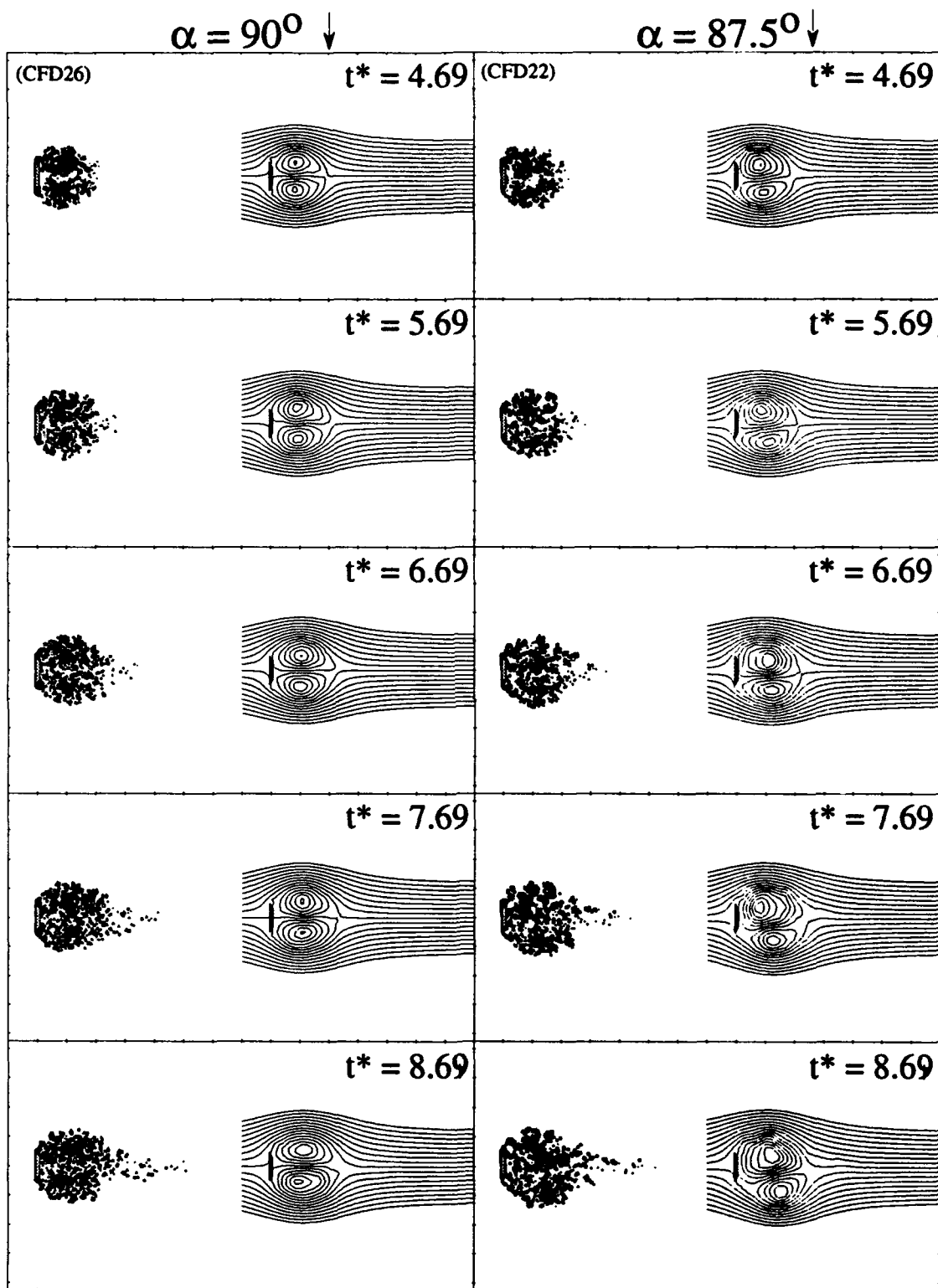


FIG. 5.6 Effect of angle of attack on shedding onset. Left column: $\alpha = 90^\circ$. Right column: $\alpha = 87.5^\circ$. $t_a^* = 1.31$, $h/C = 10.3\%$, α and t^* as noted; force histories shown in Fig. 5.5. Symbols are vortex positions, symbol area denoting circulation; stream function contours are given for comparison

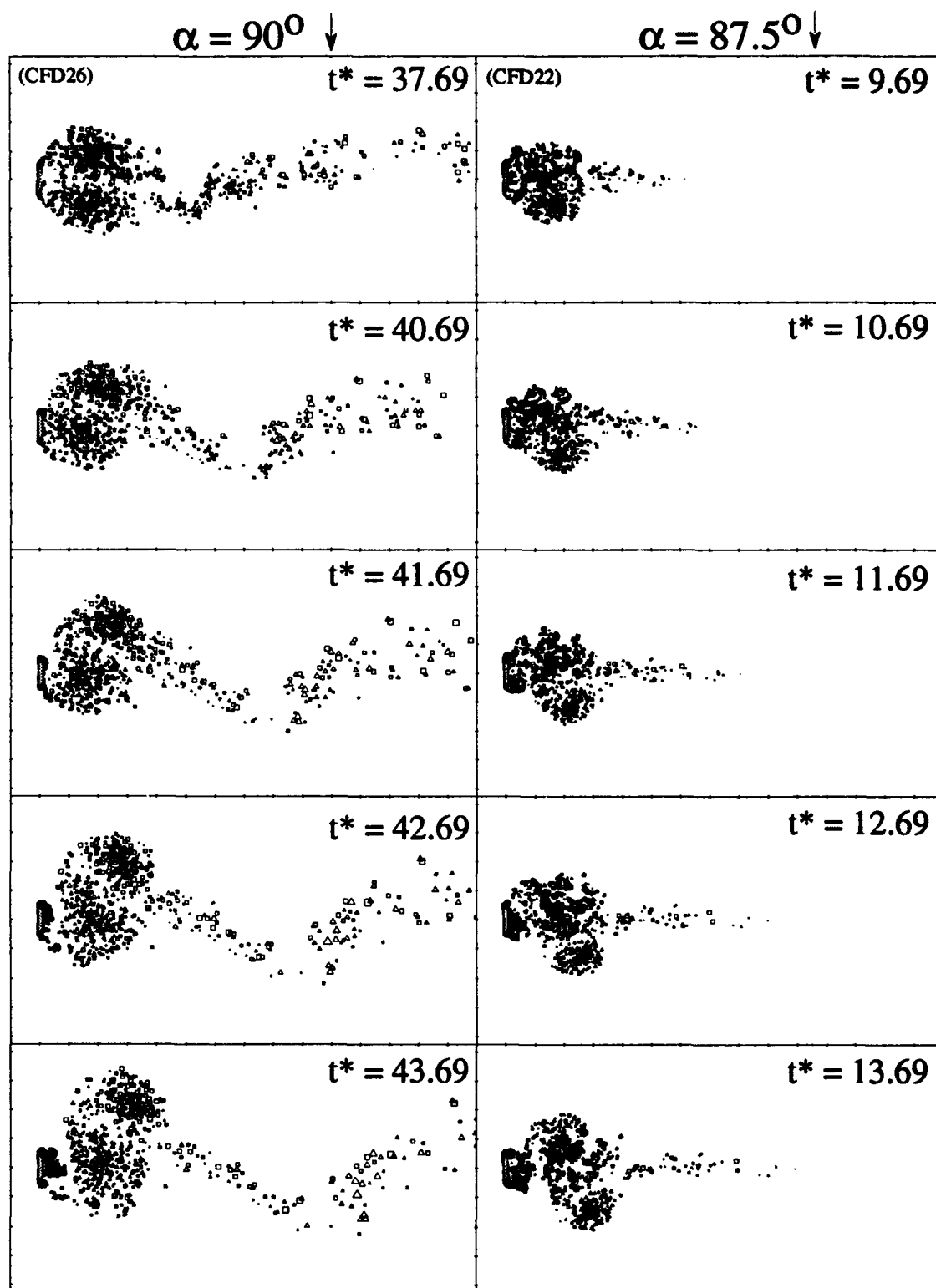


FIG. 5.7 Effect of angle of attack on shedding onset - continued from Fig. 5.6; note shift in time for $\alpha = 90^\circ$.
 $t_a^* = 1.31$, $h/C = 10.3\%$, α and t^* as noted; force histories shown in Fig. 5.5

of the symbols representing vortices is proportional to their circulation, with triangles and squares denoting positive and negative vorticity respectively; iso-streamfunction contours are also given for comparison.

At early time ($t^* < 8$) the shape of the starting bubbles in both cases appear remarkably similar; outwardly very little exists to suggest that at $t^* = 8.69$ the value of $C_d \approx 1.8$ for $\alpha = 87.5^\circ$ is almost twice that seen in the $\alpha = 90^\circ$ case. Externally, aside from a slight asymmetry of the bubble itself, the only noticeable difference is that the shear layer in the $\alpha = 87.5^\circ$ case appears somewhat more unstable. The upper shear layer in particular seems to have more large scale structure than the $\alpha = 90^\circ$ case. Note, however, that although the external shape is symmetric, internal to the bubble the upper vortex core is considerably closer to the plate, as can easily be seen from the streamfunction; this may account at least in part for the increased shear layer instability and the significantly higher drag.

With a bevel angle of 30° on the downstream face of the plate, the upper bevel is more nearly aligned with the flow (and more nearly perpendicular to the lift direction); this may give an additional geometrical reason for the increased instability of the upper shear layer, and also would explain the higher than expected lift; although what part of the drag increase may be due directly to the increased Reynolds stresses in the upper shear layer itself is not yet clear. This vortex asymmetry and increased upper shear layer instability at $\alpha = 87.5^\circ$ is not confined to this case, and can be seen quite clearly in a comparison of Fig. 5.22 and Fig. 5.24, which will be presented later.

Further flow visualization results taken throughout the shedding transition are given in Fig. 5.7. The results shown for $\alpha = 87.5^\circ$ are a continuation of those in Fig. 5.6, but 29 chord lengths have elapsed in the data shown for $\alpha = 90^\circ$. In both cases, the first row is at a time immediately prior to the sharp increase in C_d associated with the transition to shedding; at $\alpha = 90^\circ$ this occurs at $t^* = 39$, while at $\alpha = 87.5^\circ$ it occurs much earlier at $t^* = 11$. The middle row, at $t^* = 43$ and 13 respectively, represents the peak drag level immediately after onset. Note that a couple of times have been left out of the $\alpha = 90^\circ$ results to synchronize them with $\alpha = 87.5^\circ$.

The most obvious difference between these cases is that C_d increases from ≈ 0.8 to ≈ 5.0 between the first and third frames for $\alpha = 90^\circ$, while at $\alpha = 87.5^\circ$ the initial drag is *higher* ($C_d = 1.7$) and the final drag is considerably lower ($C_d = 3.7$) for the same three frames.

Considering first the $\alpha = 90^\circ$ case, the force fluctuations in the low drag $\overline{C_d} = 0.9$ region are apparently caused by cross-stream oscillations of the initially symmetric bubble (which have also been seen experimentally, for example by Sarpkaya and Ihrig, 1986) which is possibly being forced by the wake instability present in vorticity which has "leaked" into the far wake. In the first frame the upper vortex is slightly lower than for an exactly symmetric condition, while in the second frame it has shifted upward beyond the edge of the plate. This is the final fluctuation to occur before shedding, the breaking and subsequent rollup of the upper vortex sheet has begun in frame two and it continues rolling up tightly behind the plate, inducing

the peak drag and positive lift at the time of frame three. Subsequent frames show the breaking of the lower vortex sheet and the start of its roll up (frame five), which induces a negative peak in C_l . Note the much higher Strouhal number for the first several shedding cycles in this case.

At $\alpha = 87.5^\circ$ the situation is somewhat different; so much earlier in the motion there is less vorticity in the wake, the C_d level in the first frame is considerably higher (double), the upper shear layer is more unstable, and the upper vortex is smaller and closer to the plate than at a corresponding time for $\alpha = 90^\circ$. Despite this increased upper instability the lower shear layer/vortex is geometrically encouraged to be the first to shed, so that the lower vortex sheet is the first to break and roll up, as indicated by the initial negative excursion in C_l at $t^* = 11.69$. This initial roll up is not as tight as in the $\alpha = 90^\circ$ case; it seems that the larger amount of opposite sign wake vorticity directly behind the plate in the third frame at $\alpha = 90^\circ$ forces the initial vortex sheet roll up to be tighter behind the plate than at $\alpha = 87.5^\circ$, resulting in the much larger drag overshoot.

One would expect that if the increased minimum drag level at $\alpha = 87.5^\circ$ is primarily due to the upper shear layer being more unstable and having more structure (higher Reynolds stresses), and that if this instability is generated at least in part by finite plate thickness, then changing the thickness ratio at a fixed α may have a consistent effect on both the minimum level of drag and the final shedding transition time.

5.7 Plate Thickness

The numerical model used here was not able to do a zero thickness plate; in fact for h/C less than about 4% marked changes in the time averaged pressure coefficient distribution on the upstream face of the plate began to appear, indicating that some unwanted downstream influence was being felt on the upstream face due to the extreme fineness in the streamwise direction. For this reason $h/C = 4\%$ is the minimum thickness that will be presented.

The most obvious affect of increasing h/C is the increased rms level of the C_l fluctuations, as can be seen from Fig. 5.8. C_l rms is almost directly proportional to h/C for the three thinnest plates, from C_l rms = .18 at $h/C = 4\%$ to C_l rms = .42 at $h/C = 10.33\%$; indicating that the primary near wake flow is not altered significantly. At $h/C = 20\%$ however, the increase in C_l rms is lower; perhaps indicative of a large scale change in the near wake structure.

Based purely on base pressure, for a plate with $h/C = 20\%$ we would expect a C_l fluctuation of roughly 20% of \bar{C}_d ; actual results indicate 25 to 35% fluctuation levels; as noted above this is perhaps indicative of the influence of the bevels and the slight angle of attack. Although the onset time may vary, shedding in all these cases begins with an initial negative excursion in C_l accompanying the sudden drag rise, indicating that the lower vortex is the first to be shed.

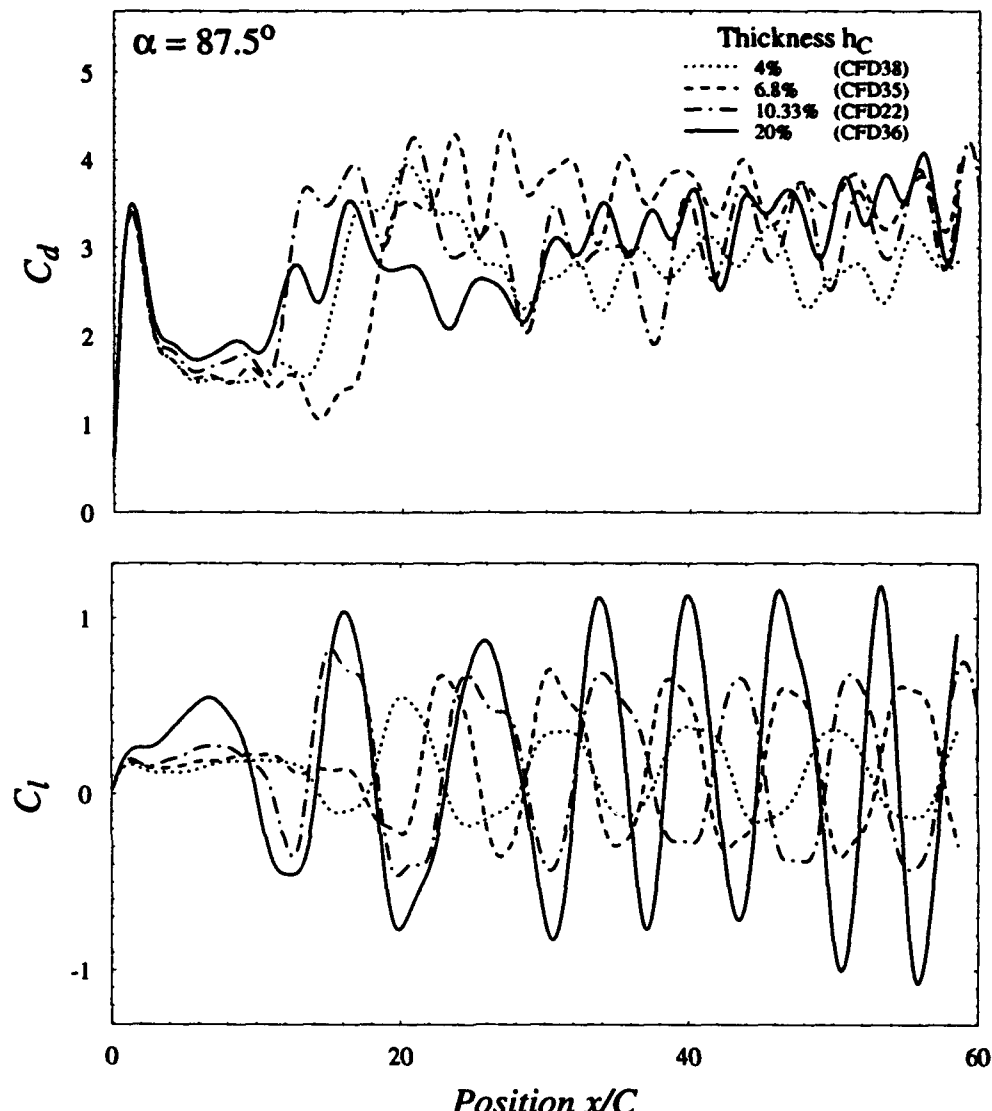


FIG. 5.8 Effects of plate thickness. $\alpha = 87.5^\circ$; $t_a^* = 1.31$; Solid Line: $h/C = 20\%$, $C_l \text{ rms} = .60$; Chain Line: $h/C = 10.33\%$, $C_l \text{ rms} = .42$; Dashed Line: $h/C = 6.8\%$, $C_l \text{ rms} = .30$; Dotted Line: $h/C = 4\%$, $C_l \text{ rms} = .18$

Several other runs at intermediate thickness which were performed (although they are not shown) indicate there is a slight propensity for a decreased time to shedding and increased minimum drag as h/C is increased. However, from the runs that are shown, this is obviously not a consistent change. As has been suggested in the literature, increasing the thickness, at least up to a point, essentially moves the downstream face of the plate closer to the (low pressure) vortex cores, thus increasing the drag in the initial symmetric region even with no change in the global flow. Why the shedding would begin earlier with increased h/C is not clear, although one could imagine the proximity of the downstream face to the vortex core region could be a destabilizing influence and result in increased asymmetry.

It appears, due to the lack of consistent changes due to thickness, that the greater instability of the upper shear layer is *not* a direct influence on the increased minimum drag. However with beveled edges, very close to the tip the shear layers see an identical geometry regardless of thickness, so the lack of effect for these cases is perhaps not surprising.

5.8 Acceleration Profiles

Results using a $h/C = 6.8\%$ thick plate, chosen to match the one used for the various experimental acceleration profiles, are shown for several different acceleration times in Fig. 5.9.

For the $\alpha = 90^\circ$ case there is no consistent change in the location of the shedding onset or the degree of overshoot. Since the initial flow is geometrically symmetric all of the curves drop to roughly the same post-acceleration level before shedding begins, except in the case of $t_a^* = 20$, where the end of the acceleration and the onset of shedding coincide. The small expanded scale inset indicates that the C_{d_i} level is consistently about 15% higher than the theoretical values, which are $C_{d_i} = 0.6, 0.16$ and $.04$ for $t_a^* = 1.31, 5$ and 20 , respectively. Of the four runs shown for $\alpha = 90^\circ$, two of the initial lift peaks are positive and two are negative, indicating that the initial vortex to be shed is arbitrary with a symmetric geometry.

The $\alpha = 87.5$ case shows some disagreement in the post-acceleration pre-shedding region, although there does appear to be some correlation between shedding onset and t_a^* in this case, other runs with intermediate values of t_a^* (which are not shown) do not support this conclusion.

The impulsively started $t_a^* = 0$ case has a considerably later shedding onset and lower minimum drag than any of the other cases. This is an anomalous result; notice that although there is a slight decrease in lift immediately prior to the onset of shedding, the actual lift peak (during the time when drag is increasing sharply) is *positive*; the opposite of all the other $\alpha = 87.5^\circ$ cases studied. This indicates that despite the $\alpha = 87.5^\circ$ angle of the plate, the *upper* vortex is in fact the first to shed in this case. This has been confirmed by flow visualization (Fig. 5.10), which indicates that a loss of vorticity from the upper vortex into the far wake at about $t^* = 16$ (which can be seen to roll up in later frames), allowed the lower vortex to move more directly behind the plate (indicated by the initial drop in C_l), allowing the (already unstable) upper vortex sheet to break and roll up at about $t^* = 20$. The loss of vorticity from the upper vortex may have been a result of an oscillation of the entire bubble due to instabilities in the far wake; this oscillation offsetting the geometrical asymmetry and resulting in a temporarily symmetric, low drag flow. Note the much lower drag overshoot and the much longer shedding period associated with first few shedding cycles; indicative of the flow taking considerable time to recover from this anomalous beginning.

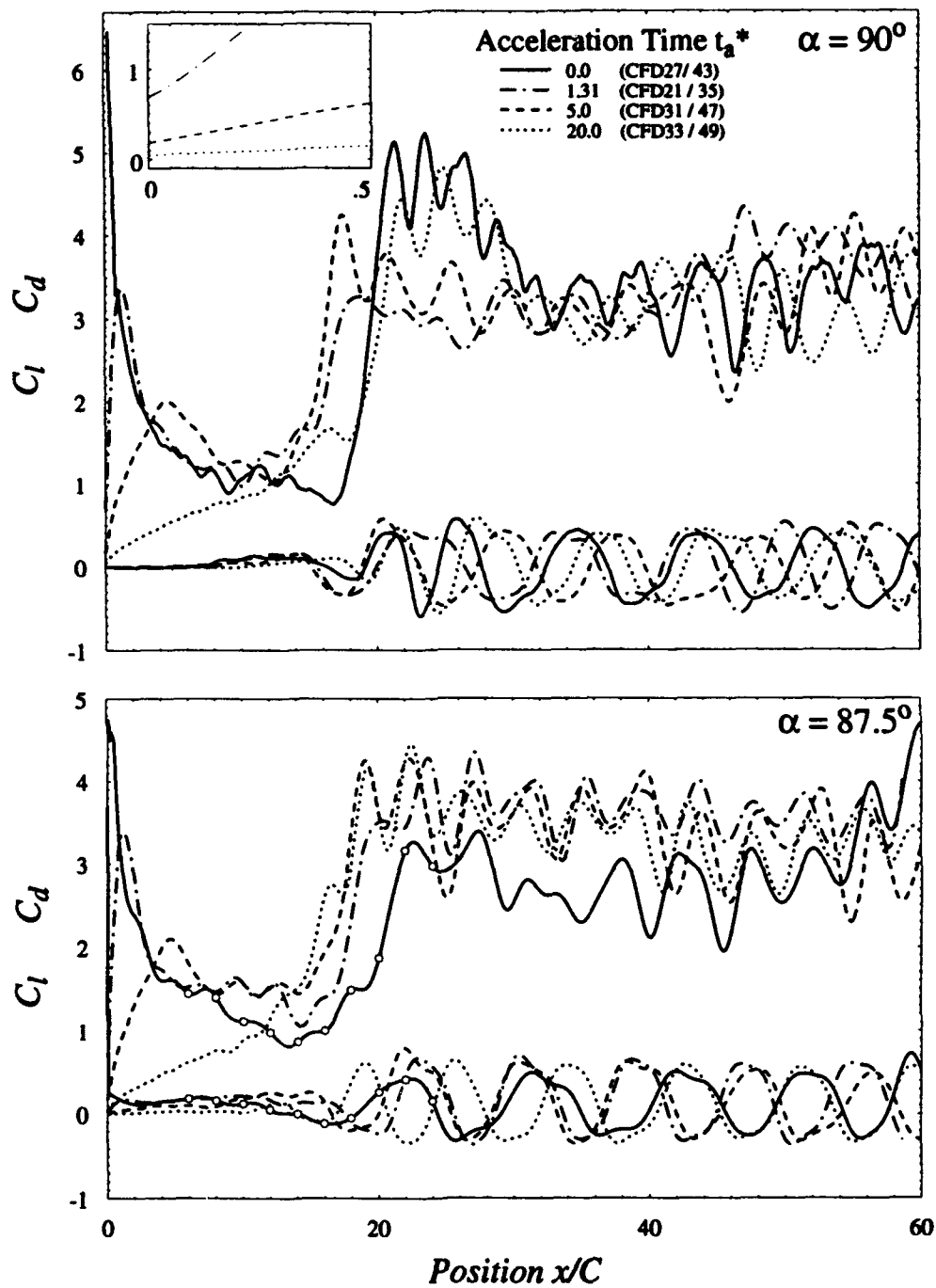


FIG. 5.9 Non-dimensional acceleration times. $h/C = 6.8\%$; Solid Line: $t_a^* = 0.0$; Chain Dotted Line: $t_a^* = 1.31$; Dashed Line: $t_a^* = 5.0$; Dotted Line: $t_a^* = 20.0$

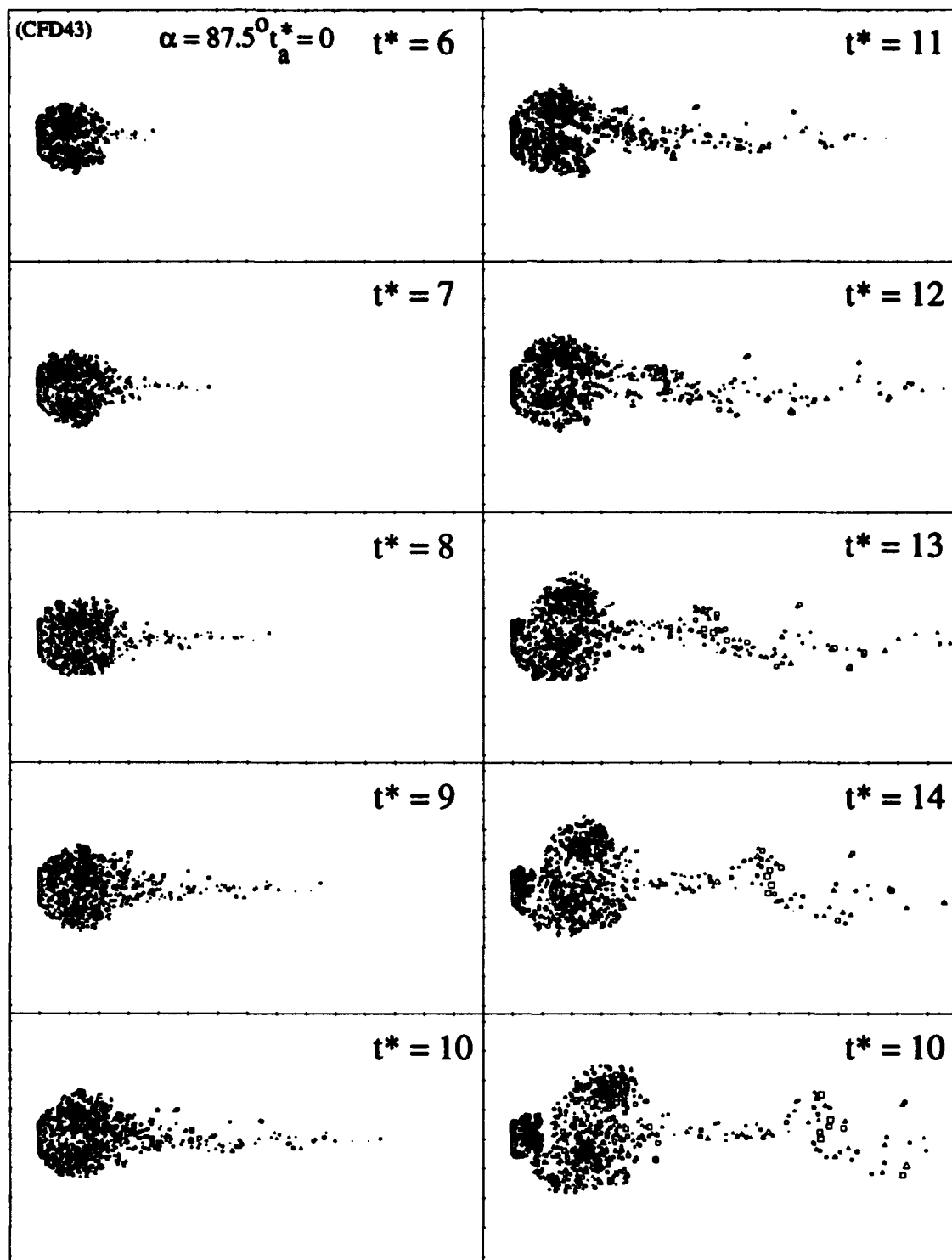


FIG. 5.10 Shedding onset at $\alpha = 87.5^\circ$ with a low drag post-acceleration region. $t_a^* = 0.0$, $I/C = 6.8\%$, t^* as noted; force histories are shown in Fig. 5.9

5.9 Circulation Decay

The title of this section was chosen to encourage some skepticism about the physical validity, or at least physical interpretation, of the method of vortex decay described herein.

It has been thought in the past that two-dimensional vortex element models lacked sufficient mixing in the near wake, and thus did not cancel enough opposite-sign vorticity, and thus over-estimated the steady-state drag level relative to experiments. Several schemes to improve the mixing have been proposed, including imposing a random walk in space on the vortices with each time step; or simply decaying vortex strength with time.

In a 1980 paper, Kiya and Arie presented the results of a very simple two-dimensional vortex model of the flow about a nearly normal flat plate; to simulate the cancellation of vorticity in the near wake they exponentially reduced the strength of the shed vortices as a function of their age. Both the force coefficient and flow visualization results presented by Kiya (Fig. 5.11) are remarkable in their similarity to the experimental results of Ch. 3. For this reason a similar scheme was attempted on this code, to see if equivalent results would be obtained.

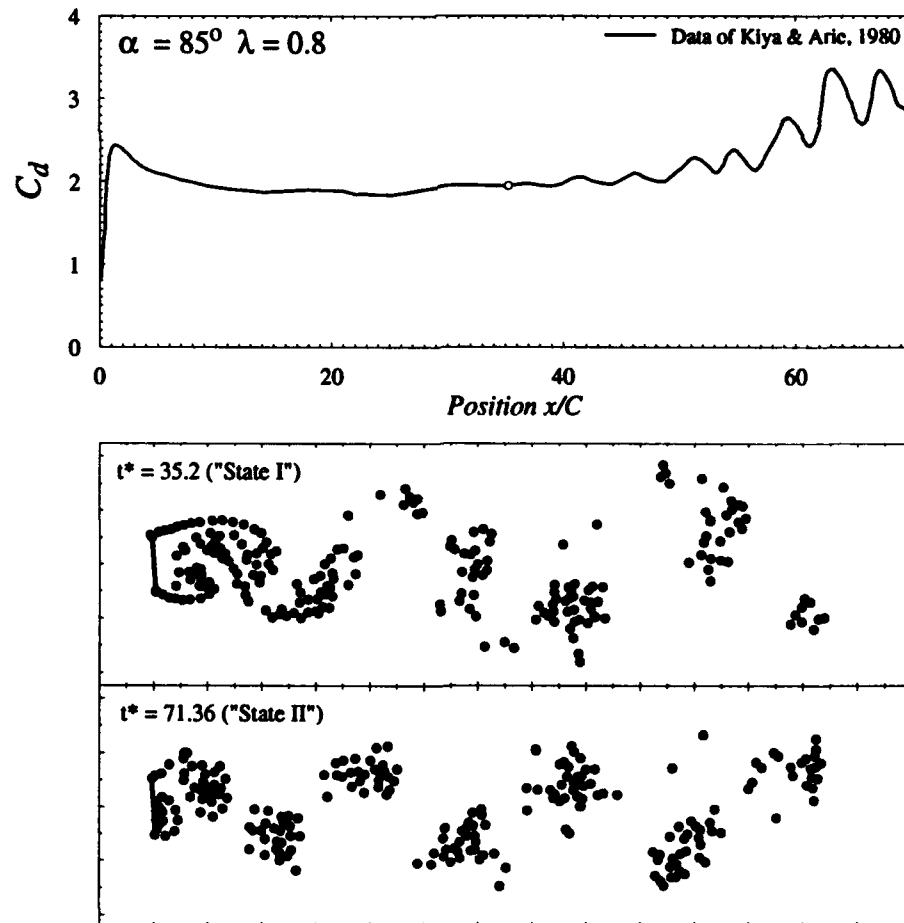


FIG. 5.11 Data from Kiya and Arie, 1980. $\alpha = 85^\circ$; $\lambda = 0.8$

Following Kiya (and many others), we introduce an exponential decay of vorticity:

$$\Gamma_i(t) = \Gamma_{oi} \left(1 - \exp \left(\frac{-\tau}{Age_i} \right) \right).$$

Arguments can be made about the physical interpretation of the decay time constant τ (typically relating it to some form of Reynolds number), but here we simply continue Kiya's development and introduce a related parameter λ :

$$\lambda = \frac{1}{N_s} \sum_{i=1}^{N_s} \left(1 - \exp \left(\frac{-\tau}{i\Delta t} \right) \right).$$

We can think of λ as the amount of circulation (vorticity) remaining in each shed vortex at the end of some number of steps N_s , where N_s is typically taken to be the number of time steps per Strouhal shedding period: $N_s = T_s/\Delta t$; here we take $T_s = 1/.15 = 0.67$. Given some desired value of λ , we can numerically solve the above equation for the required τ . Parameters such as λ or τ are typically chosen so that some simulation result matches one which has been experimentally determined.

The physical interpretation of such a scheme is somewhat unclear; it is certain that no physical process results in a direct decay of one sign of vorticity at anything like the rates used to simulate mixing of opposite signs. Since we are in effect imposing an arbitrary time scale τ on the flow; the (decayed) vorticity distribution in the wake is likely to differ significantly from the experimental result. There is also a deeper philosophical argument about the expediency of forcing a purely two-dimensional model to "correctly" simulate an inherently three-dimensional flow by introducing parameters which have a large influence on the model, have no clear physical counterpart, and which are essentially chosen so as to match the results which we wish to match.

Having said this, Fig. 5.12 indicates that λ can indeed be chosen to provide somewhat better qualitative agreement with experiments. Decreasing λ increases the initial low drag level and decreases the mean \bar{C}_d after shedding begins. Although the point at which shedding starts seems to be about the same regardless of λ , the onset occurs over a much greater distance. The initial peak height is increased somewhat for $\lambda < 0$, although at the same time the width of the initial peak is increased, so the change in peak level may be an effect of filtering acting on a longer initial region. The rms level of C_l and C_d decreases with decreasing λ , to the point that it is very hard to distinguish the start of shedding with $\lambda = 0.8$; at this λ the forces remain almost constant at $C_d = 2.4$. A value $\lambda = 0.86$ seems to provide about the best qualitative agreement to experimental results.

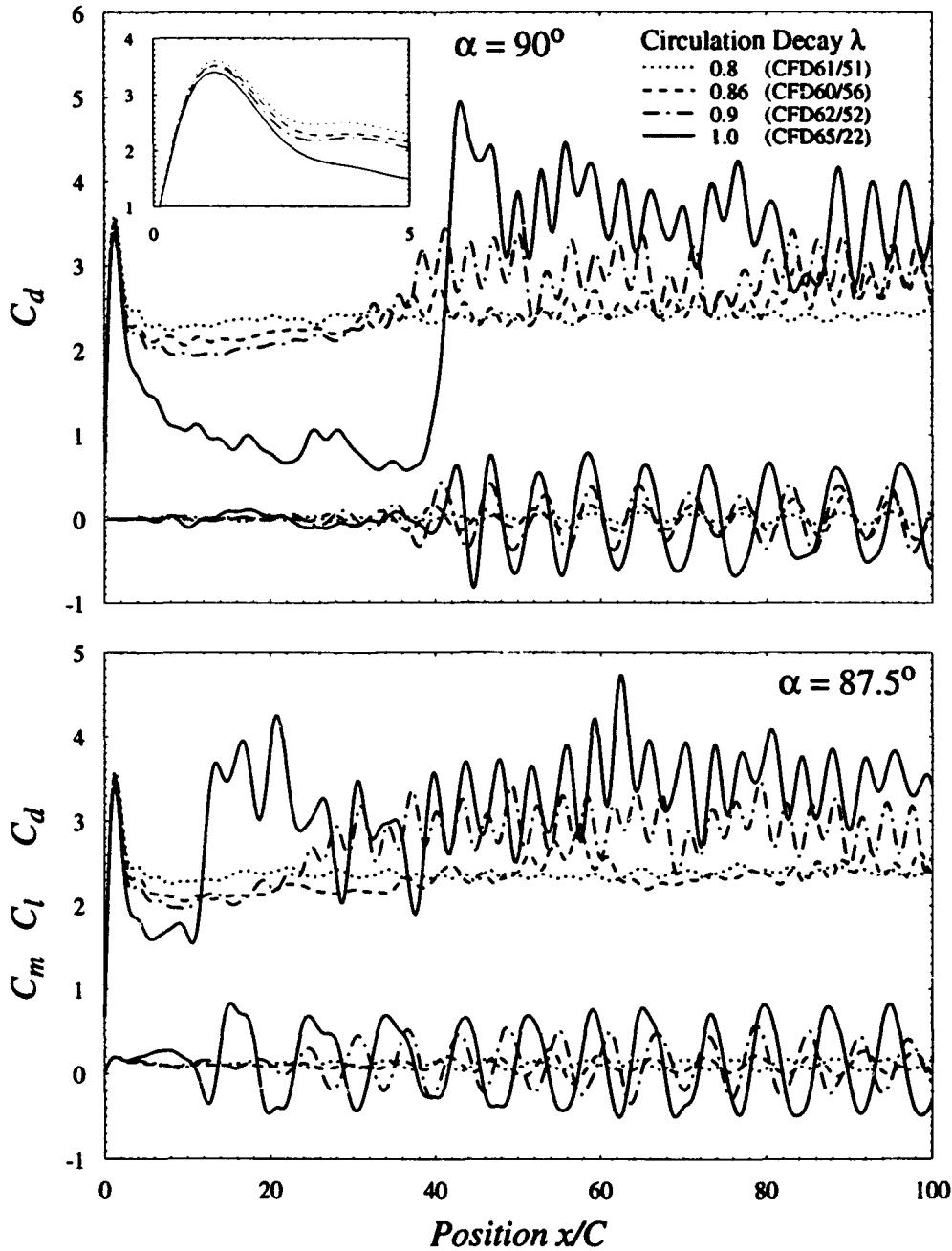


FIG. 5.12 Effects of circulation decay parameter λ ; α as noted; $t^* = 1.31$; $h/C = 10.3\%$; Solid Line: $\lambda = 1.0$; Chain Line: $\lambda = 0.9$; Dashed Line: $\lambda = 0.86$; Dotted Line: $\lambda = 0.8$

Fig. 5.13 gives vortex position and stream function flow visualizations at $t^* = 18.69$ (in the initial symmetric region) for the four values of λ of Fig. 5.12. For $\lambda = 1.0$ (no decay) the wake is very symmetric, the shear layers leave the plate at a steep angle to the freestream, and there is little evidence of any wake instability in the vorticity which has left the symmetric bubble and been convected downstream. Decreasing

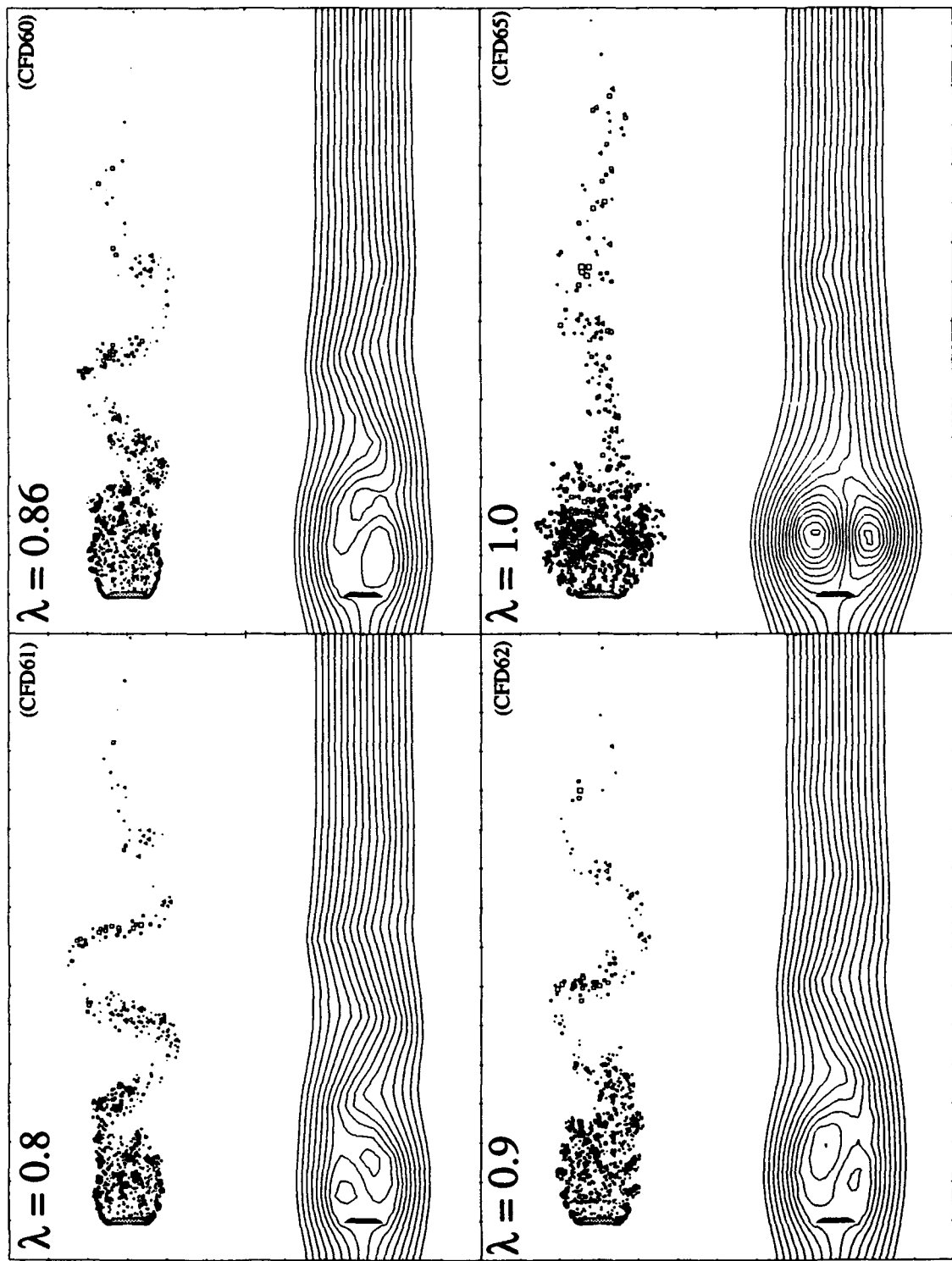


FIG. 5.13 Effect of circulation decay λ at $t^* = 18.69$. $\alpha = 90^\circ$, $t_a^* = 1.31$, $l/C = 10.3\%$, λ as noted

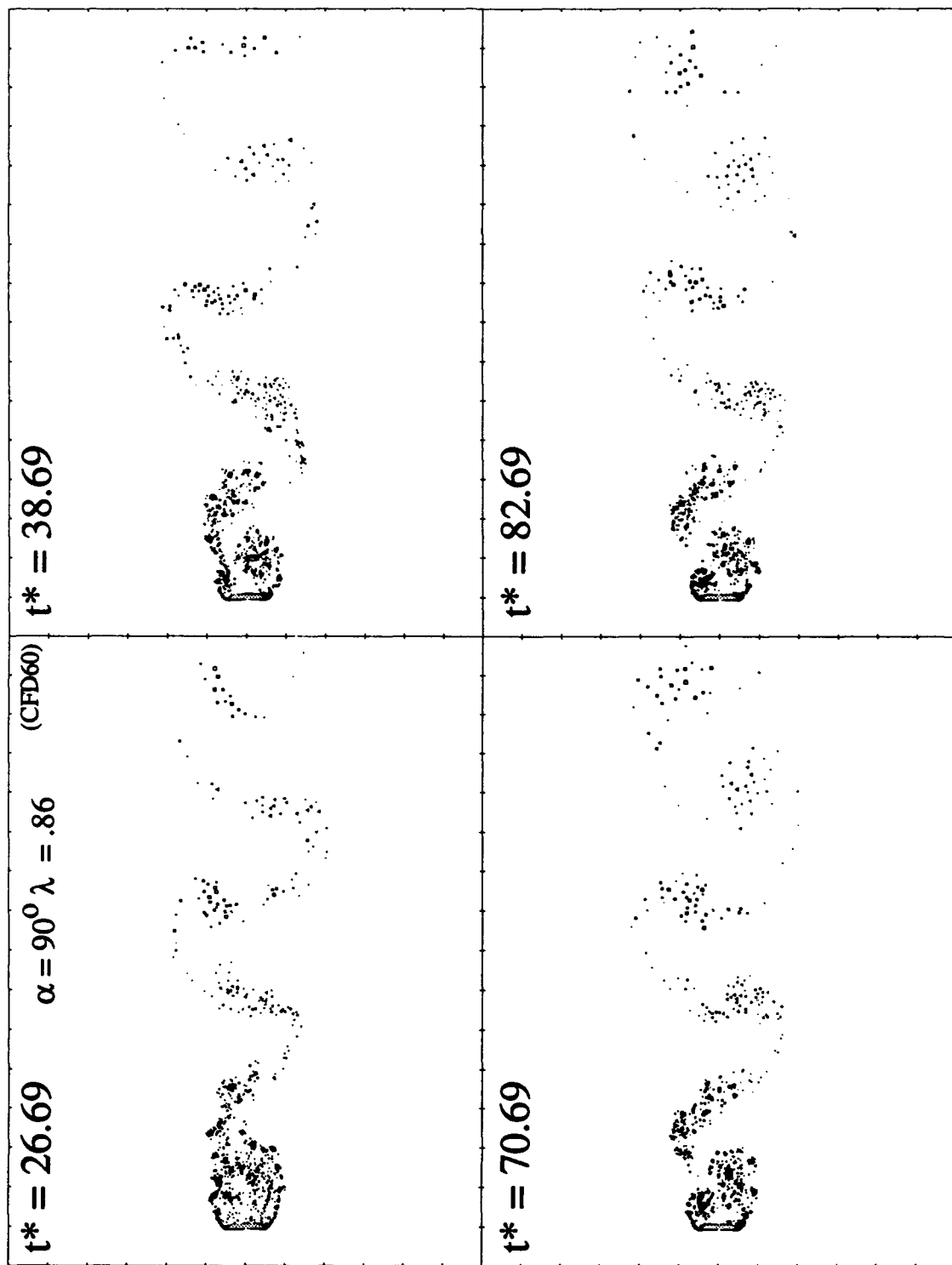


FIG. 5.14 Shedding at different times (at \approx same phase) for $\lambda = 0.86$. $\alpha = 90^\circ$; $t_a^* = 1.31$; $HC = 10.3\%$; t^* as noted

λ initially results in a longer and considerably narrower formation region - the shear layers leave the body at a shallower angle to the freestream. The vorticity in the far wake is more unstable, with the instability affecting the symmetry of the formation region; further decreasing λ tends to shorten this region, although the phase remains about the same.

There is considerably more structure in the shear layers, a Kelvin-Helmholz like rollup is easily distinguishable in the $\lambda = 0.86$ and $\lambda = 0.8$ plots; leading to the speculation that the increased drag associated with decreased λ is at least in part due to the higher Reynolds stresses in these cases; the $\alpha = 87.5^\circ$ results however show even more structure for these λ , but have almost the same drag levels - indicating that the increased Reynolds stresses have little direct effect.

It is also possible that the increased wake instability may affect the formation region itself, resulting in a much earlier transition to an asymmetric high-drag regime. The instability moves slowly upstream until near wake roll-up and true vortex shedding begin at roughly the same time as in the $\lambda = 1.0$ case, but without the long lasting initial symmetry typical of that case. A time sequence of flow visualizations for $\lambda = 0.86$ is shown in Fig. 5.14; each of these plots is at roughly the same phase of shedding, as determined from force results. This sequence shows the transition from a low drag/large formation region at $t^* = 26.69$ to the tighter rollup and higher drag levels of $t^* = 82.69$.

5.10 Merging Parameter

It was thought that some degree of increased "mixing" could be achieved by manipulating the merging parameter D_0 . A large value of D_0 indicates a more stringent merging criterion, with the result that vortex merging tends to occur farther downstream and vortices are more evenly distributed between the near and far wake. Conversely, decreasing D_0 results in the majority of vortices being closer to the plate, with increased resolution in that area. A larger D_0 is therefore somewhat analogous to increased mixing, although for two opposite sign vortices to merge they must first be in proximity and D_0 does not directly modify vortex positions. Fig. 5.15 presents results for several cases of D_0 . There is no consistency to the shedding onset nor the steady-state levels achieved; only the $D_0 = 3.0$ result seems to have a consistently lower $\overline{C_d}$. Again it is interesting to note for these cases that while the onset of shedding is shifted considerably, until shedding begins the curves are almost identical, with no change in minimum drag level. In this respect D_0 is similar to other parameters (N_w , N_v , Δt etc.) and unlike geometrical changes or the circulation decay parameter λ which do change the minimum drag.

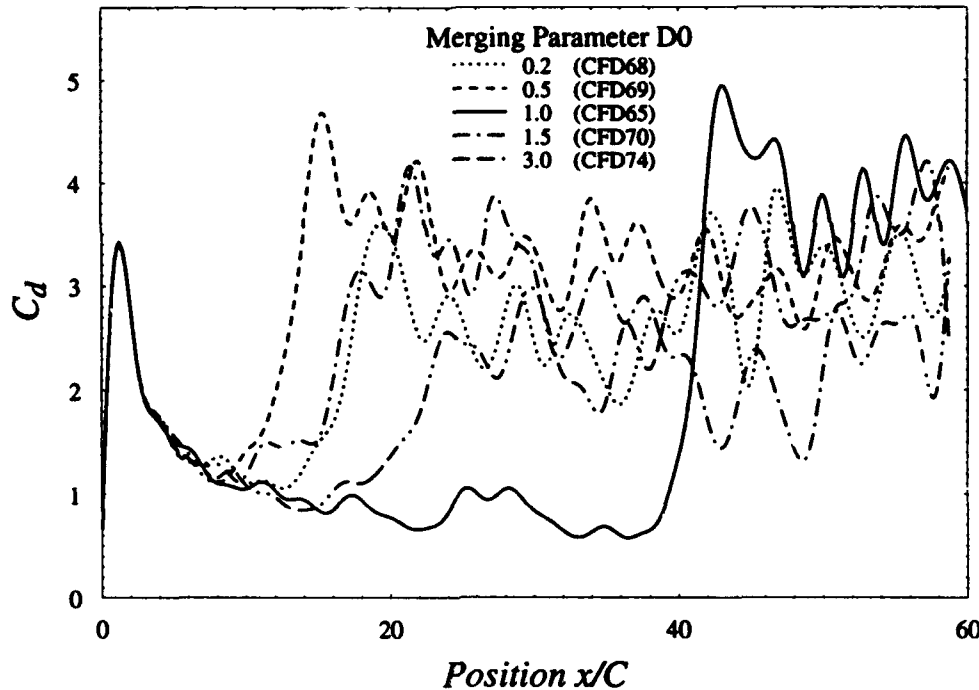


FIG. 5.15 Effects of merging parameter D0 on non-impulsive start. $\alpha = 90^\circ$; $t_a^* = 1.31$; $h/C = 10.3\%$; Chain Line: $D_0 = 1.5$; Solid Line: $D_0 = 1.0$; Dashed Line: $D_0 = 0.5$; Dotted Line: $D_0 = 0.2$

5.11 Long Time Histories

One of the primary goals of this numerical investigation was to establish steady-state behavior by allowing the simulation to run considerably longer than had been done in the past. Fig. 5.16 and Fig. 5.17 present force histories from such long runs, for $\lambda = 1.0$ and $\lambda = 0.86$ respectively.

Considering first $\lambda = 1.0$, the first 100 chord lengths of motion are apparently representative of the remainder of the run; although the $\alpha = 87.5^\circ$ case appears to have a greater amount of long period fluctuation in C_d . For $\alpha = 90^\circ$ $\bar{C}_d = 3.26$ for $40 \leq t^* \leq 400$; for the same interval $C_{d\text{rms}} = 17.6\%$, $\bar{C}_l = -.014$, $C_{l\text{rms}} = .43$ and $S_l = .121$. The $\alpha = 87.5^\circ$ results have similar values: $\bar{C}_d = 3.19$, $C_{d\text{rms}} = 15\%$ and $S_l = .122$; with the slightly asymmetric angle of attack, $\bar{C}_l = .142$ and $C_{l\text{rms}} = .43$.

When λ is reduced to 0.86 (Fig. 5.17), the character of the signals change, with considerably lower force and rms levels and a higher Strouhal frequency. For the same interval as above, $\bar{C}_d = 2.6$, $C_{d\text{rms}} = 7.5\%$, $\bar{C}_l = .003$, $C_{l\text{rms}} = .14$ and $S_l = .161$ for $\alpha = 90^\circ$; and $\bar{C}_d = 2.5$, $C_{d\text{rms}} = 7.4\%$, $\bar{C}_l = .107$, $C_{l\text{rms}} = .12$ and $S_l = .161$ for $\alpha = 87.5^\circ$.

Note the relative drops from $\lambda = 1$ to $\lambda = .86$ in $\overline{C_d}$ (20%) and C_l rms (67%) at $\alpha = 90^\circ$, and that there is a 25% drop in $\overline{C_l}$ at $\alpha = 87.5^\circ$ for the same change in λ . If the main effect of decreased λ was applied uniformly across the pressure distribution on the downstream face of the plate, then C_l rms at $\alpha = 90^\circ$ could be expected to drop the same percentage as $\overline{C_d}$ at $\alpha = 90^\circ$ (and $\overline{C_l}$ at $\alpha = 87.5^\circ$). That C_l rms drops considerably more in the first case ($\alpha = 90^\circ$) and only slightly more in the second ($\alpha = 87.5^\circ$) is an indication that the primary effect of λ is to reduce the vortex roll up near the edges of the plate (which contribute the most to C_l).

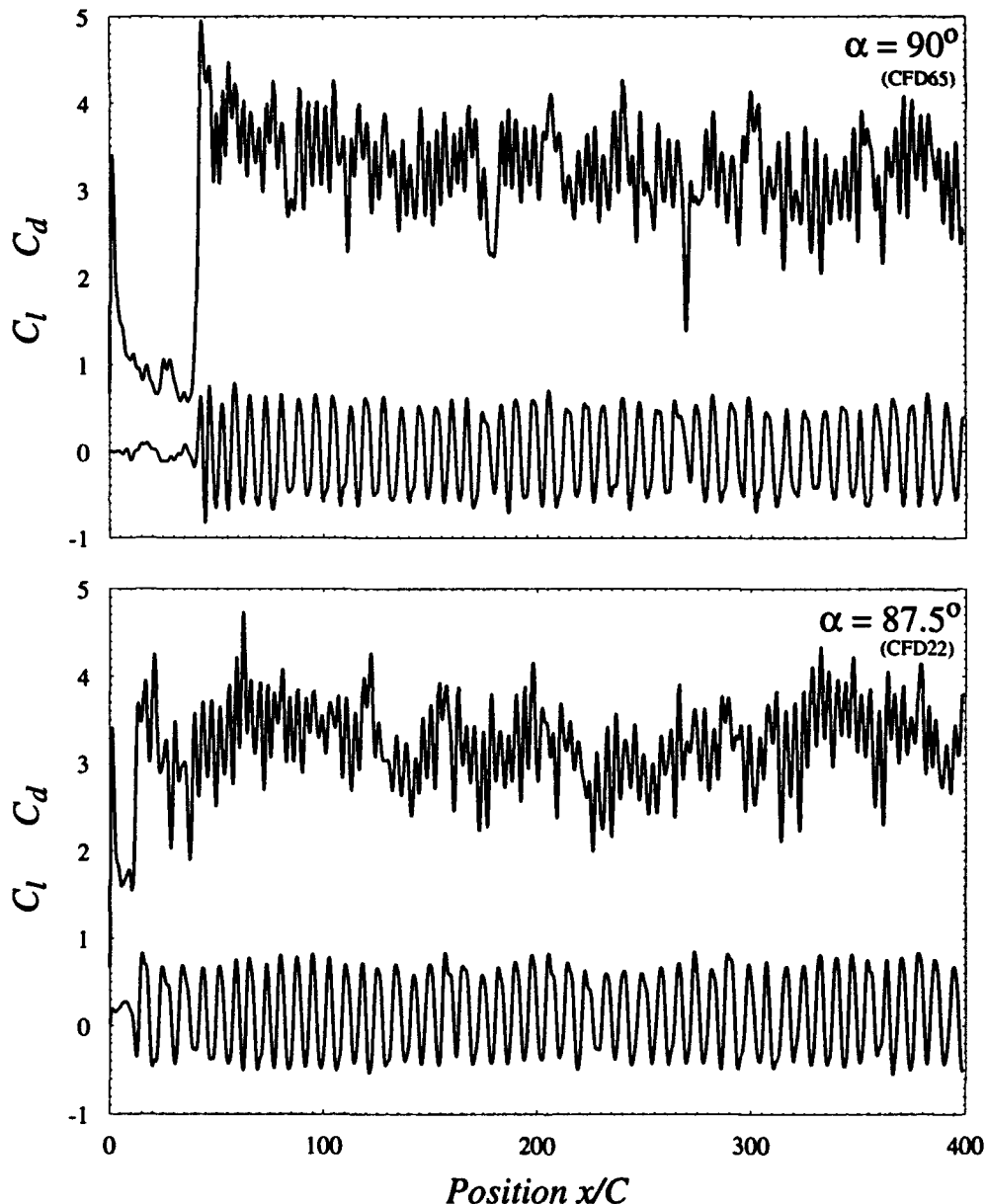


FIG. 5.16 Long time histories. $\lambda = 1.0$; $t_a^* = 1.31$; $h/C = 10.3\%$. Average quantities for $40 \leq t^* \leq 400$: at $\alpha = 90^\circ$: $S_t = .121$, $\overline{C_d} = 3.26$, C_d rms = .57, $\overline{C_l} = -.01$, C_l rms = .43; at $\alpha = 87.5^\circ$: $S_t = .121$, $\overline{C_d} = 3.25$, C_d rms = .50, $\overline{C_l} = 0.142$, C_l rms = .43

At $\lambda = 0.86$ a low frequency modulation is quite apparent in both signals, which looks remarkably similar to the long period modulation seen in the free surface water tunnel experimental results. It is not clear whether this modulation was present in the $\lambda = 1.0$ case and was simply masked by the much higher rms levels, or whether it is something new which has been introduced by way of $\lambda = 0.86$ circulation cancellation. Simply increasing the filtering of the $\lambda = 1.0$ data to obtain roughly the same rms levels as the $\lambda = .86$ results does not indicate the existence of such a well defined modulation, nor does it result in a similar modulation of the shedding peaks in the lift signal, as is seen at $\lambda = .86$; there may be a connection between this time scale and the imposed time τ , but further discussion of this will be delayed until Ch. 7.

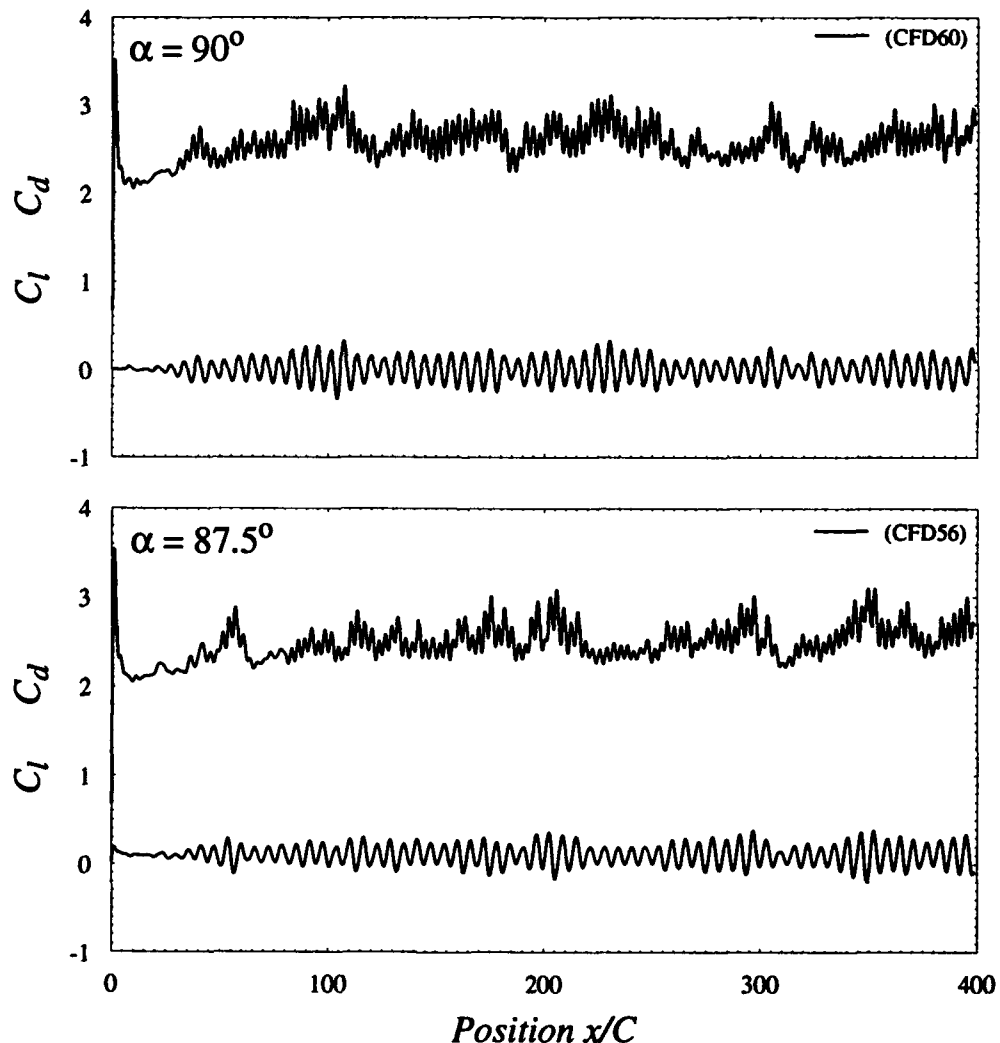


FIG. 5.17 Long time histories with circulation decay. $\lambda = 0.86$; $t_a^* = 1.31$; $h/C = 10.3\%$. Average quantities for $40 \leq t^* \leq 400$: at $\alpha = 90^\circ$: $S_t = .161$, $\bar{C}_d = 2.6$, $C_d \text{rms} = .2$, $\bar{C}_l = .003$, $C_l \text{rms} = .14$; at $\alpha = 87.5^\circ$: $S_t = .161$, $\bar{C}_d = 2.52$, $C_d \text{rms} = .19$, $\bar{C}_l = 0.107$, $C_l \text{rms} = .12$

Power spectra of the long time histories are shown in Fig. 5.18. We see the marked shift in S_t from .121 (17% below experimental) to .161 (10% above experimental). The peak at $3 \times S_t$ is more apparent in the $\lambda = 0.86$ case and both shedding peaks appear sharper than the equivalent $\lambda = 1.0$ results. Both cases exhibit the increased roll-off at $f^* \simeq 2$, again remarkably similar to the experimental result.

Time averaged pressure coefficients are shown in Fig. 5.19; they are presented with the perpendicular distance from the C_p curve to the surface of the plate $\equiv (1 - C_p)/10$. This presentation reduces the distortion of the profile due to the bevels on the plate. The pressure coefficient on the upstream face of the plate is unaffected by λ , while the downstream base pressure is increased with decreasing λ . A smaller λ also apparently reduces the "lobes" due to vortex rollup which are apparent in the $\lambda = 1.0$ case. The time over which the pressure is integrated has a considerable influence on the profile, as can be seen from the $\alpha = 87.5$ case; only the initial profile shows much asymmetry due to the unsteady startup.

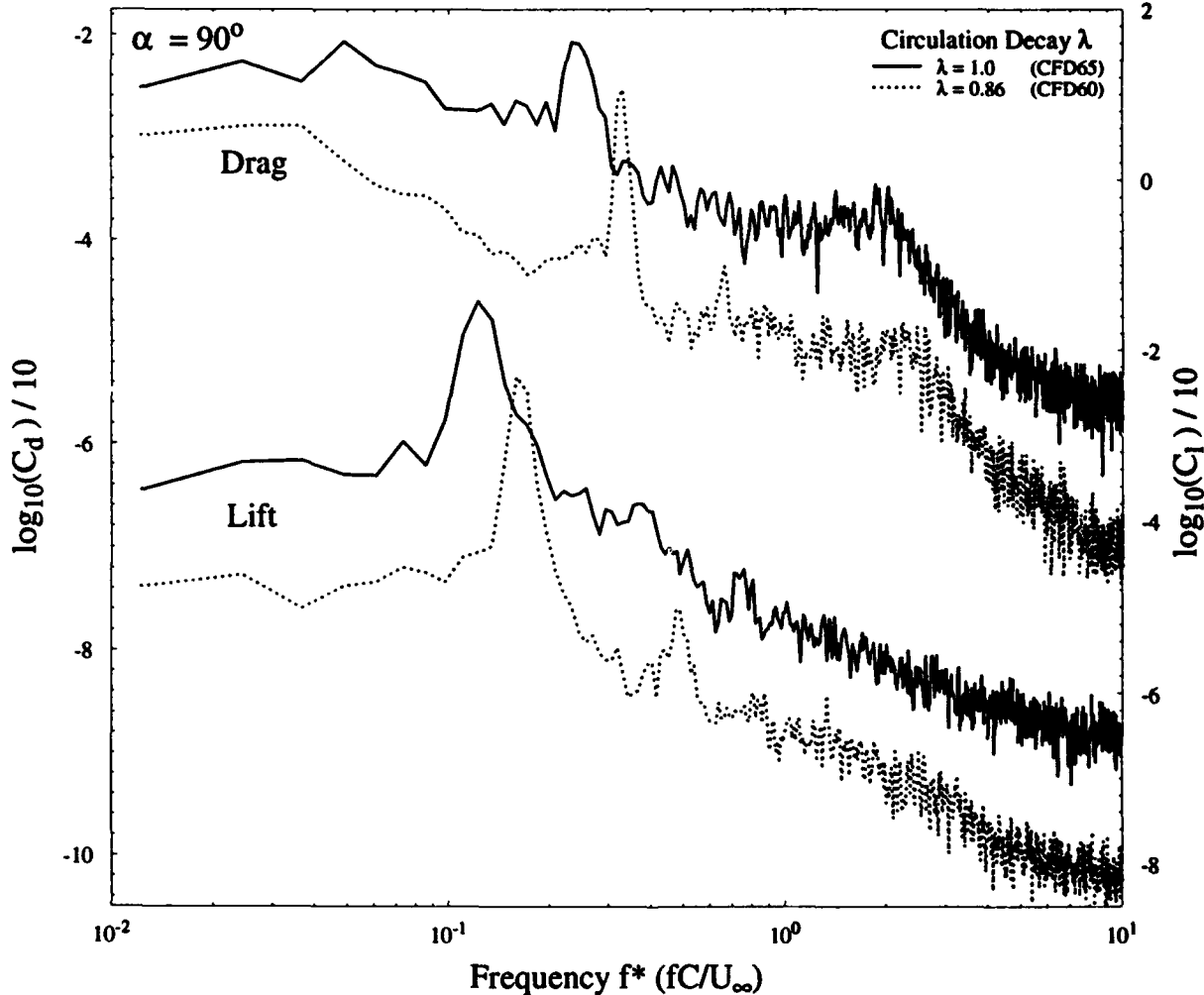


FIG. 5.18 Power spectra for $\lambda = 1.0$ (solid line) and $\lambda = 0.86$ (dotted line). Spectra taken for $40 \leq t^* \leq 400$. For $\lambda = 1.0$, $S_t = .121$; for $\lambda = 0.86$, $S_t = .161$

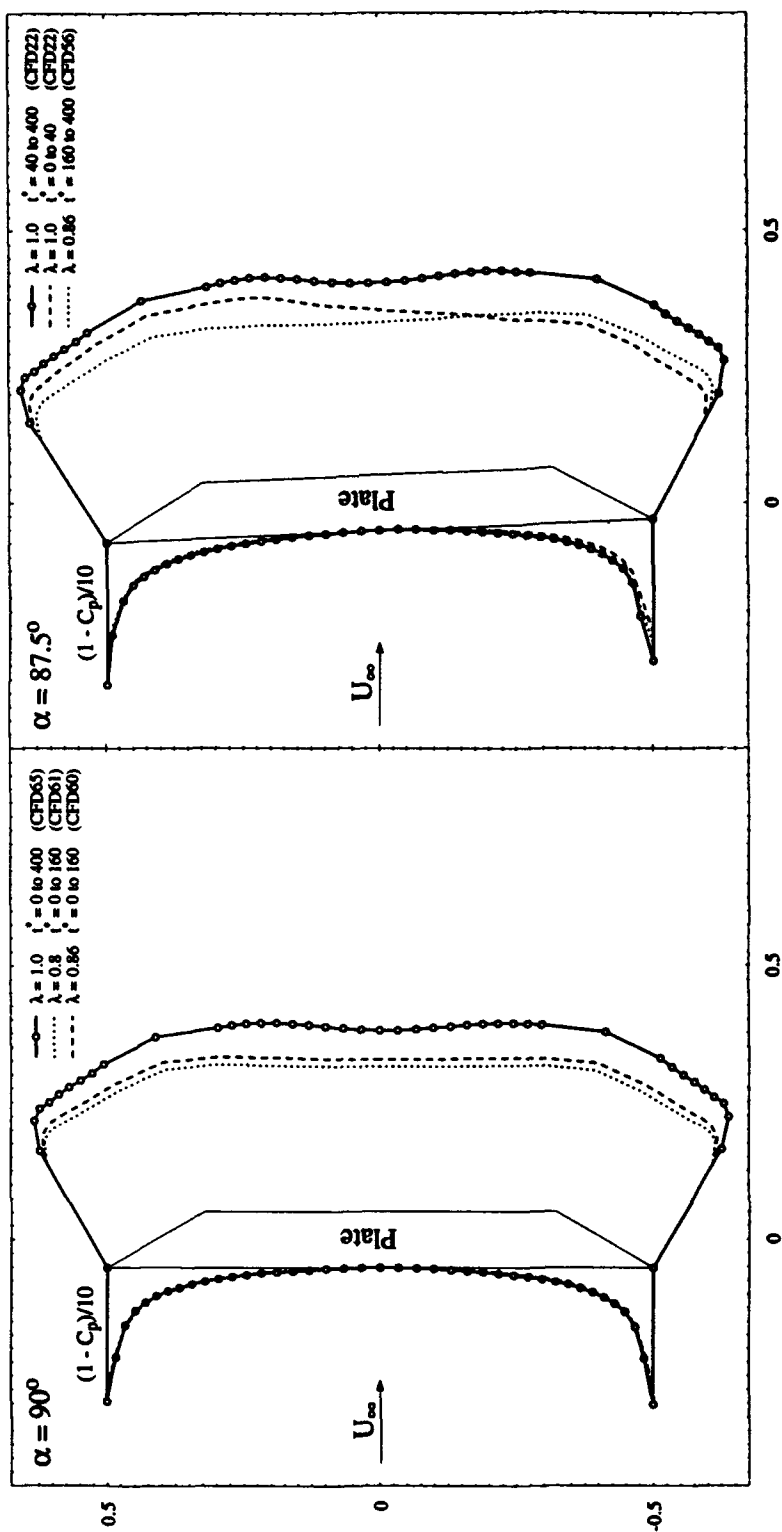


FIG. 5.19 Time averaged mean pressure coefficient distributions for $\alpha = 90^\circ$ and 87.5° - distance normal to plate surface $= \frac{(1 - C_p)}{10}$; α and averaging times as noted. $t_a^* = 1.31$, $h/C = 10.3\%$

5.12 Vortex Flow Visualizations

Flow visualization results for a plate $h/C = 16.25\%$ (the same as that used for experimental flow visualizations) were obtained for $\alpha = 90^\circ$ and $\alpha = 87.5^\circ$ at both $\lambda = 1.0$ and $\lambda = 0.86$. For comparison purposes, these are presented at the same scale and in the same manner as the experimental results of Ch. 3 and Ch. 6.

Fig. 5.20 and Fig. 5.22 to Fig. 5.25 give force histories and flow visualizations for the $\lambda = 1.0$ case. Note again for $\alpha = 87.5^\circ$ the increased structure in the upper shear layer at early time, and the much earlier flow development. This increased structure may be due in part to the increased thickness h/C relative to previous cases.

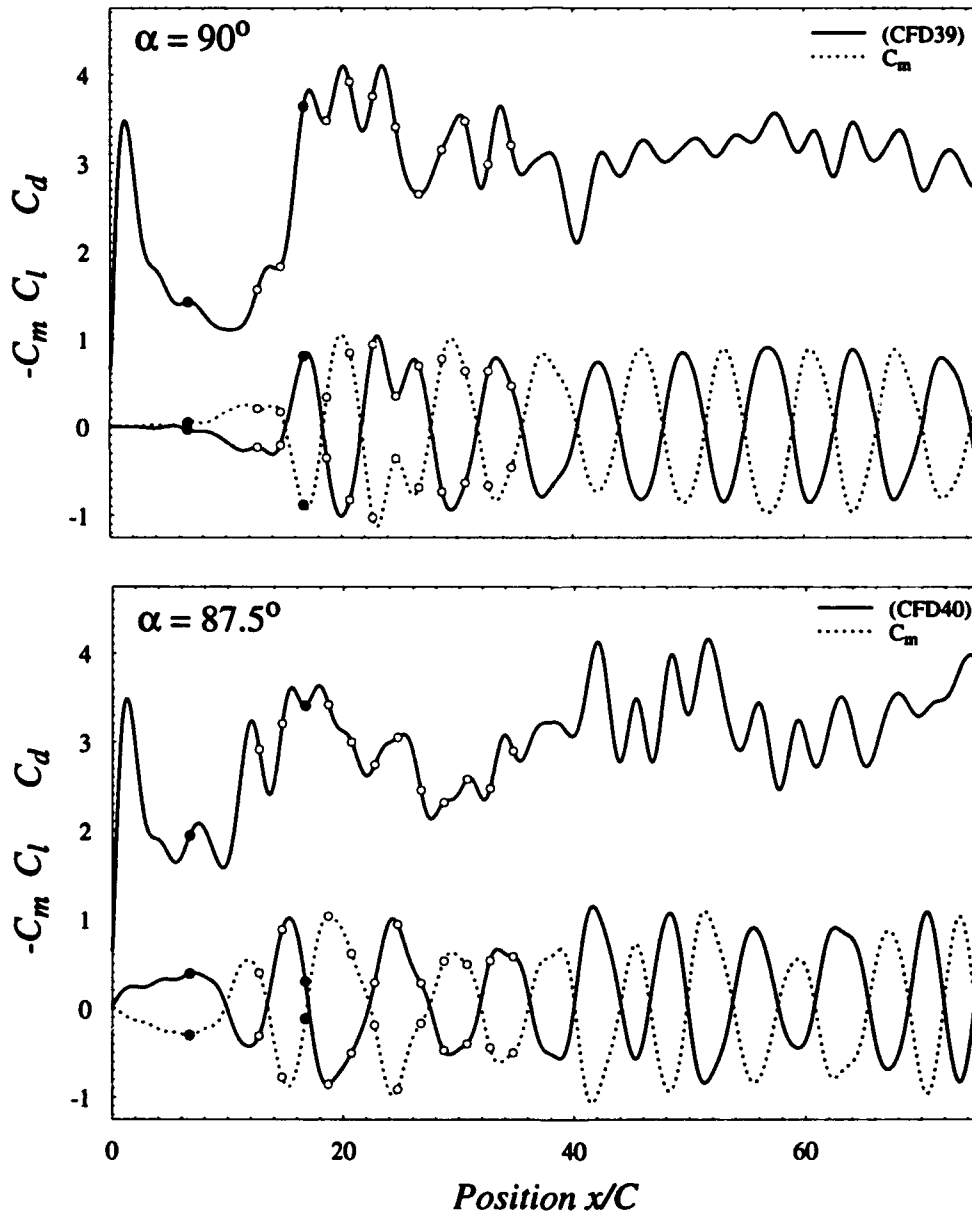


FIG. 5.20 Force histories for numerical flow visualization runs. α as noted; $\lambda = 1.0, t_a^* = 1.31, h/C = 16.25\%$. Symbols denote times of vortex position plots in Fig. 5.22, Fig. 5.24 (solid symbols) and Fig. 5.23, Fig. 5.25 (open symbols)

The $\lambda = 0.86$ case (Fig. 5.21 and Fig. 5.26 through Fig. 5.29) again shows considerably more structure in the shear layers; particularly the upper shear layer at $\alpha = 87.5^\circ$. Since the initial force levels at $\alpha = 87.5^\circ$ and $\alpha = 90^\circ$ are almost identical, the shear layer instability likely does not have a large direct effect on the forces. Flow visualizations taken throughout the shedding onset confirm the slow buildup of forces and shedding amplitude are associated with a slow decrease in the formation distance, this decrease occurring considerably earlier for the $\alpha = 87.5^\circ$ case.

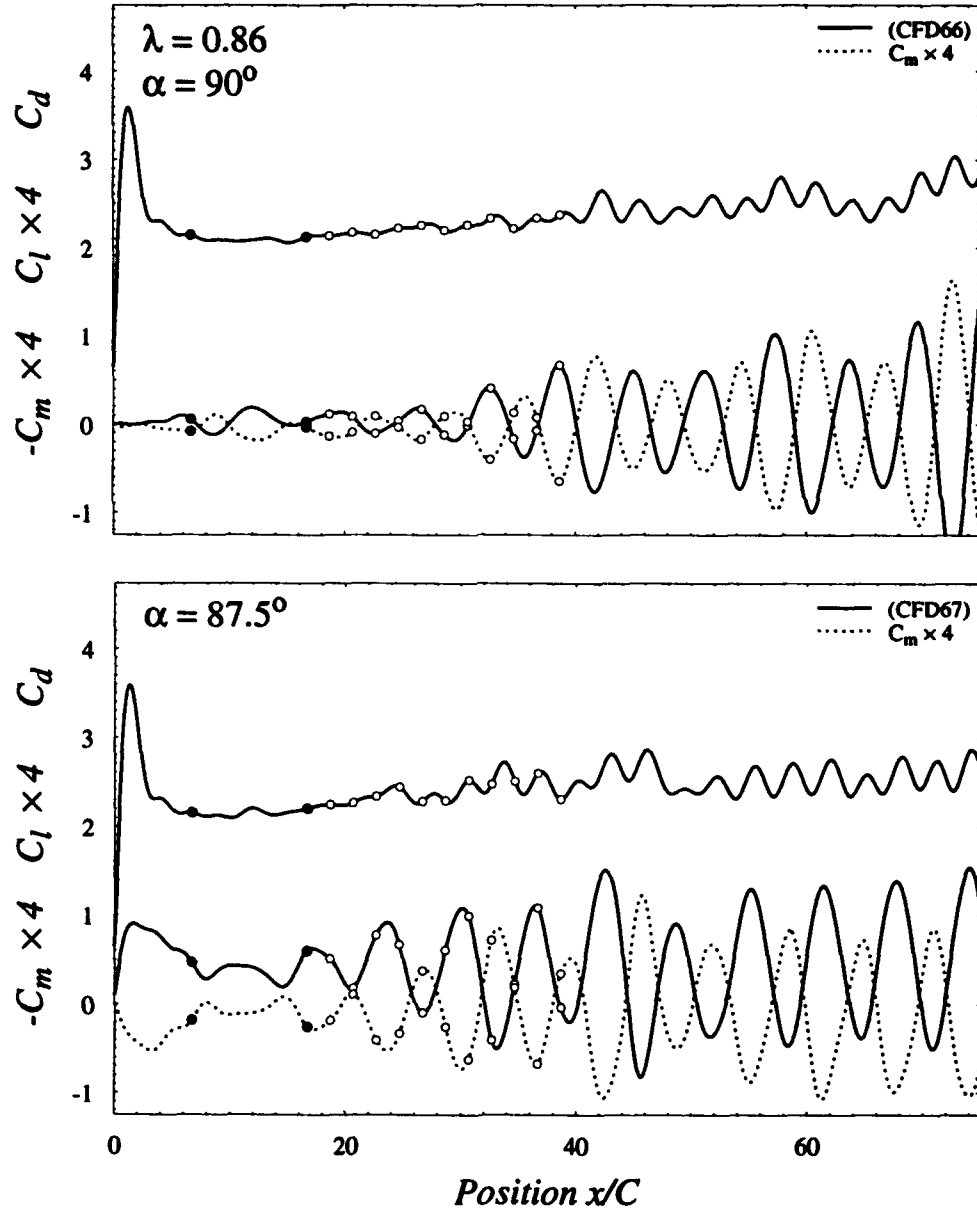


FIG. 5.21 Force histories for numerical flow visualization runs. α as noted; $\lambda = 0.86$, $t_a^* = 1.31$, $l/C = 16.25\%$. Symbols denote times of vortex position plots in Fig. 5.26, Fig. 5.28 (solid symbols) and Fig. 5.27, Fig. 5.29 (open symbols)

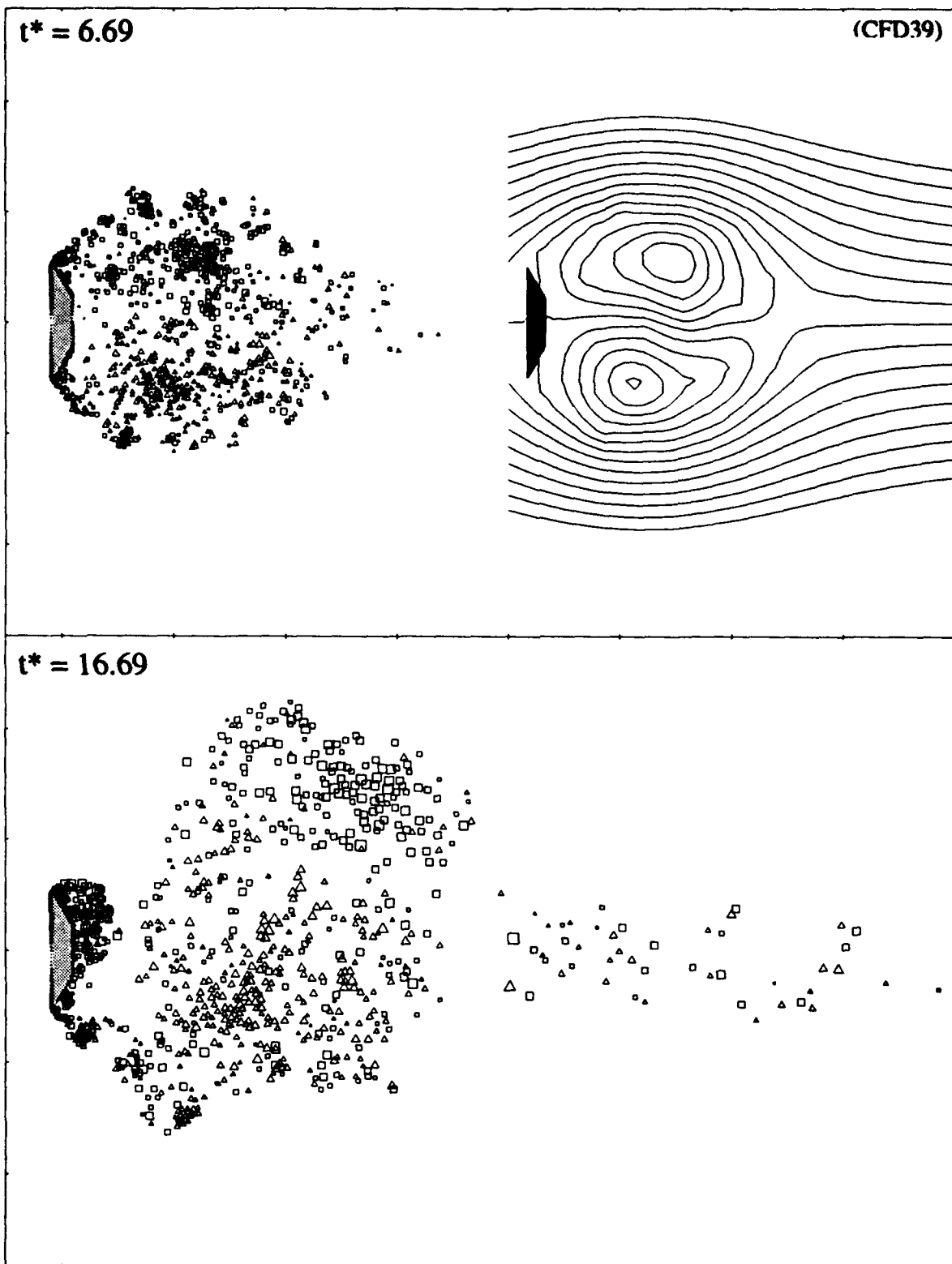


FIG. 5.22 Numerical flow visualizations, times as noted. $\lambda = 1.0, \alpha = 90^\circ, t_a^* = 1.31, hC = 16.25\%$

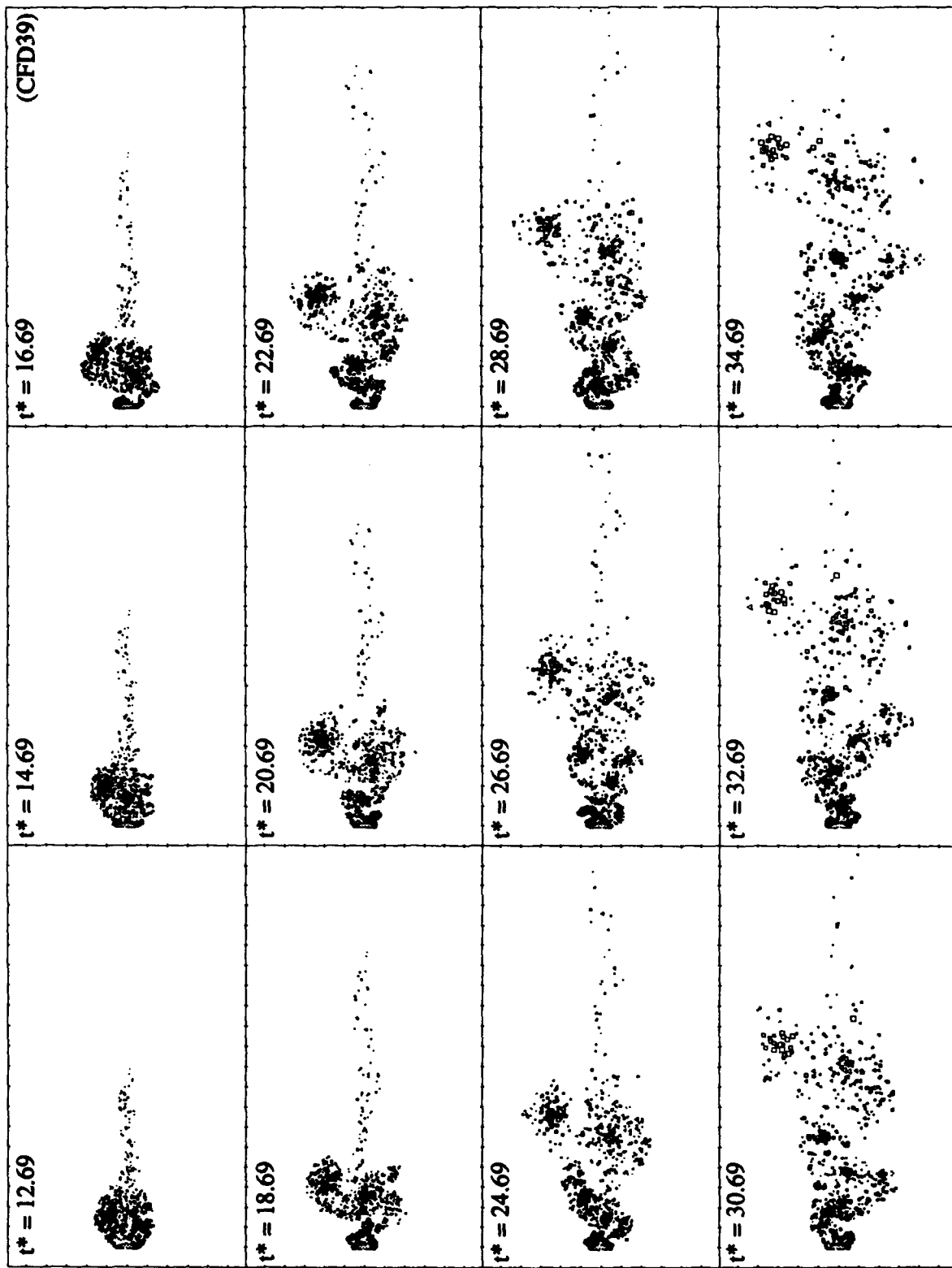


FIG. 5.23 Numerical flow visualizations, times as noted. $\lambda = 1.0, \alpha = 90^\circ, t_a^* = 1.31, hC = 16.25\%$

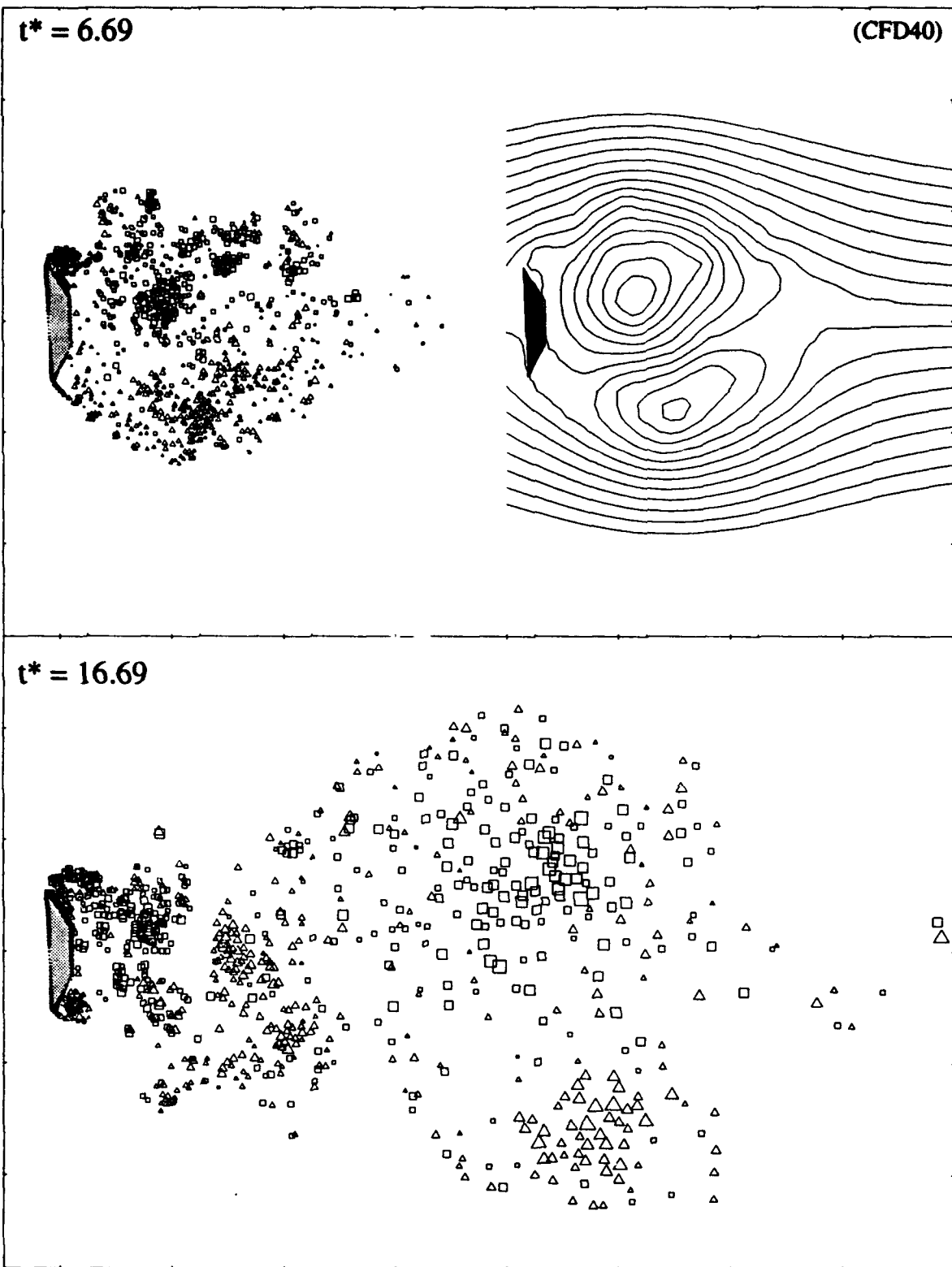


FIG. 5.24 Numerical flow visualizations, times as noted. $\lambda = 1.0, \alpha = 87.5^\circ, t_a^* = 1.31, hC = 16.25\%$

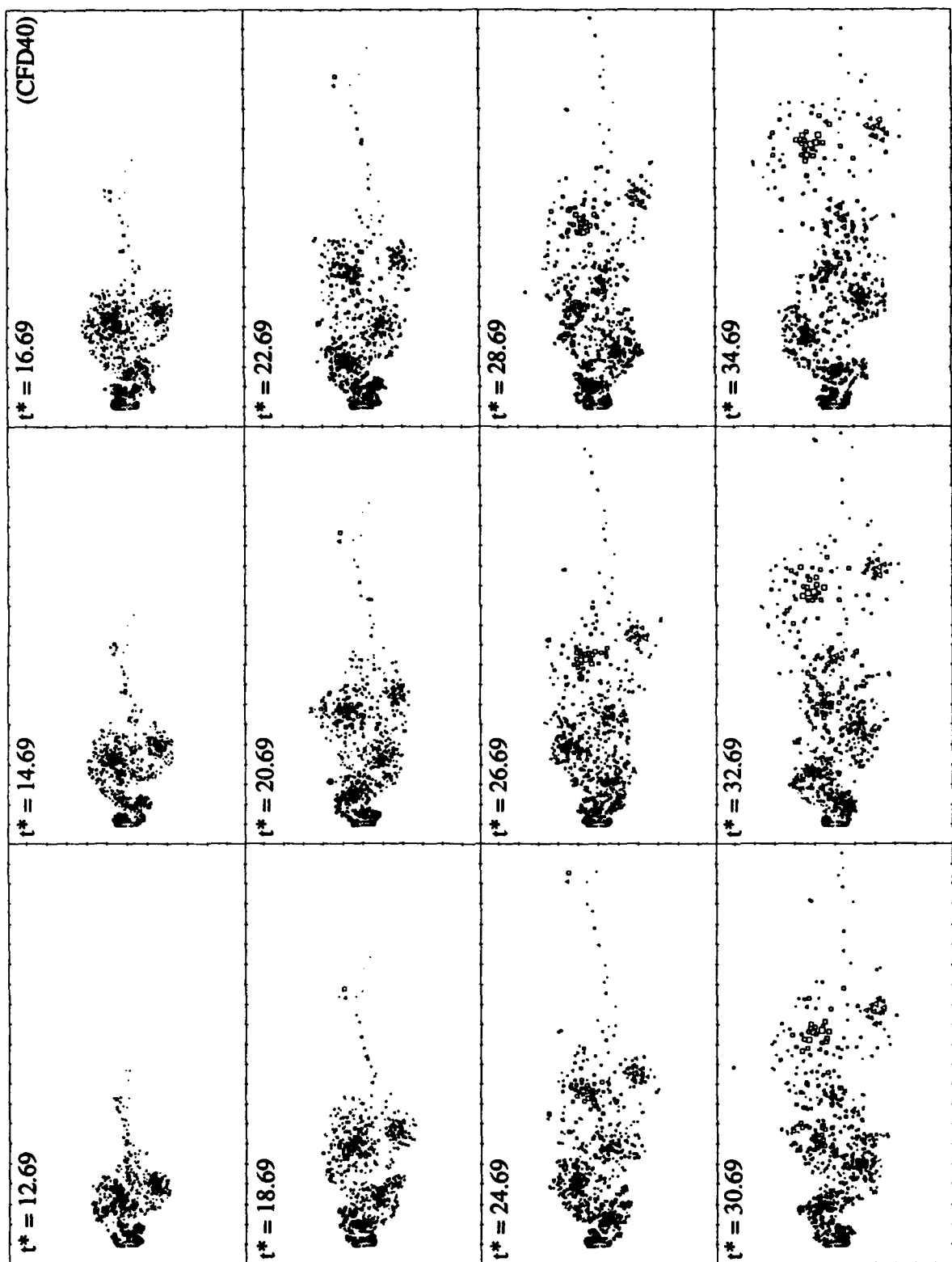


FIG. 5.25 Numerical flow visualizations, times as noted. $\lambda = 1.0, \alpha = 87.5^\circ, t_a^* = 1.31, hC = 16.25\%$

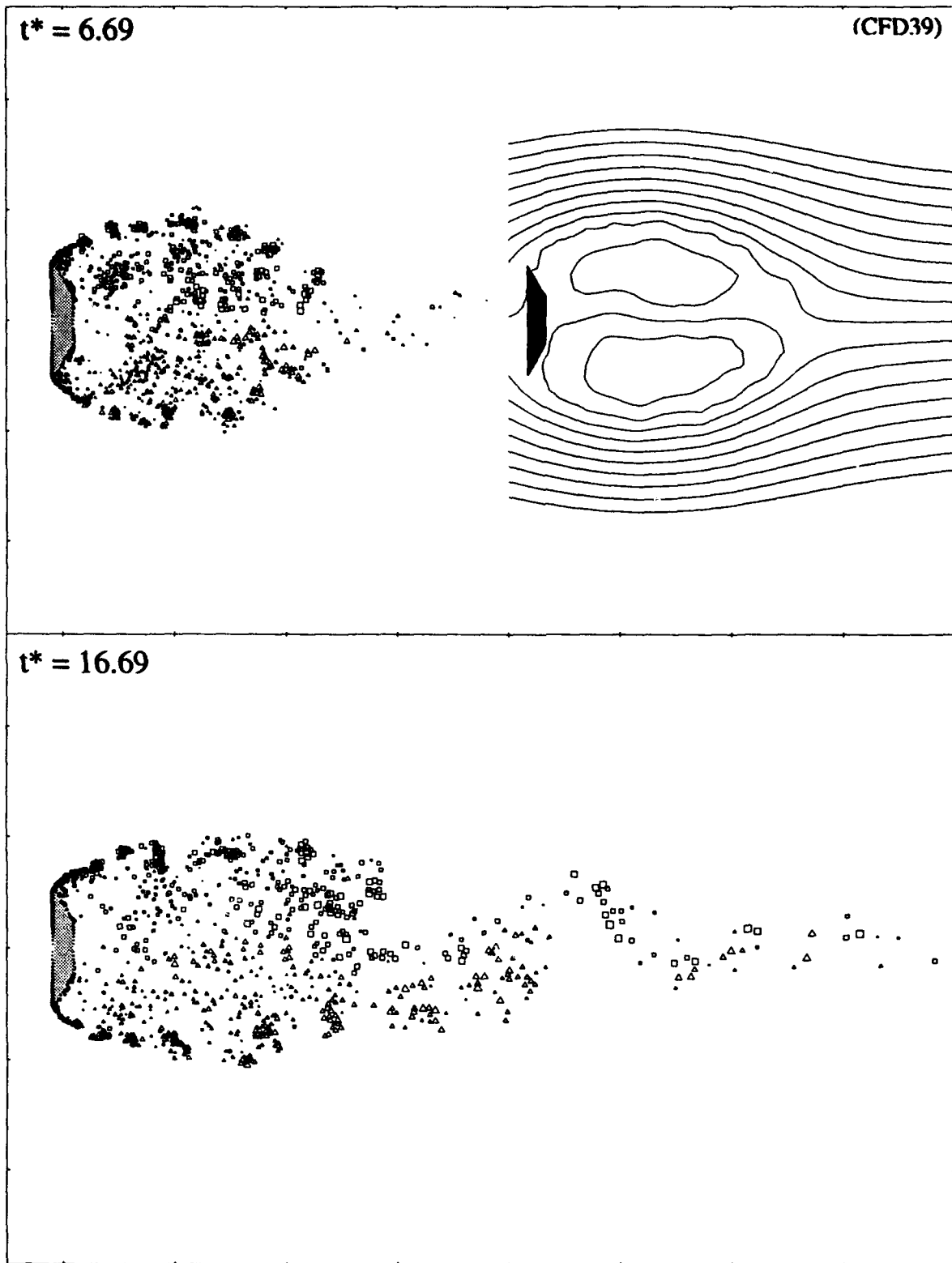


FIG. 5.26 Numerical flow visualizations, times as noted. $\lambda = 0.86, \alpha = 90^\circ, t_a^* = 1.31, hC = 16.25\%$

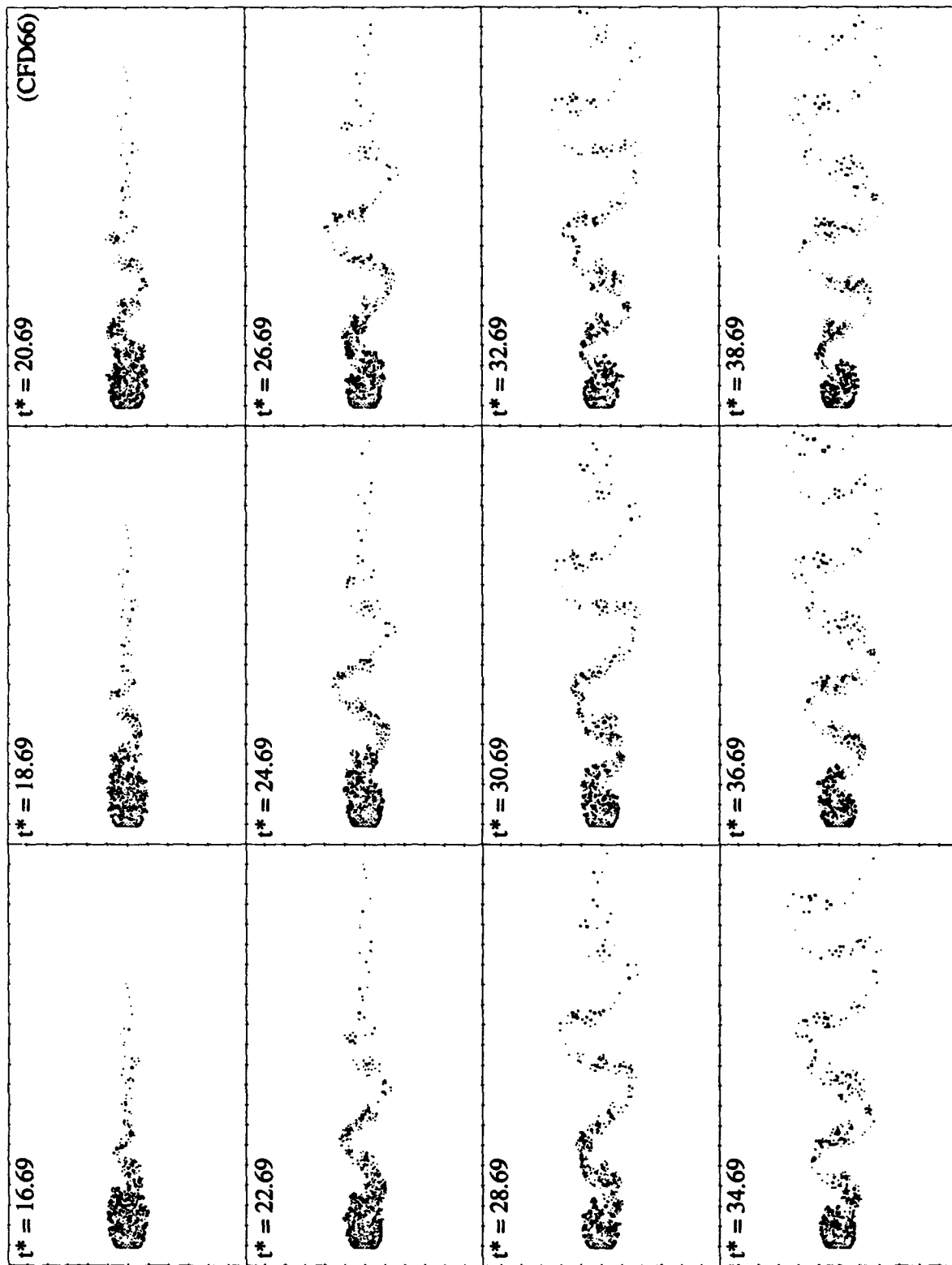


FIG. 5.27 Numerical flow visualizations, times as noted. $\lambda = 0.86$, $\alpha = 90^\circ$, $t_a^* = 1.31$, $h/C = 16.25\%$

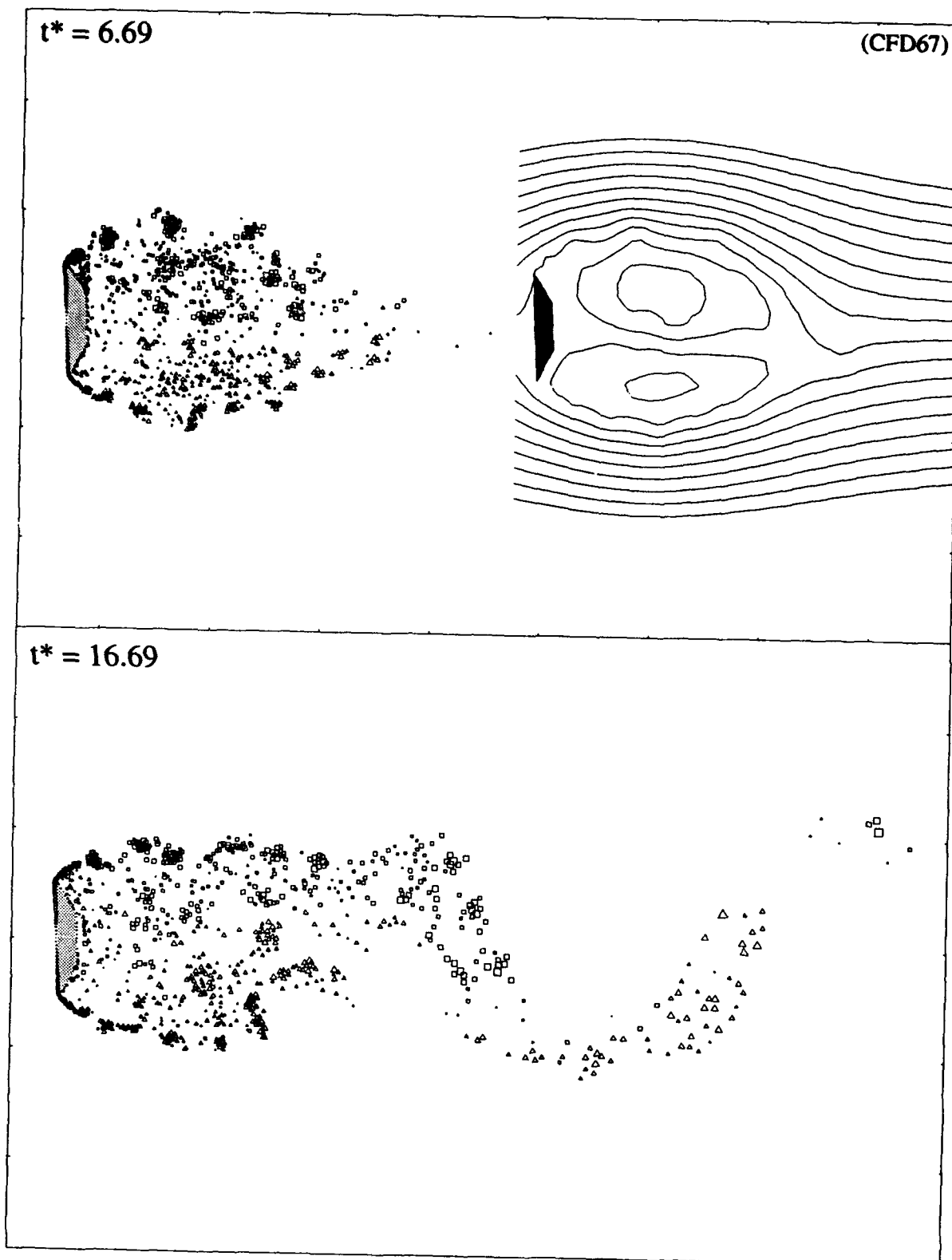


FIG. 5.28 Numerical flow visualizations, times as noted. $\lambda = 0.86, \alpha = 87.5^\circ, t_a^* = 1.31, h/C = 16.25\%$

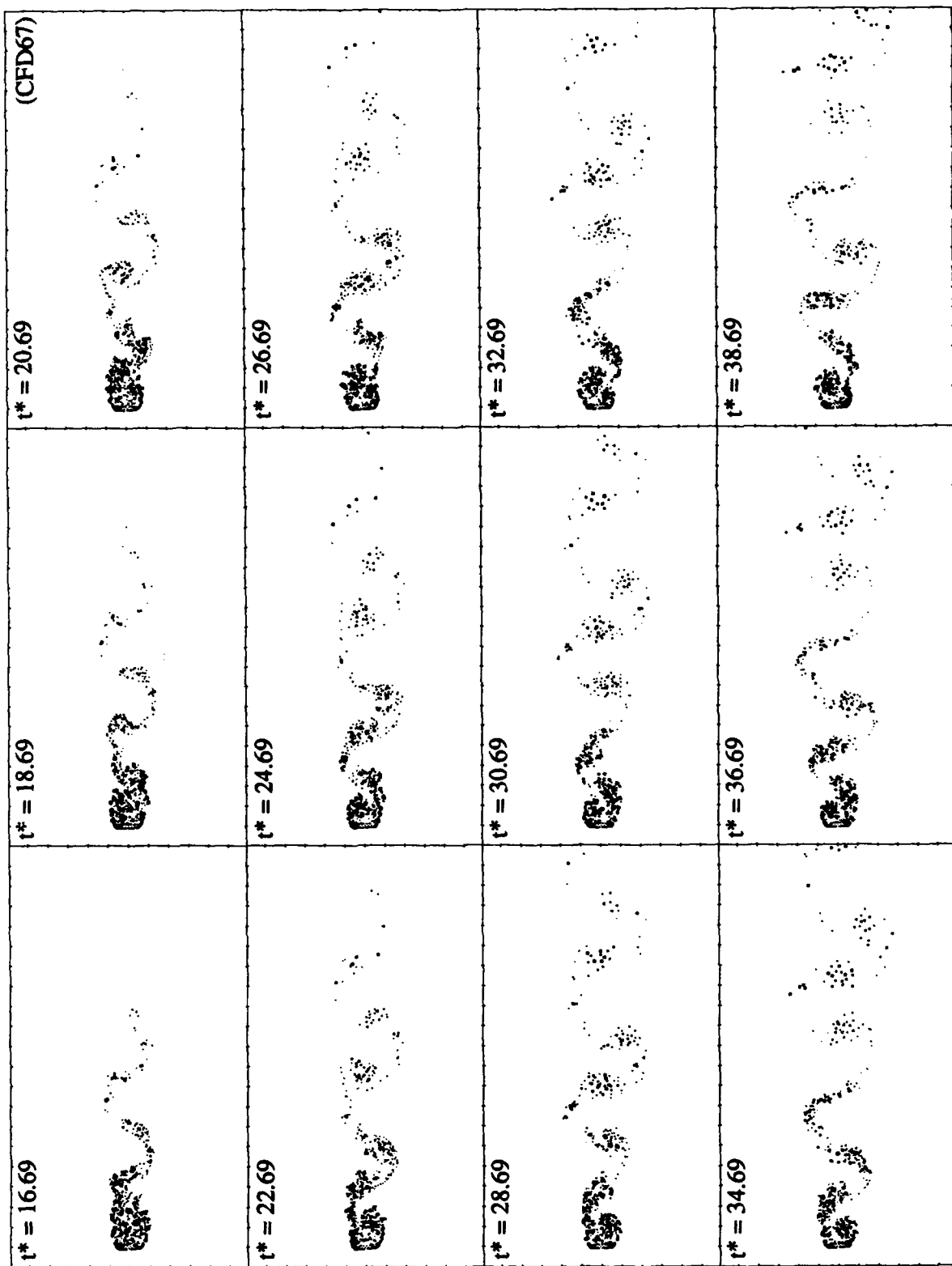


FIG. 5.29 Numerical flow visualizations, times as noted. $\lambda = 0.86, \alpha = 87.5^\circ, t_a^* = 1.31, hC = 16.25\%$

5.13 Summary

In summary, the initial low drag ($\overline{C_d} = 0.9$) region at $\alpha = 90^\circ$ is associated with the symmetric nature of the recirculating bubble. A slight geometric asymmetry sufficient to upset this symmetry results in one vortex moving closer to the plate, increasing both the instability of the upper shear layer and the drag. Without an imposed asymmetry, a wake induced oscillation of the bubble will eventually cause it to break and shedding to begin; the point at which this occurs is particularly sensitive to small changes in model parameters, even those not directly affecting symmetry.

The dynamics of recirculating region itself is a regulating factor; even for geometrically asymmetric plates, sufficiently strong flow induced fluctuations can result in a symmetric bubble, a delayed onset of shedding, and recovery of the low drag region. Such flow induced oscillations may also reduce upper shear layer instability, further increasing the probability that the upper vortex is the first shed.

Imposing circulation decay on the model results in increased pre-shedding and reduced post-shedding drag levels. The reduction in steady-state drag is a result of a much increased formation distance, while the pre-shedding increase is likely the result of an almost immediate breakdown of the closed, symmetric bubble. The role that the increased shear layer instability apparent for $\lambda < 1$ plays in affecting this breakdown is not clear, but it is unlikely that it directly affects the drag significantly. Finally, circulation decay introduces a new time scale to the flow, which may account for the slow shedding onset and later steady-state modulation in force levels, corresponding to slow changes in the formation distance as seen in the flow visualizations.

CHAPTER 6

Stratified X-Y Towing Tank Experiments

6.1 Preface

When trying to establish the separate affects of large and small scale three-dimensional motions, one is faced with having to eliminate, or reduce, or at least *change*, small scale motions which are intrinsic to all experiments. One way to do this is to introduce a strong, stable, spanwise (*i.e.*, vertical) density gradient; motions in the direction of this gradient then being damped by the effects of buoyancy, with the largest motions being most strongly affected. Such a density gradient was achieved by stably stratifying the towing tank using salt. The following chapter outlines results from some experiments which are identical in procedure, apparatus and parameters to those presented in Ch. 3, but this time performed in a stably stratified X-Y towing tank .

6.2 X-Y Towing Tank Stratification

The technique used to stratify the towing tank is explained in detail by Clark *et al.*, 1967, and is outlined only briefly here. The towing tank was initially divided in half by a removable barrier held (tightly) in place by the carriage as illustrated in Fig. 6.1(a). The desired amount of salt was then added to one side and mixed thoroughly. The barrier was gently removed, resulting in a two layer stratification with the denser salt water on the bottom as in Fig. 6.1(b). Two 15 cm chord ($\frac{1}{3}$ the total depth) flat plates, spanning the tank on either side of the carriage, were then dragged through the two layer system; the plates were oriented so as to be roughly in the middle of the two layers, with one plate about 5 cm higher than the other. Turbulence in the wake of the plates then (theoretically) induced a linear density gradient. This technique seemed to work best with less stratification; if the initial two layer system was too stable, then the mixing achieved with one pass of the flat plates resulted in very steep density gradient in the center, with relatively less gradient at the top and bottom of the tank. Further mixing with the plates shallowed the gradient in the middle, but usually at the expense of almost eliminating any gradient at top and bottom.

Density profiles were measured indirectly (see Appendix A) using a platinum through-flow conductivity probe, which gave a direct measure of NaCl content. The probe was calibrated using known amounts of salt and distilled water; specific gravity was measured simultaneously with a hydrometer, yielding a specific gravity (S_g) vs. conductivity curve. Lowering the probe into the tank with an attached scale to indicate depth gave profiles such as those shown in Fig. 6.3.

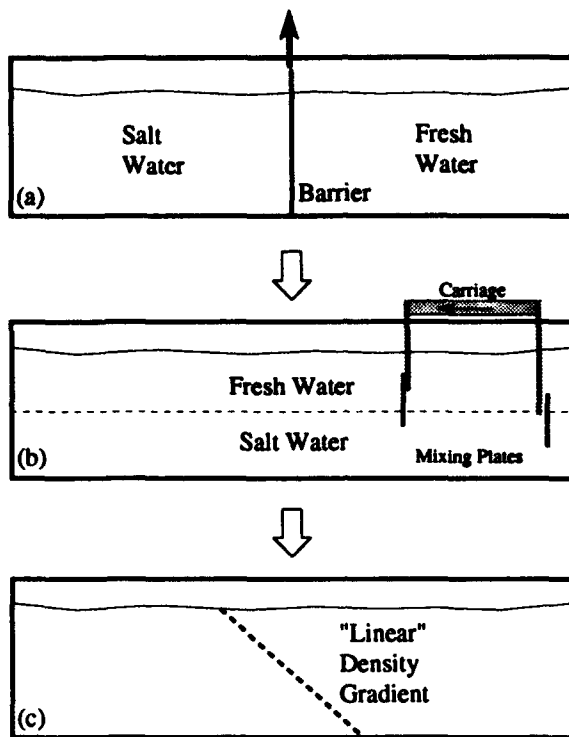


FIG. 6.1 Method used to stratify the X-Y towing tank

Flow visualization in these stratified flows was accomplished by density matching (using salt) food coloring to the density of the surrounding fluid at the mid-span of the plate. This dye was then introduced to the flow using the same flow visualization plate as was described previously, with the dye flow through the porous upstream face of the plate being restricted to a narrow chordwise slit at mid-span. Dye was backlit with fluorescent tubes below the tank and the perpendicular spanwise plane imaged from above. No full span visualizations were performed due to the difficulty of introducing correctly density matched flow tracers over the entire span of the plate.

Further details of the stratification method and calibration techniques can be found in Appendix A, while other procedures, such as those used for force measurements, were identical to those outlined in Ch. 3.

6.3 Richardson Number

The primary governing parameter for stratified flows is the Richardson number:

$$Ri \cong g \frac{\partial S_g}{\partial z} \frac{C^2}{U_\infty^2};$$

where g is gravity and $\frac{\partial S_g}{\partial z}$ is the fluid specific gravity gradient in the spanwise direction. Essentially this number gives a ratio of buoyancy to inertial forces; above a certain critical Richardson number Ri_c , motions in the direction of a stable density gradient are strongly suppressed. The value of Ri_c is typically taken to be of order 0.25 (see for example, pp. 352 Tritton, 1988). Note that the above definition is based on

chord as a length scale, so fluid motions of the same scale as the chord should be increasingly suppressed as Ri exceeds about 0.25. Due to the inverse quadratic dependence of Ri on chord length, the Ri for length scales smaller than the chord length decreases rapidly, the Ri_c for length scales on the order of $0.1C$ being 25 when defined as above. The "correct" length scale to use, or rather the minimum length scale which must be eliminated to effectively provide a two-dimensional flow, is rather hard to estimate *a priori*, other than to say that it should probably be larger at smaller Reynolds numbers, and that it is almost certainly smaller than the chord length.

Thus we are likely to require the chord based Ri to be very large to realize appreciable affects on small scale three-dimensional motions. Given that the value of g was fixed for these experiments, and that there is an upper bound on $\frac{\partial S_g}{\partial z}$ fixed by the saturation limits of salt water, we are left to increase C or decrease U_∞ to achieve higher Richardson numbers. Unfortunately this is the exact opposite of what we would like to do to increase the amount of force generated and thus the resolution of the force measurement.

Consider again the example of Sec. 3.2, that of an experiment with $C = 5\text{cm}$, $d = 50\text{cm}$, and $Re \approx 1000$, with a correspondingly high 11% uncertainty in C_d . This same experiment with a $\frac{\partial S_g}{\partial z} \approx 0.22 \text{ m}^{-1}$, which was the maximum achieved in the X-Y towing tank, results in $Ri \approx 13.5$. This level of Ri could be expected to effectively dampen motions of length scale roughly $\frac{1}{7}C$.

Due to the large errors in C_d , and the relatively small effects expected due to stratification, it was necessary to ensemble average a large number of experiments to achieve acceptable levels of uncertainty. For this reason fifty experiments were performed, both stratified and unstratified, using a 5cm plate at a Reynolds number of 1000 ($Ri \approx 13.3$), and 25 experiments at $Re \approx 5000$, ($Ri \approx 0.53$). All of the same correction procedures, to remove the effects of waviness in the tank rails and unwanted inertial effects, were done in the manner outlined in Ch. 3, where the corresponding unstratified results have already been presented.

Stratification Number	Salt Used (kg)	$\frac{\partial S_g}{\partial z} (\text{m}^{-1})$	Ri (at $Re = 1000$)	Ri (at $Re = 5000$)
1	91	0.074	5.01	0.2
2	182	0.124	8.45	0.34
3	218	0.22	13.33	0.53

FIG. 6.2 Results of three different stratifications of the X-Y towing tank. Values quoted are $C = 5.0 \text{ cm}$

6.4 Stratification Profiles

Results of three different tank stratifications are given in tabular form in Fig. 6.2 with the actual density profiles for stratification #3 being shown in Fig. 6.3 (the other two profiles are given in Appendix A). Five different attempts had to be made at stratifying the tank using the above techniques to provide the three stratifications used; although they are not perfectly linear, they are no doubt adequate to show some of the effects to be expected in a stratified flow.

It is somewhat ironic the the lowest gradients are inevitably achieved at the ends of the plate, introducing once again the possibility of end effects. Most of the runs presented here used the optimum NBW end condition, to eliminate as much extrinsic three dimensionality as possible; what large scale motions remained should be very heavily damped at these Richardson numbers. Although a more involved and reliable stratification technique could have been used, this technique proved remarkably simple and easy to use, and did provide reasonably good results.

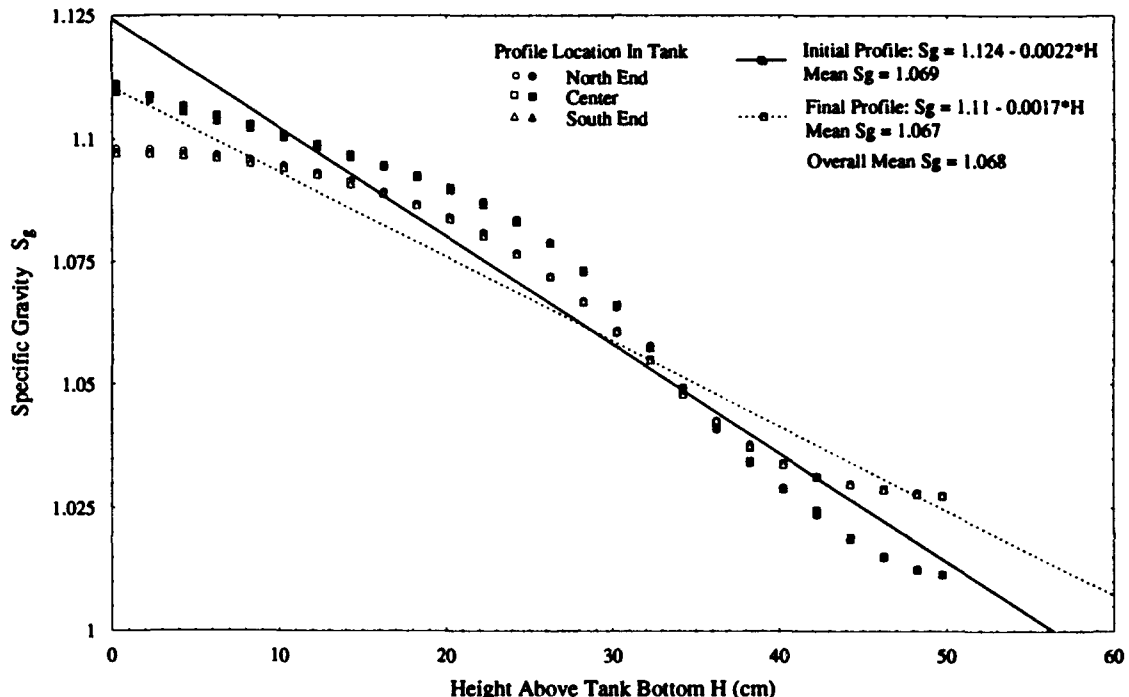


FIG. 6.3 Specific gravity profiles for stratification #3. Initial profile was prior to experiments, final profile was after 80 experimental runs

6.5 Typical Stratified Flow Result

The effects of two different levels of stratification on force histories are shown in Fig. 6.4. These runs were performed at a Reynolds number of 2500, to give the maximum possible Richardson number while preserving enough force measurement accuracy that a large number of ensemble runs were unnecessary (although the results should nonetheless be considered somewhat qualitative due to the low Reynolds number and consequent force inaccuracies). As has been previously described, the NBW end condition was used to give the minimum amount of large scale three dimensionality and thereby isolate the effects of changes in small scale intrinsic motions.

It is apparent that stratification has very little effect at these Richardson numbers; the minimum drag to which the levels fall immediately after the acceleration is lower, and it persists longer for the stratified cases, but the difference is minimal. There is also a tendency, most apparent for $\alpha = 87.5^\circ$, for the drag to overshoot to a higher value when shedding does begin, but the final steady-state values are essentially the same for all cases.

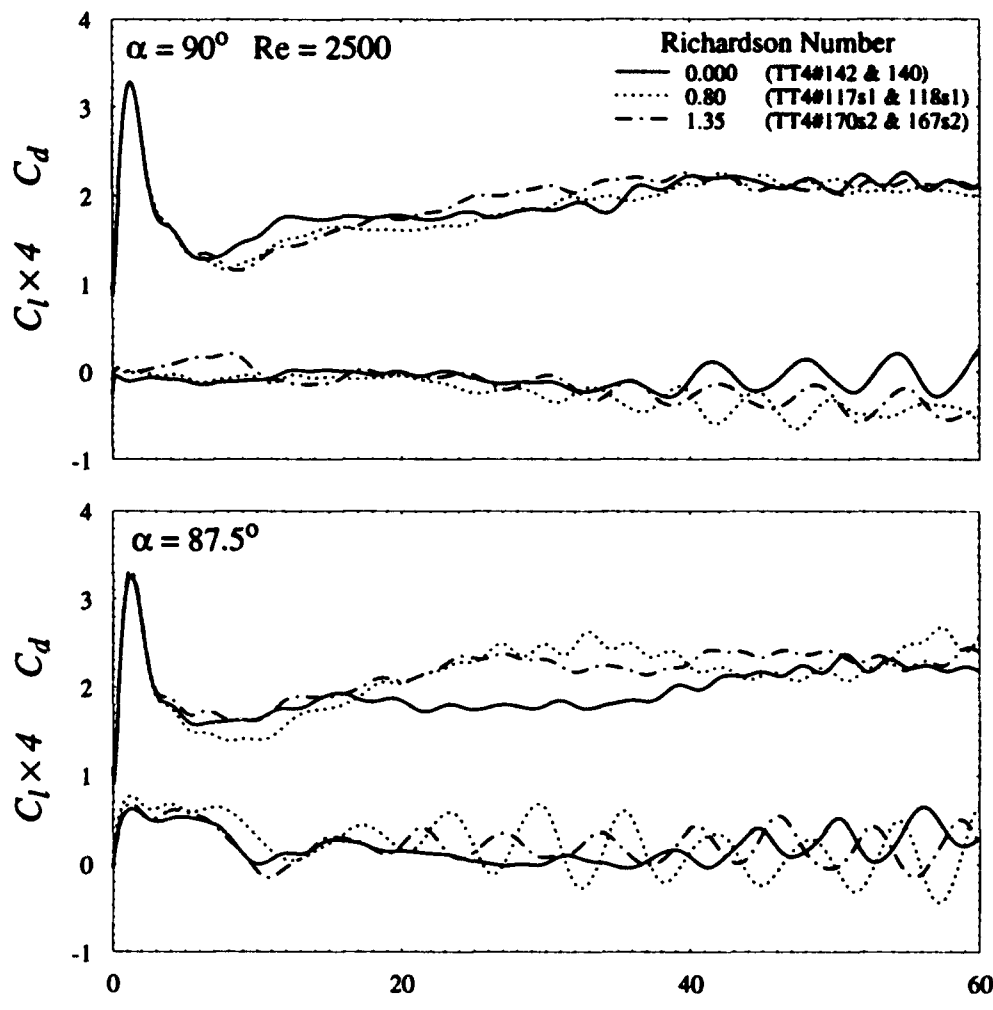


FIG. 6.4 Richardson number effects. $C = 5\text{cm}$, $AR = 10$ (NBW end condition), $l/C = 6.8\%$, $Re = 2500$, $t_a^* = 1.31$, α as noted. Solid Line: No Stratification, $Ri = 0.0$; Dotted Line: Stratification #1, $Ri = 0.8$; Chain Line: Stratification #2, $Ri = 1.35$

6.6 End Conditions

The lack of identifiable stratification effects on the small scale inspired an examination of two flows with very different large scale motions present - the no-end-plate NEP and near-bottom-wall NBW end condition cases. It was thought that stratification of the NEP case may have resulted in a flow similar to the NBW end condition due to the presumed elimination of large scale three-dimensional motions. Fig. 6.5 confirms this to some extent, although in the limited run length available it is difficult to establish steady-state effects.

Considering first the $AR = 10$ case, in the last 25 chord lengths the NBW case begins organized shedding, and in the last 15 chord lengths the stratified NEP condition also experiences the drag rise and increased lift fluctuation typical of shedding onset. The stratified NEP condition has a considerably lower drag minimum than either of the other cases, and appears to follow a path similar to the NBW condition

although with considerably later and lower amplitude shedding. The initial peak heights of the *NEP* cases are both equal, and considerably lower than the *NBW* case. Note the strong vortex shed initially by the unstratified *NEP* case before the lack of an end plate suppresses subsequent shedding.

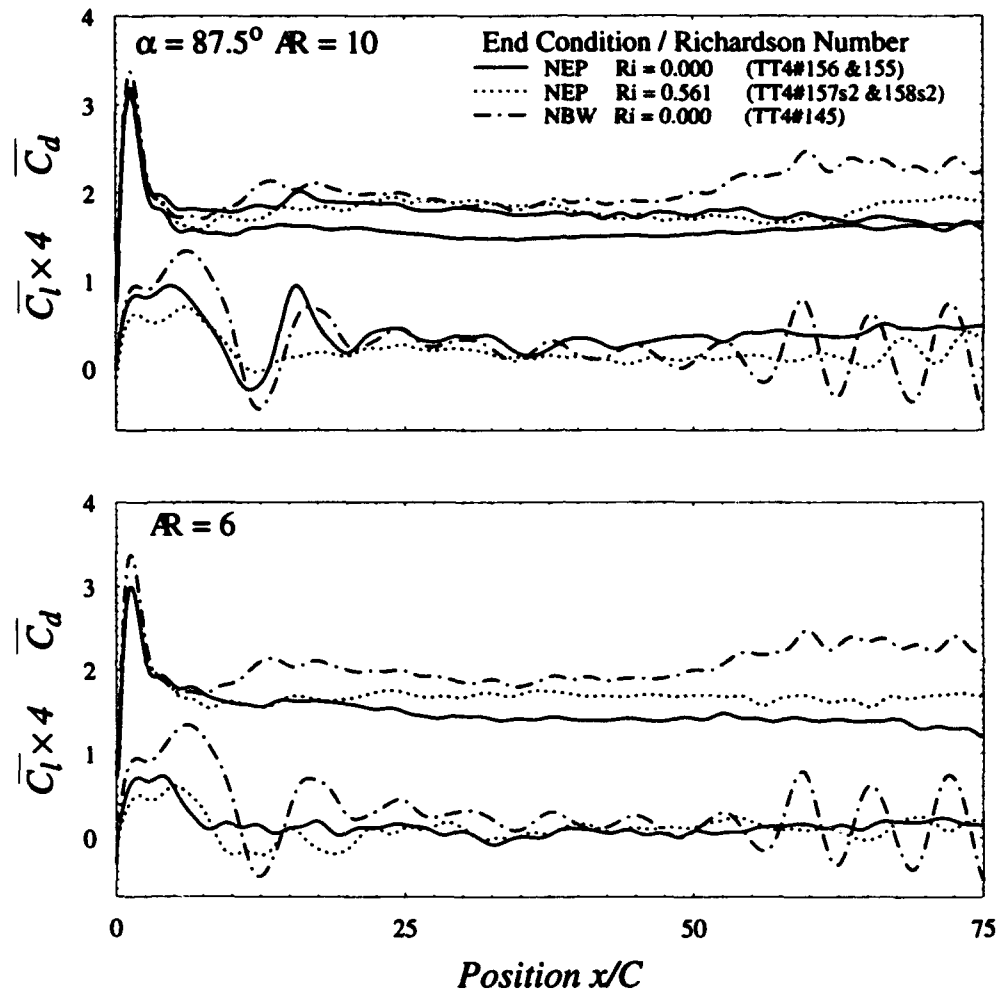


FIG. 6.5 Effects of stratification on large scale (end condition) effects. $C = 4\text{cm}$, AR as indicated, $h/C = 16.25\%$, $Re = 2500$, $t_a^* = 1.31$, $\alpha = 87.5^\circ$. Solid Line: No end plate, no stratification; Dotted Line: No end plate, stratification #2, $Ri = 0.56$; Chain Line: *NBW*, no stratification. Note that the *NBW* $AR = 10$ case shown is the same in both plots

Stratification effects are more apparent at an aspect ratio of 6 (note that the *NBW* result shown is still the $AR = 10$ result). The stratification increases the mean drag considerably, although organized shedding is still effectively suppressed for both *NEP* cases. The fact that the drag is lower in the unstratified case would indicate that the base pressure is increased considerably, without an apparent increased incoherence of vortex shedding.

The initial peak height is the same stratified or unstratified; which is not surprising if one supposes that the initial flow is two-dimensional regardless of end condition. However, both *NEP* peaks are considerably lower than the *NBW* peak, with the difference being larger at $AR = 6$. Why would two supposedly two-

dimensional flows have such different initial peaks? One may surmise that the base pressure is set by a local condition near the end of the plate, which is small enough that it is not suppressed by the stratification, but which nonetheless affects a large span of the plate. The nature of this small scale end disturbance is not clear; two possibilities are flow around the end of the plate (which in the large scale is suppressed by the stratification) and the lack of a no-slip boundary condition (which would still be an affect even with perfectly two-dimensional flow).

Conceptually, one may think of increasing the level of both NEP curves until they match the $NBIV$ case during the initial peak. This would effectively eliminate the hypothesized differences due to "small scale" aspect ratio/base pressure effects. What remains would be the differences due to large scale motions, such as the increase in the post-acceleration drag minimum and the later suppression of organized vortex shedding. These differences are considerably smaller between the stratified NEP and $NBIV$ cases (particularly at $AR = 6$), indicating that the stratification does indeed suppress the larger scale motions, but it does not eliminate the "small scale" effects of aspect ratio on base pressure.

Since the base pressure during the initial peak decreases as aspect ratio increases, these "small scale" AR effects apparently do not affect the whole span of the plate, but rather some small number of chord lengths that contribute more as aspect ratio decreases. In the presumed absence of spanwise flow, this could imply a different vortex formation configuration along the span of the plate.

6.7 Ensemble Averaged Results

In order to increase the level of stratification beyond those values already presented, it was necessary to decrease the Reynolds number further, to $Re = 1000$. As has already been pointed out, this requires an ensemble average of many runs to achieve uncertainty levels comparable to those at $Re = 5000$. Unfortunately, this low Reynolds number also introduced considerable Reynolds number dependency, as evidenced by the results of Ch. 3 which showed a distinctly larger formation distance and lower vortex shedding force oscillations at $Re = 1000$ compared to $Re = 5000$. Ideally, higher Richardson numbers would be achieved without introducing changes in Reynolds number which affect the flow, by increasing chord length for example, but the maximum that was deemed acceptable was $C = 5$ cm; coupled with $\alpha = 87.5^\circ$ this provided $60C$ of motion, an early shedding onset, and as consistent and prolonged a steady-state as possible. The Richardson number for these runs at $Re = 1000$ was $Ri = 13.3$, which was felt would provide sufficient damping of small scale three-dimensional motions while at the same time retaining enough high Reynolds number behavior to make the results meaningful over a wide range of Reynolds number. Results of a fifty run ensemble at $Re = 1000$, along with a twenty six run ensemble at $Re = 5000$, are shown in Fig. 6.6.

Although the initial C_d peak height is about 0.2 lower in the $Re = 1000$ vs. $Re = 5000$ case (which is within the expected uncertainty at $Re = 1000$ anyway), there is obviously considerable difference in the later time force histories at these two Reynolds numbers. The $Re 1000$ case has a low, long lasting post-acceleration drag minimum followed by a large fast increase in drag level corresponding to the breakdown of

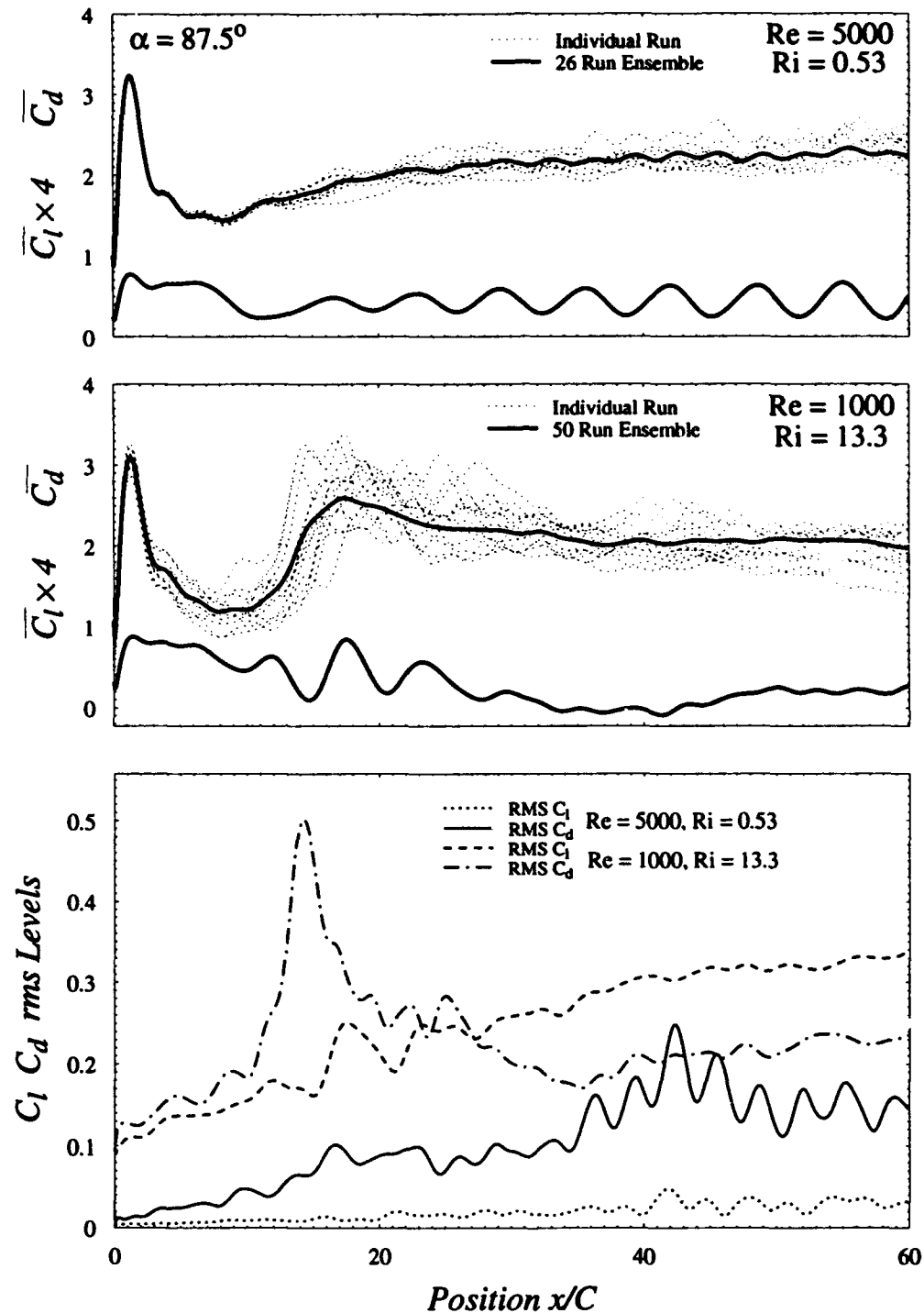


FIG. 6.6 Ensemble average and rms levels with stratification #3 for $Re = 1000$ ($Ri = 13.3$) and $Re = 5000$ ($Ri = 0.53$). $\alpha = 87.5^\circ$, $h/C = 6.8\%$, $AR = 10$ (NBW), $t_a^* = 1.31$. For $20 < t^* < 60$ at $Re = 5000$: $\overline{C_d} = 2.19$, $\overline{C_l} = 0.11$, $\overline{C_{d,rms}} = 0.133$, $\overline{C_{l,rms}} = 0.024$; at $Re = 1000$: $\overline{C_d} = 2.11$, $\overline{C_l} = 0.037$, $\overline{C_{d,rms}} = 0.219$, $\overline{C_{l,rms}} = 0.29$

the initial symmetric bubble. This drag overshoot is accompanied by several large shedding oscillations in the lift, which are rapidly damped after about three oscillations or twenty chord lengths. Unlike the $Re = 5000$ case there is little apparent correlation of vortex shedding following this initial breakdown, although there still appears to be a period $2T_s$ fluctuation in the drag history. Ensemble averaged power spectra, Fig. 6.7 indicate that although there is considerable reduction in the amplitude of the $2S_t$ shedding peak in the drag at $Re = 1000$, the S_t peak in the lift is reduced to the point of being non-existent. As was hypothesized in Ch. 3, this may be due to the considerably increased formation distance at $Re = 1000$ resulting in both a lower base pressure fluctuation and increased base pressure uniformity, reducing the drag fluctuation and effectively eliminating the fluctuating lift component.

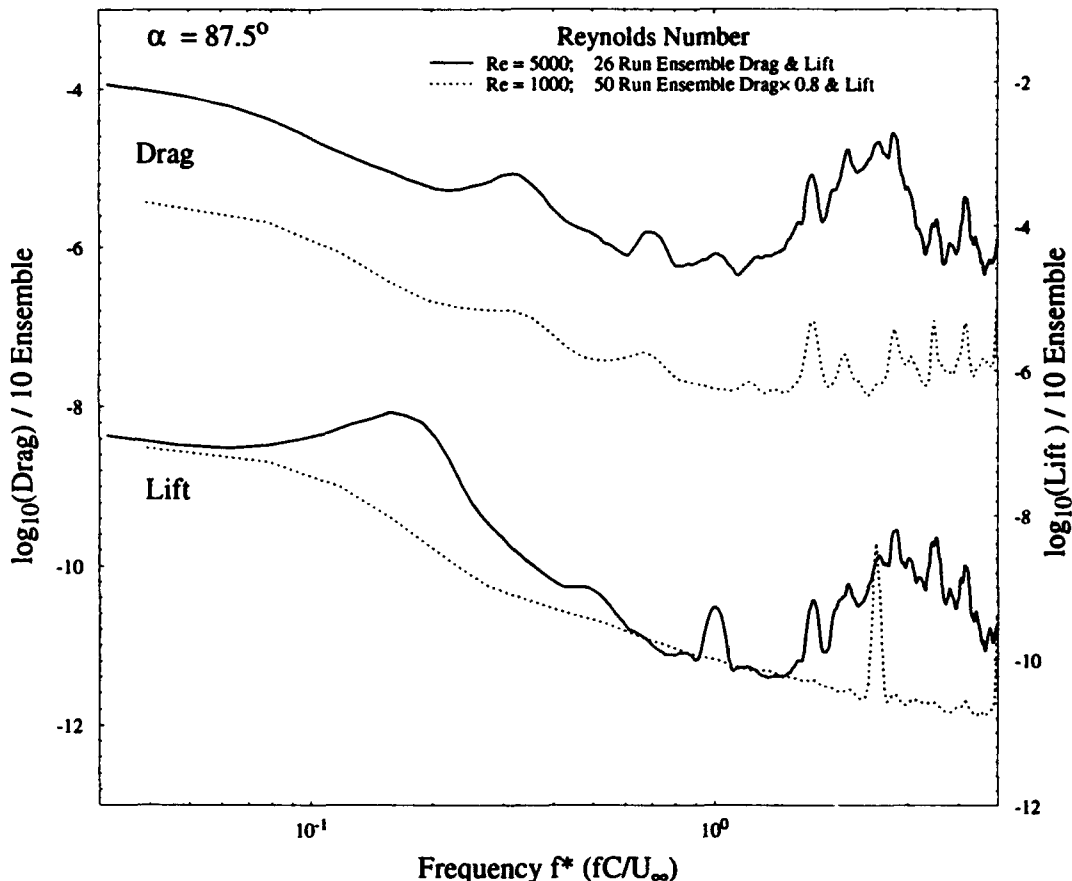


FIG. 6.7 Ensemble averaged power spectra with stratification #3 for $Re = 1000$ ($Ri = 13.3$) and $Re = 5000$ ($Ri = 0.53$). $\alpha = 87.5^\circ$, $h/C = 6.8\%$, $AR = 10$ (NBW), $t_a^* = 1.31$. Spectra are for $20 \leq t^* < 60$

The differences in rms level between $Re = 5000$ and $Re = 1000$ are most pronounced at early times $x^* = 0^+$, with C_d rms at $Re = 1000$ being about 0.1, an order of magnitude higher than at $Re = 5000$. Toward the end of the motion there is considerably less difference, the $Re = 1000$ case having a C_d rms of 0.22 vs. 0.15 for $Re = 5000$. Note again (vis. the unstratified case in Ch. 3) the increased shedding correlation apparent in the C_l , C_d and rms fluctuations. The rms level of the ensemble averaged result is $0.1/\sqrt{50} = 0.014$ for early times at $Re = 1000$, and roughly twice this later in the motion. There is a large sharp peak evident in

the $Re = 1000$ C_d rms level coincident with the breakdown of the initial symmetric bubble and the associated large increase in drag level. Although the peak level does vary somewhat more than the typical variation seen later, it appears that the large increase in rms level is primarily due to shifts in the position at which breakdown occurs, coupled with the large drag increase at that point, rather than very large variations in the post-breakdown C_d overshoot.

The initially very strong shedding oscillations and their subsequent rapid decay is unusual in light of the exact opposite nature of the shedding onset seen at $Re = 5000$. From the unstratified results of Ch. 3, which indicate a large formation distance and little shedding oscillation at $Re = 1000$, it would appear that the strong suppression of shedding is a Reynolds number effect only slightly modified by the stratification. However, the initial strong shedding oscillation may be more indicative of the short formation distance and higher force levels seen at $Re = 5000$, with the stratification serving to increase the "steady-state" force levels considerably above their unstratified or weakly stratified counterparts. Further discussion of these results will be deferred until Ch. 7.

6.8 Stratified Flow Visualizations

In an attempt to understand the initial damping and subsequent low amplitude of shedding at $Re = 1000$, flow visualizations were performed for $\alpha = 90^\circ$ and $\alpha = 87.5^\circ$. Force histories from these runs are shown in Fig. 6.8, with symbols denoting the locations of the flow visualization frames presented in Fig. 6.10 to Fig. 6.12. The sharp peak in the drag at $t^* = 50$ which is evident in both cases results from contact of the lower end of the plate with a high spot on the bottom of the tank. Force histories before this event will be unaffected, but those after are somewhat suspect. Flow visualization results were all taken prior to the plate touching, the whole run length is shown only to preserve the same horizontal scale as was used previously.

These flow visualizations were taken at $Re = 1000$ and $Ri = 5.48$, so show considerably less small scale turbulent motion than those unstratified $Re = 5000$ results already presented. At $\alpha = 90^\circ$ the flow is symmetric up to $t^* = 23$ (Fig. 6.10), when the initial recirculating bubble becomes unstable. As was the case at $Re = 5000$, this is not immediately followed by vortex shedding, instead, a long lasting region of wake instability and slowly decreasing formation distance is evident in remainder of Fig. 6.10. The length to which the formation distance ultimately decreases is considerably longer than at higher Reynolds numbers, although vortices are still being shed into the wake at the end of this formation region, resulting in a far wake not noticeably different than the classical Karman vortex street. These observations strengthen the hypothesis that a lack of fluctuation in the force signals is coupled to large formation distances and consequent base pressure uniformity and lack of fluctuation.

There is a large contrast between this result and that obtained with $\alpha = 87.5^\circ$. Fig. 6.11 indicates that the flow in the later case is highly asymmetrical even at early time ($t^* = 6.89$), with the initial bubble having broken and shedding begun by $t^* = 16.89$. The time sequence shown in Fig. 6.12 shows the bottom vortex is first to be shed, although it is smaller than a typical vortex shed later in the motion. Conversely, the

second (top) vortex shed is somewhat larger than average, and due to its positioning and strength in the wake appears to decrease the formation distance of the next vortex, a sequence which continues until by $t^* \approx 33$ the shedding has regained the large (two or three chord lengths) formation distance seemingly typical of flows at $Re = 1000$.

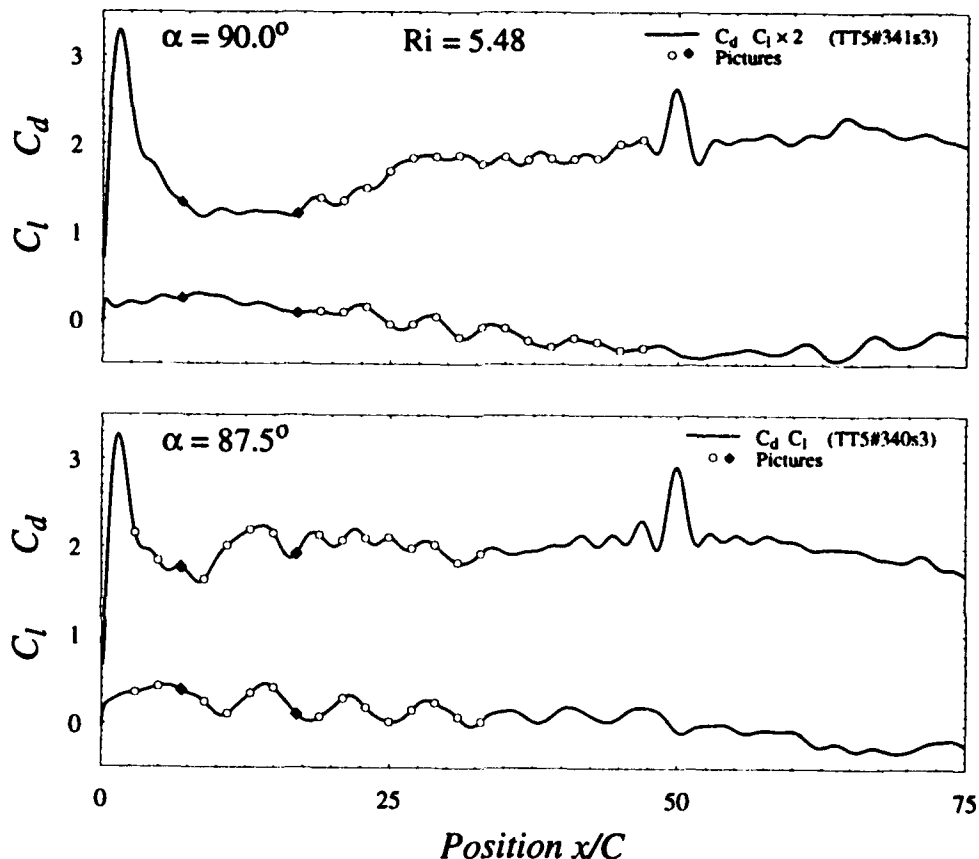


FIG. 6.8 Force histories from stratified X-Y towing tank flow visualization runs. $C = 4\text{cm}$, $Re = 1000$, $Ri = 5.48$, $\mathcal{R} = 10$ (NBW end condition), $h/C = 16.25\%$, $t_a^* = 1.31$, α as noted. Solid symbols denote positions of pictures in Fig. 6.9 and Fig. 6.11; open symbols are frames in Fig. 6.10 and Fig. 6.12

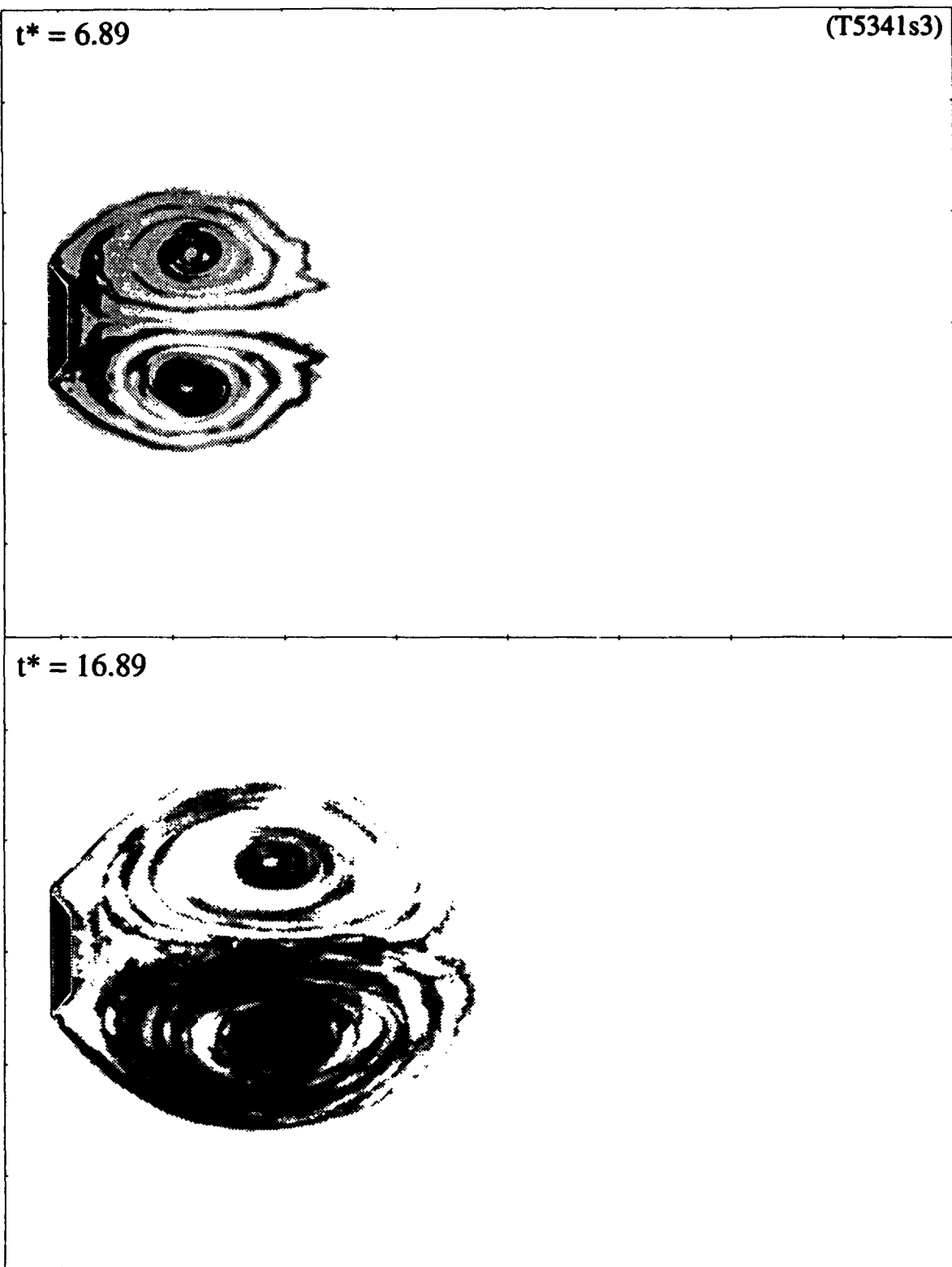


FIG. 6.9 Stratified X-Y towing tank flow visualizations; $C = 4\text{cm}$, $\alpha = 90^\circ$, $Re = 1000$, $Ri = 5.48$, $\mathcal{R} = 10$ (NBW end condition), $h/C = 16.25\%$, $t_a^* = 1.31$, t^* as noted

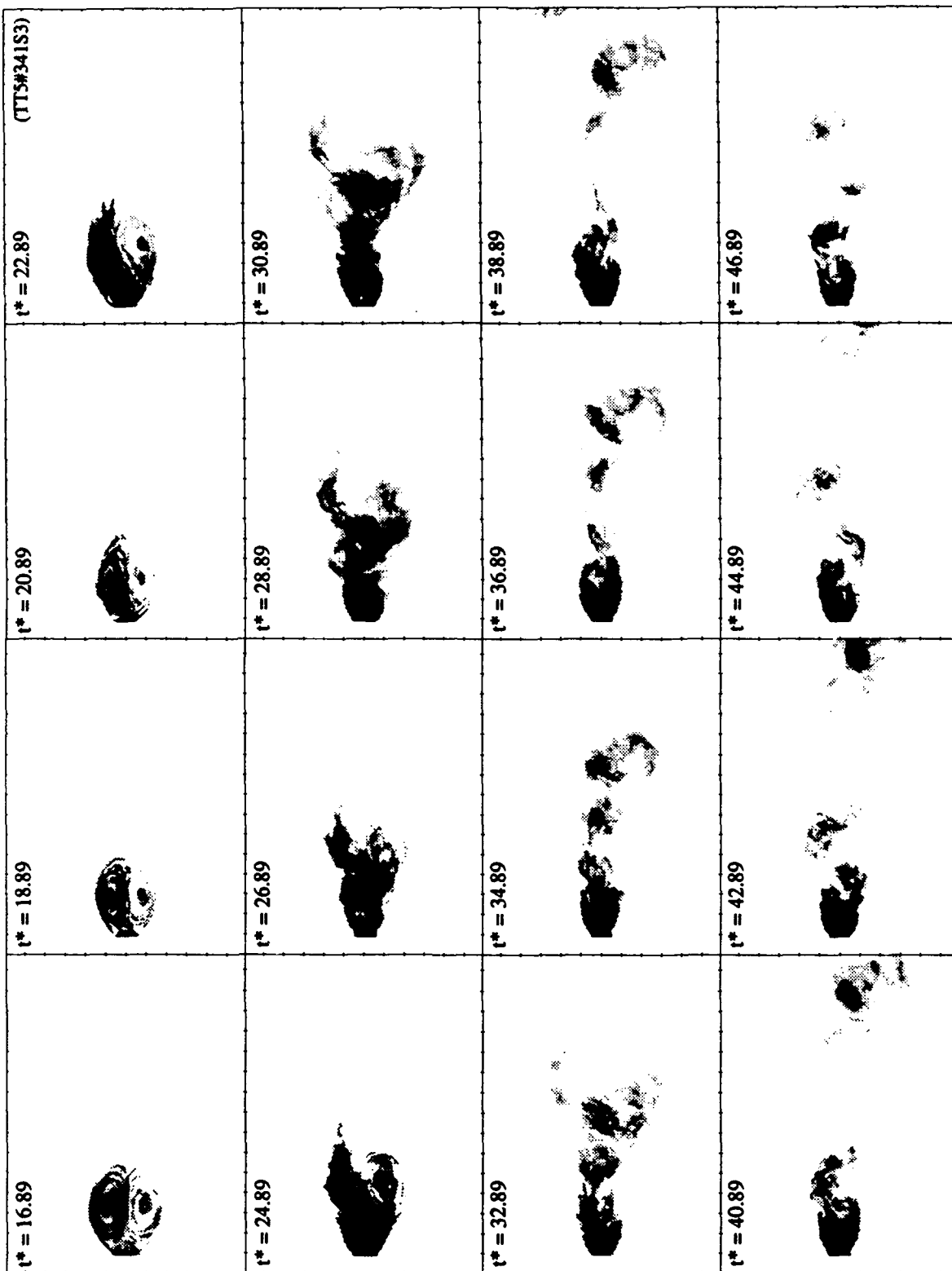


FIG. 6.10 Stratified X-Y towing tank flow visualizations; $C = 4\text{cm}$, $\alpha = 90^\circ$, $Re = 1000$, $Ri = 5.48$, $AR = 10$ (NBW end condition), $hC = 16.25\%$, $t_a^* = 1.31$, t^* as noted

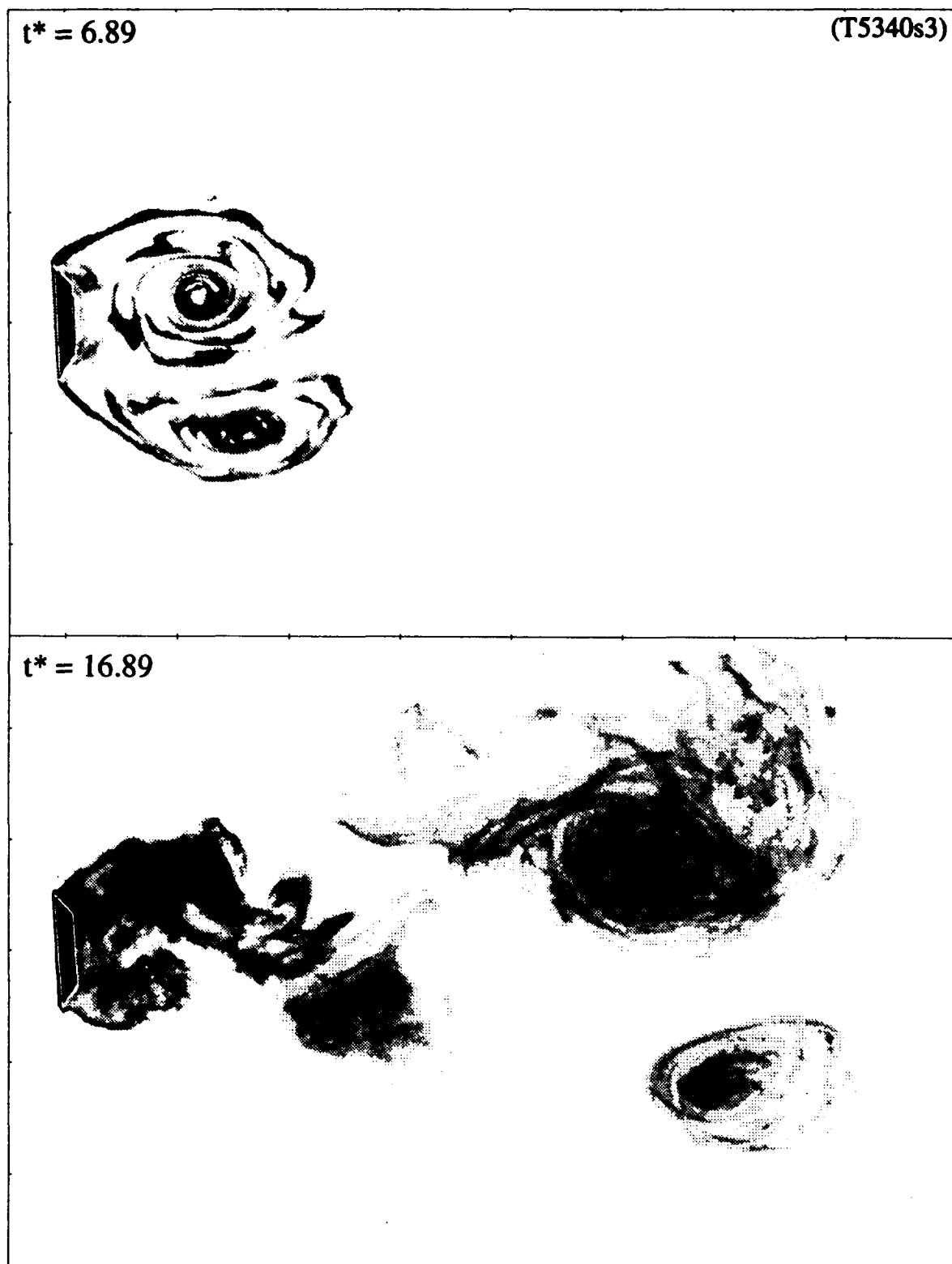


FIG. 6.11 Stratified X-Y towing tank flow visualizations; $C = 4\text{cm}$, $\alpha = 87.5^\circ$, $Re = 1000$, $Ri = 5.48$, $AR = 10$ (NBW end condition), $h/C = 16.25\%$, $t_a^* = 1.31$, t^* as noted

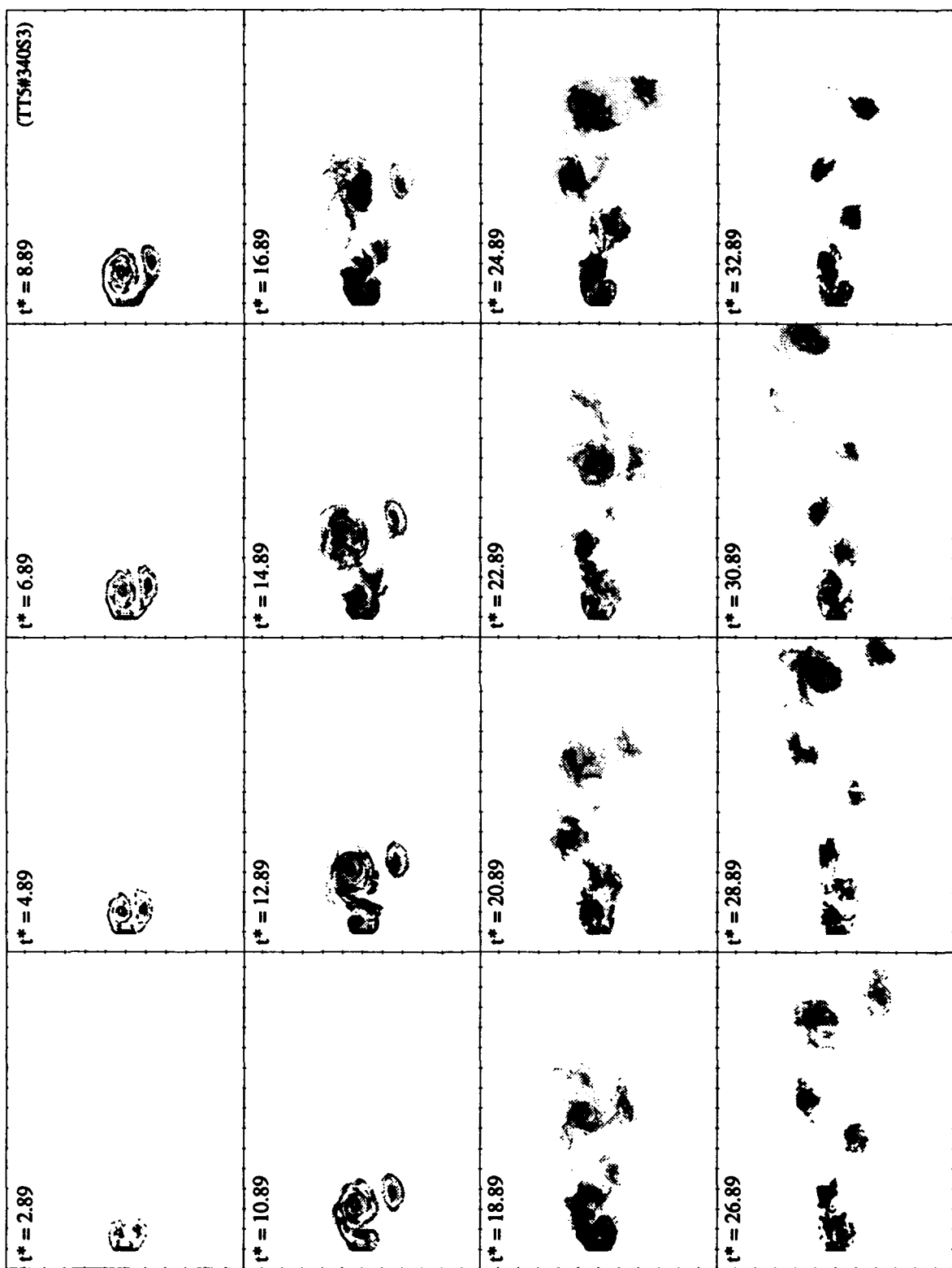


FIG. 6.12 Stratified X-Y towing tank flow visualizations; $C = 4\text{cm}$, $\alpha = 87.5^\circ$, $Re = 1000$, $Ri = 5.48$, $AR = 10$ (*NBW* end condition), $h/C = 16.25\%$, $t_a^* = 1.31$, t^* as noted

6.9 Summary

The level of stratification required to have a noticeable affect on the force histories was considerably higher than had been anticipated. This would indicate that either the stratification was ineffective in damping three-dimensional motions, that small scale three-dimensional motions are not important in the global flow, or that motions smaller than $\frac{1}{7}C$ (the minimum length scale damped at the maximum Richardson number used) are of primary importance.

The suppression of shedding force fluctuations at $Re = 1000$ is not as immediately apparent as in the unstratified case, with several shedding oscillations apparent before the amplitude decreases. It seems likely that the large formation distance and low oscillation levels apparently typical of $Re = 1000$ flows are offset somewhat by the stratification, with the first several shedding cycles being more reminiscent of high Reynolds number ($Re = 5000$) flow, albeit at a higher mean drag level.

With sufficient stratification there is obviously a significant effect in the initial startup regime, with a longer lasting drag minimum and a larger overshoot at the beginning of shedding. How significantly affected the "steady-state" force levels are relative to the unstratified case is one topic to be discussed in the following chapter.

CHAPTER 7

Comparison Of Results

7.1 Preface

This chapter will discuss and compare many of the results presented in the preceding four chapters. If additional details are required, the reader is referred back to the relevant chapter in which the results were originally given. We begin by expanding on some previous points that require some additional emphasis.

In the most general terms, a bluff body submersed in a freestream manifests its presence through changes in momentum of the surrounding fluid. In a time averaged mean sense, a closed recirculating bubble of fluid "attached" to the rear of the body is separated from the surrounding freestream by a dividing streamline. The (unsteady) mechanisms by which low momentum fluid is transferred from this attached region to the high momentum freestream directly affect the forces experienced by the body. For bluff flat plates, two such mechanisms are the Reynolds stresses on the free shear layers (Kelvin Helmholtz instabilities) and on a somewhat analogous but much larger scale, the vortex shedding instability itself. The time averaged mean momentum transfer affects the mean forces, which for a stationary symmetric body in a uniform freestream will be non-zero only in the streamwise direction. On the other hand, the *unsteady* mechanisms affecting momentum transfer can change both the mean values (through changes in net momentum flux) and at the same time give rise to fluctuating forces in both streamwise and transverse directions.

For the purposes of the following discussion we consider the base pressure acting on a normal flat plate ($\alpha = 90^\circ$) of finite thickness hC with downstream edges beveled at angle β . We assume that the Reynolds number is such that viscous forces are negligible relative to pressure forces, and that the pressure on the upstream face remains constant. Further, we initially restrict the discussion to two-dimensional flow.

As noted above, the mean transverse (lift) force is zero, but we envision four ways in which the fluctuating lift can be modified. If the (instantaneous) base pressure is uniform across the chord (or symmetric about the centerline) of the plate, then no lift force will be felt: the only way in which lift can be generated is through a difference in pressure between the upper and lower beveled edges. The lift is proportional to the difference between integrals of the base pressure on the top half and bottom half (or to be exact, top and bottom bevels) of the plate, while the drag force is the sum of these two integrals.

Consider modeling the effects of vortex shedding using mean plus sinusoidal components of base pressure that are uniform but 180° out of phase on the upper and lower halves of the base. Drag force in this case will be constant and proportional to the mean component, while lift fluctuations are proportional to

(twice) the amplitude of the sinusoidal component of base pressure. Thus one way to change the fluctuating lift force is to increase the amplitude of the sinusoidal component. Another is to increase plate thickness; if this was accomplished without affecting the "flow" the lift force will increase simply because the pressure forces act on a larger area.

Now consider a sinusoidal base pressure fluctuation which is still anti-symmetric, but which is chord-wise non-uniform across top and bottom. In this case changing the bevel angle, which essentially re-distributes the area on which lift is generated (again assuming these could be accomplished without affecting the flow), will change the lift fluctuations due to the non-uniform pressure distribution being integrated over differing areas.

So far only the fluctuating lift has been affected; drag force is proportional to the mean base pressure, which has remained constant. Consider now a non-uniform, non-sinusoidal base pressure fluctuation in which the minimum base pressure peaks are smaller than the maximum peaks; or equivalently, a sinusoidal fluctuation which acts on more or less than half the plate depending on the phase of the "shedding." In this case the drag will have a component fluctuating at twice the shedding period, and an additional mean component due to the non-zero mean of the non-sinusoidal pressure fluctuation. Changes in the amplitude of the shedding will now affect both the amplitude of the lift fluctuation and the *mean* as well as fluctuating drag components. Although the drag can be forced to fluctuate (without an increased mean level) if the top and bottom halves are out of phase by something other than 180° , this fluctuation will occur at the shedding frequency, and no physical mechanism has been seen which would give rise to such fluctuations.

Now extend the above arguments to a "quasi two-dimensional" flow case in which the plate has spanwise length S , but the "shedding" at each spanwise location is uncorrelated, differing randomly in phase from that at any other location. Spanwise integration in this case is exactly analogous to an integration in time over one shedding period. The instantaneous forces exerted on the plate in such a flow are constant and equal to their time averaged mean value, which for lift is zero and for drag is proportional to the mean base pressure plus any mean base pressure change due to the non-uniform/non-sinusoidal nature of the shedding. There can be no fluctuations in either the lift or the drag in such a flow. As spanwise correlation increases, the mean drag level will remain unchanged, but *fluctuations* in both lift and drag will increase, eventually attaining their "two-dimensional" values when shedding is perfectly correlated spanwise. Essentially, spanwise uncorrelated flow results in an (integrated) *symmetric* (although not necessarily uniform) and *steady* base pressure distribution .

Obviously a real flow is much more complex, shedding is only one of several possible mechanisms of momentum transfer; each of which has its own effects on mean and fluctuating force levels. Increasing spanwise correlation in a real three-dimensional flow could be expected to fundamentally alter the nature of the shedding at each spanwise location, rather than merely bringing each location more into phase. Due to the increase in spanwise vorticity component accompanying the decrease in three-dimensionality the vortices will roll up in closer proximity to the body (decreased formation distance) giving higher base pressure fluctuation

levels and a decreased mean base pressure, resulting in a higher *mean* drag and higher lift and drag fluctuation levels. Experimentally, it is not clear if it is possible to have increased lift and drag fluctuations which are not accompanied by an increased mean drag level, although it is possible to have drag fluctuations (with a symmetric base pressure) without accompanying lift fluctuations.

7.2 Comparison to Previous Results

Although numerous flow visualizations of unsteady starting motions of normal flat plates are available in the literature (see for example Prandtl and Tielens, 1932 or Taneda and Honji, 1971), these are typically performed at low Reynolds number ($Re \ll 1000$) and do not include force measurements. Only two previous unsteady high Reynolds number experimental force measurement results could be found (Sarpkaya, 1992) and only one of these, Sarpkaya and Kline (1982), involved a similar geometry to that used for these experiments. The other, Sarpkaya and Ihrig (1986), used a 62% thick rectangular cylinder. In both cases a blow down vertical water tunnel was used with test bodies spanning a square test section, force measurement accuracy was claimed as $\pm 5\%$, and the velocity was constant "within $\pm 0.5\%$," although no velocity uncertainty was quoted and no blockage corrections were performed. Details of data filtering (intentional or otherwise) were not provided, and it was difficult to establish acceleration times and velocity profiles for the two results, although a best estimate would be $t_a^* = 0.18$ for Sarpkaya and Kline and $t_a^* \simeq 0.43$ for Sarpkaya and Ihrig. Both of these results are compared to "typical" X-Y towing tank results at $\alpha = 90^\circ$ in the top plot of Fig. 7.1 while the results of Sarpkaya and Ihrig at $\alpha = 100^\circ$ are compared to current results at $\alpha = 85^\circ$ and 95° in the bottom plot.

Except for the initial peak height, the agreement to Sarpkaya and Ihrig at $\alpha = 90^\circ$ is very good, given the considerable differences in body geometry. The larger "steady-state" drag level is directly attributable to the increased body thickness (Nakaguchi, 1968). There is a large discrepancy between the Sarpkaya and Kline result and both Sarpkaya and Ihrig and the current results for early times; given the estimated values of t_a^* the initial peak heights are considerably lower than those found in the current experiments. The "steady-state" level in Sarpkaya and Kline is much higher than either of the other two results, and the qualitative post-acceleration drag minima is not seen. For $\alpha = 85^\circ$ and 95° the agreement of the current results to those of Sarpkaya and Ihrig at $\alpha = 100^\circ$ is again very good; a large part of the increased level of lift fluctuation is attributable to the larger angle of attack and much thicker ($\times 6$) body geometry in the latter case. Given the scarcity of unsteady force results in general, it is perhaps not surprising that no published stratified results could be found for comparison to the experiments of Ch. 6.

As was noted in Ch. 4, results obtained in the free surface water tunnel are in generally good agreement with past steady-state results, many of which are given in Fig. 1.1. Although the results presented here have not been corrected for the effects of blockage, when they are corrected (Sec. 4.5) they are within $\pm 2\%$ of the force levels found by (for example) Fage and Johansen, with a similar agreement in Strouhal number.

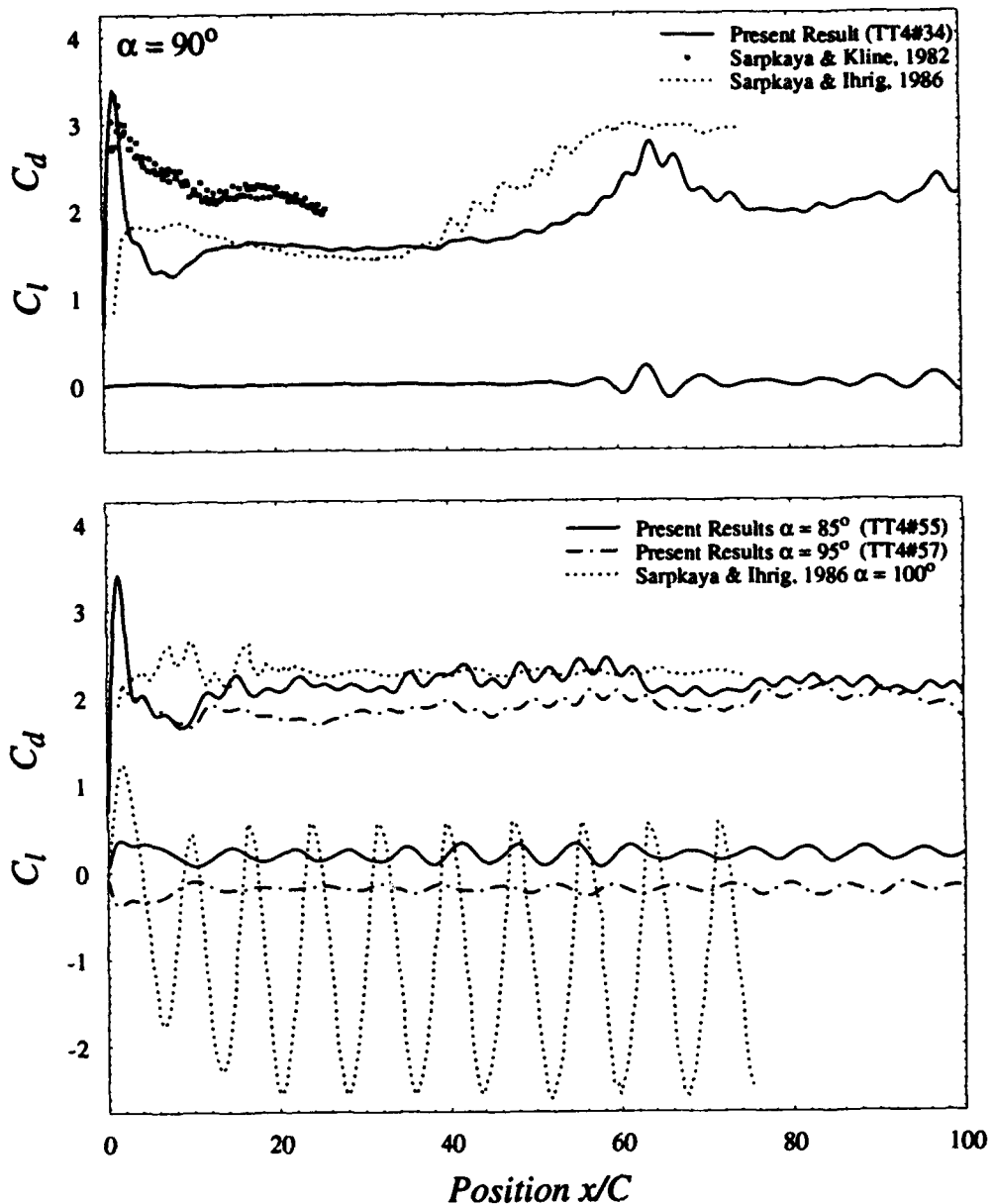


FIG. 7.1 Experimental C_d comparison to previous results. For top plot $\alpha = 90^\circ$: Solid line; current results ("Typical case" TT4#34), $AR = 17$, $h/C = 10.3\%$, $Re = 5000$, $t_a^* = 1.31$. Symbols; Sarpkaya & Kline (1982) $AR = 8$, $h/C = 11\%$, $Re = 21000$, $t_a^* \approx 0.18$; Dotted line: Sarpkaya & Ihrig (1986) $AR = 28$, $h/C = 62\%$ (Rectangular Cylinder), $Re = 20000$, $t_a^* \approx 0.43$. For lower plot: Solid & Chain lines; current results, $\alpha = 85^\circ$ (TT4#55) & $\alpha = 95^\circ$ (TT4#57), $AR = 10$, $h/C = 10.3\%$, $Re = 5000$, $t_a^* = 1.31$. Dotted Line; Sarpkaya & Ihrig (1986), $\alpha = 100^\circ$, $AR = 28$, $h/C = 62\%$ (Rectangular Cylinder), $Re = 20000$, $t_a^* \approx 0.43$

The measurement of the τ_o characteristic of the long period shedding modulation is unique to this thesis, so no similar data exists for comparison, although both Schewe (1983) and Szepessy (1992) have noted and studied similar long period modulations for circular cylinders; their results will be discussed in more detail below.

Finally, the current 2d numerical model is compared to the results of Chua (1990) and Dutta (1988) in Fig. 7.2. The post-acceleration drag minimum is slightly higher for the current results, but this is likely due to the finite thickness of the current model (5%) relative to the other two results which used infinitesimally thin plates. The point at which the drag level suddenly increases and shedding begins differs in the three cases, but as was pointed out in Ch. 5, the shedding onset is known to be sensitive to small perturbations (Kuwahara, 1973). Steady-state force results are comparable in all three cases, with long time mean drag levels of 3.6 for Chua, 3.39 for Dutta and 3.26 for the current model. Typical Strouhal numbers do not compare as well; the current result giving 0.121 vs. 0.11 for Chua and 0.154 for Dutta.

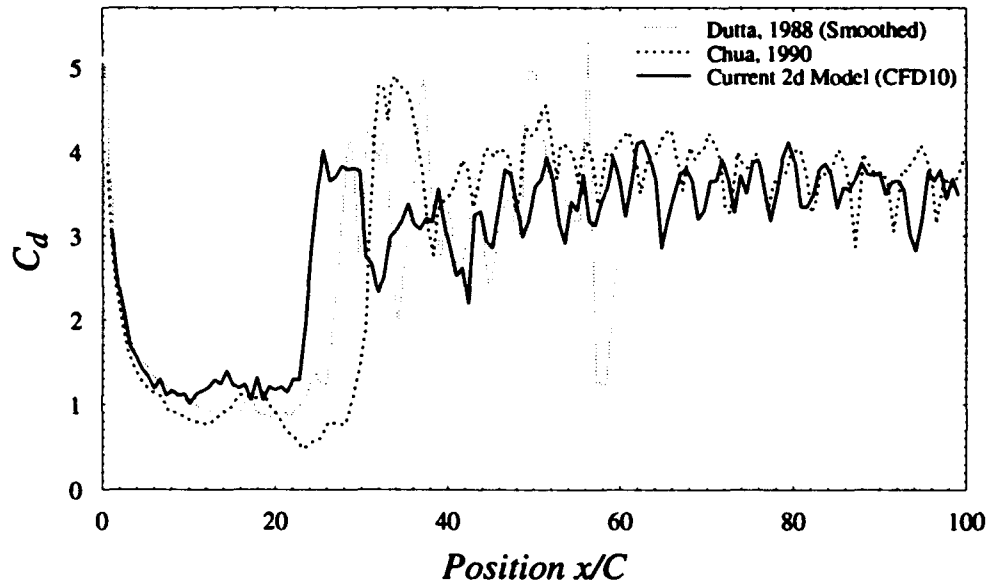


FIG. 7.2 Numerical model C_d comparison to different vortex element models. Solid line: current results, $\alpha = 90^\circ$, $t_a^* = 0.0$, $h/C = 5\%$. Dotted line: Chua (1990), $h/C = 0$. Grey line: Dutta (1988), $h/C = 0$

7.3 X-Y Towing Tank And Free Surface Water Tunnel Results

7.3.1 Unsteady Starting Regime

Consider first the individual $\alpha = 90^\circ$ X-Y towing tank experimental result shown in Fig. 7.3. One of the surprising results to come from this case was the long and complex force history apparent prior to the achievement of "steady-state shedding".

For small enough t_a^* , an initial peak in the drag accompanies the end of the acceleration region, followed by a drag minimum which is associated with a closed symmetric wake bubble with very little momentum transfer to the freestream. Both of these results were expected, but the subsequent region with a low drag ($C_d \approx 1.6$) and no vortex shedding force oscillation was not. This result was repeatable, as can be seen from the ensemble averaged result in Fig. 7.3, which indicates that this region typically lasted for

twenty to thirty chord lengths of motion before the onset of vortex shedding and an increase in the mean and fluctuating force levels. Flow visualizations taken throughout this region (Fig. 3.23 and Fig. 3.24) indicate a large formation distance (of perhaps six chord lengths) containing essentially stagnant fluid being pulled along by the plate, with vorticity being shed into the far wake at the downstream end of this region. Later in the motion the far wake actually looks fairly typical of the classical picture of a vortex street; only close to the body are the dynamics of the near wake and formation region considerably different.

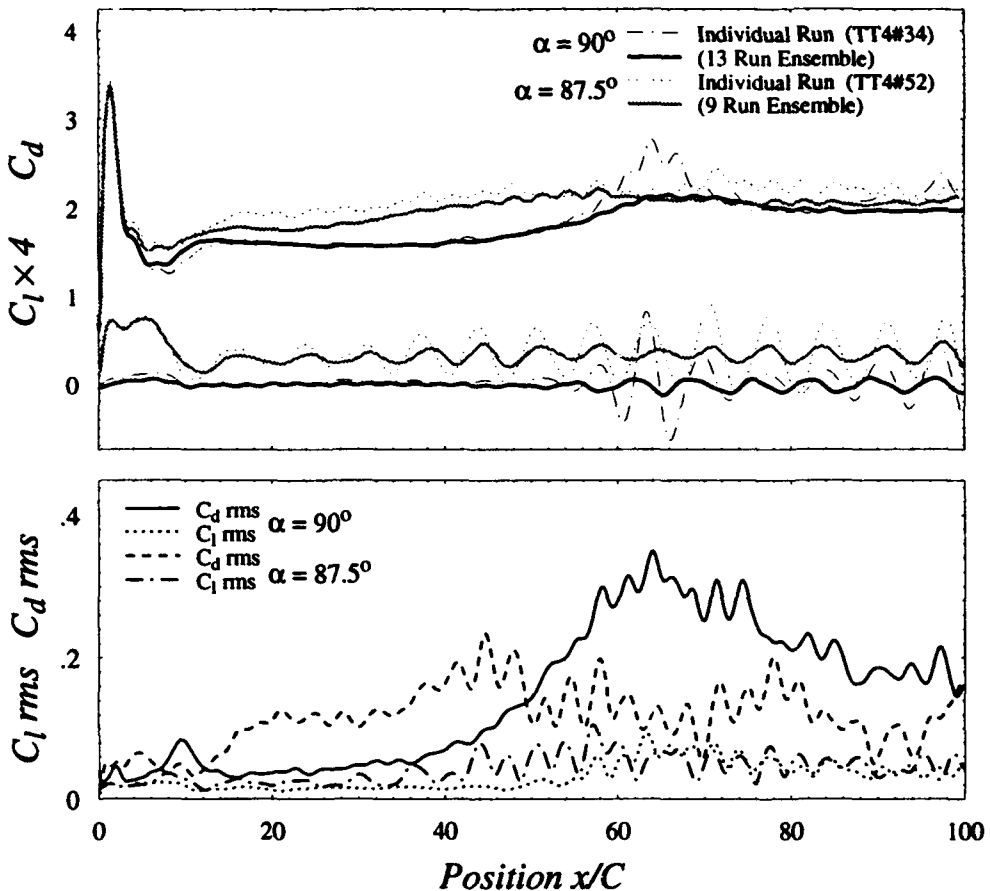


FIG. 7.3 Effects of angle of attack for ensemble averaged results at $Re = 5000$ with $h/C = 10.3\%$, $t_a^* = 1.31$, α as noted. At $\alpha = 90^\circ$ thin chain line is individual run; thick solid line is 13 run ensemble. For $\alpha = 87.5^\circ$ thin grey line is an individual run; thick dotted line is a 9 run ensemble

It appears from flow visualization results that the flow during this regime is very similar to that about a normal flat plate with a wake splitter plate, see for example Arie and Rouse (1956). Roshko (1992) proposes a model of this flow based on a balance of stresses on the free shear layers (which at high Reynolds number are primarily Reynolds stresses, rather than viscous stresses), the base pressure on the plate, and a pressure ($\equiv p_\infty$) at the "reattachment region," or downstream (mean) stagnation point at the end of the bubble. This gives a formation length of $8.1C$ and $C_d = 1.47$ for steady flow with no vortex shedding. Given that for the current result the downstream end of the recirculating bubble is actively (and unsteadily) shedding vorticity

into the far wake, and that the assumption of a contribution to the pressure integral at the reattachment region of $p_\infty C$ was stated as being somewhat questionable to begin with, the agreement $C_d = 1.47$ vs. $C_d = 1.6$ is remarkably good. The somewhat shorter formation distance observed in the experiments ($6C$ vs. $8.1C$) is consistent with a larger observed drag coefficient, and may reflect the unsteady nature of the downstream boundary condition.

Exactly *why* this non-shedding region consistently follows the unsteady start of a normal plate is not entirely clear. One must assume that something in the initial condition inhibits the immediate onset of vortex shedding and contributes to the continued symmetry of the wake for large times. This may be due to either an lack of spanwise coherence (three-dimensionality) in the breakup of the initial symmetric bubble, or the almost perfect symmetry of the starting flow. The former hypothesis is supported by streakline flow visualizations performed by Noca (1991), which indicate that at the Reynolds numbers considered here the onset of three dimensional motions occurs before the end of the initial symmetric region, and that the breakdown of this region is highly three-dimensional in nature.

It appears most likely that the initial breakdown of the recirculating bubble is highly three-dimensional in nature (even if the subsequent symmetric flow is not), and tends to leave the wake without a coherent spanwise vorticity distribution on which to base initial vortex shedding. It is interesting to note that the drag level $C_d \approx 1.6$ in this region is very similar to the level of $\bar{C}_d \approx 1.45$ (cf. the above result of Roshko) seen in the non-shedding regions of low aspect ratio free surface water tunnel results with intermittent shedding, Fig. 7.4. The non-shedding regions of this flow are known from free surface water tunnel flow visualization results to be highly three-dimensional, with little or no far wake instability present in the vorticity shed into the wake. This may indicate that by the time vorticity reaches the far wake, or at least the end of the (long) formation region, sufficient mixing has taken place to largely inhibit the instability of the vorticity which is being shed. Or from another viewpoint, that the velocity profile has become sufficiently uniform to be relatively stable by the time it reaches the far wake. This would support the supposition that the non-shedding flow in the X-Y towing tank immediately following the breakdown of the initial symmetric bubble is highly three-dimensional and spanwise incoherent.

Introducing some spanwise uniform disturbance to the flow might then be expected to increase coherence along the span, or at least promote some spanwise uniformity in the initial breakdown of the symmetric bubble. A slight change in angle of attack from $\alpha = 90^\circ$ is one such disturbance, although this has an additional effect of introducing an asymmetry and so would have an effect even if the flow were perfectly coherent spanwise and the lack of shedding was due entirely to symmetry.

The effects of changing angle of attack can be seen in the individual and ensemble averaged results for $\alpha = 87.5^\circ$ in Fig. 7.3. The initial peak level is almost identical in both $\alpha = 90^\circ$ and $\alpha = 87.5^\circ$ cases, but the $\alpha = 87.5^\circ$ results have a consistently higher post-acceleration drag minimum, apparently due to the

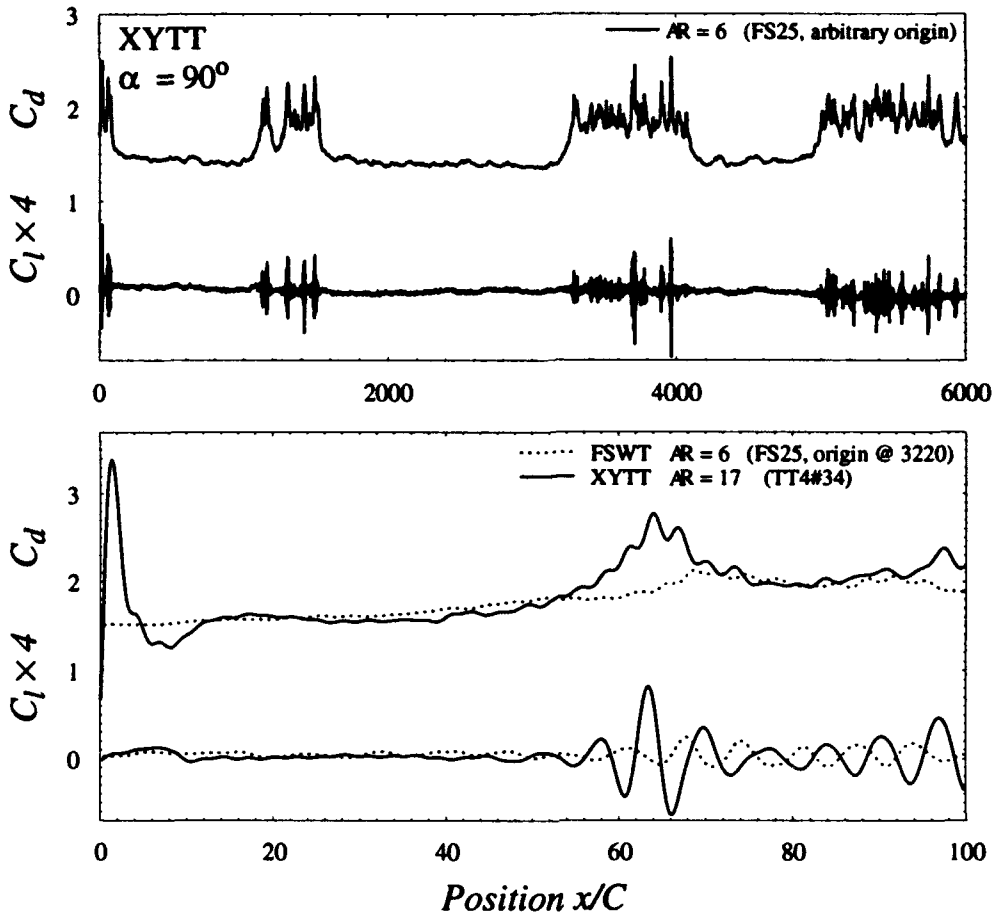


FIG. 7.4 Comparison of drag levels during intermittent shedding in free surface water tunnel and early startup up in X-Y towing tank with $\alpha = 90^\circ$, $Re \approx 5000$, $h/C = 10.3\%$. Bottom plot solid line is X-Y towing tank result ($t_a^* = 1.31$); dotted line is portion of free surface water tunnel result during shedding onset

asymmetry of the initial vortex pair formed behind the plate. After the breaking of this initial bubble, vortex shedding begins almost immediately, accompanied by an increase in the rms level (bottom plot of Fig. 7.3) which then remains fairly constant throughout the run. Note the run to run shedding repeatability evident in the fluctuations in both ensemble averaged results and the rms levels for $\alpha = 87.5^\circ$, which indicate that the shedding is beginning at roughly the same point for each run. Note too that the first few shedding cycles are of slightly decreased amplitude, increasing slowly to their steady-state level at roughly $t^* = 40$.

The $\alpha = 87.5^\circ$ shedding onset can be contrasted with the $\alpha = 90^\circ$ case, where the shedding appears to build up almost exponentially beginning at roughly $t^* = 40$, with an accompanying drag peak (see the individual $\alpha = 90^\circ$ run in Fig. 7.3) and a large increase in the drag rms level. This rms increase is more a consequence of run to run variations in onset time coupled with the large drag overshoot than it is indicative of the steady-state rms level, which by the end of the run is comparable to that seen in the $\alpha = 87.5^\circ$ case. The exponential nature of the onset can be seen more clearly in the top plot of Fig. 7.5, which gives the rectified lift force of the "typical" $\alpha = 90^\circ$ case on a logarithmic scale.

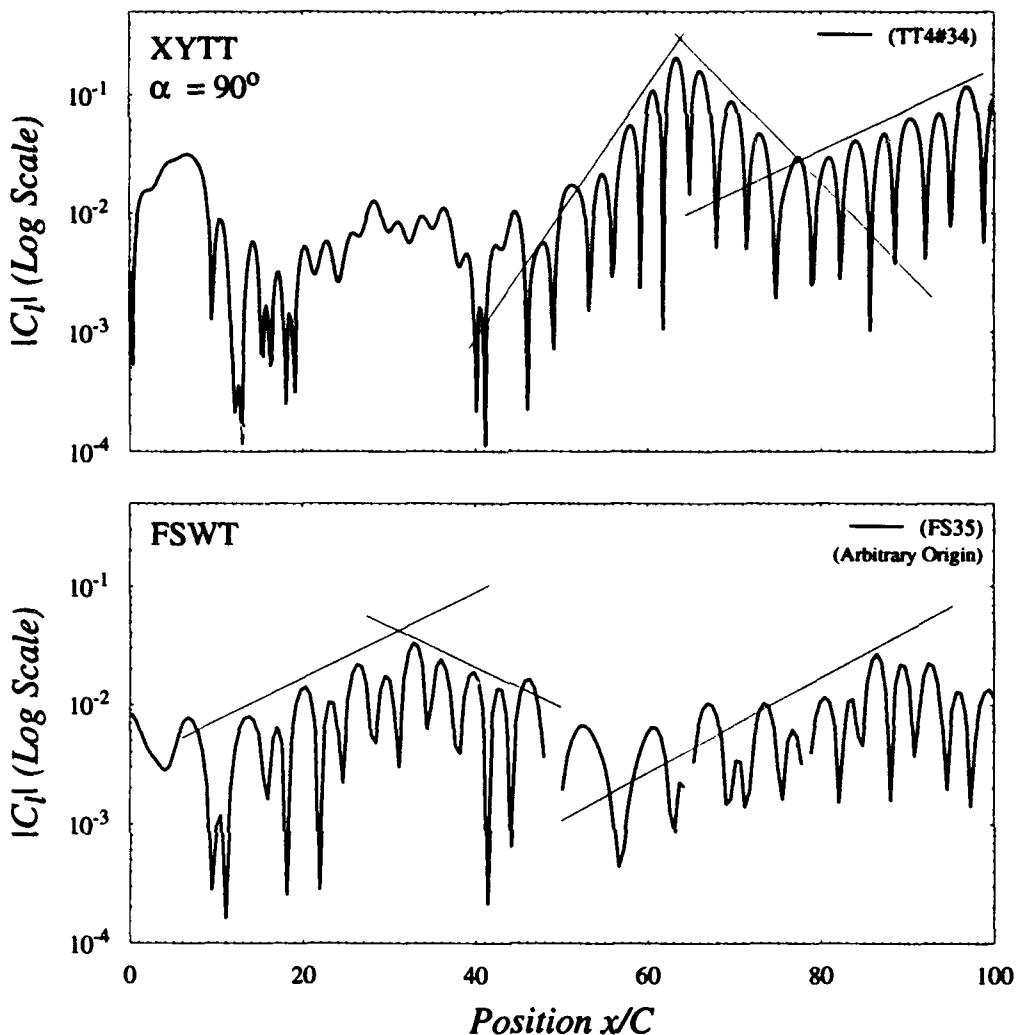


FIG. 7.5 Examples of exponential shedding onset in X-Y towing tank and free surface water tunnel with $\alpha = 90^\circ$, $Re \approx 5000$, $h/C = 10.3\%$

We may speculate that the exponential build up and the large overshoot in amplitude which accompanies the first few vortices shed (and to some extent the low amplitude of the first few shedding cycles in the $\alpha = 87.5^\circ$ case) are indicative of the importance of far wake vorticity in regulating the near wake shedding process. Although the first few vortices are shed at a fairly constant *frequency*, their wavelength is continuously increasing, as can be seen from the flow visualization results of Fig. 3.24, which show a continuous slow decrease in formation length as the amplitude of the shedding builds. In the absence of two opposite sign vortices in "normal" (steady-state) proximity in the far wake, the nascent vorticity in the near wake is influenced to a greater extent by the (opposite sign) vortex which has just been shed. This vortex has the effect of confining the nascent vortex to roll up somewhat closer to the plate than it did itself, with a resulting increase in wavelength; this process repeats until the vortices reach the plate and begin rolling up more closely than in steady-state flow, with the consequently higher mean and fluctuating force levels seen during the

shedding onset. The flow cannot sustain these (possibly two-dimensional?) force levels, and so relaxes to a more uniform steady-state shedding. Another possible interpretation of this process is that of a far wake instability propagating upstream toward the plate until it is close enough that the instability in some fashion couples with the plate in the near wake and vortex shedding begins.

7.3.2 Extrinsic Effects - Large Scale Three Dimensionality

Both aspect ratio and end condition were seen to have large effects on the global flow in the X-Y towing tank and free surface water tunnel experimental results. Changes were made to both of these parameters to effect changes in the large scale structure and note effects on the resulting flow.

Several of the observations made for various end conditions were consistent with past results obtained by other researchers. Slaouti (1981) showed that a through-free-surface upper boundary was optimum in terms of minimizing three-dimensional motions and being essentially transparent to the flow. It is important that the free surface be clean in this case, since surface contaminants can introduce a no-slip condition and the accompanying requirement that vortex lines be parallel to the free surface. If the surface is clean, then not only does it distort to match whatever pressure the flow imposes, but vortex lines end perpendicular to it and suffer no distortion from their preferred geometry.

Both the near bottom and false bottom lower end conditions appeared to provide reasonably two-dimensional results, again in agreement with Slaouti. The near-bottom-wall condition in the towing tank was exceptionally good, owing to the lack of an oncoming boundary layer, although it was important that the gap between the plate and the wall be kept small as possible to minimize flow around the end of the plate.

In most cases the combination of a free surface upper end condition, a large ($AR > 10$) aspect ratio and one of the above two lower end conditions provided a flow which was almost independent of aspect ratio. Thus for $AR \gtrsim 10$, they formed the most "nominally two-dimensional" flow obtained, in the sense of a flow with minimal extrinsic three-dimensional motions. For $AR < 10$ they provided increasing amounts of extrinsic three dimensional motion to the otherwise nominally two dimensional flow.

A free lower end, on the other hand, gave the largest three-dimensional effects, increasing the base pressure and in many cases suppressing organized vortex shedding altogether (Fig. 3.15). For large enough aspect ratio the effect of a free end could be negated somewhat, with at least some portion of the plate being reasonably two dimensional.

End plates somewhat smaller than those recommended by Stansby (1974) for circular cylinders provided an intermediate end condition; at sufficiently low aspect ratios they were less effective than the ABW end condition in suppressing large scale three-dimensional motions (although they still had significantly lower amounts of three dimensionality than did the free end), while for sufficiently high aspect ratios ($AR > 10$) they behaved similarly (Fig. 3.15). Fox and West (1990) indicate that effects of (properly sized) end plates

extend roughly 3.5 diameters inboard, with two-dimensional flow over the remaining span of the cylinder. Thus to a greater extent than the *NBW* or *FBW* conditions the end plates provided a method of modifying the relative amount of three dimensionality for differing aspect ratio.

For a fixed aspect ratio, angling of the end plate or false bottom (Williamson, 1989) gave yet another technique of modifying extrinsic effects. At $\mathcal{A}R = 6$ in the free surface water tunnel (Fig. 4.16) the shedding was intermittent with a *FBW* parallel to the oncoming flow. Angling the false bottom outward $+5^\circ$ (decreasing base pressure) resulted in consistent shedding, albeit with a large amplitude long period modulation. An inboard angle of -5° (increasing base pressure) eliminated shedding entirely. Another example is provided in Fig. 3.16, which shows a qualitatively similar result for an unsteady starting motion of a model with angled end plates. The exact mechanism by which the flow is modified in these cases is not entirely clear. The fully separated flow on the angled end walls should in some sense provide a similar (turbulent) boundary condition for either inboard or outboard angles. It may be that the primary influence of the end plate is to change the base pressure uniformly along the span, with resulting changes in the free shear layer geometry and vortex shedding behavior.

A similar base pressure effect is seen by changing aspect ratio with a consistent end condition, although for the free surface water tunnel results (which showed the greatest effects) this had the unfortunate side effect of considerably changing blockage. Nonetheless, for $\mathcal{A}R < 15$ there was a marked increase in base pressure (decrease in C_d) with decreasing aspect ratio, which resulted in the intermittent vortex shedding at $\mathcal{A}R = 6$ discussed above and the elimination of vortex shedding for $\mathcal{A}R = 4$. For additional details of end condition and aspect ratio effects, the reader should refer back to Ch. 3 or Ch. 4.

7.3.3 Reynolds Number Effects

When this research was originally undertaken, it was felt that the flow about a sharp edged flat plate should be essentially Reynolds number independent for $Re \gtrsim 1000$ (although admittedly Flaschbart (1935) placed the minimum Reynolds number at 3000 based on changes in drag coefficient below this level). Although they are not directly related to studies of flow three dimensionality, the Reynolds number effects seen in Fig. 7.6 are important since they directly impact the stratified flow results to be presented below. It was very difficult to accurately measure force levels at low Reynolds numbers (see Sec. 3.2) and many corrections had to be applied, with the result that lift in particular was inaccurate, since it could not be corrected as easily as the drag result. Relative to the $Re = 5000$ result, the $Re = 1000$ case shows a reduced mean drag level (consistent with Flaschbart) and a lack of shedding oscillation in either the lift or the drag (the large negative lift is likely a consequence of the force errors referred to above). Along with the (stratified) flow visualization results of Fig. 6.12 these would indicate that the vortices are forming farther downstream (larger formation length), with a correspondingly steadier and more uniform base pressure. Note the increased rms levels in the $Re = 1000$ case, indicative of the low force amplitudes and corresponding measurement uncertainties, as well

as the run to run repeatability apparent in the form of fluctuations in the ensemble averaged force and rms levels at $Re = 5000$. Although it is more evident in the stratified results to be presented below, it appears that the shedding force fluctuations are reduced to a greater extent in the lift than they are in the drag (see Fig. 6.7), possibly because the shedding is occurring at the downstream end of a large formation region, which tends to make the base pressure fluctuations which do occur more uniform across the breadth of the plate.

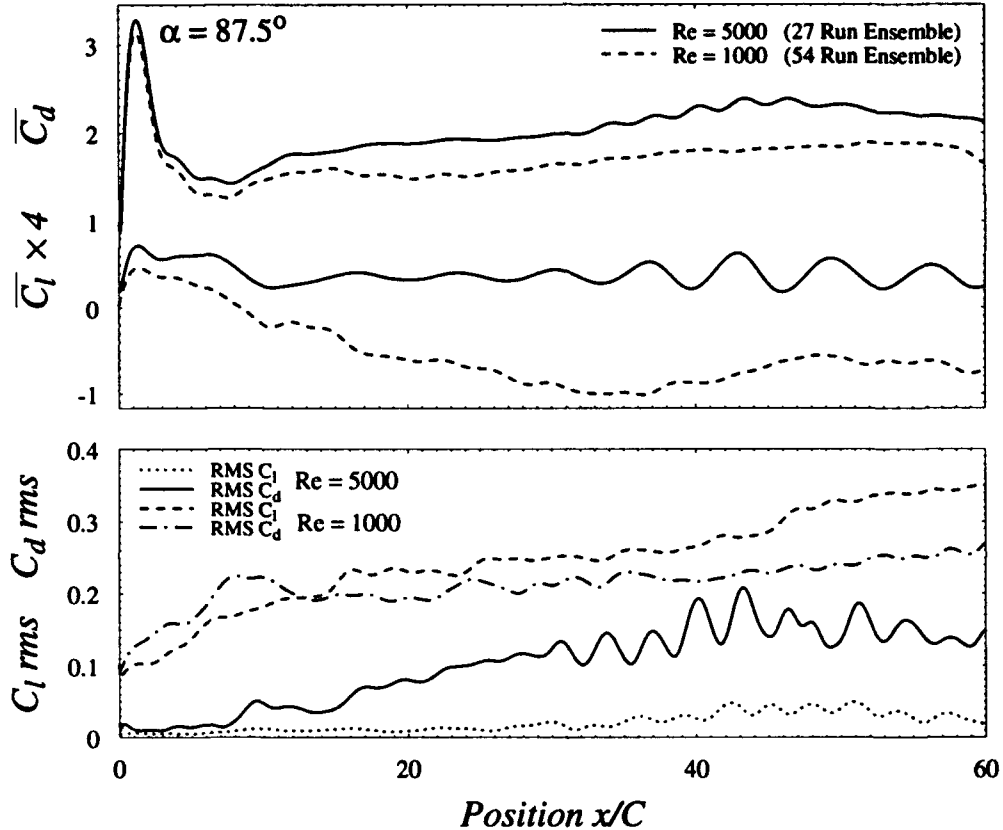


FIG. 7.6 Comparison of ensemble averaged experimental runs at $Re = 5000$ and $Re = 1000$ with $\alpha = 87.5^\circ$, $h/C = 6.8\%$, $t_a^* = 1.31$. Solid line is 27 run ensemble at $Re = 5000$; dashed line is 50 run ensemble at $Re = 1000$. Rms levels as noted

7.3.4 Shedding Modulation

The "steadiness" of the steady-state shedding achieved at the end of the towing tank runs was somewhat in doubt, as can be seen from Fig. 7.7, which shows the long period shedding amplitude modulation which was apparent in both the X-Y towing tank and free surface water tunnel results. This modulation has been seen and commented on before, particularly in regard to flow around circular cylinders, but it is only recently that any direct investigations have been published (Schewe, 1983 and Szepessy, 1992). From flow visualization in the free surface water tunnel it appears that the shedding modulation is accompanied by (or results from) a slow change in formation length. This modulation occurs on a time scale six to ten times that of the vortex shedding period, and results in a 20% fluctuation in drag level and a corresponding large change in rms lift

amplitude. Increasing aspect ratio tends to decrease the period of the modulation up to a point, but for $\mathcal{AR} > 10$ the period is fairly constant at about $6 T_s$, indicating that in the limit of infinite aspect ratio (nominally flow) this modulation may still exist. The increased period with decreased aspect ratio may be reflective of other effects, such as changes in base pressure from decreasing blockage, which lead eventually to the intermittent shedding at $\mathcal{AR} = 6$ referred to above.

Angling of the false bottom (particularly outward) at constant aspect ratio tended to increase the period of the modulation, indicating that changes in large scale three dimensionality or base pressure may also affect the modulation.

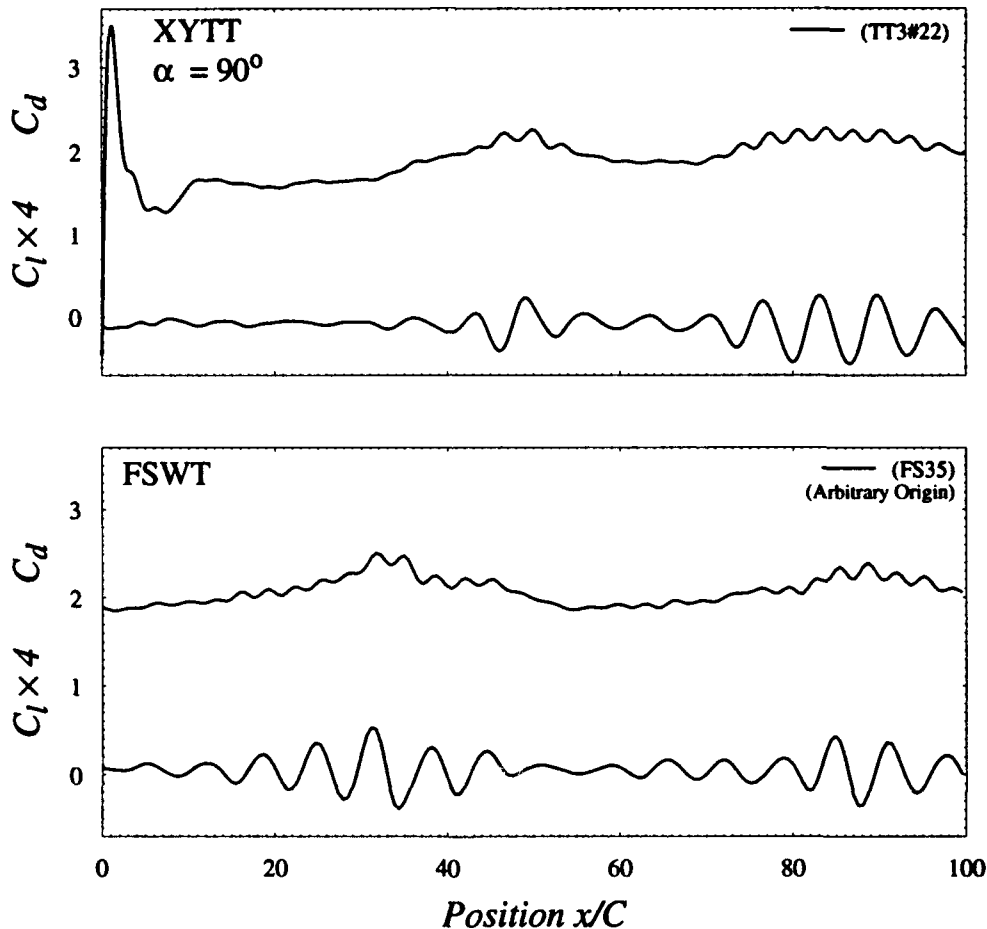


FIG. 7.7 Examples of long period shedding modulation in X-Y towing tank and free surface water tunnel with $\alpha = 90^\circ$, $Re \approx 5000$, $h/C = 10.3\%$

These results are consistent with those found by Szepeesy (1992) for high Reynolds number flows about a circular cylinder, although the flows considered here are considerably less sensitive to Reynolds number changes due to the fixed separation points. Instantaneous measurements of Strouhal period were not made, but particularly in the starting flow it appears that the period increases with increasing fluctuation level, again consistent with the results of Szepeesy.

The mechanism by which this modulation takes place is not exactly clear. The rise and fall of amplitude appears in many cases to occur exponentially (bottom plot of Fig. 7.7), reminiscent of the shedding onset seen at $\alpha = 90^\circ$ in the X-Y towing tank result. It is again possible that the wake vorticity tends to regulate the shedding process, and that the modulation results from an interaction of a downstream wake instability and a near wake shedding instability which are coupled at the end of the formation region. Schewe (1983) proposes a mechanism whereby individually coherent "cells" along the span, slightly out of phase with each other, contribute to the overall force fluctuation. The characteristics of this fluctuation are then a function of the number of these cells (ie. the aspect ratio) and the degree to which they are in phase at any given time. This interpretation would presumably lack a modulation at infinite AR , although if the cells are large enough spanwise (6C, for example) none of the aspect ratios considered here would have more than three or four cells along the span and a very large aspect ratio would be required to reduce the modulation.

7.4 Comparison Of Numerical and Experimental Results

We begin a comparison of results from experiments and 2d numerical models by examining the two "typical" cases for $\alpha = 90^\circ$ which were presented in Ch. 3 and Ch. 5 and which are presented again in the upper left plot of Fig. 7.8.

Note that the initial peak height in the experiments is nearly identical to that seen in the numerical model, indicating that the experiments during and immediately after the initial acceleration are two-dimensional. It is possible that the acceleration itself imposes a spanwise uniform disturbance which serves to keep the flow more two-dimensional than it would be in a steady oncoming freestream.

The post-acceleration drag minimum associated with the initially symmetric recirculating bubble is considerably higher in the experimental case ($C_{d_{min}} \simeq 1.3$) than in the numerical model, which approaches the Kirchhoff value $C_{d_{min}} \simeq 0.9$ and remains at roughly that level until about $t^* = 40$. As was noted before, this low drag region in the 2d model is sensitive to small disturbances; *asymmetric* disturbances in particular have a large effect, as can be seen from the $\alpha = 89.9^\circ$ case shown in the same plot. This 0.1° change in α effectively eliminates the low drag region and results in much better agreement with the experimental result immediately following the acceleration. Even if the experiments were perfectly two-dimensional and free of perturbations (which they were not) it is unlikely that this region would be seen, since the experimental uncertainty in α was $\pm 0.25^\circ$. That the experiments consistently achieve a minimum at all indicates that the flow is at least qualitatively similar to the 2d numerical model during the symmetric recirculating wake regime.

One obvious qualitative difference occurs after the breakdown of the symmetric bubble; namely, the 2d model does not exhibit the characteristic non-shedding region seen in the experiments at $\alpha = 90^\circ$. This lends additional support to the argument that this region results from a three-dimensional and spanwise incoherent flow state present immediately after the symmetry breaks. The shear layers in the purely two-dimensional model are obviously unstable enough (or perhaps lack sufficient small scale Reynolds stresses) that they begin rolling-up on a large scale immediately following the breaking of the initial bubble.

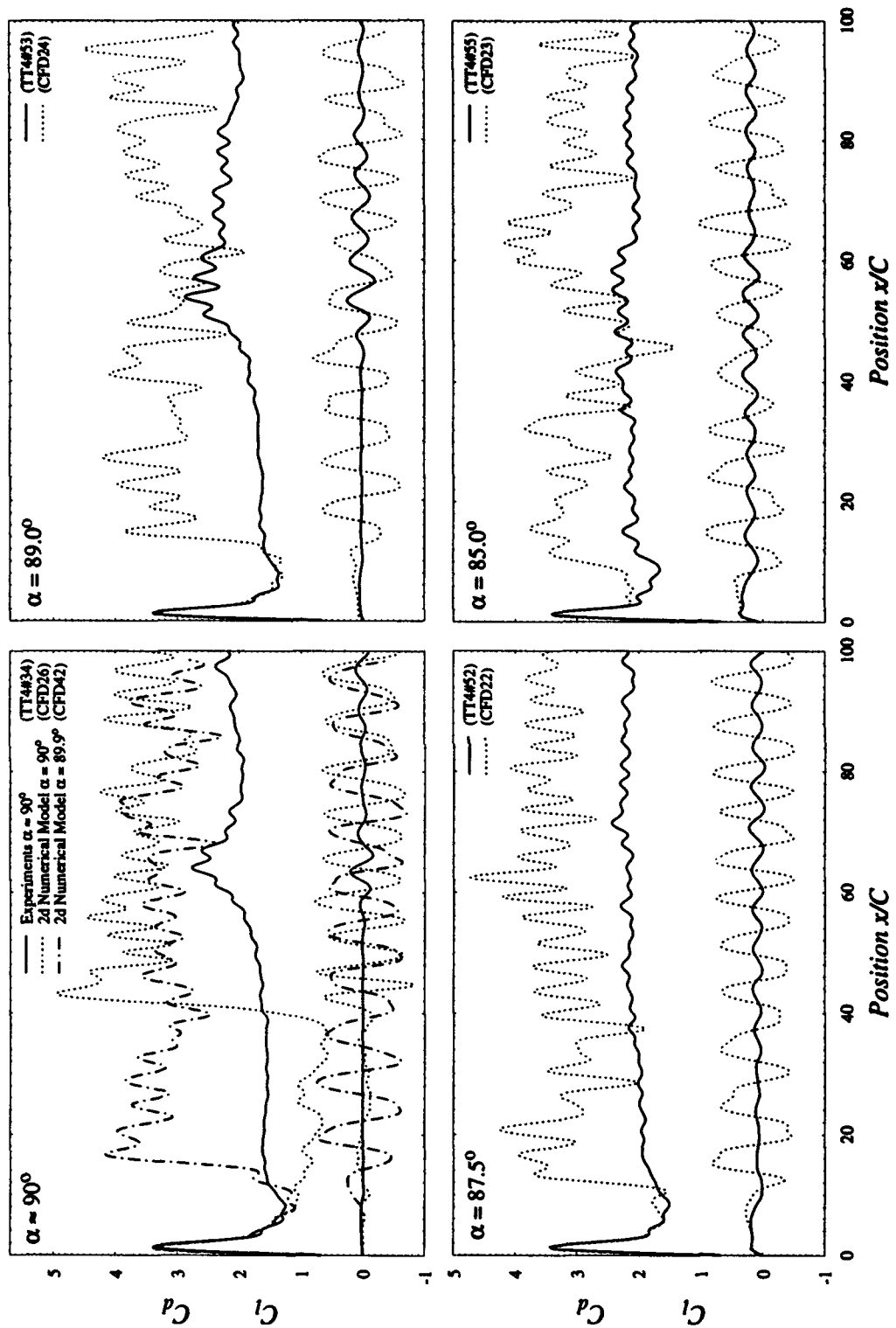


FIG. 7.8 Comparison of experimental and 2d numerical model results for various angles of attack (as noted) with $h/C = 10.3\%$, $t_a^* = 1.31$. Solid line is experimental results; dotted line is 2d numerical model and chain line is 2d model at $\alpha = 89.9^\circ$ (in first plot)

After shedding begins the 2d model has mean and rms force levels roughly 65% higher than experimental values. This is likely a reflection of the increased degree of three-dimensionality apparent in the experiments, which decreases spanwise correlation and results in a larger formation distance and correspondingly lower forces levels. This point will be returned to several times in the following discussions.

For larger geometrical asymmetries of $\alpha = 89^\circ$ and $\alpha = 87.5^\circ$, Fig. 7.8 again shows the post-acceleration agreement with experiments to be quite good up to the onset of shedding, indicating the experimental starting bubble is reasonably two-dimensional even in asymmetric cases. For $\alpha = 85^\circ$ the degree of asymmetry is sufficient that shedding begins immediately following the acceleration in the 2d model, and the post acceleration agreement is not as good as in the previous two cases.

Fig. 7.9 presents comparisons at $\alpha = 87.5^\circ$ for several different acceleration times t_a^* . In all cases the agreement during and immediately following the acceleration is very good, although the initial peak height is somewhat higher for the 2d model, particularly in the $t_a^* = 0.5$ case. This is likely a reflection of experimental limitations of carriage velocity and acceleration making the experimental velocity profile somewhat inaccurate at this level of acceleration.

The values of C_d , found experimentally are quite inaccurate, again due to the difficulty of obtaining smooth and uniform starting motions as well as "end effects" due to subsequent digital data filtering. Although the C_d level is difficult to compare the initial slope of the drag coefficient curve agrees well for all cases.

Turning now to a comparison of "steady-state" flow results from the free surface water tunnel and long time runs of the 2d model, we begin with Fig. 7.10, which compares normalized pdf distributions (histograms) of lift and drag for $\alpha = 90^\circ$ and $\alpha = 87.5^\circ$. The 2d model obviously has much higher rms fluctuation levels - even when the 2d result is normalized to have the same mean as the experimental result the peak is much lower and broader. This increased fluctuation in the drag would indicate a greatly decreased formation distance and tighter vortex roll-up than in the experimental case. Note, however, that the qualitative shift to a lower and broader peak with a change from $\alpha = 90^\circ$ to $\alpha = 87.5^\circ$ is similar in the experimental and numerical results - indicating that the exactly symmetric $\alpha = 90^\circ$ case has a somewhat higher fluctuation level. As a general impression, it is somewhat surprising that as small an asymmetry as $\pm 2.5^\circ$ can result in such noticeable changes in the character of the force levels.

There is an even greater difference in the lift pdfs illustrated in the lower plot of Fig. 7.10. Here the numerical pdf has a shape characteristic of a sinusoidal shedding oscillation superimposed on a lower frequency fluctuating component of about 20% the amplitude; changing α does little more than shift the curve to a higher mean value. The experimental pdfs, on the other hand, are characteristic of a similar shedding fluctuation which has in addition been modulated in time (in the sense of the amplitude being multiplied by some envelope function). In light of the long period shedding modulations seen in the free surface water tunnel this is perhaps not surprising; note, however, that a change from $\alpha = 90^\circ$ to $\alpha = 87.5^\circ$ again results in a higher, narrower peak, although this may be due to a decreased long-period rms, rather than an increased modulation.

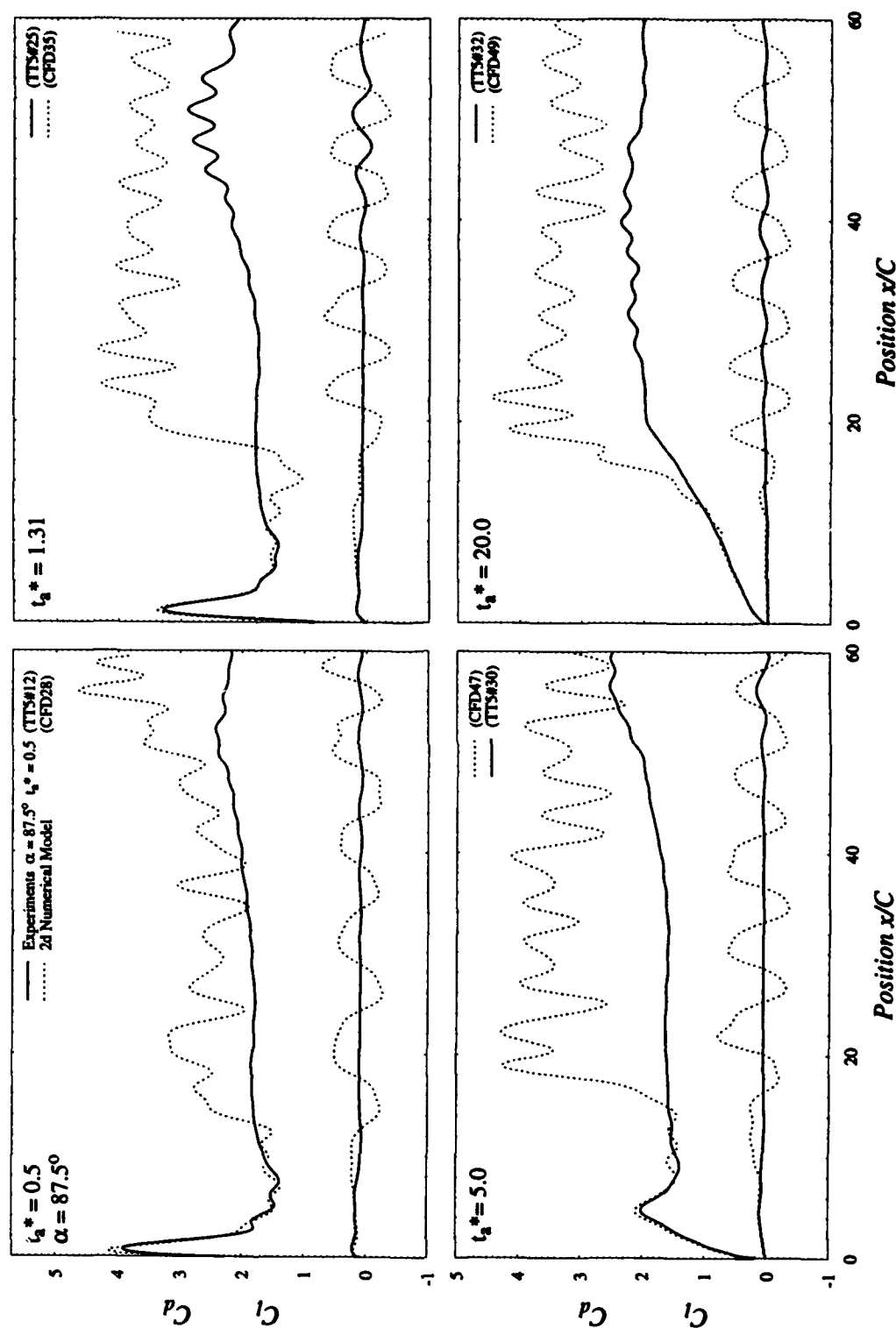


FIG. 7.9 Comparison of experimental and 2d numerical model results for various acceleration times (t_g^* as noted) with $\alpha = 87.5^\circ$, $h/C = 6.8\%$. Solid line is experimental results; dotted line is 2d numerical model

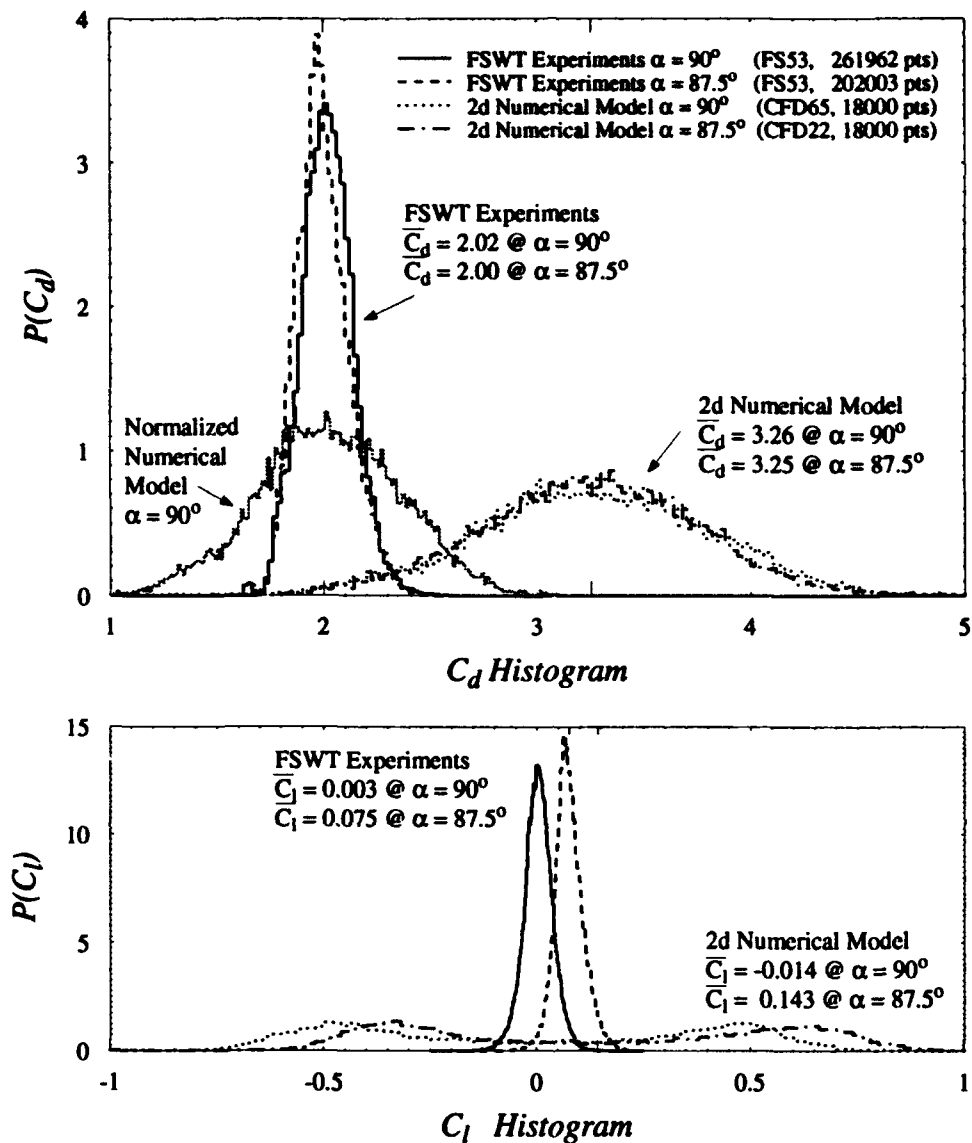


FIG. 7.10 C_d and C_l PDF (normalized histogram) comparison of experiments and 2d numerical model with $h/C = 10.3\%$. Free surface water tunnel experiments at $Re = 6000$, $\mathcal{AR} = 10$: solid line is $\alpha = 90^\circ$, $\bar{C}_d = 2.02$, $\bar{C}_l = 0.003$, 261962 total points; dashed line is $\alpha = 87.5^\circ$, $\bar{C}_d = 2.00$, $\bar{C}_l = 0.075$, 202,003 total pts. 2d numerical model has 18,000 points for $40 < t^* < 400$: dotted line is $\alpha = 90^\circ$, $\bar{C}_d = 3.26$, $\bar{C}_l = -0.014$; chain line is $\alpha = 87.5^\circ$, $\bar{C}_d = 3.25$, $\bar{C}_l = 0.143$. Grayed line is numerical model normalized to have same mean as experimental result

Fig. 7.11 compares long time average pressure coefficient distributions for the experimental results of Fage and Johansen (1927), 2d numerical model results of Chua (1990) modeling an infinitesimally thin plate, and several variations on the current 2d numerical model. The agreement on the upstream face of the plate is good, although the current finite thickness 2d models tend to have somewhat lower values of C_p toward the edges of the plate. This is perhaps an indication that the numerical code is quite sensitive to the thickness of the plate - as this decreases, either by design ($h/C = 4\%$) or by virtue of the bevel angle on the edges of the plate, the upstream flow is influenced to an increasing extent by the flow downstream of the model.

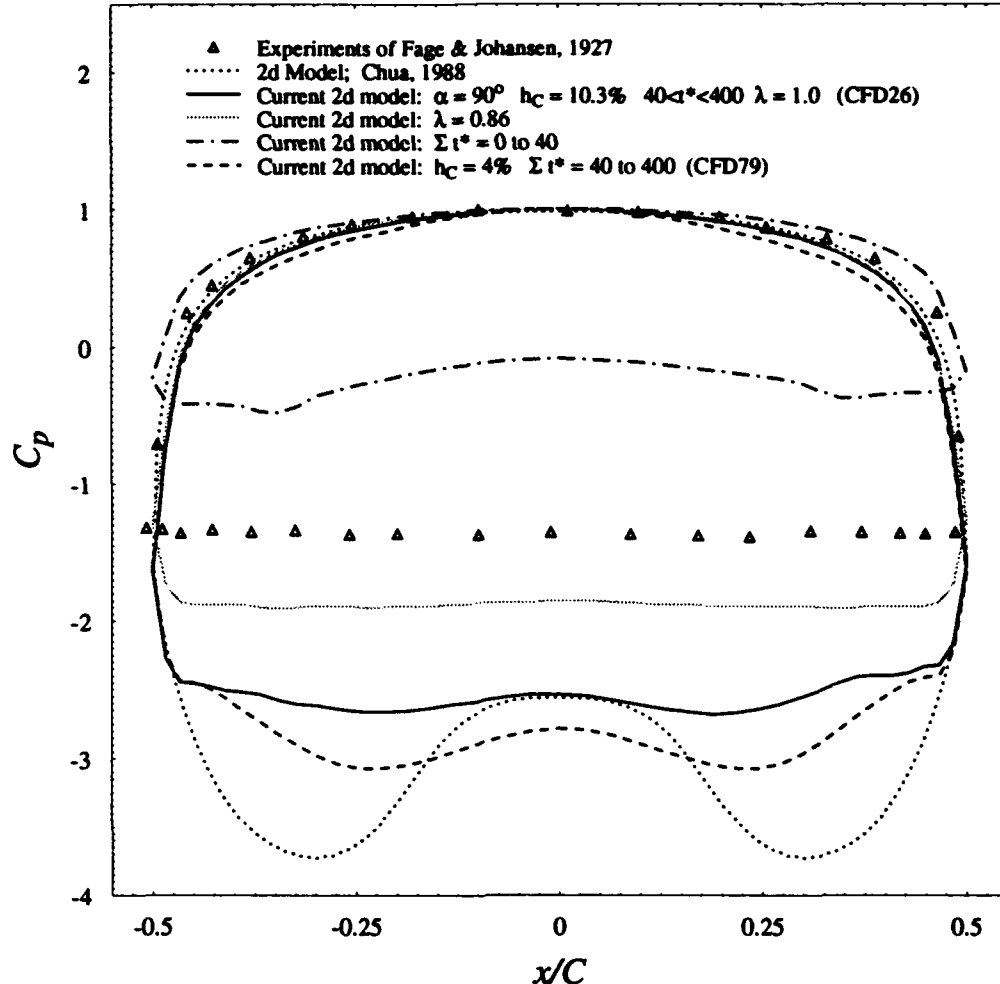


FIG. 7.11 Numerical model time averaged pressure coefficient at $\alpha = 90^\circ$. Comparison to previous numerical result and Fage & Johansen (1927). Current results: Solid line averaged for $40 < t^* < 400$, $t_a^* = 0.0$, $h/C = 10.3\%$, $\overline{C_d} = 3.26$; Chain line averaged for $0 < t^* < 40$; Dashed line $h/C = 4\%$, $\overline{C_d} = 3.47$. Dotted line: Chua (1990), $h/C = 0$, $\overline{C_d} = 3.6$. Symbols: Experiments of Fage & Johansen (1927), $\overline{C_d} \approx 2.0$

The influence of plate thickness is seen even more clearly on the downstream face of the plate, where the infinitesimal thickness result of Chua exhibited large lobes due to the tight roll-up and corresponding low pressures associated with the short formation distance and vigorous vortex shedding. The current results do not exhibit these lobes to the same extent; although they are still present, their amplitude decreases as the thickness increases. The effects of the downstream bevels on the current model can also be seen in the form of small side lobes in the pressure distributions. The time interval over which the C_p integration is performed is also important, as can be seen from the C_p distribution at early time, which was integrated for $0 < t^* < 40$ and shows the effects of the unsteady start. Due to the somewhat limited amount of steady-state shedding time available, including this time period in the overall integration resulted in a considerably different distribution, thus the current results were integrated for $40 < t^* < 400$.

Aside from the higher average base pressure in the experiments, which was to be expected given the lower drag levels, the most striking difference between the experimental and numerical base pressure distributions is the almost perfect uniformity of the pressure in the experimental case. This uniformity has been confirmed many times, for example the data of Arie and Rouse (1956) indicated a uniform base pressure distribution both with and without a wake splitter plate. It seems clear that spanwise averaging in the experiments (*i.e.*, three-dimensionality) is at least partially responsible for the increased uniformity, although increased "two-dimensional" mixing in the near wake would also result in a more uniform distribution (*vis-à-vis* the 2d numerical result with circulation decay, which will be discussed in more detail below). However, the effects of three-dimensional motions in this case are somewhat indirect, since by itself spanwise averaging will not change the time averaged base pressure distribution; instead, it results in a larger formation distance, which in turn implies lower amplitude base pressure fluctuations with a more uniform distribution.

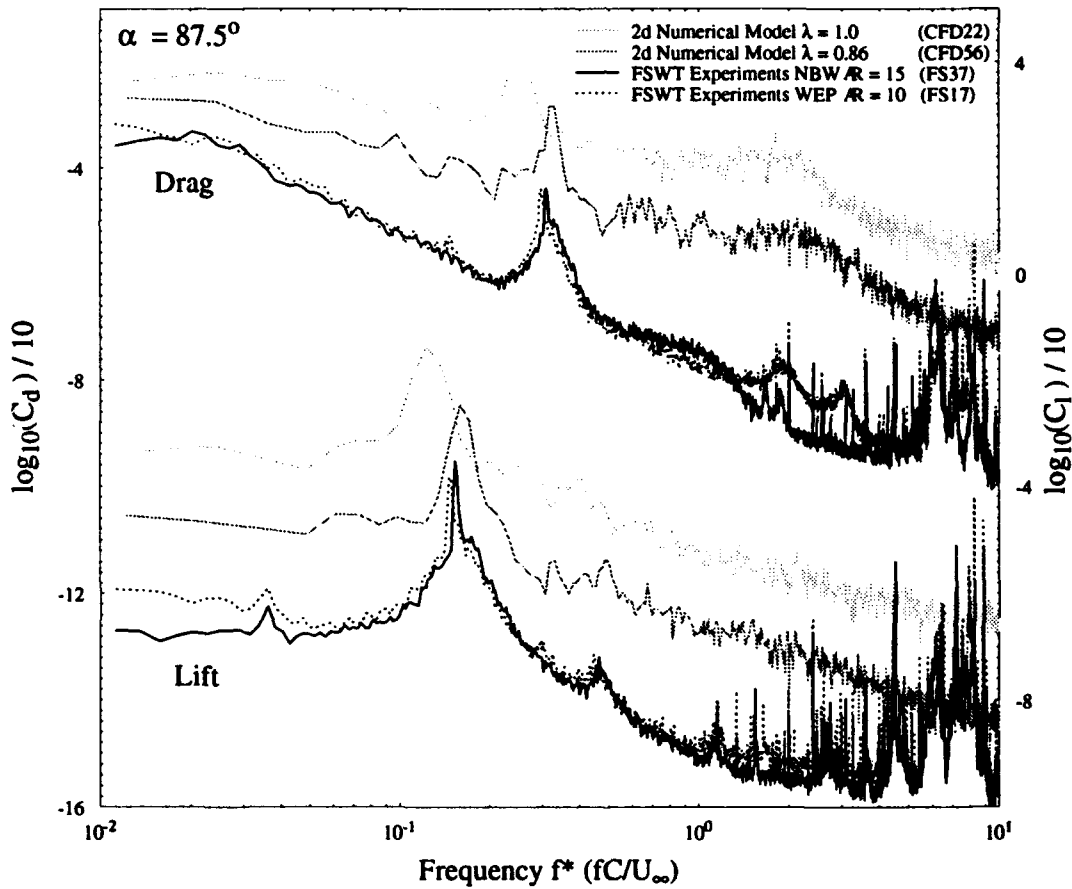


FIG. 7.12 Power spectra of experimental and 2d numerical model force coefficients with $\alpha = 87.5^\circ$, $I/C = 10.3\%$, $Re = 5000$. Solid line is experiments with $NBW@0^\circ$ and $AR = 15$, $S_t = 0.154$. Dotted line is experiments with $WEF@0^\circ$ and $AR = 10$, $S_t = 0.154$. Light grey line is 2d numerical model, $\lambda = 1.0$ (no circulation decay), $S_t = 0.12$. Dark grey line is 2d model, with circulation decay $\lambda = 0.86$, $S_t = 0.16$

Although the shedding in the 2d model is of higher amplitude, it is generally at a somewhat lower Strouhal frequency than that seen in experiments ($S_t \approx 0.12$ vs. $S_t \approx 0.15$), as can be seen from Fig. 7.12, which presents power spectral comparisons of experimental and two-dimensional model results. Note the slight peak in the lift spectra at $3S_t$ seen in both results, as well as the increased roll off in the drag signal for $f^* \gtrsim 16S_t$ in the numerical case. This increased roll off may be the end of a broad band of frequencies associated with shear layer instabilities (Kelvin-Helmholz structures), although why these would occur only in the drag is not clear. The peaks and increased roll-off in the experiments are in good qualitative agreement with the numerical result, although they occur at a lower frequency ($10S_t$) and the experimental noise level is sufficiently high that there is some doubt whether these peaks were generated by the flow.

7.4.1 Circulation Decay

We now consider 2d numerical results for which the circulation of shed vorticity was forced to decay in time with $\lambda = 0.86$ (which roughly represents the percentage of initial circulation remaining after one shedding cycle). This value of λ was chosen to give the best *qualitative* agreement to the experimental free surface water tunnel results, which are given in the lower plot of Fig. 7.13 for comparison. Although the qualitative comparison is good, the mean and fluctuating force levels ($\overline{C_d} = 2.6$) are still higher than experimental values, and the Strouhal frequency (Fig. 7.12) has increased from $S_t = 0.12$ to $S_t = 0.16$, bracketing the experimental result $S_t = 0.154$.

Further decrease in λ will decrease the mean drag level into somewhat better agreement with the experiment, but the shedding fluctuation is all but eliminated, as can be seen from Fig. 5.12, and the Strouhal shedding period is further increased, moving it farther from experimental results.

It is interesting that $\lambda = 0.86$ gives an increased but more uniform base pressure (Fig. 7.11), due to the increased formation distance and decreased shedding amplitude evident in both the force and flow visualization results (Fig. 5.12 and Fig. 5.26 to Fig. 5.29). Accompanying this change is a long period amplitude modulation remarkably similar to that seen in the experiments. Qualitatively this change is most noticeable in the lift pdf given in Fig. 7.14, which relative to the $\lambda = 1.0$ case is more characteristic of the modulated sinusoidal oscillation seen in the experiments, albeit with a higher fluctuation amplitude. The qualitative shape of the drag pdf is also similar to the experiments, with a longer tail at the high end.

Note from the top plot of Fig. 5.12 that during and immediately after the acceleration the $\lambda = 0.86$ model does not agree as well to experiments as the $\lambda = 1.0$ case. Here $\lambda = 0.86$ overcompensates for presumed experimental three-dimensionality, again indicating that initially the experiments are in fact two-dimensional.

Finally, there is some evidence (Fig. 5.12) that with $\lambda = 0.86$ the initial onset of shedding occurs exponentially, with good qualitative agreement to the experimental result.

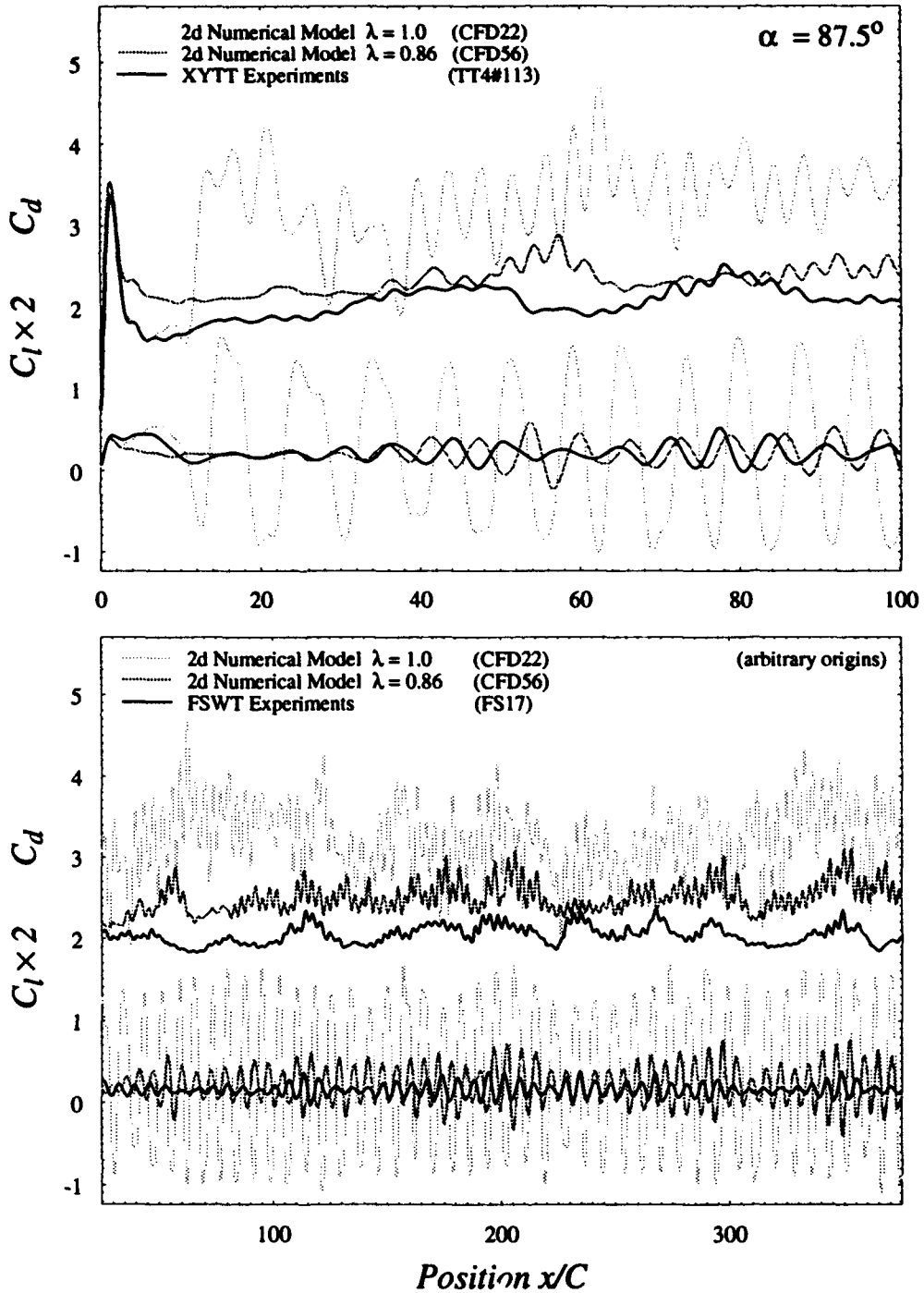


FIG. 7.13 Comparison of results from experiments and 2d numerical models with and without circulation decay; $\alpha = 87.5^\circ$, $Re \approx 5000$, $h/C = 10.3\%$. Top plot: $t_a^* = 1.31$, Solid line is experimental result from X-Y towing tank $\overline{C_d} = 2.0$; light grey line is 2d model, $\lambda = 1.0$ (no circulation decay), $\overline{C_d} = 3.25$; dark grey line is 2d model with circulation decay $\lambda = 0.86$, $\overline{C_d} = 2.6$. Bottom plot: free surface water tunnel results, same symbols but note change of horizontal scale

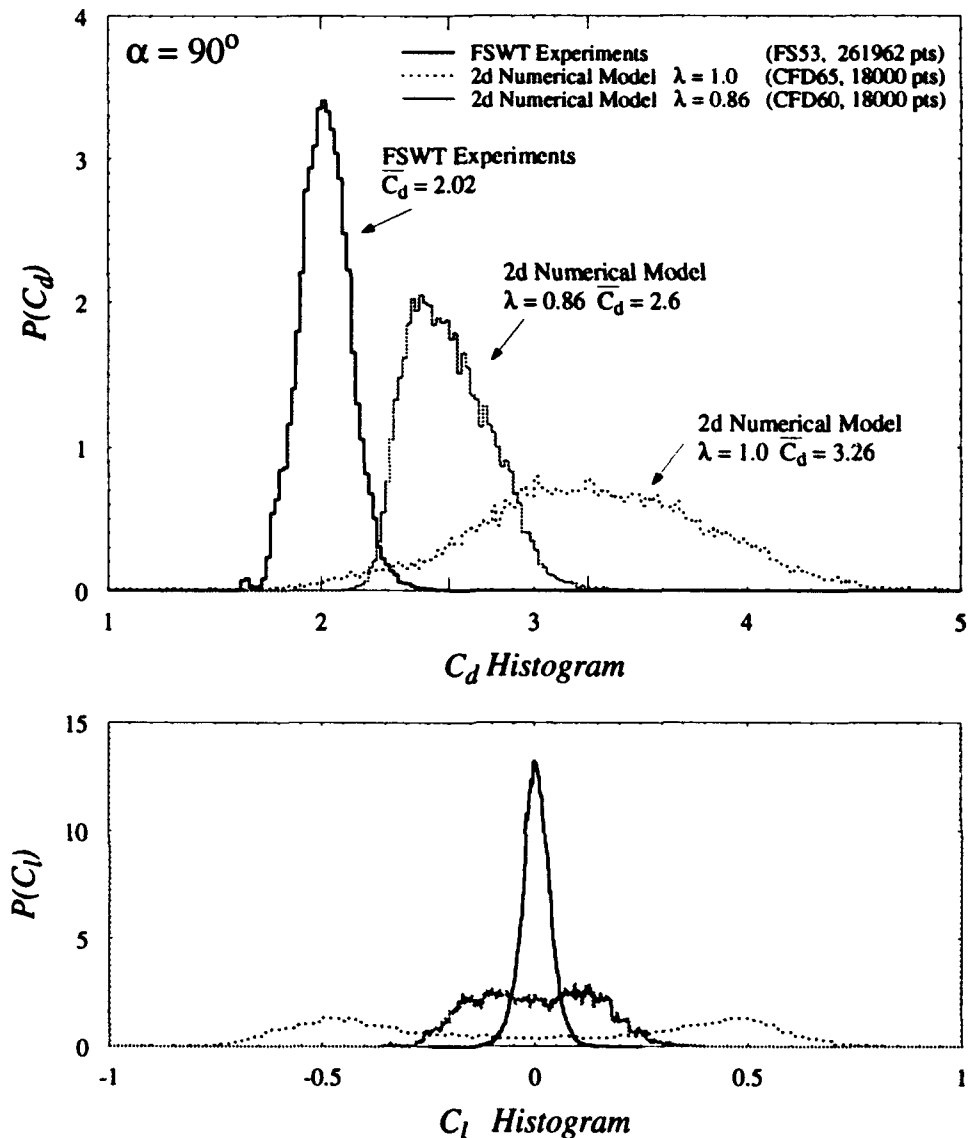


FIG. 7.14 C_d and C_l PDF (normalized histogram) comparison of experiments and 2d numerical models with $\lambda = 1.0$ and 0.86 . $\alpha = 90^\circ$, $h/C = 10.3\%$. Solid line is for free surface water tunnel experiments at $Re = 6000$, $AR = 10$, $\bar{C}_d = 2.02$. Dotted line gives 2d numerical model result with $\lambda = 1.0$, $\bar{C}_d = 3.26$. Dark grey line is 2d numerical model with $\lambda = 0.86$, $\bar{C}_d = 2.6$

Although the concept of circulation decay does not have a firm theoretical formulation, it does appear to provide qualitatively (and to some extent quantitatively) improved agreement to experimental results. It obviously has large implications as far as the global flow development is concerned, with a greatly increased formation distance and reduced shedding amplitude being two immediate consequences. Although the exact mechanism by which circulation decay is accomplished may be unrealistic, the modified two-dimensional model does prove useful in interpreting experimental results.

7.5 Stratification Effects - Small Scale Three Dimensionality

Although very high levels of flow stratification were required to effect large scale changes in mean flow quantities, some changes (presumably associated with a suppression of larger scale three-dimensional structures) were evident even with relatively low stratification. In particular, the initially closed symmetric bubble for $\alpha = 90^\circ$ was of longer duration and had a lower drag minimum than in the unstratified case (Fig. 6.4). The non-shedding region following this initial low-drag regime was reduced in extent, with shedding beginning soon after the closed wake bubble broke. This may indicate that large scale three dimensional motions were responsible, at least in part, for the long lasting symmetric flow in the unstratified case. The $\alpha = 87.5^\circ$ case exhibited less difference during the initial closed wake region, but the subsequent onset of shedding came earlier and was accompanied by a more immediate increase in drag level, as can be seen from both Fig. 6.4 and from the ensemble averaged results at $Re = 5000$, $Ri = 0.53$ presented in Fig. 7.15.

More significant effects were noticed when Richardson number was increased to $Ri = 13$ (middle plot of Fig. 7.15). Here the initial low-drag region was of longer duration and had a lower drag minimum; its eventual breakdown was accompanied by vigorous shedding and a large overshoot in the force levels before a slow decay to steady-state levels. The abruptness of this shedding transition can be seen in the drag rms level, which has a significant peak due to the force overshoot and slight variations in the time of shedding onset. Rms levels at later time are similar to those seen in the unstratified $Re = 1000$ case, neither of which exhibit the fluctuation apparent in the $Re = 5000$ result. The strong damping of the initial shedding in the stratified case and the subsequent lack of shedding oscillation is likely a reflection of viscous effects at this low Reynolds number, which were detailed in Sec. 7.3.3.

In light of the obviously large discrepancy in steady-state lift results shown in the middle plot of Fig. 7.15, it may appear somewhat difficult to determine if the increase in mean drag level is a real effect or if it is due to experimental uncertainty. The corrections which were applied to the drag results are significantly better than those which were available for the lift (Sec. 3.2), as can be seen by the agreement of the drag peaks during the acceleration relative to the lift results at over the same interval. This early time agreement inspires confidence that much of the 15% mean drag increase seen in the stratified case is a real effect.

Finally, Fig. 7.16 presents a comparison between ensemble averaged unstratified and stratified experimental results and results of a two-dimensional numerical model. The early time experimental results no longer agree as well with the numerical model as they did for the $Re = 5000$ experiments, likely due to both increased experimental uncertainty, and to low Reynolds number viscous effects which were absent in the 2d model.

If we uniformly increase the level of both experimental curves to match initial peak heights, we note that qualitative agreement to the 2d numerical model is improved in many respects by the introduction of flow

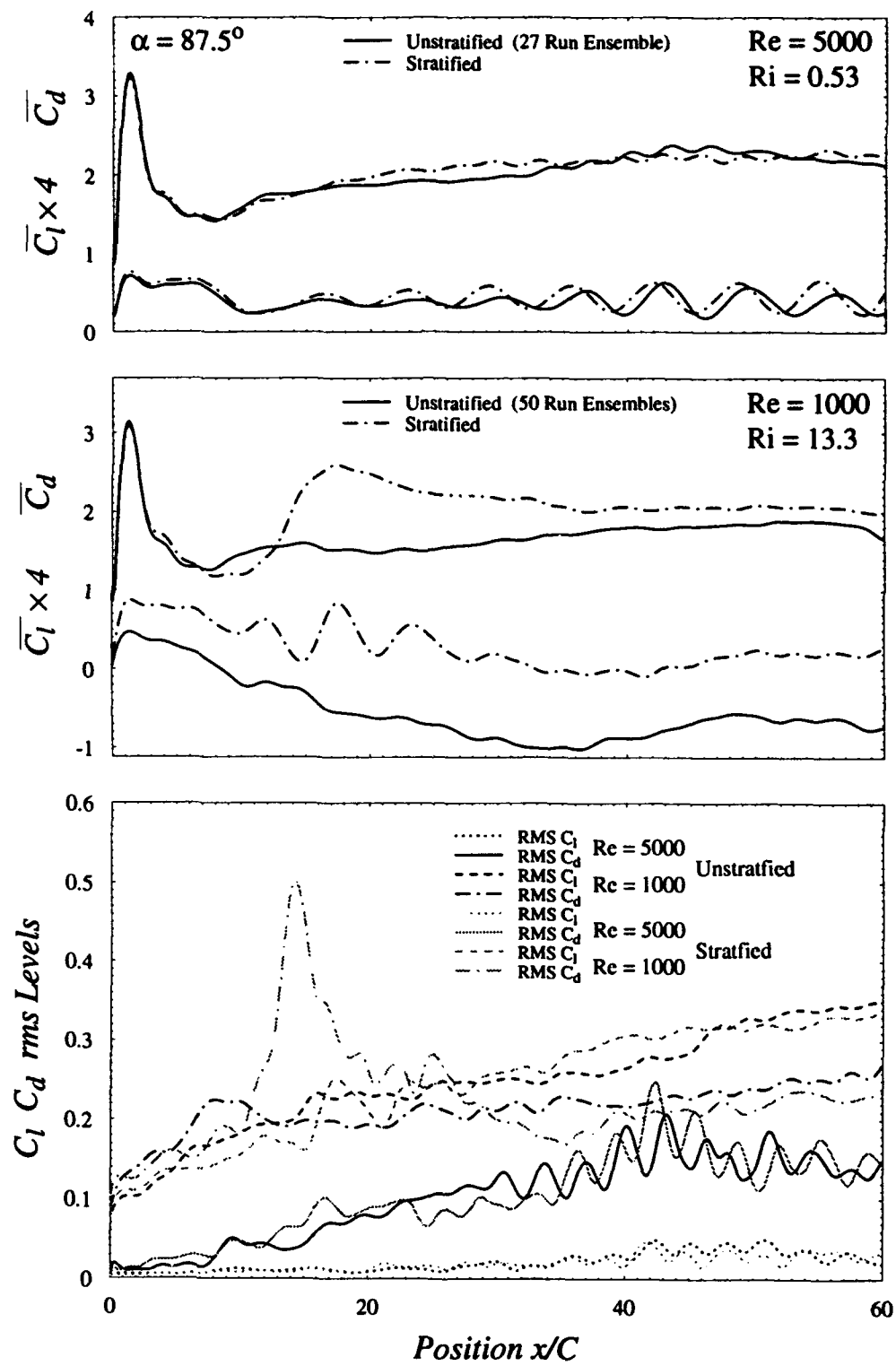


FIG. 7.15 Comparison of stratified and unstratified ensemble averaged X-Y towing tank results with $\alpha = 87.5^\circ$, $t_a^* = 1.31$, $h/C = 6.8\%$. Top plot: 27 run ensembles at $Re = 5000$; solid line: unstratified; chain line: stratified, $Ri = 0.53$. Middle plot: 50 run ensembles at $Re = 1000$; solid line: unstratified; chain line: stratified, $Ri = 13.3$. Bottom plot: rms levels as noted

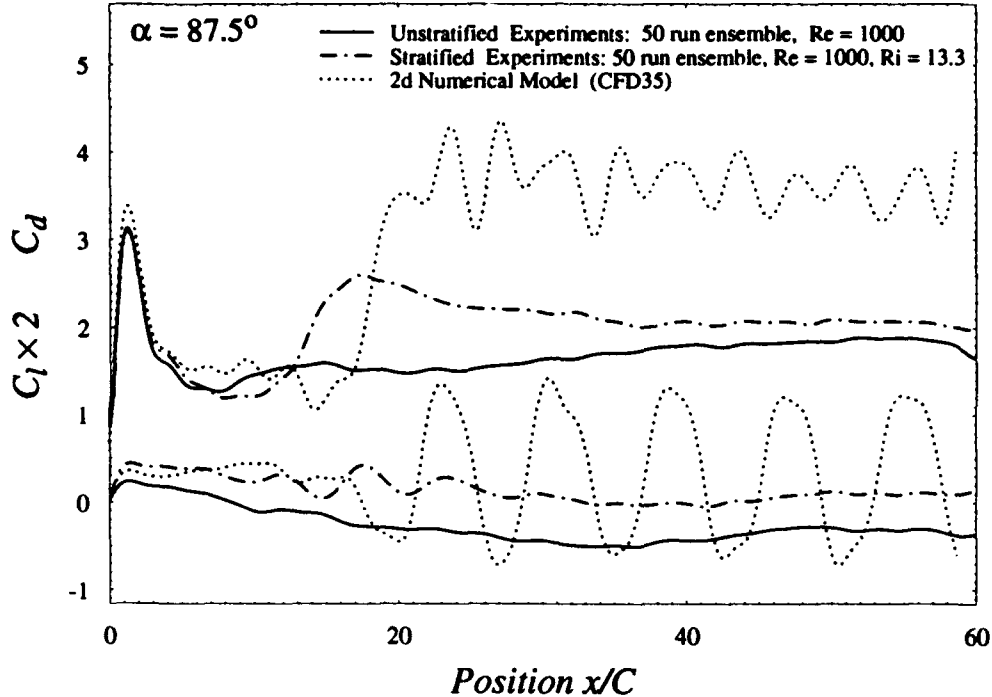


FIG. 7.16 Comparison of unstratified and stratified experimental and 2d numerical model results. 50 run ensemble averaged experimental results, $\alpha = 87.5^\circ$, $Re = 1000$, $h/C = 6.8\%$, $t_a^* = 1.31$. Solid line is unstratified; chain line is stratified results with $Ri = 13.3$ and dotted line is 2d model

stratification. The initial low-drag closed wake region is of longer duration with lower minimum drag, and is followed by a higher drag overshoot and slightly higher mean drag levels, all qualitatively similar to effects seen in the 2d model. The steady-state drag level still differs significantly from the purely two-dimensional case, although the experimental trend is in the correct direction. It is interesting to speculate what drag level would have been achieved in the stratified case if it could have been performed at a higher Reynolds number and not so affected by viscous effects. Given the typical character of other $\alpha = 87.5^\circ$ higher Reynolds number results, namely that initial shedding is *not* accompanied by a large drag overshoot (as it is in the $\alpha = 90^\circ$ case), it may be reasonable to assume that steady-state high-Reynolds-number stratified drag levels would approach those of the initial peak seen in the low Reynolds number stratified case, *i.e.*, significantly closer to the 2d numerical result than the unstratified flow.

Exactly how representative the current 2d numerical model is of a "true" two-dimensional flow is somewhat debatable, but it seems clear that two-dimensional force levels are considerably higher than those seen in "nominally two-dimensional" experiments. The failure of significant flow stratification to increase the experimental drag to the levels seen in the 2d model must indicate that much of the remaining difference between the two results is due to small scale ($< 0.2C$) intrinsic three-dimensional motions.

7.6 Remaining Questions

Several aspects of this research effort could benefit from further investigation. Firstly, the force levels and flow behavior in a high Reynolds number "two-dimensional" experimental flow (achieved through flow stratification or any other means of minimizing intrinsic three-dimensional motions) would be of great interest. Until the advent of much improved computer models which can reliably model fully three dimensional flows (and presumably as a subset, two-dimensional ones), this may be one of the few avenues by which the effects of small scale three dimensionality on the global flow development can be explored. These effects have been shown to be many and varied, ranging from the non-shedding regime in the X-Y towing tank to the long period shedding modulation seen most clearly in the free surface water tunnel .

Each of these effects deserves further study, with an emphasis on the role three-dimensionality plays in their development. This is a somewhat different tactic than has been used in the past, where explorations have in some sense centered on examining the development of three dimensional motions themselves, rather than the effect they have on the global flow development, which provides considerable additional insight.

- 7.28 -

CHAPTER 8

Conclusions

Experimentally realizable flows are inevitably three-dimensional, containing both large scale extrinsic three-dimensional motions resulting from environmental or end effects, and generally smaller scale intrinsic motions associated with fundamental flow instabilities which would be present even in the limit of infinite aspect ratio. Many of the effects of these three-dimensional motions are seen in the long and complex history of an unsteady starting motion of a normal flat plate.

Plate aspect ratio and end condition proved to be the most important factors affecting the large scale three-dimensional motions present in the flow. A "near bottom" lower end condition and a "through free surface" upper end condition provided the most nominally two-dimensional flow in the sense of minimizing large scale extrinsic three dimensionality. This combination of end conditions gave results which were essentially independent of aspect ratio. In contrast, a free lower end gave the most large scale three-dimensional effect due to flow around the end of the plate raising the base pressure and reducing organized vortex shedding; with large enough aspect ratios some of these effects were reduced. A small end plate provided a condition midway between the above two cases; with sufficiently large aspect ratios (> 10) the flow was similar to that seen in the near wall case, while for small aspect ratio the shedding amplitudes were reduced. Some additional end condition effects will be considered below.

The early time agreement between a two-dimensional numerical model and experimental results obtained in the X-Y towing tank indicates that the experimental flow is two-dimensional until the initially closed recirculating wake breaks. Although immediately following the unsteady starting motion the 2d numerical model attains the low minimum drag predicted by the Kirchhoff-Rayleigh theory ($C_d \simeq 0.9$), the reason for this correspondence is unclear. It seems certain that the mechanism involved is more complex than that envisioned in the original theory, and the agreement may be coincidental. In any event this low drag region is sensitive to small perturbations; at $\alpha = 89.9^\circ$ the numerical model gave good quantitative agreement with the experimental values of $C_d \simeq 1.3$ found in this region. Subsequent to the breakdown of this initial bubble the numerical model transitions immediately to "steady" vortex shedding, with a Strouhal frequency of 0.12 (lower than the experimental value of 0.15) and a drag level $\overline{C_d} \simeq 3.3$, or about 65% higher than steady-state experimental results.

In contrast, experimental results for $\alpha = 90^\circ$ indicate that immediately following the breaking of the closed wake there is a long lasting region with low drag ($C_d \simeq 1.6$) and no vortex shedding, which is presumed to result from a lack of spanwise coherence in the initial bubble breakdown. The drag level

attained in this region is comparable to that predicted by Roshko (1992) for a closed recirculating wake bubble dominated by Reynolds stresses in the free shear layers. This region is not as apparent in flows with even relatively low levels of spanwise stratification, again implying that large scale incoherence of the initial breakdown may be responsible for the subsequent symmetry of the flow.

The eventual onset of shedding at the end of this non-shedding regime occurs exponentially, with an initially slow decrease in formation length as a wake instability progresses upstream. During this exponential decrease the force levels build up to a peak before returning to their final steady-state values. This process is perhaps a good illustration of the role which (organized) far wake vorticity can play in regulating the near wake shedding. Small spanwise-uniform geometrical asymmetries, in the form of an angle of attack change to $\alpha = 87.5^\circ$, resulted in a more uniform breaking of the closed wake and an immediate transition to steady-state shedding.

Although only indirectly connected to the ultimate goals of this research, it is interesting to note that experimental results at $Re = 1000$ were found to have a larger formation length than results obtained at higher Reynolds number. This gave slightly higher mean base pressures with significantly reduced rms levels and greater uniformity - which reduced the mean drag and effectively eliminated force oscillations due to shedding, particularly in the lift. Thus the presumed "Reynolds number independence" of fully separated flows (particularly with fixed separation points) begins at Reynolds numbers somewhat greater than $Re = 1000$.

Imposing circulation decay in the numerical model, by way of simulating increased mixing in the near wake (intrinsic three dimensionality), resulted in a lower steady-state drag ($\overline{C_d} = 2.6$), higher Strouhal frequencies and qualitative features similar to those seen in the experimental case, including a larger formation region, an exponential onset of shedding in the $\alpha = 90^\circ$ case and a long period shedding modulation in the steady-state flow. The early time agreement to experiments was not as good for this more "three-dimensional" model (the numerical drag was higher), perhaps once again illustrating the two-dimensionality of the experiments for early time.

So called "steady-state" shedding had long period amplitude modulations which were most easily seen in the free surface water tunnel results. This gave a 20% fluctuation in drag level and a modulation of the rms lift, the period of which decreased with increasing aspect ratio from about $10T_s$ at $AR = 8$ to $6T_s$ at $AR = 15$, although it appeared fairly constant for $AR \gtrsim 10$. It remains unclear if this modulation could be expected to occur in a "nominally two-dimensional" flow, *i.e.*, a flow with an infinite aspect ratio containing only intrinsic three dimensionality. Although aspect ratio and end condition changes have a significant effect on the modulation, these effects seem to decrease with increasing aspect ratio, implying that ultimately the modulation is a result of intrinsic three dimensionality and would be present even in the limit of infinite aspect ratio.

For $AR < 8$ shedding was found to occur intermittently, with long intervals of time during which the wake had a large formation length and no organized vortex shedding in the classical sense. The drag in these

intervals was $\bar{C}_d \approx 1.5$, close to the value found for the symmetrical region in the unsteady X-Y towing tank experiments. End conditions, particularly the angle of the false bottom in the free surface water tunnel, were found to have a large effect on the vortex shedding in these low AR cases, with the shedding being either enhanced or eliminated by positive or negative (outward or inward) end plate angle. At larger aspect ratio, increasing end plate angle affected both the amplitude of the shedding (which was decreased) and the period of the modulation, which was increased. This may be due to the changes in mean base pressure which angling the end plates induce, since the fully separated flow on the end plate should provide a similar boundary condition with either positive or negative angles.

As was noted above, small stratification gradients in the X-Y towing tank were effective in eliminating large scale three-dimensional motions and promoting a longer lasting closed-wake low-drag region following the unsteady acceleration. The break down of this symmetric bubble was more spanwise uniform and eliminated (or at least decreased) the subsequent non-shedding interval apparent before the onset of shedding.

Although it was difficult to impose a large enough stratification to eliminate small scale intrinsic three-dimensional motions, significant effects were noticed at a Richardson number of 13; which could be expected to reduce motions on the order of $0.2C$ and larger. Unfortunately, to achieve this required the Reynolds number to be low enough ($Re = 1000$) that significant viscous effects were apparent, in particular the larger formation distance and lower fluctuation amplitudes characteristic of unstratified flow at this Reynolds number. Nonetheless, such a stratification increased the time during which the initial symmetric bubble remained closed, and decreased the minimum drag level attained in this region. The breakdown of this bubble was accompanied by more vigorous shedding than was seen in the unstratified case, with a much larger overshoot in the drag level. The subsequent decay in shedding amplitude to the levels seen in the unstratified case was likely attributable to the low Reynolds number. Although the uncertainty in force measurements was quite large, there was apparently a 10% to 15% increase in mean drag level between the stratified and unstratified results.

In summary then, although large scale extrinsic three-dimensional motions can have a major impact on the global flow development (to the point of being able to effectively eliminate vortex shedding by manipulating end conditions or aspect ratio) it appears that the main differences between "nominally" and perfectly two-dimensional flows are due to small scale intrinsic three-dimensional motions.

Reducing these motions in the experimental flow (through stratification) gives behavior qualitatively more similar to the 2d numerical model - namely increased mean and fluctuating force levels, a longer lasting starting bubble with lower corresponding minimum drag and large force increases accompanying the onset of shedding. Modeling the effects of these motions to the 2d case (by the somewhat questionable technique of circulation decay) gives qualitatively similar results to the experiments - namely lower mean and fluctuating forces, exponential shedding onset and long period shedding modulation.

It is unclear what minimum length scale must be eliminated from the experiments to give the 2d result. In terms of "spanwise averaging" in a nominally two-dimensional flow, one must presumably integrate over a span comparable to the largest intrinsic three-dimensional structure present. This scale is not immediately obvious, but past experimental results would indicate it is on the order of at least one chord length, and thus should have been significantly reduced by flow stratification. Thus the main differences between two and three-dimensional flows must be attributable to smaller scale motions.

Although questions may be raised about the accuracy of the two-dimensional model used in these investigations (essentially, what results would be expected in a "true" two-dimensional flow?), it appears that the primary influence of small scale three-dimensional motions in the "nominally two-dimensional" experiments is to significantly increase the formation length and thereby reduce both mean and rms force levels from those which would be seen in a purely two-dimensional flow.

REFERENCES

ABERNATHY, F.H. [1962] "Flow Over An Inclined Plate," *ASME Journal of Basic Engineering*, **61**, WA-124

ARIE, M.& ROUSE, H. [1956] "Experiments On Two-dimensional Flow Over A Normal Wall," *Journal of Fluid Mechanics*, **1**, 129-141

AWBI, H.B. [1983] "Effect Of Blockage On The Strouhal Number Of Two-dimensional Bluff Bodies," *Journal of Wind Engineering and Industrial Aerodynamics*, **12**, 353-362

BATCHELOR, G.K. [1967] *An Introduction To Fluid Dynamics - 1st edition*, Cambridge University Press, Cambridge

BEARMAN, P.W. & TRUEMAN, D.M. [August 1972] "An Investigation Of The Flow Around Rectangular Cylinders," *Aeronautical Quarterly*, **23**, 229-237

CASTRO, I.P. [1971] "Wake Characteristics Of Two-Dimensional Perforated Plates Normal To An Air-Stream," *Journal of Fluid Mechanics*, **46:3**, 599-609

CHEIN, R. & CHUNG, J.N. [1988] "Discrete-Vortex Simulation Of Flow Over Inclined And Normal Plates," *Computers & Fluids*, **16:4**, 405-427

CHUA, K., LISOSKI, D., LEONARD, A. & ROSHKO, A. [1990] "A Numerical And Experimental Investigation Of Separated Flow Past An Oscillating Flat Plate," *ASME FED International Symposium on Nonsteady Fluid Dynamics, Book No. H00597*, **92**, 455-464

CHUA, K. [April, 1990] "Vortex Simulation Of Separated Flows In Two And Three Dimensions," Ph.D. Thesis, California Institute of Technology

CIMBALA, J.M., NAGIB, H.M. & ROSHKO, A. [1988] "Large Structure In The Far Wakes Of Two-Dimensional Bluff Bodies," *Journal of Fluid Mechanics*, **190**, 265-298

CLARK, C. D., STOCKHAUSEN, P.J. & KENNEDY, J.F. [Feb. 15, 1967] "A Method For Generating Linear Density Profiles In Laboratory Tanks," *Journal of Geophysical Research*, **72:4**, 1393-1395

CORTELEZZI, L. [June 1992] "A Theoretical And Computational Study On Active Wake Control," Ph.D. Thesis, California Institute of Technology

COURCHESNE, J. & LANEVILLE, A. [Dec. 1979] "A Comparison Of Correction Methods Used In The Evaluation Of Drag Coefficient Measurements For Two-dimensional Rectangular Cylinders," *ASME Transactions*, **101**, 506-510

DELANY, N.K. & SORENSEN, N.E. [Nov. 1953] "Low-Speed Drag Of Cylinders Of Various Shapes," *NACA Technical Note 3038*

DUTTA, P.K. [April 1988] "Discrete Vortex Method For Separated And Free Shear Flows," Ph.D. Thesis, Indian Institute of Science, Bangalore-560012, India

EL-SHERBINY, S.E. & MODI, V.J. [Jan. 1983] "Blockage Effect On Vortex Shedding From Bluff Bodies," *The Arabian Journal for Science and Engineering*, **8:1**, 61-66

FAGE, A. & JOHANSEN, F.C. [Feb. 1927] "On The Flow Of Air Behind An Inclined Flat Plate Of Infinite Span," *British ARC R&M*, **1104**, 81-106

FAIL, R., LAWFORD, J.A. & EYRE, R.C.W. [June 1957] "Low-speed Experiments On The Wake Characteristics Of Flat Plates Normal To An Air Stream," *British ARC R&M*, **3120**, 69-91

FLACHSBART, V.O. [Feb. 1935] "Der Widerstand Quer Angeströmter Rechteckplatten Bei Reynoldsschen Zahlen 1000 Bis 6000," *Zeitschr. f. angew. Math. und Mech.*, **15**, 32-37

FOX, T.A & WEST, G.S. [1990] "On The Use Of End Plates With Circular Cylinders," *Experiments In Fluids (Technical Notes)*, **9**, 237-239

GERRARD, J.H. [1966] "The Mechanics Of The Formation Region Of Vortices Behind Bluff Bodies," *Journal of Fluid Mechanics*, **25:2**, 401-413

IGARASHI, T. [1986] "Correlation Between Heat Transfer And Fluctuating Pressure In The Separated Region Of A Bluff Body," *Heat Transfer 1986 - Proceedings of the Eighth International Conference, San.Francisco, CA*, 1023-1028

KIRCHHOFF, G. [1869] "Zur Theorie freier Flüssigkeitsstrahlen," *Crelle*, **Ixx**, [also Gesammelte Abhandlungen (1882), 416-427]

KIYA, M. & ARIE, M. [Sept. 1980] "Discrete-vortex Simulation Of Unsteady Separated Flow Behind A Nearly Normal Plate," *JSME Bulletin*, **23:183**, 1451-1458

KIYA, M. & MATSUMURA, M. [May 1988] "Incoherent Turbulence Structure In The Near Wake Of A Normal Plate," *Journal of Fluid Mechanics*, **190**, 343-356

KNISELY, C.W. [1990] "Strouhal Numbers Of Rectangular Cylinders At Incidence: A Review And New Data," *Journal of Fluids & Structures*, **4**, 371-393

KUBO, Y., MIYAZAKI, M. & KATO, K. [1989] "Effects Of End Plates And Blockage Of Structural Members On Drag Forces," *Journal of Wind Engineering and Industrial Aerodynamics*, **32**, 329-342

KUWAHARA, K. [Nov. 1973] "Numerical Study Of Flow Past An Inclined Flat Plate By An Inviscid Model," *Journal of the Physical Society of Japan*, **35:5**, 1545-1551

LAMB, H. [1932] *Hydrodynamics - 6th edition*, Cambridge University Press, Cambridge

LANG, D.B. [1985] "Laser Doppler Velocity and Vorticity Measurements in Turbulent Shear Layers," Ph.D. Thesis, California Institute of Technology

LEONARD, A. [1993] *Private communication*

LINDSEY, W.F. [1938] "Drag Of Cylinders Of Simple Shapes," *NACA Report No. 619*

MASKELL, E.C. [Nov. 1963] "A Theory Of The Blockage Effects On Bluff Bodies And Stalled Wings In A Closed Wind Tunnel," *ARC R&M*, **3400**

MODI, V.J. & EL-SHERBINY, S.E. [Sept. 1977] "A Free-streamline Model For Bluff Bodies In Confined Flow," *ASME Journal of Fluids Engineering*, **99**, 585-592

NAKAGUCHI, H., HASHIMOTO, K. & MUTO, S. [Jan. 1968] "An Experimental Study On Aerodynamic Drag Of Rectangular Cylinders," *Journal of the Japan Society for Aeronautical and Space Sciences*, **16**, 1-5

NOCIA, F. [1991] *Private communication*

PEARCE, J.A., QASIM, A., MAXWELL, T.T. & PARAMESAWARAN, S. [1992] "A Computational Study Of Coherent Wake Structures Behind 2-D Bluff Bodies," *Journal of Wind Engineering and Industrial Aerodynamics*, **41-44**, 2853-2861

PRANDTL, L. & TIETJENS, O.G. [1934] *Applied Hydro- and Aeromechanics - 1st edition*, United Engineering Trustees, Inc. Dover Edition 1957, New York

RAGHAVAN, V., MCCROSKEY, W.J., VANDALSEM, W.R. & BAEDER, J.D. [Jan. 1990] "Calculations Of The Flow Past Bluff Bodies, Including Tilt-Rotor Wing Sections At $\alpha = -90^\circ$," *AIAA 28th Aerospace Sciences Meeting, Reno*, **90-0032**

RAMAMURTHY, A.S., BALACHANDAR, R. & VO, D.N. [July 1989] "Blockage Correction For Sharp-edged Bluff Bodies," *Journal of Engineering Mechanics*, **115:7**, 1569-1576

RANGA-RAJU, K.G. & SINGH, V. [1975-1976] "Blockage Effects On Drag Of Sharp-Edged Bodies," *Journal of Industrial Aerodynamics*, **1**, 301-309

RAYLEIGH, L. [Dec. 1876] "Note on Hydrodynamics," *Philosophical Magazine*, **II**, 441-447
[also *Papers*, **i**, 297-304]

ROSHKO, A. [July 1954] "A New Hodograph For Free-Streamline Theory," *NACA Technical Note 3168*

ROSHKO, A. [July 1954] "On The Drag And Shedding Frequency Of Two-dimensional Bluff Bodies," *NACA Technical Note 3169*

ROSHKO, A. [Feb. 1955] "On The Wake And Drag Of Bluff Bodies," *Journal of the Aeronautical Sciences*, **22**, 124-132

ROSHKO, A. [Dec. 1992] "Perspectives On Bluff Body Aerodynamics," *Second International Colloquium on Bluff Body Aerodynamics and Applications, Melbourne, Australia*

SARPKAYA, T. [1975] "An Inviscid Model Of Two-dimensional Vortex Shedding For Transient And Asymptotically Steady Separated Flow Over An Inclined Plate," *Journal of Fluid Mechanics*, **68, part I** 109-128

SARPKAYA, T. & KLINE, H.K. [1982] "Impulsively-Started Flow About Four Types Of Bluff Body," *Journal Of Fluids Engineering*, **104**, 207-213

SARPKAYA, T. & IHRIG, C.J. [March 1986] "Impulsively Started Steady Flow About Rectangular Prisms: Experiments And Discrete Vortex Analysis," *Journal Of Fluids Engineering*, **108**, 47-54

SARPKAYA, T. [Sept. 1992] "Brief Reviews Of Some Time Dependent Flows," *Journal Of Fluids Engineering*, **114**, 283-298

SCHEWE, G. [1983] "On The Force Fluctuations Acting On A Circular Cylinder In Crossflow From Subcritical Up To Transcritical Reynolds Numbers," *Journal of Fluid Mechanics*, **133**, 265-285

SCHUBAUER, G.B. & DRYDEN, H.L. [1935] "The Effect Of Turbulence On The Drag Of Flat Plates," *NACA Report No. 546*

SLAOUTI, A. & GERRARD, J.H. [1981] "An Experimental Investigation Of The End Effects On The Wake Of A Circular Cylinder Towed Through Water At Low Reynolds Numbers," *Journal of Fluid Mechanics*, **112**, 297-314

SPALART, P.R., LEONARD, A. & BAGANOFF, D. [1983] "Numerical Simulation Of Separated Flows," *NASA TM, 84328*

SPALART, P.R. [1988] "Vortex Methods For Separated Flows," *NASA TM, 100068*

STANSBY, P.K. [Jan. 1974] "The Effects Of End Plates On The Base Pressure Coefficient Of A Circular Cylinder," *Aeronautical Journal*, **78**, 36-37

STANTON, T.E. [Dec. 1903] "On The Resistance Of Plane Surfaces In A Uniform Current Of Air," *Minutes of Proceedings of the Institution of Civil Engineers*, **156**, 78-139

SZEPESY, S. & BEARMAN, P.W. [1992] "Aspect Ratio And End Plate Effects On Vortex Shedding From A Circular Cylinder," *Journal of Fluid Mechanics*, **234**, 191-217

TANEDA, S. & HONJI, H. [Jan. 1971] "Unsteady Flow Past A Flat Plate Normal To The Direction Of Motion," *Journal Of The Physical Society Of Japan*, **30:1**, 262-272

TOKUMARU, P.T. [May, 1991] "Active Control Of The Flow Past A Cylinder Executing Rotary Motions," Ph.D. Thesis, California Institute of Technology

TRITTON, D.J. [1988] *Physical Fluid Dynamics - 2nd edition*, Clarendon Press, Oxford

WARD, T.M. [Dec. 1976] "The Hydrodynamics Laboratory At The California Institute Of Technology - 1976," *ASME Journal of Fluids Engineering*, **98:4**, 740-750

WIESELSBERGER, VON C. [1922] "Weitere Feststellungen über die Gesetze des Flüssigkeits- und Luftwiderstandes," *Physikalische Zeitschrift*, **XXIII**, 219-224 [also 1923, Der Widerstand Verschiedener Körper in *Ergebnisse der Aerodynamischen Versuchsanstalt zu Göttingen*, II. Lieferung, 33-35]

WILLIAMSON, C.H.K. & ROSHKO, A. [1988] "Vortex Formation In The Wake Of An Oscillating Cylinder," *Journal of Fluids and Structures*, **2**, 355-381

WILLIAMSON, C.H.K. [1989] "Oblique And Parallel Modes Of Vortex Shedding In The Wake Of A Circular Cylinder At Low Reynolds Numbers," *Journal of Fluid Mechanics*, **206**, 579-627

APPENDIX A

Further Details of Apparatus and Procedures

A.1 Preface

This appendix presents additional descriptions of apparatus, procedures and experimental parameters, organized in roughly the same order as in the main text.

A.2 Flat Plate Details

Fig. A.1 gives details of the various flat plate models used in the investigations. The ID of each model is that used in the run sheets given in Appendix B for reference purposes.

Plate Ident.	Chord C (mm)	Thickness h (mm)	h/C Ratio	Max Span S (mm)	Bevel β (deg)	Max AR	Weight (grams)	Material	Comments
Cf_1	30	3.1	10.3%	500	30	16.7	66.7	Carbon Fibre	Primary Model
Cf_2	20	3.3	16.3%	460	30	23	39.1	Carbon Fibre	Smallest Chord
Cf_3	50	3.4	6.8%	500	30	10	123.9	Carbon Fibre	Used for Startup Runs
Cf_4	80	3.2	4%	500	30	6.3	195.6	Carbon Fibre	Largest Chord Thinnest
Al_3	40	6.5	16.3%	550	30	13.8	191.7	Aluminium	Flow Viz. Model
Wd_1	50	10	20%	500	30	10	192.8	Wood/Carbon Fibre	Thickest

FIG. A.1 Flat plate model details

A.3 Flow Visualization Camera

A schematic of the control mechanism for the 35mm camera and motor drive used for flow visualization pictures is shown in Fig. A.2. A function generator with programmable starting delay and pulse spacing was triggered by the motion start trigger from the carriage system and released the camera shutter at known intervals. The flash sync from the camera drove a relay to give a signal output which was recorded along with other collected data, such as force balance output; thus the exact timing of pictures relative to force measurements could be determined.

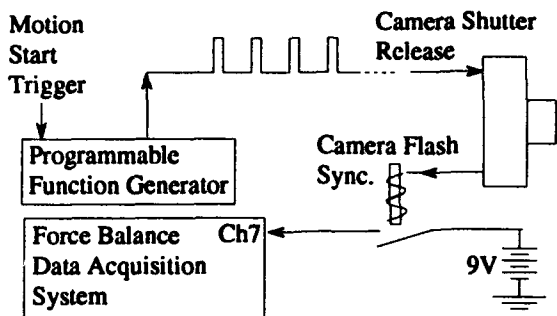


FIG. A.2 Camera control circuit

A.4 Force Balance Calibration

The force balance was calibrated using a set of known weights and the apparatus shown in Fig. A.3. Loads were applied to each load cell in turn and the response of it and the other two cells recorded. To minimize the effects of the pulley sticking, values were recorded while both increasing and decreasing the load. A typical calibration sheet is shown in Fig. A.4. Note that the cross-derivative terms in the final calibration matrix ($\text{Newtons} = f_n(\text{Volts})$) are four orders of magnitude lower than the diagonal terms, indicating very little cross-talk between load cells. The maximum deviation of recorded voltage levels from the best fit line was ≈ 0.01 Volts, or 0.002 Newtons. The uncertainty in the calculated slope (K_1_Σ), and thus the uncertainty in the balance, was $\approx \pm 0.03\%$; this was confirmed by repeated calibrations which consistently gave results to this level of repeatability.

Additional calibrations were done with the loads suspended below the level of the balance to induce vertical moments similar to those that are applied when a test model is mounted. These indicated very little sensitivity (0.25%) to out of plane moments for values typical of those found in experimental runs.

A.5 Force Balance Data Analysis

A block diagram for a typical force balance data analysis is shown in Fig. A.5. Interface 5lb strain gauge load cells were supplied with 12.5V excitation from 3 regulated DC power supplies. Their output went to a two-stage amplifier with a total gain of 3200 and a 4th order Butterworth analog low-pass filter with 25Hz. cutoff frequency. Output from this amplifier was recorded using a 12bit RC Electronics "ComputerScope" data acquisition system in a Zenith AT computer.

For the X-Y towing tank experiments a Setra 141b capacitance accelerometer simultaneously recorded carriage accelerations in the X direction. The output of this accelerometer (0.5 Volt/g) was amplified with a gain of 100 and then filtered with a 4th order Butterworth analog low-pass filter with 100Hz. cutoff frequency. This output was then recorded on the 5th ComputerScope channel.

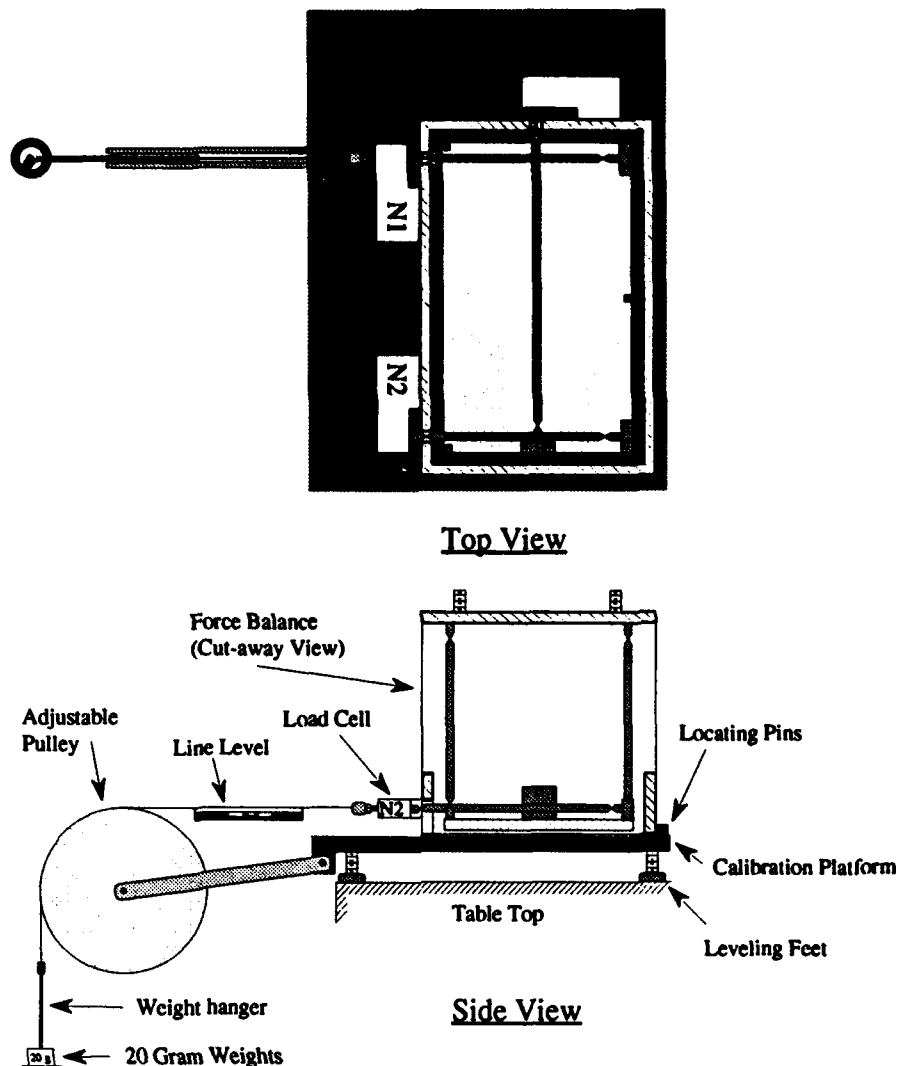


FIG. A.3 Schematic of apparatus used to calibrate the force balance

Typically about 10 seconds of data prior to the motion was taken to establish a tare level for the load cells, recording was then triggered by the carriage motion start trigger. Software allowed real time averaging of 16 samples to one 16 bit integer which was written to disk for subsequent analysis. Raw sampling rates were $64\mu\text{sec}$ to $256\mu\text{sec}$, or 1024 to 4096 16bit integers/second.

Numerous runs were performed with no water in the tank to determine a best fit line between the drag force response at a given plate mass and the X accelerometer output level. For experimental runs the mass of the plate corrected for buoyancy (mass of displaced water) was multiplied by this slope to give an effective inertial mass, which was multiplied by the accelerometer channel and subtracted from the measured drag forces. The drag history was further corrected during the acceleration by subtracting the displaced fluid mass times the programmed acceleration profile. This removed unwanted inertial forces due to both carriage acceleration and tipping.

X-Y TOW TANK FORCE BALANCE CALIBRATION
RECORD DATE: 03/18/92

CHNL: Exct
(V) Amp#1 Gain Amp#2 Gain Offset #1 Filt c/o Offset #2

Description: Calibration#10 (MAC: FrcBalCal_10)
Using 20g Weight Set (19.995g)
HP5326b DVM 10s Avg (10V Range)

N1 12.500 800*4 1 off 25Hz off
N2 12.500 800*4 1 off 25Hz off
D 12.500 800*4 1 off 25Hz off

	Weight (g)	N1onN1 (Volts)	N1onN2 (Volts)	N1onD (Volts)	N2onN1 (Volts)	N2onN2 (Volts)	N2onD (Volts)	DonN1 (Volts)	DonN2 (Volts)	DonD (Volts)
Point #1	0	-0.3271	-0.113	-0.0524	-0.3144	-0.1236	-0.057	-0.316	-0.1105	-0.0401
Point #2	Wt.Pan	-1.3226	-0.1176	-0.0495	-0.3227	-1.1526	-0.056	-0.3124	-0.1175	-1.0448
Point #3	20	-2.3699	-0.1216	-0.0506	-0.3261	-2.2447	-0.051	-0.3151	-0.1138	-2.1002
Point #4	40	-3.417	-0.1245	-0.0534	-0.3304	-3.3461	-0.051	-0.3182	-0.112	-3.1539
Point #5	60	-4.4767	-0.1251	-0.0568	-0.3323	-4.4442	-0.0519	-0.319	-0.1138	-4.2097
Point #6	80	-5.5289	-0.1341	-0.0534	-0.3345	-5.5426	-0.0519	-0.3157	-0.1177	-5.2659
Point #7	100	-6.5761	-0.1419	-0.0538	-0.3379	-6.6387	-0.0532	-0.3158	-0.1119	-6.3247
Point #8	120	-7.6293	-0.1396	-0.0505	-0.3406	-7.7402	-0.0543	-0.3158	-0.1148	-7.3825
Point #9	140	-8.682	-0.1418	-0.0518	-0.3446	-8.8375	-0.0565	-0.318	-0.1145	-8.433
Point #10	160	-9.732	-0.1526	-0.0496	-0.3498	-9.9345	-0.0559	-0.3204	-0.1184	-9.4894
Point #11	180	-10.791	-0.1552	-0.0488	-0.3576	-11.03	-0.0523	-0.3202	-0.1166	-10.545
Point #12	160	-9.7394	-0.15	-0.0509	-0.3528	-9.9326	-0.0546	-0.3183	-0.1144	-9.4946
Point #13	140	-8.6891	-0.1512	-0.0514	-0.3475	-8.8392	-0.0512	-0.3159	-0.1127	-8.4365
Point #14	120	-7.6373	-0.148	-0.0491	-0.3366	-7.7447	-0.0512	-0.3128	-0.1142	-7.3825
Point #15	100	-6.5843	-0.1395	-0.05	-0.3308	-6.6487	-0.0534	-0.3158	-0.1124	-6.3316
Point #16	80	-5.5383	-0.1386	-0.0504	-0.3367	-5.5482	-0.0557	-0.3248	-0.1148	-5.2727
Point #17	60	-4.489	-0.1293	-0.0527	-0.3288	-4.4507	-0.0538	-0.3195	-0.1178	-4.2211
Point #18	40	-3.4325	-0.123	-0.0552	-0.3249	-3.3552	-0.0515	-0.3181	-0.1167	-3.1666
Point #19	20	-2.3833	-0.1233	-0.0551	-0.3222	-2.2581	-0.0558	-0.3194	-0.1088	-2.1081
Point #20	Wt.Pan	-1.3318	-0.1148	-0.0493	-0.3188	-1.1593	-0.0529	-0.3202	-0.1078	-1.0513
Point #21	0	-0.3254	-0.1154	-0.0489	-0.3142	-0.119	-0.0504	-0.3243	-0.1097	-0.0407

Fitting Volts = K0 + K1*Weight :

Fit to N1onN1(1,19) vs.Weight: Max_err = 0.0115049 V Fit to N2onD(1,19) vs.Weight: Max_err = -0.00297599 V
K0 = -1.325; K1 = -0.052568; K1_Sigma = 2.42443e-5 K0 = -0.053; K1 = -3.63074e-06; K1_Sigma =
Fit to N1onN2(1,19) vs.Weight: Max_err = 0.00560629 V 8.29374e-6
K0 = -0.117; K1 = -0.000219961; K1_Sigma = 1.2694e-5 Fit to DonN1(1,19) vs.Weight: Max_err = -0.00718769 V
Fit to N1onD(1,19) vs.Weight: Max_err = -0.00476602 V K0 = -0.317; K1 = -4.45439e-06; K1_Sigma = 1.2575e-5
K0 = -0.052; K1 = 1.35533e-05; K1_Sigma = 9.49873e-6 Fit to DonN2(1,19) vs.Weight: Max_err = 0.00500049 V
Fit to N2onN1(1,19) vs.Weight: Max_err = 0.00756881 V K0 = -0.113; K1 = -1.7081e-05; K1_Sigma = 1.18026e-5
K0 = -0.320; K1 = -0.000186952; K1_Sigma = 1.31954e-5 Fit to DonD(1,19) vs.Weight: Max_err = -0.0068357 V
Fit to N2onN2(1,19) vs.Weight: Max_err = 0.00831223 V K0 = -1.05; K1 = -0.0527657; K1_Sigma = 1.7437e-5
K0 = -1.155; K1 = -0.0548706; K1_Sigma = 1.70153e-5

$$\begin{cases} N1 \\ N2 \\ D \end{cases} = \begin{cases} -5.256803e-02 & -1.869519e-04 & -4.454388e-06 \\ -2.199608e-04 & -5.487057e-02 & -1.708098e-05 \\ 1.355332e-05 & -3.630741e-06 & -5.276567e-02 \end{cases} \begin{cases} N1 \\ N2 \\ D \end{cases} = \begin{cases} -5.358617e+00 & -1.905728e-02 & -4.540660e-04 \\ -2.242210e-02 & -5.593331e+00 & -1.741180e-03 \\ 1.381582e-03 & -3.701061e-04 & -5.378764e+00 \end{cases} \begin{cases} N1 \\ N2 \\ D \end{cases}$$

Grams Volts Newtons

$$\begin{cases} N1 \\ N2 \\ D \end{cases} = \begin{cases} -1.866180e-01 & 6.358331e-04 & 1.554814e-05 \\ 7.481142e-04 & -1.787869e-01 & 5.781264e-05 \\ -4.798591e-05 & 1.246543e-05 & -1.859163e-01 \end{cases} \begin{cases} N1 \\ N2 \\ D \end{cases}$$

Newtons Volts

FIG. A.4 Typical force balance calibration record. (Calibration # 11, 03/18/92)

Since only X-acceleration information was available, lift and moment could not be corrected in a similar manner; they were instead corrected by removing the actual lift and moment values (scaled for plate mass) found at various carriage positions with no water in the tank. For very sensitive runs ($Re = 1000$) an identical plate was used for the no-water results and forces (corrected for buoyancy) subtracted directly, without need of an intermediate interpolation for plate mass. This corrected for the majority of carriage tipping errors, although it did not account for changes in carriage tip due to distortions in the tank when it was filled.

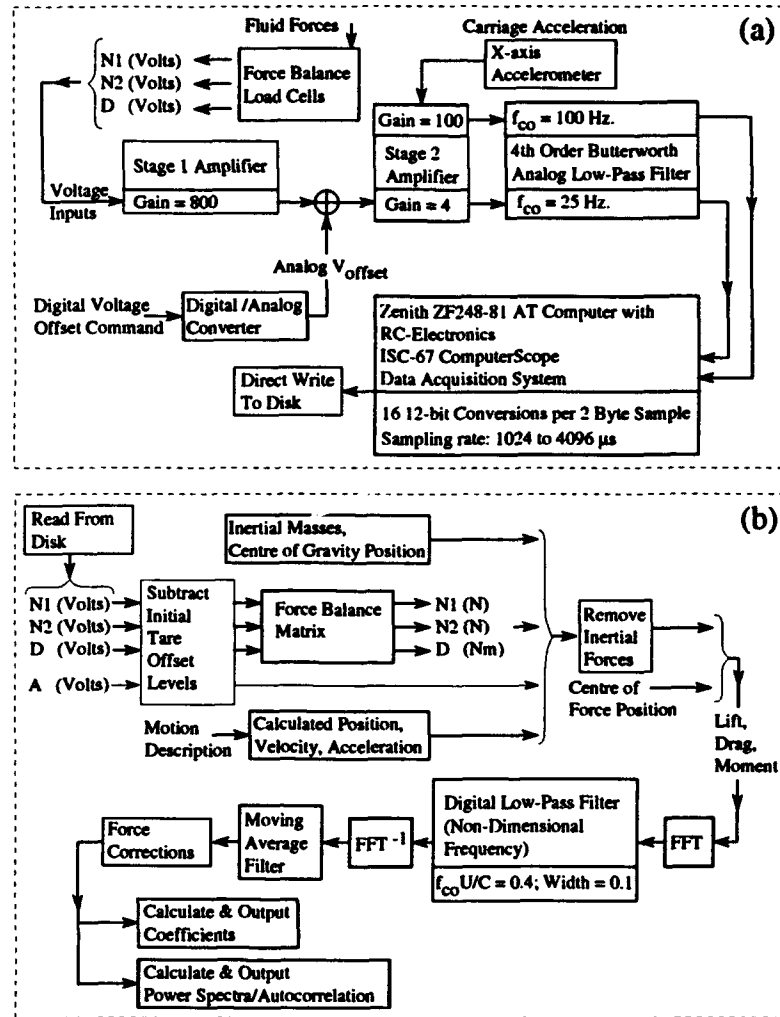


FIG. A.5 Force balance amplifier and data analysis block diagram.(a) performed during experiments; (b) post processing

Post processing began by averaging the pre-motion data to establish tare offset voltage levels and then subtracting these levels from all subsequent values. In the X-Y towing tank values for the model mass, displaced fluid volume, accelerometer output and a description of the carriage motion were used to determine non-fluid dynamic inertial force histories as described above, which were then subtracted from the force

levels determined by the force balance. The position of the model relative to the force balance was input and the resultant lift, drag and moment on the model determined. Power spectra of the force histories were calculated, followed by digital low-pass filtering in non-dimensional frequency as was described in Ch. 2 and final force coefficient calculation based on either programmed or LDV steady-state freestream velocity, fluid density and submerged model area. The width (-3dB) and cutoff of the digital filter could be specified; unless otherwise indicated $f_{co} = .4$ and $f_w = .1$ for all the results presented.

Depending on the relative position of the force balance and the model mount the accuracy of the resulting coefficients, particularly moment, could be strongly affected. Typically the model was mounted off center from the force balance to allow flow visualizations to be obtained, as was previously described. In this configuration small errors in angle of attack adjustment, which was accurate to only about 0.25° , would result in large offsets in mean pitching moment results, since both lift and drag then contributed strongly to moments at the balance center.

A.6 X-Y Towing Tank

The X-Y towing tank carriage system used DC servo motors with optical position encoders and tachometer feedback to control the X-Y position of the carriage. A block diagram of the X-Y towing tank electronics is shown in Fig. A.6; an amplifier with velocity feedback from the servo motors established a motor velocity proportional to input command voltage. Position feedback to a Galiei motion control board in a Epson XT computer supplied this command voltage based on a desired carriage velocity profile. As described previously, this velocity profile was entered as linear and sinusoidal velocity coefficients for each axis, as well as acceleration and deceleration profiles.

Accuracy of the carriage motion was determined both from accurately timing and measuring the carriage motions and by an accelerometer which was rigidly attached to the exterior frame of the force balance. This accelerometer was oriented so as to measure accelerations in the freestream direction; it was connected to the 5th channel of the force balance amplifier with an excitation of 15 Volts, a gain of 100 and a analog f_{co} of 100 Hertz; all of which yielded a 50 Volt/g signal level. It was calibrated by tipping it known amounts from horizontal and recording the response due to gravity. Output of the accelerometer during experimental runs, integrated and corrected for carriage rail waviness, is shown in Fig. A.7. It served as an additional check on the carriage motion and gave an indication of the level of vibration experienced by the balance system. Note that theoretically a constant acceleration was applied, giving a linear velocity profile in time, with the resulting profile vs. position as shown.

Motions were accurate to within about ± 1 mm and ± 5 msec for carriage velocities of 10 cm/s over the length of the tank and runs of thirty seconds duration, accelerometer output indicated good velocity accuracy, although large amplitude accelerations (vibrations) were present at high frequencies. These were

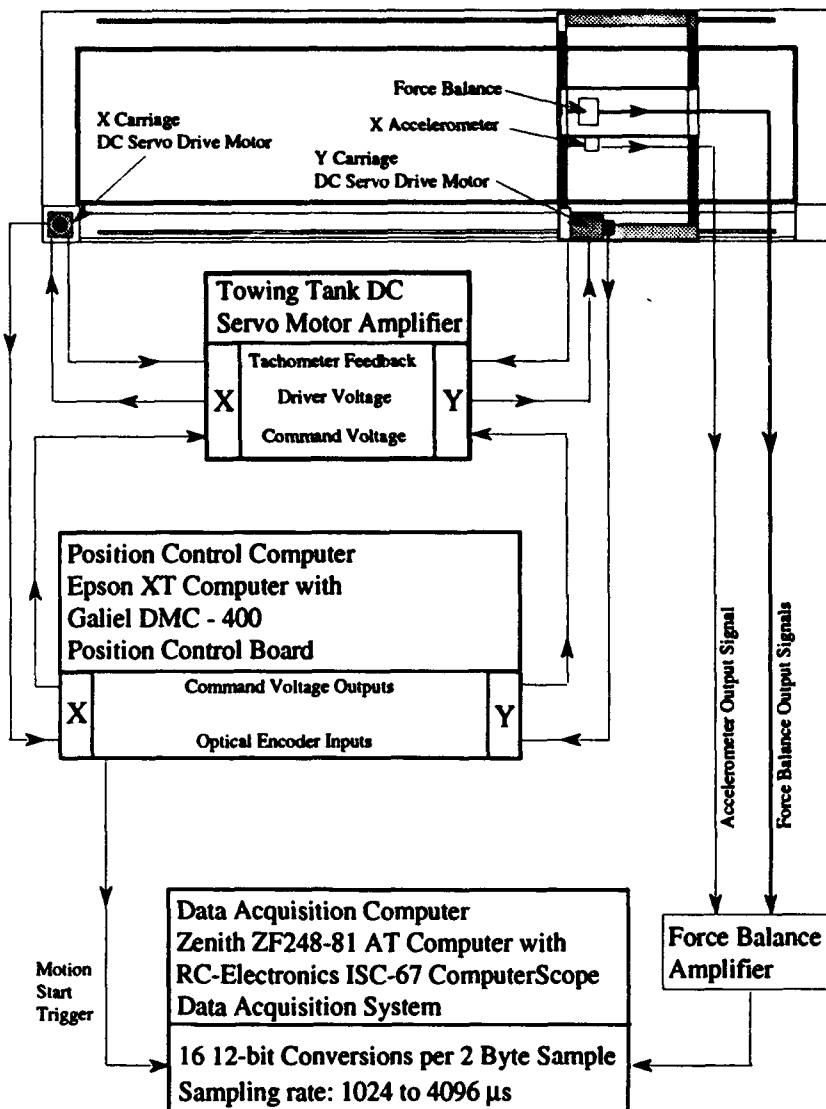


FIG. A.6 Layout of X-Y towing tank drive system electronics

filtered out with both analog and digital low-pass filtering; typically the frequency of these vibrations was sufficiently high above the shedding and other fluid dynamic frequencies so as to have a minimal impact on the large scale flow development.

Waviness in the carriage rails was due in part to different levels of water in the tank flexing the structure different amounts. The affect this had on the distance from the bottom of the carriage to the tank bottom for different water depths can be seen in Fig. A.8. Since the gap width for the *NBW* end condition was set at 0.1 mm from the highest point on the bottom, this figure also indicates how the width of this gap would vary at different locations along the tank. In addition, the variation of carriage to water surface distance is shown, giving a relative change of depth for models mounted on the tank. Since typical plate depths were about fifty cm, this change amounted to about a 0.1% fluctuation.

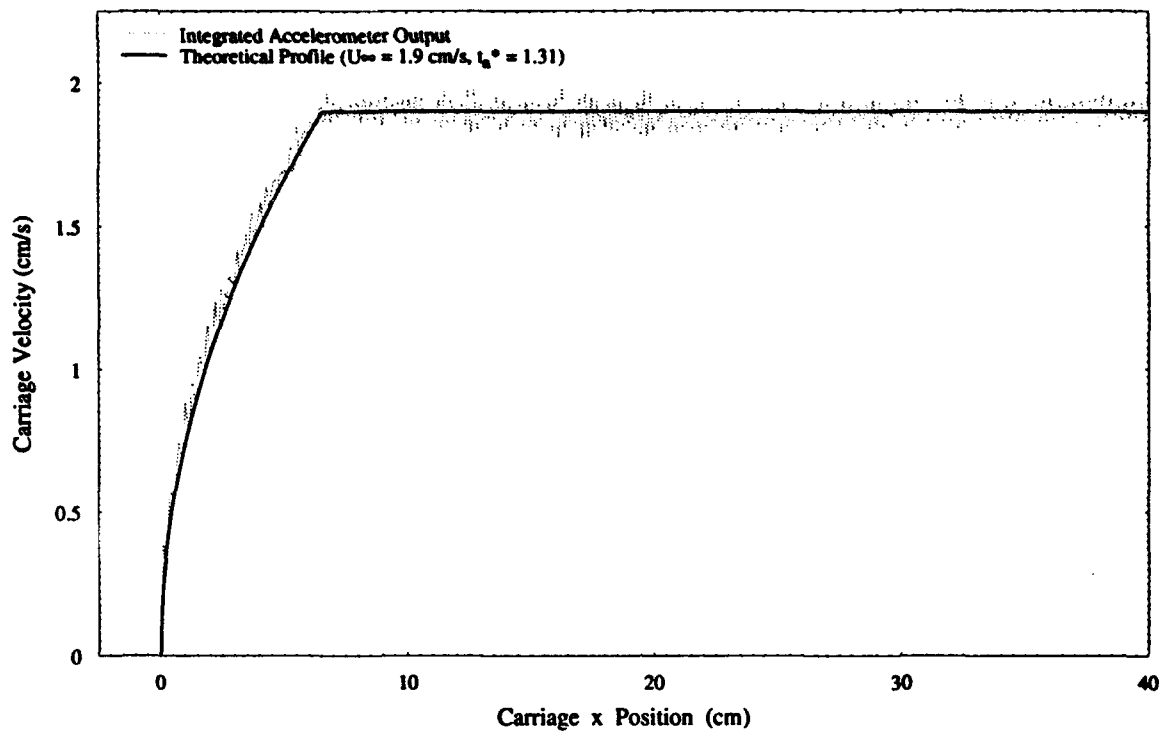


FIG. A.7 Integrated x accelerometer output giving velocity vs. position. Note the constant acceleration (linear velocity in time) starting profile

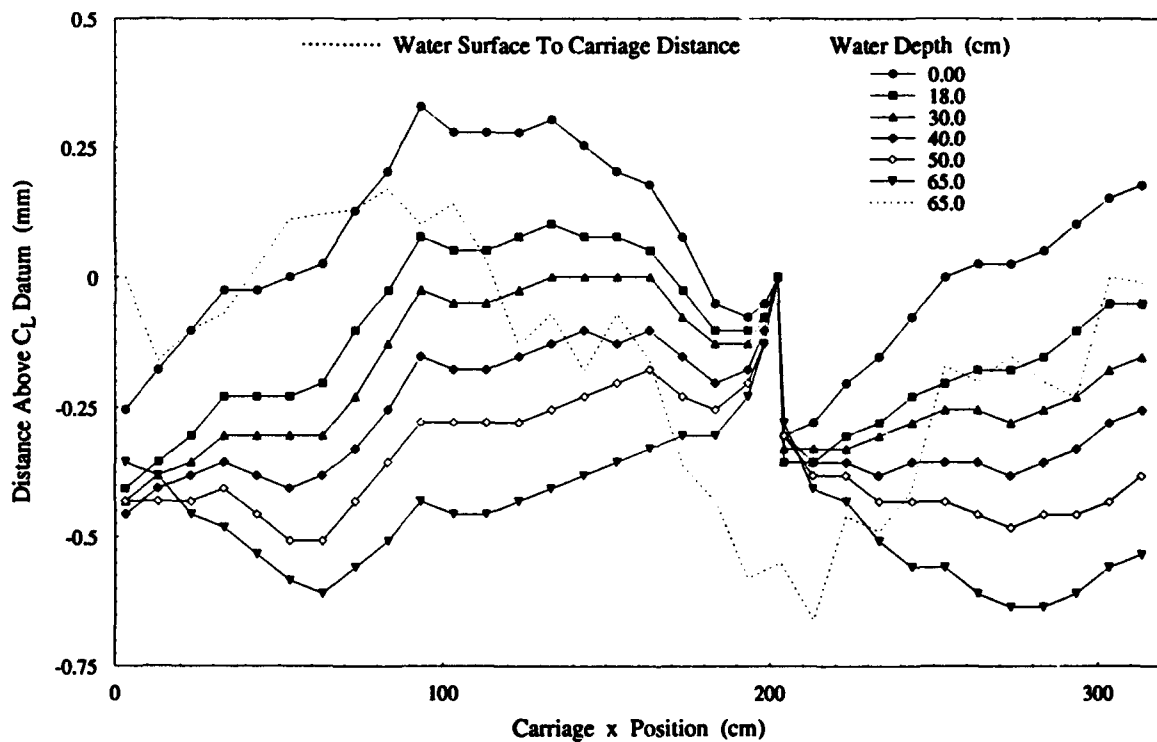


FIG. A.8 Height profile of X-Y towing tank bottom with varying water depths. Dotted line → distance of water surface above carriage datum

A.7 Free Surface Water Tunnel

Determining force coefficient values in the water channel required a very accurate knowledge of the freestream velocity. In addition, since forces levels fluctuated about 20%, it was important to record a time history of tunnel velocity fluctuation coincident with the force record. Both of these objectives were met by slightly modifying an existing LDV system designed Dan Lang for previous experiments (Lang, 1985 and Tokumaru, 1991). The system used is shown in Fig. A.9; it differs from the previous system only in the way in which LDV frequencies were analyzed and recorded.

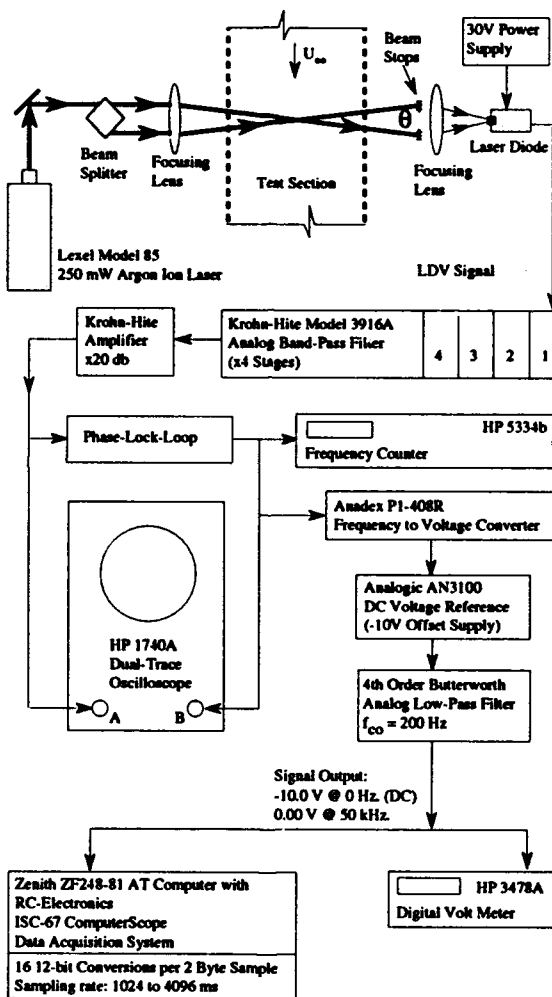


FIG. A.9 Layout of single channel free surface water tunnel LDV System

For these experiments, once the LDV signal was amplified and band-pass filtered it was input to a phase lock loop which locked a square wave onto the LDV frequency. This square wave was then input to a calibrated frequency to voltage converter which output a voltage level proportional to the input frequency. After some further filtering and a voltage offset this signal was then recorded simultaneously with those of the force balance load cells.

The frequency to voltage converter was calibrated using a known frequency square wave to yield a voltage to frequency curve; in subsequent data analysis the recorded LDV voltage was converted back to frequency using this calibration. The tunnel velocity was then determined from this frequency using the formula:

$$U_{\infty} = \frac{\lambda f}{2 \sin(\frac{\theta}{2})}.$$

Where λ is the wavelength of the Argon ion laser light, $\lambda_{ArgonIon} = 514.5\text{nm}$, f is the recorded LDV frequency and θ is the angle between the LDV beams, determined by measuring beam separation at two widely separated points.

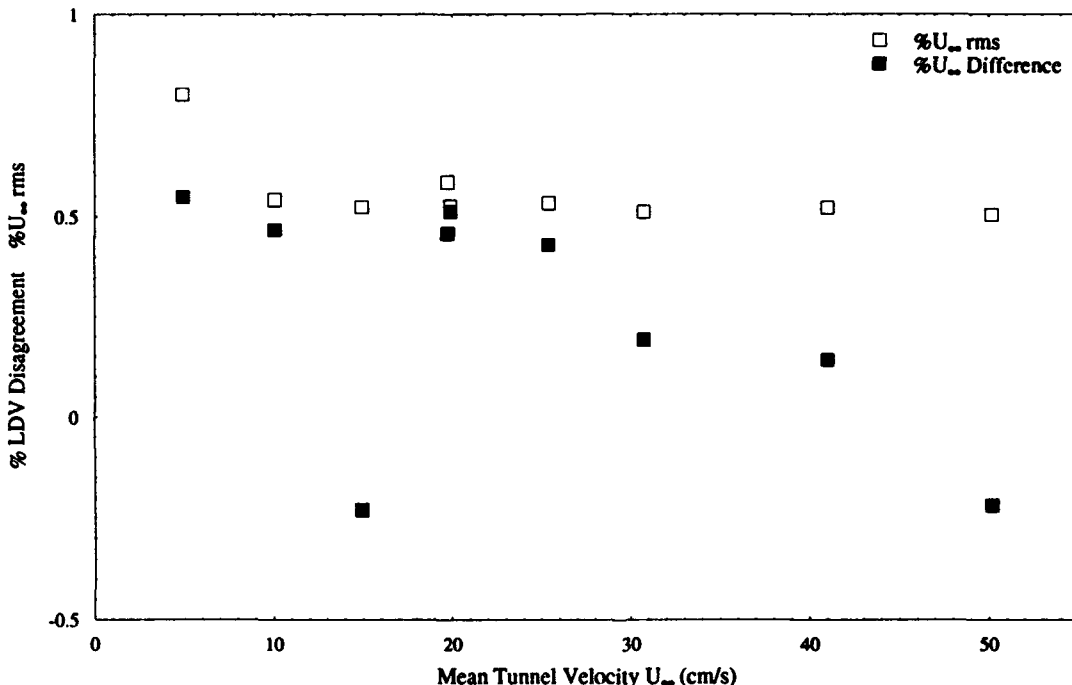


FIG. A.10 Comparison of two LDV measuring systems. Filled symbols: percentage disagreement in mean velocity; open symbols: percentage rms velocity

Errors in all these quantities indicated about a 0.5% overall error level in tunnel velocity measurement. An entirely separate method of determining and recording LDV frequency had previously been developed (Lang, 1985); although it was slightly more accurate and reliable, it was very difficult to correlate readings with those of force measurements, so this technique was used as a check only. Several examples of both techniques were recorded, with the percentage differences in mean velocity levels shown in Fig. A.10. These results also indicate a disagreement of about 0.5%, leading to a force coefficient uncertainty of 1% to 2%.

To determine how far above the floor of the tunnel models had to be placed to be outside of the boundary layer, several velocity profiles were taken at the mid-plane of the tunnel, at the same streamwise location as the models would later be mounted. Results for profiles of streamwise and vertical velocity are shown in Fig. A.11. From these it was determined that the lower ends of models should be a minimum of 6 cm from the tunnel floor.

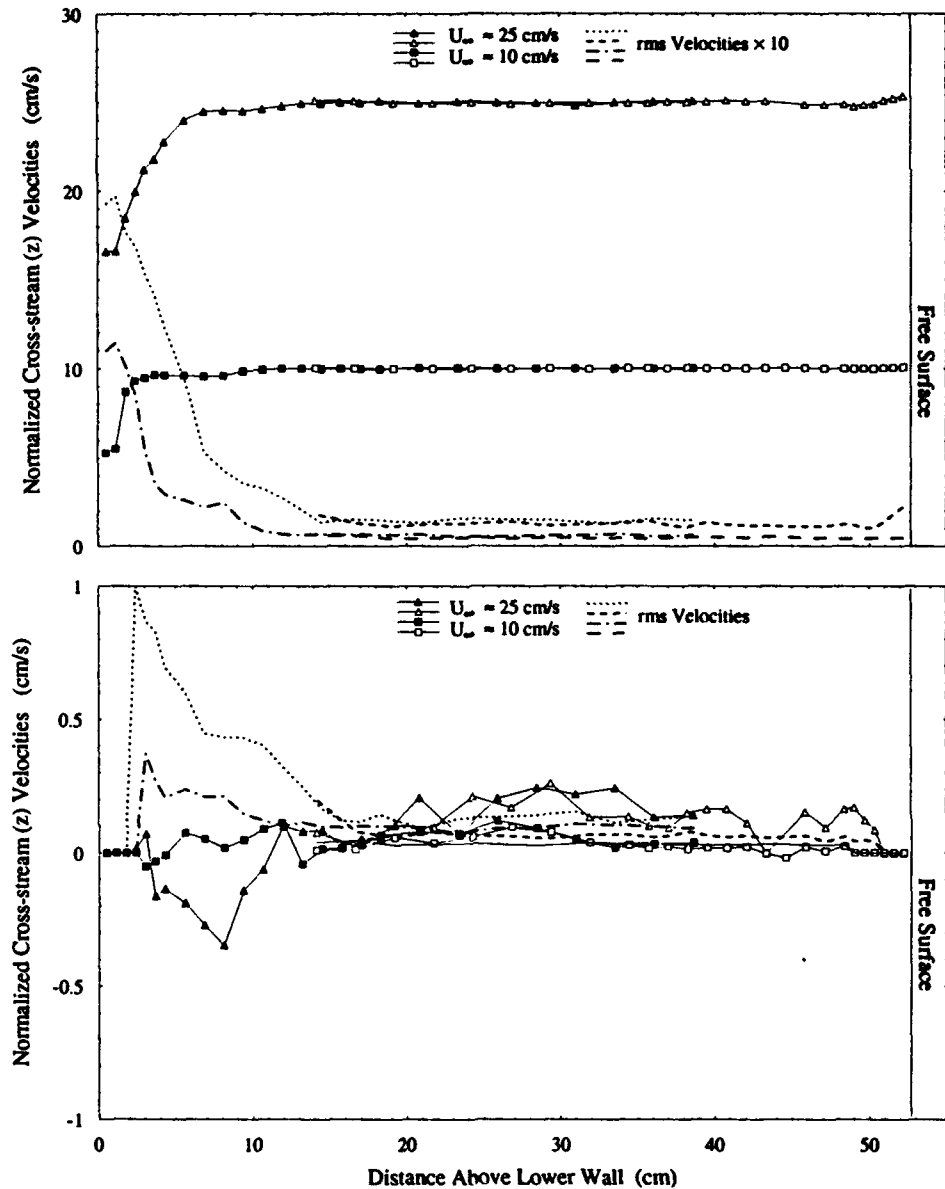


FIG. A.11 Streamwise and Cross-stream (z direction) velocity profiles in free surface water tunnel . Filled symbols: lower $\frac{1}{2}$ of test section; open symbols: upper $\frac{1}{2}$ of test section

Subsequent tunnel freestream velocity measurements were made at the location upstream of the model shown in Fig. 4.1. When a false bottom wall was installed, the side plates used to support it (see Fig. 4.1 and Fig. 2.7) subtracted 1.3cm from the width of the working section, so as a first-order correction this freestream velocity was increased by $\frac{1.3}{51} = 2.5\%$.

Data analysis for the water channel experiments was very similar to that used for the X-Y towing tank, with the exception that freestream velocity was not known *a priori*; instead, it was determined by the mean of the recorded LDV velocity signal over the length of each run. As previously described, initial and final tare

levels for the balance were determined in separate measurements with a guard in place around the model to isolate it from background drift velocities. Since typical run times were much longer than those used in the X-Y towing tank, balance zero levels drifting slowly with time became a problem, indicated by initial and final tare levels being different by up to 30 mV. This error was reduced by linearly correcting the tare levels from the beginning to the end of each run or set of runs, effectively making this uncertainty about 15 mV, or .003N.

At the higher tunnel velocities (30 and 40 cm/sec) surface waves were very apparent, while the water levels on the upstream and downstream faces of the plate differed by up to 1cm, which would introduce considerable error in calculated force coefficients for these velocities. The capillary wave speed in this tunnel was \approx 20 cm/sec; this was the maximum velocity used for the runs presented.

A.8 X-Y Towing Tank Stratification Profiles

The towing tank was stratified with Culinox 999 pure salt using the procedures outlined in Sec. 6.2. Resulting density profiles were measured indirectly using a platinum through-flow conductivity probe, which gave a direct measure of NaCl content. The probe was calibrated using known amounts of salt and distilled water; specific gravity was measured simultaneously with a hydrometer, yielding a S_g vs. conductivity curve, Fig. A.12.

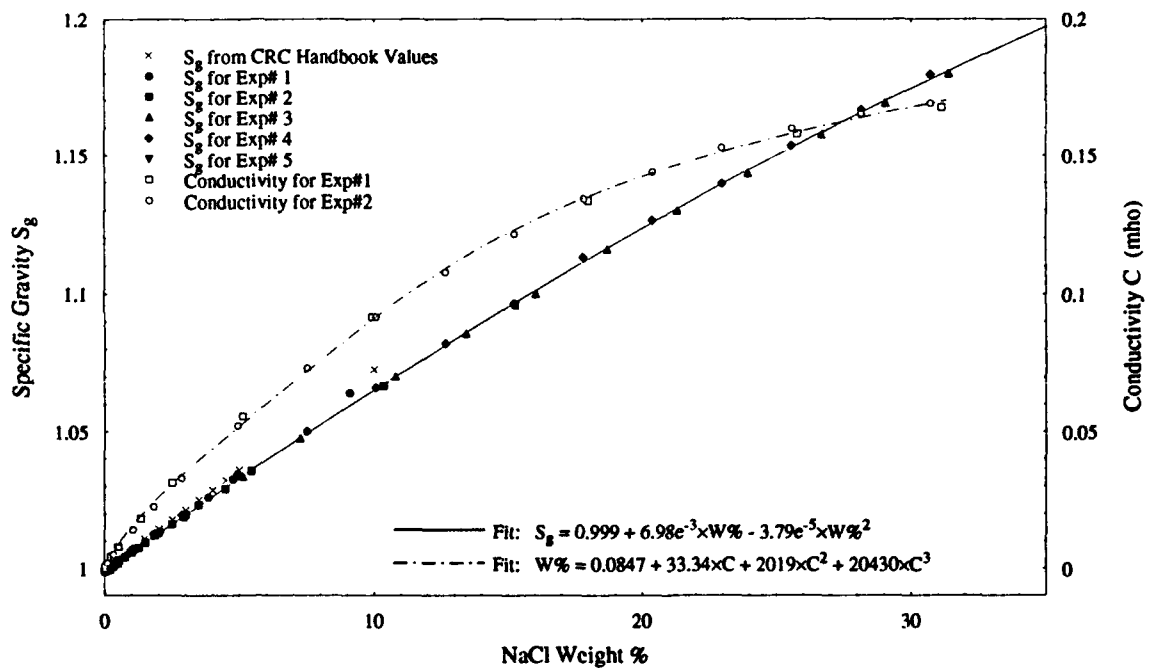


FIG. A.12 Conductivity probe calibration

The probe was lowered into the tank with an attached scale to indicate depth, as shown schematically in Fig. A.13. At even vertical intervals water was sucked into and through the probe, the resulting measurement gave an accurate indication of the density at that depth; water was then expelled from the probe before moving on to the next depth.

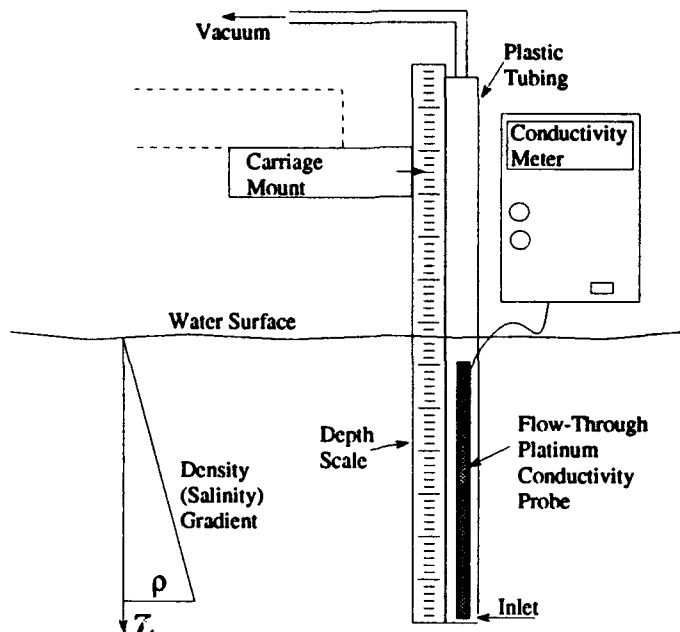


FIG. A.13 Schematic of conductivity probe used to measure density (salinity) gradients.

Profiles were typically taken from bottom to top at three X locations in the tank, although some profiles were taken top to bottom to note the effects, which were negligible. These profiles varied very little from place to place in the tank, and were quite robust, remaining fairly steep even after numerous experimental runs, as evidenced by Fig. A.14.

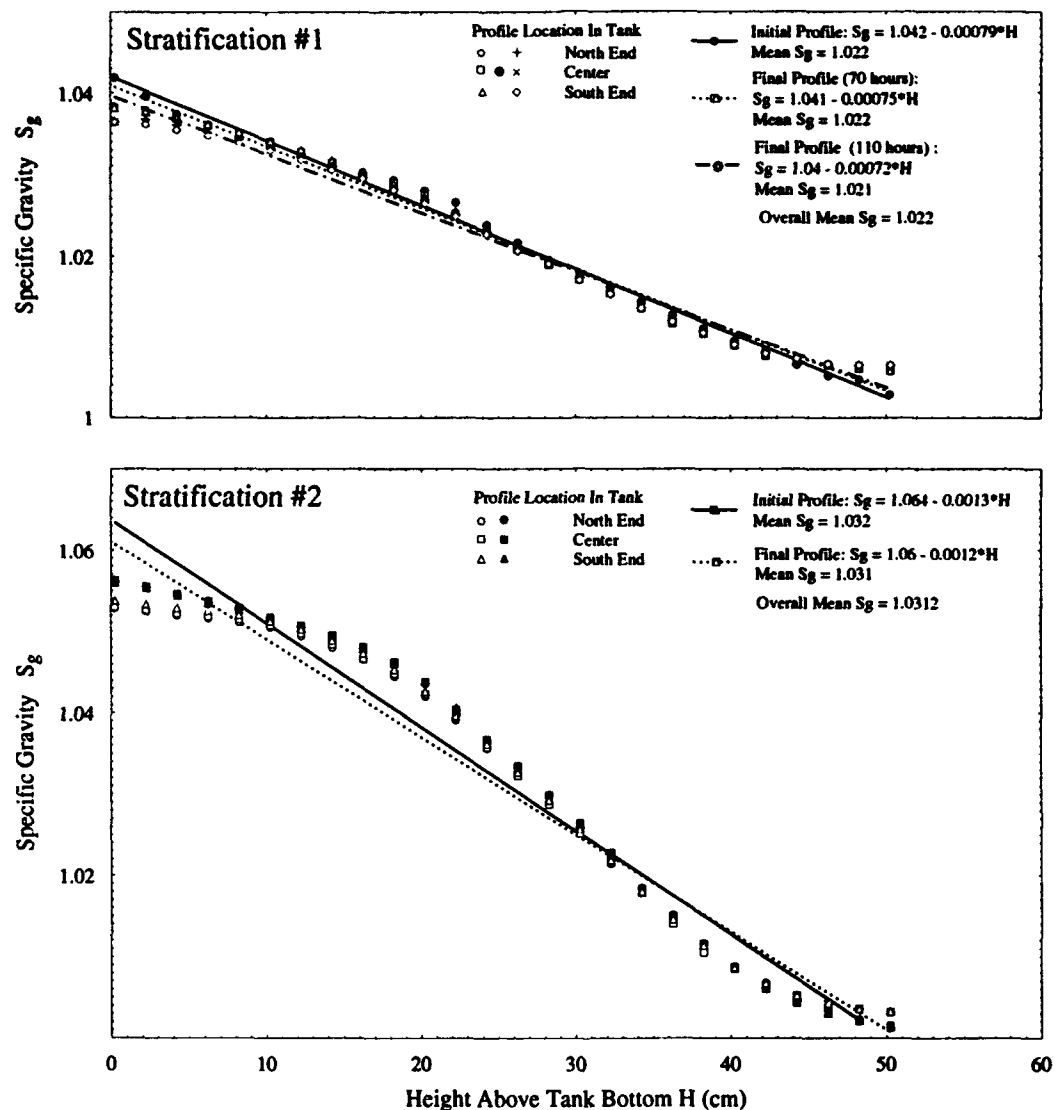


FIG. A.14 Specific gravity profiles for stratifications #1 and #2. Initial profiles were prior to experiments; for stratification #1 final profiles were taken after 70 hours and 25 experimental runs and again after 110 hours. Final profile for stratification #2 was after 50 hours and 20 experimental runs

APPENDIX B

Experimental Conditions

Due to the large number of possible parameters for each experiment, it was difficult to present all of the conditions relative to a result each time that result was given. This appendix cross-references and summarizes experimental parameters in five tables. A reference number has been given for each result presented elsewhere, and all relevant experimental parameters (such as the model used, Reynolds number, acceleration times, etc.) can be found under that number in one of the following tables, or in the table of flat plat model parameters, Fig. A.1. Tables Fig. B.1 and Fig. B.2 present values for the initial X-Y towing tank runs, referenced as "TT4#." Table Fig. B.3 is for free surface water tunnels results referenced as "FS#." Computational results referenced "CF#" can be found in Fig. B.4. Finally, towing tank results "TT5#" are in table Fig. B.5. The tables use the following abbreviations:

AR = Aspect Ratio AR ; AoA = Angle of Attack α ; U = Freestream (Carriage) Velocity U_∞

Re = Reynolds Number Re ; C = Chord; T/C = Thickness/Chord Ratio h/C

EPA = End Plate Angle; NEP = No End Plate; WEP = With End Plate

NBW = Near Bottom Wall; Mass = Mass of Plate In Grams

w/s = Mass of Plate+Support (Support Mass = 340.6g)

Ta* = Non-dimensional Acceleration Time t_a^*

Nodes = # of CFD nodes used to describe plate

The following after a number denotes:

nw = No water s1 = Stratification #1 s2 = Stratification #2

s3 = Stratification #3 (D#) = Flow Visualization Run using Film #

FIG. B.1 Page one of run parameters for unstratified X-Y towing tank experiments (TT4#, see Ch. 3)

Plate_Id = Cf_2		Plate_Id = Al_3		Plate_Id = Cf_1	
C = 2cm; Mass 39.1g (W/S 379.7)		C = 4cm; Mass 191.7g (W/S 532.3)		C = 3cm; Mass 66.7g (W/S 407.7g)	
T/C = 16.25s		T/C = 16.25s		T/C = 10.3s	
U=24 cm/s	U=5.9 cm/s	U=11.8 cm/s	U=24 cm/s	U=8 cm/s	U=15.75 cm/s
Re=5000	Re = 2500	Re = 5000	Re = 10000	Re = 2500	Re = 5000
Ri(s1)=0.005	Ri(s1)=0.332	Ri(s1)=0.083	Ri(s1)=0.020	Ri(s1)=0.531	Ri(s1)=0.026
Ri(s2)=0.0085	Ri(s2)=0.561	Ri(s2)=0.140	Ri(s2)=0.034	Ri(s2)=0.896	Ri(s2)=0.042
AoA=90	AoA=95	AoA=90	AoA=90	AoA=90	AoA=90
No End Plate(NEP)					
AR = With End Plate(NEP)					
6	Near Bottom(NBM)				
No End Plate(NEP)	69				
+20					
+15					
+12.5					
+10					
+7.5					
+5					
With End Plate(NEP)	+2.5				
10	EPK =				
0	927				
-2.5					
-7					
-10					
-15					
-20					
Near Bottom(NBM)	847	848	849	841	850, 861
No End Plate(NEP)					
13	Near Bottom(NBM)				
No End Plate(NEP)	8100				
AR = With End Plate(NEP)	8101				
17	Near Bottom(NBM)				
No End Plate(NEP)	8102				
AR = No End Plate(NEP)	8103				
18	Near Bottom(NBM)				
No End Plate(NEP)	8104	8145		8112*	
19	Near Bottom(NBM)	8125*1	8126*1	8110*	8111*
20	Near Bottom(NBM)	8162*2	8160*2	8124*1	8161*2
21	No End Plate(NEP)	8105		8154	8176*2
22	With End Plate(NEP)	8106		845	855
23	With End Plate(NEP)	8107		852	853
24	Near Bottom(NBM)	8108		854	851
25	No End Plate(NEP)	8109		856	858
26	With End Plate(NEP)	8110		857	864
27	Near Bottom(NBM)	8111		860	861
28	No End Plate(NEP)	8112		862	863
29	With End Plate(NEP)	8113		864	865
30	Near Bottom(NBM)	8114		866	867
31	No End Plate(NEP)	8115		868	869
32	With End Plate(NEP)	8116		870	871
33	Near Bottom(NBM)	8117		872	873
34	No End Plate(NEP)	8118		874	875
35	With End Plate(NEP)	8119		876	877
36	Near Bottom(NBM)	8120		878	879
37	No End Plate(NEP)	8121		880	881
38	With End Plate(NEP)	8122		882	883
39	Near Bottom(NBM)	8123		884	885
40	No End Plate(NEP)	8124		886	887

FIG. B.2 Page two of run parameters for unstratified X-Y towing tank experiments (TT4#, see Ch. 3)

		Plate_Id = CL_1		Plate_Id = AL_	
		C = 3cm; Mass = 66.7g (w/e 407.3)		C = 4cm; Mass = 39.1g (w/e 379.7)	
		T/C = 10.38		T/C = 16.35%	
U=5 cm/s	U=10 cm/s	U=15 cm/s	U=20 cm/s	U=25 cm/s	U=30 cm/s
Re = 1500	Re = 3000	Re = 4500	Re = 6000	Re = 7500	Re = 9000
AcA=90	AcA=90	AcA=90	AcA=85	AcA=90	AcA=90
AR = 1	No End Plate(NEP)	With End Plate(NEP)	With End Plate(NEP) EPA = 0	With End Plate(NEP) EPA = +5	With End Plate(NEP) EPA = -5
4	With False Bottom	With False Bottom	With End Plate(NEP) EPA = 0	With End Plate(NEP) EPA = +5	With End Plate(NEP) EPA = -5
6	With False Bottom	With False Bottom	With End Plate(NEP) EPA = 0	With End Plate(NEP) EPA = +5	With End Plate(NEP) EPA = -5
8	With False Bottom	With False Bottom	With End Plate(NEP) EPA = 0	With End Plate(NEP) EPA = +5	With End Plate(NEP) EPA = -5
10	With False Bottom	With False Bottom	With End Plate(NEP) EPA = 0	With End Plate(NEP) EPA = +5	With End Plate(NEP) EPA = -5
15	With False Bottom	With False Bottom	With End Plate(NEP) EPA = 0	With End Plate(NEP) EPA = +5	With End Plate(NEP) EPA = -5
22	With End Plate(NEP)	With End Plate(NEP)	With End Plate(NEP) EPA = 0	With End Plate(NEP) EPA = +5	With End Plate(NEP) EPA = -5

FIG. B.3 Run parameters for free surface water tunnel experiments (FS3#, see Ch. 4)

FIG. B.4 Run parameters for CFD experiments (CFD#, see Ch. 5)

Plate_Id = Cf_3		Plate_Id = Al_3			
C = 5cm; Mass 191.7g (wts 532.3); TIC = 16.25%					
AR = 10					
U=1.9 cm/s					
Re=1000	U=9.5 cm/s	U=14.25 cm/s	U=19 cm/s		
Re=5000	Re = 7500	Re = 10000	Re = 10000		
Ri(5)=13.33	Ri(5)=0.533	Ri(5)=0.237	Ri(5)=0.133		
Ri(5)=87.5	AlA=50	AlA=90	AlA=90		
Ta* = 5	#12, #149nw, #150nw, #209nw, #214nw, #215nw	#26, #172nw	#30, #197.5 AlA=90		
Ta* = 1.0	#13, #151nw #152nw	#27, #173nw	#34, #197.5 AlA=90		
Ta* = 1.31	#40->#93, #184nw- #208nw- #234nw- #259nw- #260s.3->#311s3	#1->#11, #14, #23, #22, #153nw->#157nw #210nw, #213nw, #216nw #312s.3->#338s3	#34, #153 #123(D92), #124(D94), #340s.3 (D99)		
Ta* = 2.5	Near Bottom (NBW)	#15, #158nw #159nw #211nw #212nw #217nw	#29, #174nw		
Ta* = 5.0	5.0	#16, #24 #160nw	#30, #161nw		
Ta* = 10.0	10.0	#17, #163nw	#31, #162nw		
Ta* = 20.0	20.0	#18, #164nw	#32, #165nw		
Ta* = 30.0	30.0	#19, #167nw	#33, #166nw		
Ta* = 45.0	45.0		#20, #168nw		
Ta* = 55.0	55.0		#21, #171nw		
AR = 10 (12.5 for Al_3)		AR = 12.5			
U=24 cm/s					
Re=1000	Re = 5000	Re = 5000	Re = 5000		
Ri(5)=0.0335	Ri(5)=0.221	Ri(5)=0.221	Ri(5)=0.0335		
AlA=50	AlA=90	AlA=90	AlA=90		
			AlA=87.5		
			AlA=87.5		
			#115(D82), #116(D83), #117(D84), #118(D85), #121(D88), #131nw, #141nw, #142nw		
			#128(D98), #129nw, #130nw, #144nw		
			#119(D86), #133nw, #134nw		
			#127(D97), #135nw, #136nw		
			#125(D95), #120(D87), #137nw, #138nw		
			#126(D96), #147nw, #148nw		

FIG. B.5 Run parameters for stratified X-Y towing tank experiments(TTS#, see Ch. 6)

APPENDIX C

Drag Coefficient Scaling

This appendix presents experimental and 2d numerical model drag coefficients in accordance with the non-dimensional scaling suggested by Corteletti (1992) for a general power law velocity starting profile: $U(t) = U_\infty t^m$ for $0 < t < t_a$ with $m = 1$. Time scaling remains unchanged ($t^* = x/C$), but the drag coefficients are reduced by C_d , during the acceleration and scaled by the *instantaneous* freestream velocity $U(t)$ at time t , rather than a constant U_∞ as was used previously. Theoretically this scaling is only applicable during (short) accelerations, but it appears to collapse the data for later times, although rather than a single post acceleration drag level, two levels are apparent. Note similarities between the experimental and numerical results: in both cases the $t_a^* = 5.0$ result crosses from one curve to another immediately following the acceleration, while smaller t_a^* cases all follow a lower level curve and larger t_a^* cases follow a higher curve.

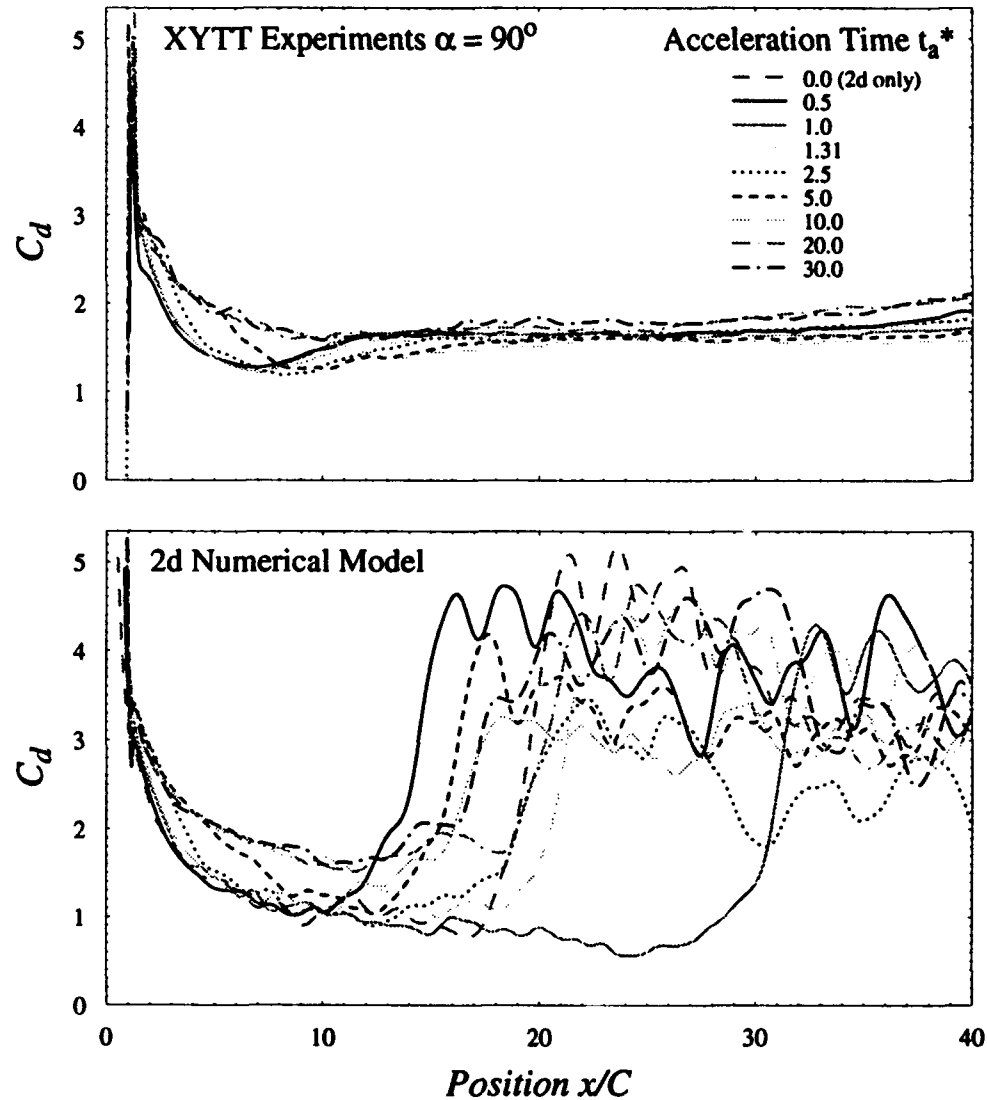


FIG. C.1 Drag coefficient scaling. $C_d = (C_d - C_{d,i}) \times (U_\infty/U(t))^2$